STANFORD SYNCHROTRON RADIATION

1992 ACTIVITY REPORT

Stanford University • Stanford • California

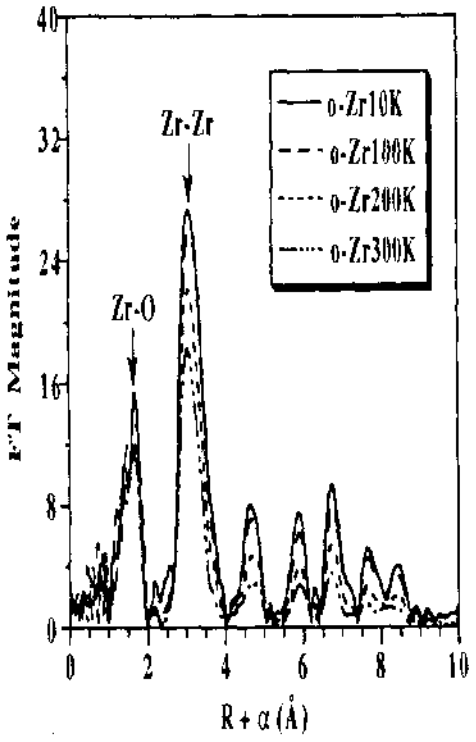

Figure 2. Temperature dependence of Zr-FT for pure orthorhombic zirconia

Our study has experimentally demonstrated the intrinsic instability of the fluorite-type Zr cation network. Coherent scattering between central Zr ion and distant cations is weaker and vibration modes of the Zr-cation network are softer in tetragonal zirconia than in monoclinic, orthorhombic, or stabilized cubic zirconia. In addition, the outer four oxygens in the 8-fold coordinated Zr-O polyhedron are only loosely bonded and are subject to very large static and dynamic distortions. This effect is illustrated by the expanded portion of the Fourier transform shown in Figure 3.

Dopant Structure

We have also successfully performed EXAFS experiments at the dopant absorption edges for doped zirconia solid solutions. Dopants studied include the Ge-, Nb-, and Y-K edges as well as Ce-L_{III} edge. In particular, we have obtained Nb EXAFS data with a very high signal/noise ratio using the SSRL Ge detector array. This experiment was essentially impossible using a conventional fluorescnece ion chamber due to the very strong absorption of Zr at Nb-K edge energy. Analysis of these data is in progress.

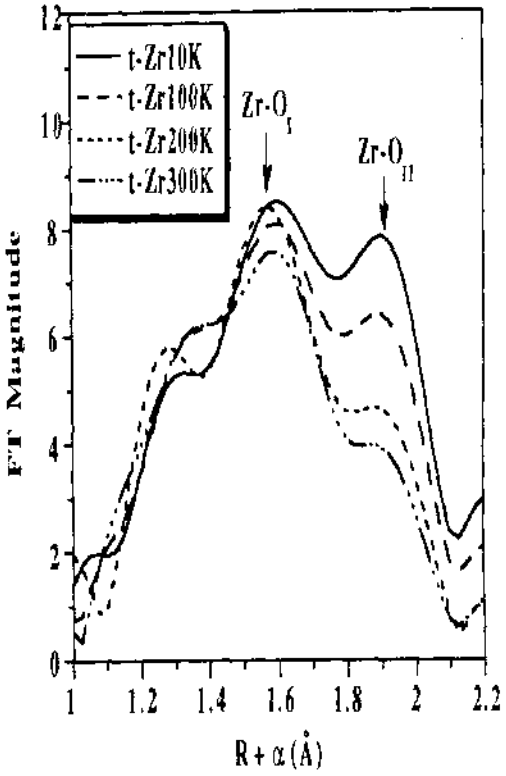

Figure 3 Temperature dependence of Zr-O shell in tetragonal zirconia solid solution

Conclusions

It is found that, for all of zirconia solid solutions studied, the dopant-oxygen distances are significantly different from the Zr-O distances. The dopant-cation distances, on the other hand, are usually very close to the Zr-Zr distance, confirming the formation of solid solutions. A general structural picture for zirconia solid solutions is one that places the dopant cations randomly on the Zr sites in the cation network, but with distorted and sometimes very different dopant-oxygen polyhedra surrounding these dopants. In the case of Ge^{4+} doping and Y-Nb co-doping, short-range cation ordering has been suggested from our EXAFS results.

Based on the above structural information and other EXAFS results obtained from NSLS, we are beginning to obtain a complete picture of the atomistic origins of phase stabilization in zirconia.

Acknowledgements

Supported in part by a grant from the NSF (DMR-8807024).

Reconstructions and Structural Transitions of the CaF_2/Si(111) Interface

C. A. Lucas, G. C. L. Wong* and D. Loretto

Center for Advanced Materials, Materials Sciences Division, Lawrence Berkeley Laboratory, University of California, Berkeley, CA 94720, *and Department of Physics, University of California, Berkeley, CA 94720.

Introduction

CaF_2/Si (111) is a prototypical system for studying atomic and electronic structure at the ionic/covalent interface. As a consequence there has been a wide range of experiments aimed at determining the interface structure and a number of models have been proposed [1,2]. Despite this attention no consistent picture has emerged. Conflicting results have been attributed to differences in sample preparation and the varying sensitivity of experimental techniques [3,4,5]. The problem relates to more general issues concerning the differences between surface and interface structure. In particular, it is questionable whether the structure observed at monolayer coverages, which is accessible to many standard surface probes, is representative of the true interface between two materials [6]. The latter can only be studied with techniques that employ highly penetrating beams, such as x-ray diffraction and transmission electron microscopy (TEM). It is the structure of the buried interface that influences the electronic properties.

The aim of our program is to combine x-ray diffraction and TEM to study the CaF_2/Si(111) interface. The samples are grown by molecular beam epitaxy (MBE), enabling strict control of the growth conditions. This combination of state-of-the art technologies offers a unique opportunity to study the relatively unexplored phenomena of phase transitions and reconstructions at buried interfaces.

Sample Preparation

CaF_2 was grown by MBE on well-oriented (miscut<0.5°) Si (111) substrates in an ISA/Riber CBE 32P ultrahigh vacuum (UHV) system. The Shiraki etched Si substrates [7] were outgassed thoroughly and then heated to 880°C to remove the protective oxide. Cooling to the growth temperature (720°C) routinely resulted in a sharp (7x7) reflection high-energy electron diffraction (RHEED) pattern. CaF_2 was deposited by evaporation from an effusion cell at 1150°C. During deposition the pressure was typically ~$1x10^{-10}$ torr at a growth rate of ~1 CaF_2 triple layer (TL) per 30 seconds. At 720°C CaF_2 films with a thickness of ~7TL's (~22Å) were grown. This is below the critical thickness for strained layer growth (~12TL's). The sample was then cooled to room temperature where, due to the smaller lattice mismatch, it is possible to grow more CaF_2 in a layer-by-layer mode without introducing strain relieving dislocations. Using this 'template' method pseudomorphic growth has been achieved up to a thickness of ~60 TL's. Samples were capped with 50Å of amorphous Si and removed from the vacuum for TEM and x-ray diffraction measurements.

Experimental Details and Results

X-ray reflectivity is a powerful technique for determining surface structure and has been employed with considerable success in studies of reconstructed metal surfaces [8,9]. The technique is analogous to LEED or RHEED measurements of the (0 0) specular rod, but the weak interaction of x-rays with matter enables use of the kinematical approximation to scattering theory, in the form of a one-dimensional Fourier summation over the layers of the crystal [10]. Figure 1 shows the reflectivity profile for a 7TL thick CaF_2 film. The measurement was performed on beam line 7-2 at the Stanford Synchrotron Radiation Laboratory using a 4-circle Huber diffractometer and a focussed 1mm (vertical) x 2mm (horizontal) incident x-ray beam (λ = 1.2398Å). The sample was mounted at the center of the diffractometer axes, with its surface normal in the vertical scattering plane. Scattered x-rays were detected by a scintillation counter after passing through 6mm (vertical) x 10mm (horizontal) slits at a distance of ~1m from the sample. Each point corresponds to a background subtracted integrated intensity obtained from θ scans at the appropriate 2θ scattering angle along the specular rod. The data has been corrected for the Lorentz factor ($\sin 2\theta$) and the variation of sample area illuminated by the x-ray beam ($\sin \theta$). No data was collected for L<0.9 reciprocal lattice units due to scattering from the amorphous Si cap which affects the low angle reflectivity data. The

intensity diverges at the Si (111) Bragg reflection and was not measured over the range L=0.98-1.02 Si(111) reciprocal lattice units (Si r.l.u.).

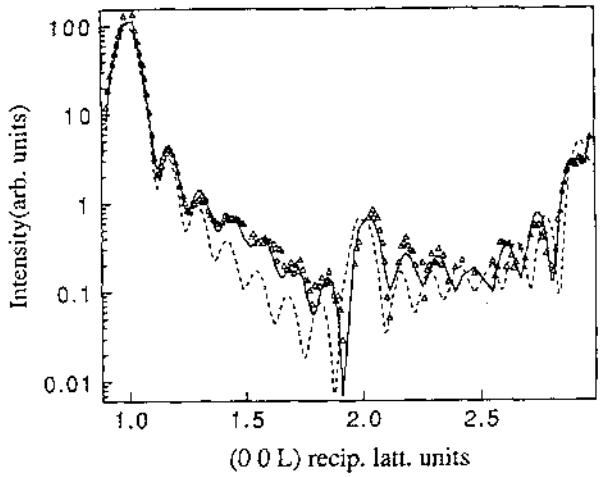

Figure 1. Measured x-ray reflectivity of a 7 triple layer (TL) CaF_2/Si(111) film. The data points are background subtracted integrated intensities corrected for the Lorentz factor and the variation in illuminated sample area. The dashed line is a calculation with a simple interface model (interface spacing d=4.55Å). The solid line is a fit to the data with a two-layer interface according to the parameters in Table I.

In a recent paper we presented similar x-ray scattering measurements from CaF_2/Si(111), over a reduced range of L (0.8-1.2) around the Si (111) Bragg reflection [11]. The measurement is sensitive to the "long-range" interface separation from the bulk of the substrate to the bulk of the film [12]. Over this L range good fits to the data were obtained with a lattice separation d = 4.55Å. This value indicates that there is a layer in between the two lattices. The dashed line in Figure 1 corresponds to a simulation with the 4.55Å interface spacing. The calculated intensity is given by the modulus squared of the structure factor F(q), where

$$F(q) = f_{Si}(q) \sum_{j=-\infty}^{0} \exp(iqz_j)$$

$$+ \exp(iqd)\{f_{Ca}(q)+2f_F\cos(qc/4)\} \sum_{k=0}^{N} \exp(iqz_k)$$

$f_{Si}(q)$, $f_{Ca}(q)$ and $f_F(q)$ are atomic form factors which include the Debye-Waller factor [13], zj are the atomic height coordinates, c is the lattice spacing of the CaF_2 film with a thickness of N triple layers, and d is the interface separation. Although the model fits the data around the (111) Bragg reflection it is clearly not a good fit to the data over the larger q range. Between Bragg reflections the scattering from atoms in bulk positions interferes destructively and is roughly equal in intensity to the scattering from an isolated monolayer [14]. The measurement is thus sensitive to the details of the interface structure projected onto the surface normal direction. An isolated monolayer at the interface is simple to include in the scattering model with an additional multiplying factor ρ_j representing a possible partial layer occupation (i.e. ρ_j varies between 0 and 1). Strain in the interface region can be accounted for by allowing the bulk layers to move away from their ideal positions. There are a number of constraints which must be imposed on the modelling procedure: we look for a model which has physically reasonable bondlengths and is consistent with previous results. It has been shown that upon initial adsorption the CaF_2 molecule dissociates to give a sub-monolayer coverage of CaF [1,4,5]. We can reproduce our data by including a CaF layer at the interface but this results in a Si-Ca separation of ~1.6Å which is not compatible with the Ca-Si bondlength (3.0-3.2Å) [15]. The best fit to the data with a two-layer interface (the next simplest model) is shown by the solid line in Figure 1. The structural parameters are given in Table I.

Table I. Parameters to the fit to the x-ray reflectivity data shown by the solid line in figure 1.

Layer	Occupation ρ_j	Displacement from ideal position (Å)	Comments
Top Si double layer	1	$\Delta_{Si}=0\pm0.1$	Displacement towards the surface
CaF (layer 1)	0.46±0.2	$d_1=2.7\pm0.1$ $\Delta_F=0$	Center of Si double layer to Ca atom i.e. F atom at $d_1+c/4+\Delta_F$
CaF (layer 2)	0.65±0.2	$d_2=2.2\pm0.1$	Ca(layer 2)-Ca(layer 1)
		$\Delta_F=-0.4\pm0.2$	i.e. F atom at $d_2+c/4+\Delta_F$
CaF_2 (first layer)	1	$\Delta_{CaF2}=-0.3\pm0.1$	Ca-Ca(layer 2) = $c+\Delta_{CaF}$

Number of CaF_2 layers, N=7 c=3.170±0.008Å (c_{Si} = 3.13559 Å)

The Ca-Si interface separation (d = 2.7Å) agrees with the ion-scattering results of Tromp and Reuter [1]. A partial occupation (~40%) of CaF at threefold hollow sites (T4/H3) is more than sufficient to saturate the Si dangling bonds. However, the vertical separation between the CaF at the interface and the next layer is too small to accommodate CaF_2 in the second layer. If we assume a second layer of CaF we obtain a good fit to the data with a partial occupation of ~60% in the second layer and bulk CaF_2 stacking above this. The interlayer spacing implies that the bondlengths are slightly larger than in bulk CaF_2. However, the angular rigidity of covalent bonding is not a feature of ionic materials where the bonding can be thought of as a low energy packing of charged spheres. The different bondlength for Ca-F, when Ca is in the +1 valence state rather than the +2 state found in CaF_2, is, therefore, not unexpected.

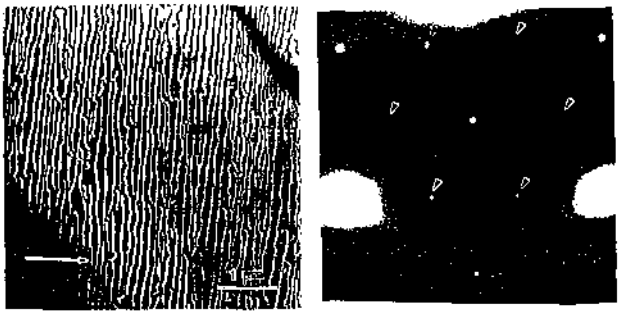

Figure 2. (a) A two-beam, bright-field transmission electron micrograph taken from a 23 TL thick CaF_2 grown using the "template" method. The [220] diffraction vector is marked. (b) Part of a [111] transmission electron diffraction (TED) pattern taken at 200 keV from an 18 TL thick CaF_2 layer. The features marked with arrows lie close to 1/3<220> positions and can be attributed to a reconstructed layer at the CaF_2/Si(111) interface.

In figure 2(a) the line defects show contrast under different two-beam conditions consistent with a displacement along $[11\bar{2}]$. Such line defects are anticipated at 1/3[111] steps on the Si substrate as a consequence of differences between the symmetry operators of the Si and the B-type CaF_2. The presence of so few defects indicates that the in-plane lattice parameter of the CaF_2 film is matched to that of the Si substrate. This agrees with the x-ray diffraction experiments which show an increase in the (111) CaF_2 lattice parameter. Furthermore, the presence of so few defects suggests an atomically smooth interface. This is also in agreement with the x-ray data, which can be modelled without atomic scale roughness.

In figure 2(b) the brightest peaks are reciprocal lattice points which have a non-zero structure factor for bulk Si and CaF_2. Weaker peaks at 1/3<224> are disallowed for the bulk but are allowed at a (111) interface/surface. The weakest features in 1/3<220> positions are consistent with a $(\sqrt{3}x\sqrt{3})R30°$ unit cell (root-3), indexed using the Si surface unit cell. It is easy to construct this symmetry in a partially occupied layer and the result therefore supports the x-ray scattering model. During growth the root-3 symmetry is not observed. As the coverage increases the RHEED pattern changes in the sequence (7x7) → (3x1) → (4x1) → (1x1). This implies that the interface is ordered differently when it is first grown from when it is buried under the CaF_2 film. A more detailed examination of the reflection positions in figure 2(b) reveals that they are systematically displaced from the root-3 positions. Preliminary grazing incidence x-ray diffraction measurements confirm the TED results. The results are shown in figure 3. One surface reflection was measured, displaced from the root-3 position and accompanied by regularly spaced satellite peaks. This scattering could be explained by the existence of stress domains, driven by an anisotropic stress on a high symmetry surface [16], leading to a weakly incommensurate interface phase [17].

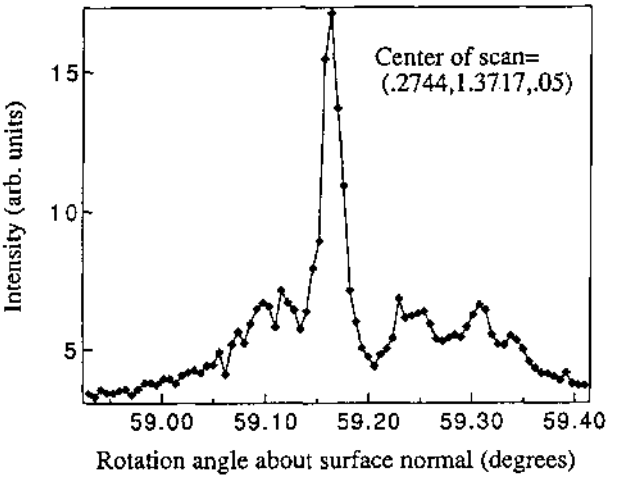

Figure 3. Grazing-incidence x-ray diffraction. A rocking scan in the vicinity of the (4/3, 1/3, .05) Si reciprocal lattice position (indexed using the conventional LEED notation for the Si (111) surface), where scattering due to a root-3 reconstruction would be observed. The peak center is actually displaced away (a rotation of ~1.9°) from the root-3 position. The central peak (17 counts per second) appears to be accompanied by regularly spaced satellite reflections.

The CaF_2/Si(111) interface described above is consistent with previous ion scattering [1] and x-ray standing wave measurements [3] of sub-monolayer coverages, which indicated that CaF is adsorbed on threefold hollow sites (T4/H3). This corresponds to the CaF-Si composite surface, the first layer of the two-layer interface. Our study of the initial stages of growth showed that the CaF-Si composite surface is progressively covered by coherently strained islands, ~3TL's thick, which eventually form a uniform epitaxial layer of CaF_2. The transition from the reconstruction observed by RHEED to the root-3 structure must occur during the formation of the overlayer. It is possible that the existence of the 2-layer interface is a consequence of the kinetic constraints against rehybridisation, after the Si bonds have been saturated (which requires only 1/3 of

a monolayer of CaF). This suggests that the interface may be not be at a global energy minimum.

We have been able to drive a structural transition from the metastable two-layer interface to an interface more characteristic of a single layer [18]. Rotating-anode x-ray reflectivity measurements, over a reduced range around the Si(111) Bragg reflection, indicated an abrupt change in the interface spacing, from d=4.55Å to d=2.9Å (the results are not presented here). The structural transition is driven by the coherent strain applied at the interface by the CaF_2 epilayer. Unrelaxed films of the same thickness (19TL's) can be prepared with the two different interface structures. For example, two films grown by the 'template' method, with homoepitaxial growth at room temperature in one case, and at 430°C in the other have different interfaces. The film grown at room temperature shows the two-layer interface. The additional strain in the 430°C film drives the interface transition. We are unable to observe the transition in unrelaxed samples grown isothermally at 720°C, even though the lattice mismatch is large. At 720°C a film will relax at 12TL's before the transition is induced. However, a thick enough relaxed 720°C film will eventually build up enough residual strain to drive the transition [19].

Summary and Future Experiments

To summarize, we have reconciled the discrepancies between previous models of the CaF_2/Si(111) interface. On the basis of x-ray diffraction and TEM measurements, we propose a two-layer interface which undergoes an irreversible transition to a lower energy structure. The results call into question traditional assumptions regarding the similarities between surface and interface structures and indicate that a variety of interesting phenomena may be observed at heteroepitaxial interfaces.

Recent TEM measurements suggest that the strain driven transition is accompanied by an incommensurate → commensurate transition in the root-3 reconstruction. We plan to measure the structure factors associated with the commensurate root-3 phase, in order to derive a detailed structural model of the interface. We are also building a heating stage to study the transition in-situ. In addition to the simple CaF_2/Si system we have grown epitaxial Si back on top of the CaF_2 layer. Measurement of non-specular crystal truncation rod scattering allows separation of the scattering components from A-type and B-type epitaxial layers. The structural information will be combined with measurements of the optical and electronic properties of the isolated, 2D semiconducting silicon.

Acknowledgements

We are grateful to Phil Cullen for technical assistance and to Tai Nguyen for help at SSRL. D.L. acknowledges the National Center for Electron Microscopy for use of its microscopes. We also thank the staff and user administration at SSRL for their hospitality and, in particular, Sean Brennan for his support on beam line 7-2. SSRL is operated by the Department of Energy, Division of Chemical Sciences. This work was supported by the Director, Office of Basic Energy Sciences, Materials Sciences Division of the U.S. Department of Energy under Contract No. ACO3-76SF00098.

References

[1] R. M. Tromp and M. C. Reuter, Phys. Rev. Lett. 61, 1756 (1988).
[2] J. L. Batstone, J. M. Phillips and E. C. Hunke, Phys. Rev. Lett. 60, 1394 (1988).
[3] J. Zegenhagen and J. R. Patel, Phys. Rev. B 41, 5315 (1990).
[4] Ph. Avouris and R. Wolkow, Appl. Phys. Lett. 55, 1074 (1989).
[5] M. A. Olmstead, R. I. G. Uhrberg, R. D. Bringans and R. Z. Bachrach, Phys. Rev. B 35, 7526 (1987).
[6] H. Hong, R. D. Aburano, D. -S. Lin, H. Chen, T. -C. Chiang, P. Zschack and E. D. Specht, Phys. Rev. Lett. 68, 507 (1992).
[7] A. Ishizaka and Y. Shiraki, J. Electrochem. Soc. 133, 666 (1986).
[8] D. Gibbs, B. M. Ocko, D. M. Zehner and S. G. J. Mochrie, Phys. Rev. B 38, 7303 (1988).
[9] B. M. Ocko, D. Gibbs, K. G. Huang, D. M. Zehner and S. G. J. Mochrie, Phys. Rev. B 44, 6429 (1991).
[10] I. K. Robinson and E. Vlieg, Surf. Sci. 261, 123 (1992).
[11] C. A. Lucas and D. Loretto, Appl. Phys. Lett. 60, 2073 (1992).
[12] I. K. Robinson, R. T. Tung and R. Feidenhans'l, Phys. Rev. B 38, 3632 (1988).
[13] the atomic form factors are obtained from polynomial fits to the values given in 'The International Tables for X-ray Crystallography, Vol. 3', (Kynoch Press, Birmingham, England, 1968).
[14] I. K. Robinson and D. J. Tweet, Rep. Prog. Phys. 55, 599 (1992).
[15] C. G. Van de Walle, Phys. Rev. B 43, 11913 (1991).
[16] O. L. Alerhand, D. Vanderbilt, R. D. Meade and J. D. Joannopoulos, Phys. Rev. Lett. 61, 1973 (1988).
[17] P. W. Stephens, P. A. Heiney, R. J. Birgeneau, P. M. Horn, D. E. Moncton and G. S. Brown, Phys. Rev. B 29, 3512 (1984).
[18] C. A. Lucas, G. C. L. Wong and D. Loretto, Phys. Rev. Lett., in press (1993).
[19] for a discussion of strain effects see, for example, the two volumes of 'Strained-Layer Superlattices', edited by T. M. Pearsall (Academic Press, San Diego, CA, 1991).

INTERLAYER FORCES BETWEEN TETHERED CHAINS

G. A. McConnell, M. C. Fair and A. P. Gast
Department of Chemical Engineering
Stanford University, Stanford, CA 94305 USA

Introduction

Interactions between polymer chains anchored at one end to a surface are of extreme fundamental interest as well as applicability in colloidal suspensions modified by adsorbed polymers. Introduction of the Surface Forces Apparatus (SFA) allowed experimentalists to examine directly the force generated by polymer layers adsorbed to essentially flat surfaces. (1) Yet, this technique cannot be unambiguously extended to systems with a high degree of curvature.

To address the interactions between polymer layers tethered to a convex surface we use amorphous diblock copolymers suspended in a preferential solvent. The unfavorable enthalpic interactions between the solvent and the insoluble block cause aggregation into spherical domains called micelles. The micelles used in these experiments contain a dense core of poly(styrene) and a diffuse corona composed of poly(isoprene) chains when suspended in decane.

Experimental

The architecture of a single micelle is dictated by polymer-solution thermodynamics. For example, Cogan et al. studied the effect of an additional solvent on the micellar structure using a lattice, mean-field theory. (2) In our case, by varying the block ratios we generate micelles exhibiting different character. For example, diblocks with small poly(styrene) blocks and larger poly(isoprene) blocks produce micelles with a low aggregation number (number of diblock chains in a micelle). As a result, the micelle has a small core with a comparitively larger corona. By reversing the block ratio we create micelles with large cores and coronas thin in comparison to the core.

The small angle X-ray experiments are ideal for studying these 10-70 nm sized micelles. At very dilute concentrations the intensity contains only intramicellar information. The Guinier approximation offers an appropriately weighted measure of the radius of gyration (Rg) for the micelle. Figure 1 displays a Guinier plot for micelles at .75 wt% formed from PSPI 30K/20K diblocks. Using Zimm analysis, we deduce the number of diblock copolymer chains in a micelle. Also, the intensity profile is essentially the Fourier Transform of the polymer density profile (sometimes referred to as the form factor) taking into account the X-ray contrast.

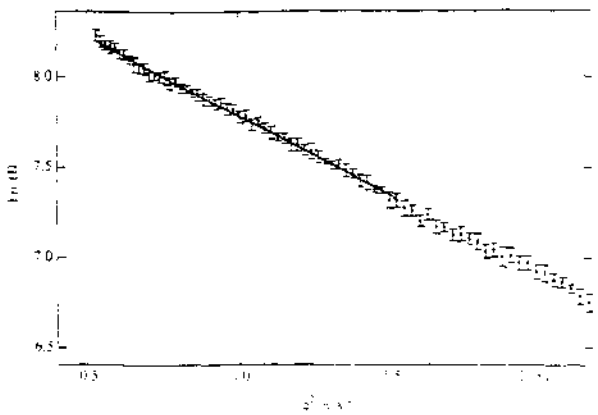

Figure 1. Guinier approximation for micelles formed from PS/PI 21K/20K diblocks at .75 wt % in decane.

It is simplest to take into account the contrast and compare the Rg with some model of the polymer profile. Gast and Cogan extended a model for star-polymers to micelles.(3) Table 1. shows a comparison between experimental values and this analytic scaling model. The overall micelle radius can be compared with with the hydrodynamic radius obtained from dynamic light scattering experiments.

TABLE 1.

Micelle diblock PS/PI	Rg X-ray	Rg model	Rh DLS	Rm model
10K/30K	108	122	153	216
10K/20K	119	133	210	248
30K/20K	165	168	284	366
46K/20K	211	196	331	436

All values are in Angstrom. (Rg) =radius of gyration. (Rh)= hydrodynamic radius . (Rm) = overall micelle radius suggested by scaling model.

In most cases the model tends to overestimate the polymer profile. We expect this trend as recent numerical mean field calculations predict a more rapid coronal decay in polymer density as the curvature is decreased.(4)

The differing architecture can easily be seen by the form factors in Figure 2. The micelles formed from the 46K/20K diblocks are, as expected, the largest micelles, having a large dense core and a thin corona. As such, their intensity profile decays most rapidly. The micelles from the 10K/20K diblocks display the slowest decay in intensity as a function of q (the magnitude of the scattering vector; where $q=(4\pi/\lambda)\sin(\theta/2)$).

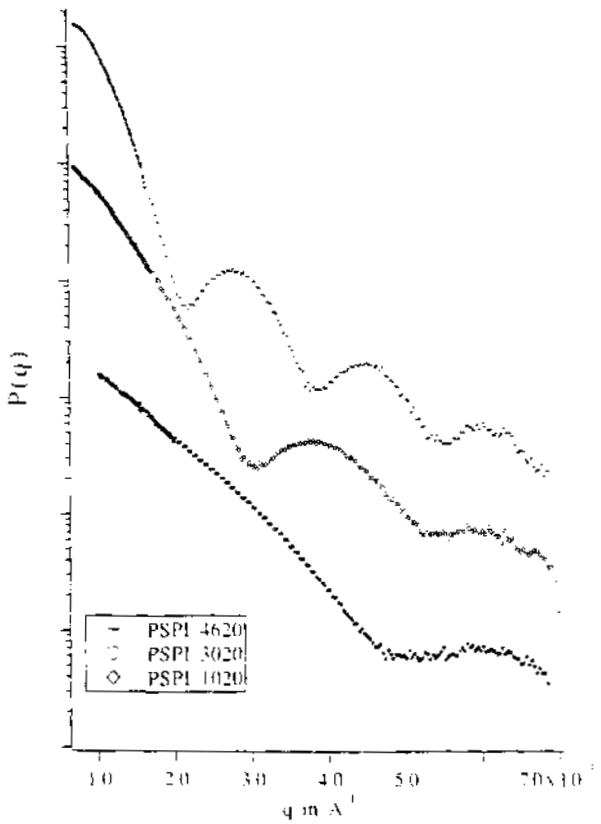

Figure 2. Form factors for micelles formed from PS/PI : 46K/20K;31K/20K; and 10K/20K respectively at .75 wt% in decane.

Upon increasing the concentration, the micelles are forced to interact with each other. At this moderate concentration, around 5-10 wt. %, the system is appropriately treated as a particulate system (particles composed of poly(styrene) cores whose interaction potential is mediated by a poly(isoprene) layer). Experiments from the SFA show that layers of sufficiently high surface densities interact through a purely repulsive mechanism. We still anticipate a purely repulsive potential as suggested by the SFA experiments because the mechanism for repulsion, osmotic stress and elasticity from chain distortions, is still applicable; however, the exact potential caused by polymers tethered at curved interfaces is yet unknown.

Experimentally, for this concentration range, the intensity profile is a product of both form and the interference caused by interactions between micelles, also referred to as the structure factor. By dividing out the form obtained from low concentration studies, we obtain an experimental structure factor. We model this through the simplest purely repulsive mechanism, that of a hard sphere. There are several limitations in this strategey. 1) The true interaction is not a hard sphere, but a softer purely repulsive interaction potential. 2) The range over which we can extract the structure factor is dictated by the form which decays as q^6, and so is at some point obscured by the noise. 3) This strategy is limited to concentrations over which the form factor obtained from low concentrations still represents the particle form at high concentrations (i.e. below overlap concentrations).

Given these limitions, we carefully extract the structure factors for our systems. Figure 3 shows experimental structure factors compared with an effective hard sphere structure factor for micelles formed from PSPI 30K/20K at 5,7.5, and 10 wt%. The effective hard sphere decreases with increasing concentration demonstrating a measure of the compressibility of the corona.

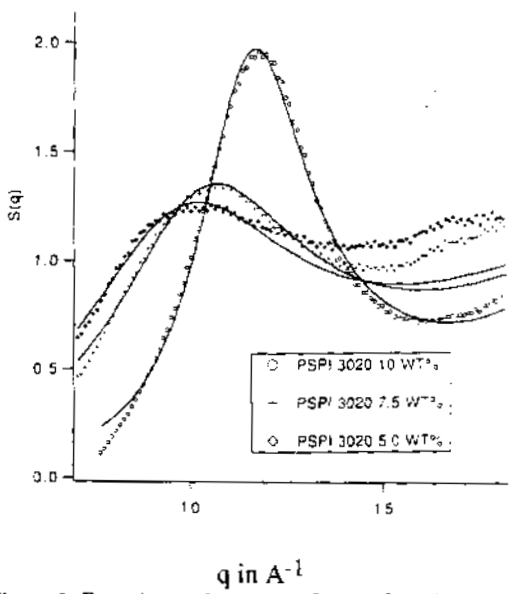

Figure 3. Experimental structure factors for micelles formed from PS/PI 30K/20K. The hard sphere radius follows: Rhs= 284 @10%;Rhs=291@7.5%and Rhs=301@5%. All values in Angstrom.

Particles interacting through purely repulsive mechanisms exhibit a variety of disorder to order transitions as the volume fraction is increased. Years ago, Hoover and Ree first explained the nature of the "freezing" transition for hard spheres. (5) Recently, Gast and Monovoukas demonstrated experimentally the relationship between potential and phase behavior for electrostatically charged colloids. (6) This data complemented theoretical work by Robbins *et al.* for Yukawa potentials. (7)

In diblock systems containing a preferential solvent, Hashimoto accounted for scattering off of ordered spherical domains, although he incorrectly identified the srtructure as simple cubic. (8) Nagler and Harkless later correctly identified that system lattice type as body-centered cubic. (9) These authors did not fully investigate the nature of the transition nor do they postulate a mechanism.

Here, we find a disorder to order transition for two of our micellar systems at moderate concentrations into what we beleive are face-centered cubic arrays. Figure 4 shows the intensity profile for micelles formed from PSPI 46K/20K diblocks at 22 wt %.

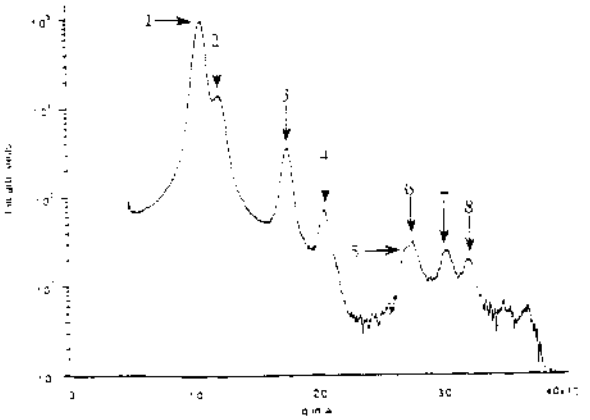

Figure 4. Micelles formed from PS/PI 46K/20K diblocks at 22 wt % in decane. Based on peak locations we conclude an FCC structure with lattice dimension = 1007 Angstrom and nearest neighbor distance of 712 Angstrom.

The profile is still a product of form and structure, but the Bragg peaks of constructive interference are readily observed. We identify several of the peaks associated with the "powder" pattern of an FCC structure. When referenced to the first peak the ratios should follow as 1:1.15:1.63:1.91:2:2.23:2.51:2.58 and 2.88. In this case, the peak at 2.23 is suppressed due to the minimum in the form factor. The presence of the higher order peaks confirms the structure although several difficulties prevent a simple fit to the absolute intensity profile. First of all, we suspect coexistense with a disorderd liquid phase which prevents the intenisty from being nonzero well off the lattice peaks. Secondly , there is some distribution about the Bragg peaks which depends on the x-ray resolution and system strain.

We feel this new information complements the recent BCC identification. The nature of the transition and and the resulting phase is dictated by the interactions of these coronal layers. It may be very possible to have phase transitions at different volume fractions and into different lattice types depending on the nature of the interaction between coronal layers.

Acknowledgements

The authors wish to thank Proctor & Gamble Co. for generously providing the diblock copolymers to conduct this work.

References

1. Pattel, S., Tirell, M. and Hadziioannou, G., *Colloids and Surfaces*, 31, p.157 (1988); Ansifar, M.A. and Luckham, P.F., *Polymer*, 29, p.329 (1988); Taunton, H. J., Toprakciouglu, C. and Klein, J., *Macromolecules*, 21, p.3333 (1988).

2. Cogan, K., Leermakers, F.A.M. and Gast, A.P., *Langmuir*, 8, p.429 (1992).

3. Cogan, K., Gast A.P. and Capel, M., *Macromolecules*, 24, p.6512 (1991).

4. Dan, N., Tirrell, M., *Macromolecules*, 25, p.2890 (1992).

5. Hoover, W.G., Ree, F.H., *Journal of Chemical Physics*, 49(8), p.3609 (1968).

6. Monovoukas, Y., Gast, A.P., *J. Colloid and Interface Sci.*, 128, p.533 (1989).

7. Robbins, M.O., Kremer, K. and Grest, G.S., *Journal of Chemical Physics*, 88(5), p.3286 (1988).

8.Shibayama, M., Hashimoto, T. and Kawai H., *Macromolecules*, 16, p. 16 (1983).

9. Harkless, C.R., *PhD. Dissertation* ; Harkless, C.R., Singh, M.A., Nagler, S.E., Stephenson, G.B. and ordan-Sweet, J.L., *Physical Review Letters*, 64 (19), p.2285 (1990).

THE ELECTROCHEMICAL INSERTION OF LITHIUM INTO PYRITE FROM NON-AQUEOUS ELECTROLYTES AT ROOM TEMPERATURE: AN *IN SITU* Fe K-EDGE X-RAY ABSORPTION FINE STRUCTURE STUDY

Donald A. Tryk, Sunghyun Kim, Daniel A. Scherson
Department of Chemistry
Case Western Reserve University
Cleveland, OH 44106-7078

Mark R. Antonio
Argonne National Laboratory
Chemistry Division
Argonne, IL 60439-4831

Violeta Z. Leger, George E. Blomgren
Technology Laboratory, Eveready Battery Company, Inc.
Westlake, OH 44145

INTRODUCTION

A better understanding of the changes in the structure and electronic properties of pyrite (FeS_2) and its corresponding lithiated derivatives, (denoted generically as Li_xFeS_2, $0 \leq x \leq 2$), induced by the chemical and/or electrochemical insertion and removal of lithium ions into and from these materials is important to the further development of Li-FeS_2 high-energy, secondary batteries. Considerable insight into certain aspects of this phenomenon has been gained based on recent studies involving a variety of spectroscopic and structural techniques, including infrared[1], ^{57}Fe Mössbauer effect spectroscopy (MES),[2-6] X-ray diffraction[2-4,7] and extended X-ray absorption fine structure (EXAFS),[3] with much of the emphasis being focused on the identification of the reaction products of these reactions.

This work will present *in situ* X-ray absorption fine structure (XAFS) results for FeS_2 before and after electrochemical insertion of one and two lithium-ion equivalents, $(Li^+)_{eq}$. Unlike other studies reported in the literature, these measurements were conducted in a specially-designed spectroelectrochemical cell using components and electrolytes very similar to those used in conventional, non-aqueous-solvent, ambient-temperature, primary Li-FeS_2 batteries. Hence, the results obtained in this study are directly relevant to processes occurring in practical devices.

EXPERIMENTAL

Spectroelectrochemical Cell

The cell used in these experiments consists of a thin lithium anode, a separator, and a thin FeS_2 cast electrode arranged in a sandwich-type configuration. This geometry provides optimal conditions for achieving a highly uniform current distribution so that the lithium incorporation (or cell discharge) will occur homogeneously over the entire FeS_2 electrode. In addition, the thickness of the complete assembly, which includes a thermally-sealed, aluminized, polymer-based casing to isolate the cell components from air, was sufficiently small so as not to attenuate the X-ray flux appreciably. This made it possible to acquire *in situ* XAFS spectra in the transmission mode in a rather straightforward fashion. However, the thickness of the pyrite cast electrode in terms of absorption lengths (μ_X = 4.6) was much larger than the ideal absorber thickness (μ_X ca. 1) for Fe K-edge XAFS. Consequently, thickness effect artifacts,[8] such as amplitude distortions,[9] were unavoidable in these initial measurements; hence, caution must be exercised when comparing the data presented herein with that obtained for the same (or similar) materials involving different values of μ_X. Nevertheless, the fact that the absorber thickness (total amount of Fe in the beam) was kept *constant* throughout the course of experimentation facilitates the direct comparison of metrical parameters of pristine FeS_2 (in

the electrode) with those for the corresponding lithiated materials generated *in situ*.

Electrochemical Measurements

In situ XAFS spectra were collected for cells which had been discharged to depths equivalent to the insertion of one and two moles of lithium per mole of FeS_2. During discharge, the cells were compressed with a C-clamp (which was removed prior to spectral acquisition) to decrease both electronic contributions (by promoting particle-particle contact) and ionic contributions to the IR drop. Throughout this procedure, the electrodes were always in contact with the electrolyte and current collectors; hence, the integrity of the cell, and therefore the *in situ* character of the measurements was never compromised. The discharge was effected using a Pine potentiostat working in the galvanostatic mode while monitoring the cell potential. The current densities involved in the discharge were small, on the order of 0.5 to 2 mA/cm^2, to avoid high electrode polarization. As a result, periods of over two hours were required to complete each one-electron discharge step (8.89 mA h capacity; 1-4 mA current). All of the cells were assembled a few days before shipment to the synchrotron facilities and discharged immediately prior to the XAFS experiments.

XAFS Measurements

XAFS data were acquired at the Stanford Synchrotron Radiation Laboratory (SSRL) (Beamline VI-2) and at the National Synchrotron Light Source (NSLS) at Brookhaven National Laboratory (Beamline X-18B). At SSRL (NSLS), the beam current was 20 to 40 mA (110 to 220 mA). The monochromator was Si(111) (Si(220)). The step size was 0.23 eV (0.77 eV) in the XANES region and 0.05 Å^{-1} (0.05 Å^{-1}) in the EXAFS region.

RESULTS AND DISCUSSION

The cell discharge curves, both as a function of time and charge, are shown in Panels A and B, Fig. 1, respectively. Also indicated in this figure are the precise times at which the XAFS spectra were collected. During the insertion of the two $(Li^+)_{eq}$ (32.2 C/electron), the cell voltage dropped by only ~0.4 V, reaching ~ 1.0 V.

The *in situ* k^3-weighted EXAFS spectra, obtained after zero, one and two electron discharge steps (see curves a through c in Figure 2, respectively), reveal a gradual loss in the fine structure as the amount of lithium in the FeS_2 is increased. These changes can be better visualized in the corresponding phase-shift-uncorrected Fourier transforms (FT) shown in Fig. 3. As indicated, the FeS_2 electrode before lithium insertion displays features characteristic of pyrite, including pronounced peaks at 1.8 and 2.9 Å, attributable to the first two Fe-S shells (both with coordination number N = 6) and also at ca. 3.4, 5 and 6 Å, assigned to the first three Fe-Fe shells in the lattice (N = 12, 6 and 24, respectively). After the insertion of one and two $(Li^+)_{eq}$, the intensities of the shells with r' > 2.5 Å decreased monotonically compared to the major Fe-S peak.

A curve fitting analysis of the Fourier-filtered Fe-S backscattering (k$^3\chi$(k)) for the FeS_2 electrode before and after insertion of one and two $(Li^+)_{eq}$ was performed with Fe-S phase and amplitude functions extracted from the first (Fe-S) backscattering in FeS_2. The resulting Fe-S interatomic distances, d(Fe-S), for FeS_2 after lithium insertion, i.e. 2.27 ±0.02 and 2.29 ±0.02 Å, for one and two $(Li^+)_{eq}$, respectively, are slightly longer than that for pyrite, for which d(Fe-S) = 2.250 ±0.005 Å[10] but are significantly shorter that those reported for Li_2FeS_2,[7] namely, 2.4126 Å (along the c-axis) and 2.3737 Å (diagonal to the c-axis). For bulk powder specimens of Li_xFeS_2 ($0.21 < x < 2.0$) prepared by deintercalation of Li_2FeS_2, Brec et al. reported Fe-S distances based on EXAFS measurements in the range 2.28 - 2.33 Å. These are consistent with those found in this work.[3] As discussed later, another possibility is that the cell discharge product is a poorly ordered form of $Fe_{1-x}S$. In some of these structures, the Fe-S distances can vary over a relatively wide range.

Further compelling evidence that the material produced by the insertion of two $(Li^+)_{eq}$ into FeS_2 is *not* crystalline Li_2FeS_2, has been obtained from *in situ* room temperature ^{57}Fe Mössbauer effect spectroscopy (MES) measurements using a spectroelectrochemical cell of similar design to that described here.[11] According to these *in situ* data, the isomer shift (δ) of the single doublet spectrum, 0.30 mm/s vs. α-Fe at room temperature, for the di-lithiated material is substantially different from those of the two doublets observed for crystalline Li_2FeS_2 in this (δ_1 = 0.47, Δ_1 = 1.59; δ_2 = 0.47, Δ_2 = 0.62 mm/s)[11] and other laboratories.[12] It is interesting to note that the presence of two doublets in the MES spectra of this material is consistent with the presence of multiple types of iron sites, arising from occupational disorder between iron and lithium at the tetrahedral sites.[3]

The reduction in the S and Fe backscattering amplitudes upon incorporating Li^+ into FeS_2 could be explained on the basis of one of the following models: i) loss of forward focusing (or net decrease in the electronic overlap between the absorbing atom and the backscattering atoms) upon modifying the geometry

surrounding iron in FeS_2; ii) loss of coherency of the EXAFS signal due to the presence of a broad distribution of d(Fe-S) and d(Fe-Fe) values. This is to be contrasted with the narrow distribution of d(Fe-S) and d(Fe-Fe) for highly crystalline pyrite; or iii) phase cancellation effects between Fe-S and Fe-Fe interactions, similar to the behavior observed for Fe-Fe and Fe-Mo interactions in $MoFe_3S_4$ clusters.[13]

Based on these arguments, the most probable structure of the electrochemically formed material involves a highly disordered (possibly amorphous) form of $Fe_{1-x}S$ (with Li_2S as an additional product). Support for this view is provided by the similarity between the values δ and Δ of crystalline FeS_2 (δ = 0.313 $\pm$0.008 mm/s; Δ 0.611 $\pm$0.003 mm/s)[14] and fine (or superparamagnetic) particles of $Fe_{1-x}S$ (δ = 0.27-0.30 mm/s; Δ = 0.54-0.77 mm/s) in one study,[15] and δ = (0.36 +/- 0.03) mm/s; Δ = (0.65 +/- 0.03) mm/s in another.[16] This observation is consistent with the fact that the *in situ* room temperature MES spectra of FeS_2 obtained for batteries of the type used in this work appears to be independent of the extent of Li-insertion up to the insertion of two $(Li^+)_{eq}$.[11]

Additional support for $Fe_{1-x}S$ as the most probable reaction product is provided by the XANES of the three specimens examined, shown in Fig. 4. Despite the much decreased resolution of the otherwise highly structured near-edge region of crystalline pyrite,[17] caused by the relatively thick specimen (*vide supra*), the insertion of Li^+ into the lattice leads, in addition to a much steeper edge jump, to a *rounding* of the XANES region. Such a lack of fine structure has been found in hexagonal $Fe_{1-x}S$[18] and was ascribed to a somewhat wide range of Fe-S distances in the distorted FeS_6 octahedra. The same phenomenon has been observed for CuS,[19] and explained in terms of the complexity of the crystal structure where Cu atoms often occupy various types of low symmetry sites. Also noteworthy, is the overall shift of the XANES toward lower energies as the amount of Li^+ in the lattice is increased, an effect that is consistent with the gradual (electrochemical) reduction of the iron centers.

It is expected that more detailed studies of the type reported here may provide much-needed insight into the general phenomenon of lithium-ion insertion and deintercalation and shed light on the nature of the processes responsible for the lack of electrochemical reversibility of ambient temperature, non-aqueous electrolyte Li-FeS_2 cells.

SUMMARY

The effects of lithium ion insertion on the structural and electronic properties of FeS_2 (pyrite) have been examined *in situ* by Fe K-edge XAFS using electrodes and electrolytes similar to those found in conventional, ambient-temperature, primary Li/FeS_2 batteries. A substantial reduction in the amplitudes of the Fe-S and Fe- Fe backscattering was observed as the amount of intercalated lithium in the FeS_2 lattice was increased from 0 to 2 Li^+ equivalents, $(Li^+)_{eq}$. After the insertion of two $(Li^+)_{eq}$, there remained only a single peak in the FT, corresponding to the closest Fe-S shell. The shells associated with the distant Fe-S and Fe-Fe interactions were no longer discernable in the FT. Curve-fitting analysis of the $k^3\chi(k)$ EXAFS for this latter material yielded an average Fe-S distance, d(Fe-S) = 2.29 $\pm$0.02 Å. In addition, the XANES revealed a rounding of the initially highly structured region of FeS_2 as the amount of inserted lithium was increased. This behavior is consistent with the formation of $Fe_{1-x}S$ and thus supports the assigment made on the basis of *in situ* MES studies of the same system.

REFERENCES

1. Gard, P.; Sourisseau, C.; Ouvrard, G.; Brec, R. *Solid State Ionics* **1986**, *20*, 231.
2. Blandeau, L.; Ouvrard, G.; Calage, Y.; Brec, R.; Rouxel, J. *J. Phys. C: Solid State Phys.* **1987**, *20*, 4271.
3. Brec, R.; Prouzet, E.; Ouvrard, G. *J. Power Sources* **1989**, *26*, 325.
4. Fong, R.; Jones, C. H. W.; Dahn, J. R. *J. Power Sources* **1989**, *26*,333.
5. Fong, R.; Dahn, J. R.; Jones; C. H. W. *J. Electrochem. Soc.* **1989**, *136*, 3206.
6. Jones, C. H. W.; Kovacs, P. E.; Sharma, R. D.; McMillan, R. S. *J. Phys. Chem.* **1990**, *94*, 832.
7. Batchelor, R. J.; Einstein, F. W. B.; Jones, C. H. W.; Fong, R.; Dahn, J. R. *Phys. Rev. B*, **1988**, *37*, 3699.
8. a. Stern, E. A.; Kim, K. *Phys. Rev. B.* **1981**, *23*, 3781; b. Goulon, J.; Goulon-Ginet, C.; Cortes, R.; Dubois, J. M. *J. Physiqu*, **1982**, *43*, 539; c. Lytle, F. W.; In *Application of Synchrotron Radiation*; Vol. 4, Winick, H.; Xian, D.; Ye, M. H.; Huang, T.; Eds., Gordon and Breach: New York, 1989, pp. 135.
9. *After-the-fact* thickness effect corrections for strongly absorbing materials, such as those studied in this work, cannot always eliminate amplitude distortions. See for example: a. B. K. Teo, M. R. Antonio, B. A. Averill, *J. Am. Chem. Soc.* **1983**, *105*, 3751; b. Antonio, M. R.; Song, I.; Yamada, H. *J. Solid State Chem.* **1991**, *93*, 183.
10. Finklea, S. III.; LeConte C. *Acta Cryst.* **1976**, *A32*, 529.
11. Fierro, C.; Leger, V.; Akridge, J.; Scherson, D. (to be submitted).
12. See for example: Melendres, C. *J. Phys. Chem.* **1978**, *82*, 2850

13. Antonio, M. R.; Teo, B. K.; Cleland, W. E.; Averill, B. A. *J. Am. Chem. Soc.* **1983**, *105*, 3477.
14. Evans, B. J.; Johnson, R. G.; Senftle, F. E.; Cecil, C. B.; Dulong, F. *Geochimica et Cosmochimica Acta*, **1982**, *46*, 761.
15. Hidaka, S.; Iino, A.; Nita, K.; Morinaga, K.; Yamazoe, N. *Bull. Chem. Soc. Jpn.* **1988**, *61*, 3169.
16. Vaishnava, P. P.; Montano, P. A.; Tischler, R. E.; Pollack, S. S. *J. Catalysis*, **1982**, *78*, 454.
17. Drager, G.; Frahm, R.; Materlik, G.; Brummer, O. *Phys. Stat. Sol.* **1988**, *146*, 287.
18. Petiau, J.; Sainctavit, Ph.; Calas, G. *Mat. Sci. Eng.* B1 **1988**, 237.
19. Sugiura, C. *J. Chem. Phys.* **1984**, *80*, 1047.

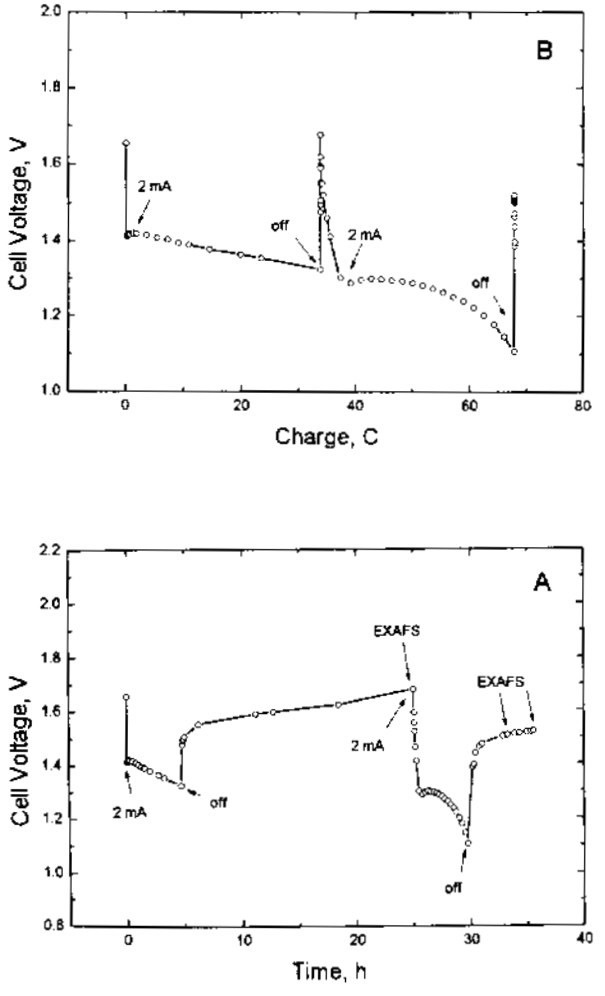

Fig. 1. Cell discharge curves as a function of time, A and charge, B. The precise times at which the XAFS spectra were collected are indicated in B.

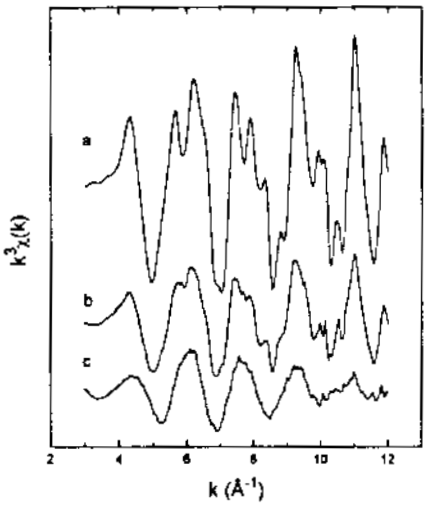

Fig. 2. *In situ* k^3-weighted EXAFS spectra obtained during the various stages of discharge, zero (Curve a), 1 (Curve b) and 2 (Curve c) electron-discharges.

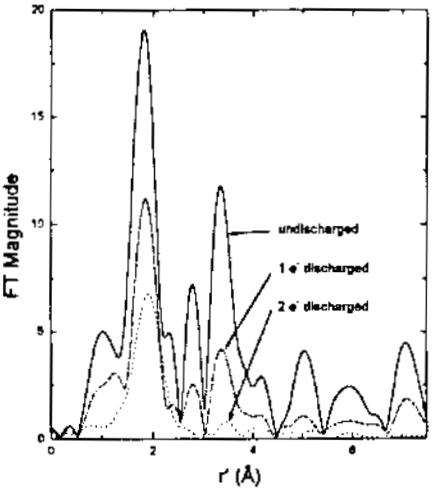

Fig. 3. Fourier transforms for the stages of discharge specified in the caption for Fig. 2.

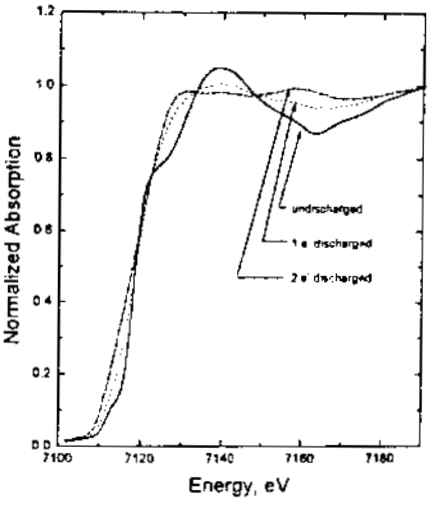

Fig. 4. XANES for the stages of discharge specified in the caption for Fig. 2.

Shallow and deep donors in $Al_xGa_{1-x}As$ semiconducting alloys

T.M. Hayes, J. Pant, and V.M. Iskandarian
Physics Department, Rensselaer Polytechnic Institute, Troy NY 12180-3590

D.L. Williamson and L. Greco
Physics Department, Colorado School of Mines, Golden CO 80401

P. Gibart
Laboratoire de Physique du Solide et Energie Solaire, CNRS, Valbonne, France

T.N. Theis
IBM T.J. Watson Research Center, Yorktown Heights NY 10598

Si, Se, Sn, and Te are all suitable electron donors in GaAs. When Al is substituted for Ga to form $Al_xGa_{1-x}As$ ($x > 0.2$), however, deep electron levels are formed rather than the desired shallow donor levels. These are called "DX centers." Their formation greatly reduces our ability to produce highly conducting n-type $Al_xGa_{1-x}As$ and they are widely regarded as *the* most significant impediment to the design of many useful devices based on these materials.

The electronic properties of DX centers have been characterized extensively. The large discrepancy between thermal and optical excitation energies (~1 eV) is attributed to the (occupied) DX center differing from the ionized donor site by a significant change in the configuration of the neighboring atoms. Experimental quantification of this change is hampered by the necessity of keeping the number of dopants well below 5×10^{18} cm^{-3}. Dopant concentrations in excess of this level lead to self-compensation and/or to the formation of impurity complexes rather than the desired isolated shallow donor levels. The structure of isolated dopants can be determined only at lower concentrations where they dominate the distribution of dopant sites. To our knowledge, only x-ray absorption fine structure (XAFS) spectroscopy can address this structural question directly for such dilute systems.

In 1988, Chadi and Chang proposed that the DX center associated with Si or S dopants in GaAs and $Al_xGa_{1-x}As$ is a negatively charged dopant atom with only three nearest neighbors [Phys. Rev. Lett. 61, 873 (1988)]. Photoexcitation of this DX center yields two conduction electrons. When ionized (i.e., positively charged), the dopant has four neighbors at the usual distance for a substitutional shallow donor site. This model can explain nearly all observed features of DX centers without elaborate further assumptions, and has consequently become a widely favored model.

In the Chadi-Chang model, the predicted difference in the distance to nearest-neighbor atoms from the ionized donor and from the DX center is insignificant. A test of the predicted structure will require accurate measurement of the *number* of nearest neighbors or of the positions of more distant neighbors. A measurement of the number is the more difficult (and less promising) of the two. Even if *all* of the dopant atoms are electrically active, one half of the donors must be ionized in the ground state, giving up their electrons to the other half of the Sn dopants (which become negatively charged). Thus the average number of nearest neighbors changes by only 12.5% between the ground state and a state where all of the Sn atoms are in ionized shallow donor sites. This

change is reduced further by the fraction of Sn atoms which are electrically active, seldom more than one-half. It is well known to be very difficult to obtain the number of neighbors accurately from an XAFS spectrum, especially in a dilute system in which the ratio of signal to noise is necessarily low (although we are helped by having chosen a relatively high-Z dopant).

In order to increase our ability to measure small differences in the structure, we prepared a sample with x=0.23 so that we can measure the Sn environment in both configurations in one sample. Specifically, if we assume for the moment that the Chadi-Chang model is correct, we can place half of the Sn dopant atoms in the DX state by holding that sample in the dark at ~80 K. After collecting many XAS spectra in that state, we can cool the sample to ~20 K and use light-emitting diodes to photoexcite the DX centers, producing a persistent-photoconductivity (PPC) sample with nearly all Sn dopants in the ionized shallow donor configuration. The spectra from these two configurations of the *same sample* can be compared directly to quantify differences in Sn environment.

The Sn doping level was adjusted to obtain the largest possible concentration of electrically active dopants while still avoiding the formation of other Sn impurity configurations. The resulting dopant concentration is ~2×10^{18} cm^{-3}.

Finally, we avoided grinding our samples to a powder, which may well have contributed to the evolution of the Sn environment with time in earlier measurements, by designing a new sample holder in which the sample orientation can be oscillated during the measurement. This approach has been used by G.S. Cargill, amongst others, to reduce or eliminate the very large features due to Bragg diffraction which can make useless the XAS spectrum from a single crystal sample. Its effectiveness is illustrated in fig. 1. A portion of the spectrum obtained from single crystal $Al_xGa_{1-x}As$:Sn below the Sn K edge is shown in fig. 1a. The feature in the center is due to diffraction, and is very large on the scale of the XAFS. That feature disappears within the statistical noise if we oscillate the sample by a few degrees about the beam direction, as is shown in fig. 1b.

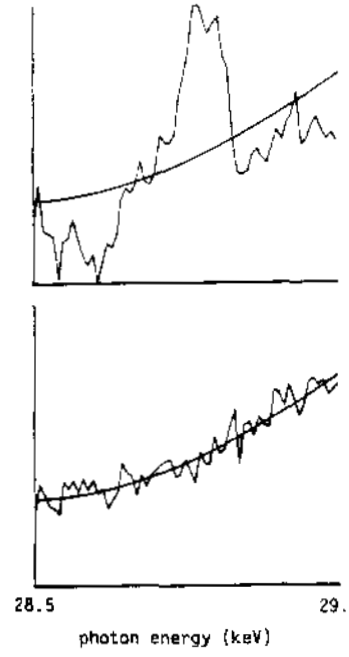

Figure 1. A portion of the x-ray absorption spectrum below the Sn K edge in a single crystal of $Al_xGa_{1-x}As$:Sn is shown (a) without and (b) with oscillating the sample by a few degrees about the beam direction. The feature at the center of the region is approximately 20% of the height of the Sn K edge.

We have accumulated data from our new sample. Preliminary analysis does indeed show a pronounced difference between the Sn environments in the two states. As expected, the Sn environment in the PPC state is quite similar to that in the zincblende structure. The DX state is quite different. Detailed analysis is in progress.

Acknowledgements: This research is supported by NSF Grant Nos. DMR-9006956 and DMR-8902512. The measurements were made at SSRL which is funded by the DOE Office of Basic Energy Sciences and the NIH Biotechnology Resource Program.

STRUCTURAL CHEMISTRY OF Cr SOLUTIONS

F. W. Lytle, The EXAFS Company, Seattle WA
R. B. Greegor, The Boeing Company, Seattle WA
B. Ray Stults, Pacific Northwest Laboratories, Richland WA

This report discusses the degree of structural detail that can be obtained from high quality EXAFS data on solutions. The fluorescence mode data were obtained using Si(220) crystals in the monochromator from 0.1 M solutions with multiple scans to K = 20 $Å^{-1}$. The nearly noise free EXAFS extended to ~ 16 $Å^{-1}$. The top half of Fig. 1 shows Fourier transform (K^2, Cr-O phase corrected, multiplied by R^2) data from Cr^{3+} solutions prepared from $CrCl_3 \cdot 6H_2O$. One solution, dashed line, was boiled to remove all the Cl to prepare the species $[Cr^{3+}(H_2O)_6]$. The other, solid line, was kept cool to prepare the species $[Cr^{3+}Cl_2(H_2O)_4]$. Inspection of the region of the first major peak shows both the water in the 1st coordination shell and the shoulder on the side due to the 2 Cl atoms at slightly longer distance. Beyond this is are peaks at ~ 2.8-3.0 Å due to 2nd shell water molecules. The region of the Fourier transform which included the 1st and 2nd H_2O peaks was back transformed and least square fitted to determine accurate bond distances. In the $[Cr^{3+}(H_2O)_6]$ the 1st H_2O is at 1.99 ± 0.01 Å, the 2nd H_2O at 2.83 ±0.03 Å. It is apparent that the presence of the Cl atoms pushes the 2nd H_2O molecules further away to ~ 3.0 Å. The peak at about 4 Å is due to neighboring Cr atoms presumably bridge-bonded via Cr-OH-Cr, since Cr is slightly acidic in water. The identity of the species causing this peak was proved by back-transforming the peak and comparing the shape of the envelope with that from Cr in a reference material. It may also be inferred that the two Cl atoms are trans to each other, otherwise the inversion symmetry of the molecule would be broken and the 1s to 3d pre-peak in the XANES (not shown) would be more intense.

In Fig. 1, bottom, the Fourier transforms (K^2, Cr-O phase corrected multiplied by R^2) from the EXAFS of solutions prepared from K_2CrO_4 and $K_2Cr_2O_7$ are shown. Solid chromates and dichromates have Fourier transforms similar to the respective solutions out to ~ 4 Å. The first neighbor peak at 1.65 ± 0.01 Å is due to three of the tetrahedrally-bonded O atoms of the $[CrO_4]^{2-}$ or $[Cr_2O_7]^{2-}$ anions. In solid dichromates there are 3 O at ~ 1.65 Å with a longer bond of ~ 1.9 Å linking the anion to the nearest Cr atom in the adjacent anion. It is evident that in solution both the chromate (yellow, pH = 7) and dichromate (orange, pH = 3) solutions form dimers bridging through an O at ~ 2 Å, i. e. the shoulder on the main peak. The relative heights of the first peak indicate that the solution prepared from $[Cr_2O_7]^{2-}$ has the more extensive linkage reflecting the known equilibrium between the two species. (1) The peak at 3.03 ± 0.05 Å is due to the adjacent oxygen-bridged Cr^{6+} species. The identity of this peak was proved by the shape of the envelope of the inverse transform of the peak. The Cr-O-Cr bond angle is ~ 90° which is considerably less than the tetrahedral angle. It appears that the dimer is collapsing upon itself, perhaps due to the pressure of the surrounding water molecules. The negative charge of the anions appears to push the H_2O molecules from the solvent away since there are no peaks in the Fourier transform due to H_2O within the 5 Å range of the graph.

1. F. A. Cotton and G. Wilkinson, **Advanced Inorganic Chemistry**, 3rd Edition, p. 841, Interscience Publishers, 1972.

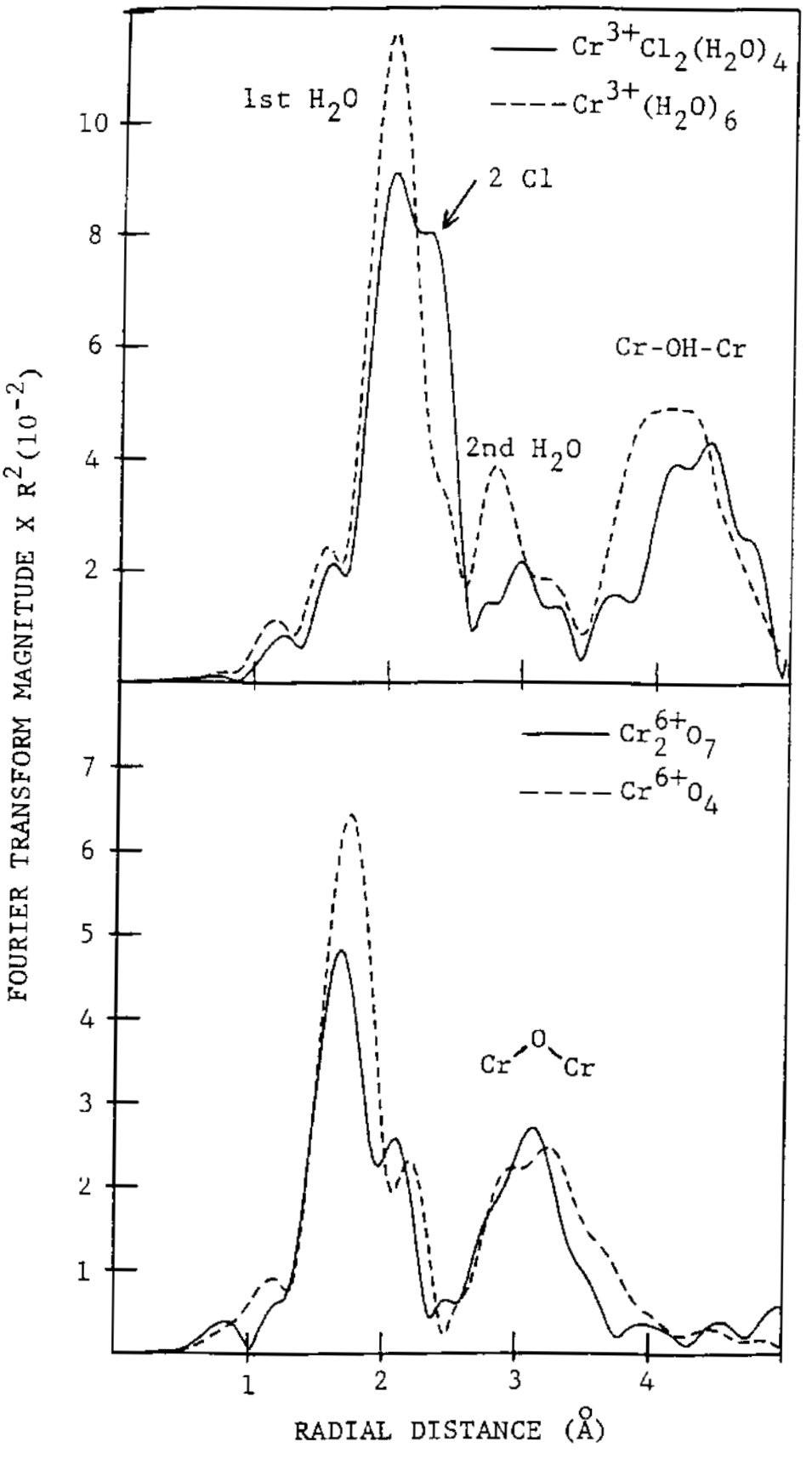

Fig. 1 Top, comparison of the Fourier transforms of EXAFS from 0.1 M solutions of $[Cr^{3+}(H_2O)_6]$, dashed, and $[Cr^{3+}Cl_2(H_2O)_4]$, solid. The identity of the peaks is indicated. Bottom, comparison of the Fourier transforms of solutions made from chromate and dichromate.

Determination of the Strain Distributions in Metallic Thin Films and Lines as a Function of Temperature using Grazing Incidence X-ray Scattering

Paul R. Besser, Richard P. Vinci, Ramnath Venkatraman, John C. Bravman
Department of Materials Science and Engineering, Stanford University
and Sean Brennan
Stanford Synchrotron Radiation Laboratory

I Introduction

The general mechanical behavior of highly textured planar aluminum alloy thin films on silicon during thermal cycling has been extensively studied and documented.[1] Film stresses are commonly obtained from volume-averaging x-ray methods and substrate curvature techniques that yield an average value of stress. By their nature, these methods are unable to measure strain gradients that may arise through the film thickness. They are also unsuitable for identifying rapid relaxation mechanisms. During the past two years, we have performed experiments on planar aluminum films using Grazing Incidence X-ray Scattering (GIXS) at SSRL to determine the magnitude of strain gradients in Al films at elevated temperatures.[2] Strain relaxation has also been studied. The work began with that study of the mechanical properties of uniform Al films and has now progressed to the examination of lines of Al and Cu.

In the integrated circuit (IC) industry, uniform films are lithographically patterned to produce metal lines. Just as thin film mechanical properties differ from those of bulk materials, the properties of metal lines differ from those of continuous films. A passivation layer covering the metal lines further complicates the mechanical behavior and leads to large strains.[3] The GIXS techniques developed for planar films have been applied, with some geometry considerations, to lithographically patterned lines of Al.[4] The result is a method for measuring strain distributions through the thickness and strain relaxation of unpassivated and passivated Al alloy lines. A better understanding of the relaxation and failure mechanisms operating in the materials will be gained from the work.

The mechanical behavior of copper metallizations, a possible replacement for Al due to higher conductivity and resistance to electromigration, has not been widely investigated.[5] Prediction of the properties of copper is complicated by the need for a diffusion barrier underlayer and by the lack of a fiber texture in most copper films.[6][7] The lack of strong texture and the presence of another thin film layer beneath the copper may result in mechanical behavior that differs significantly from that of aluminum.[8] This tendency has already been displayed during a series of experiments we performed on planar Cu films. GIXS was used to determine the variation of strain with temperature of Cu films deposited on oxidized Si and on Cu films over a tungsten layer on oxidized silicon.

II GIXS Background

Over the past years GIXS has been used extensively to study the structure of thin films and interfaces.[9,10] Doerner and Brennan[11] demonstrated the use of GIXS in determining the strain distribution in thin aluminum films by measuring the change in the Al in-plane peak position with penetration depth. Recent GIXS work by Shute and Cohen[12] found the stresses in Al-0.5%Cu films at room temperature to be uniform through the thickness. Venkatraman et al.[2] used GIXS to study the strain distributions in Al and Al alloy uniform films during thermal cycling. Besser et al.[4] showed the feasibility of using GIXS to study strain distributions and strain relaxation in unpassivated Al alloy lines.

GIXS utilizes the principle of total external reflection (TER). For most materials, the index of refraction is less than unity at X-ray energies. According to Snells Law, X-rays going from a material of higher index of refraction (air) to one having a lower index (the diffracting material) will be perfectly reflected below a certain critical angle of incidence. The critical angle of incidence for TER is typically less than a degree. The penetration depth of x-rays into the

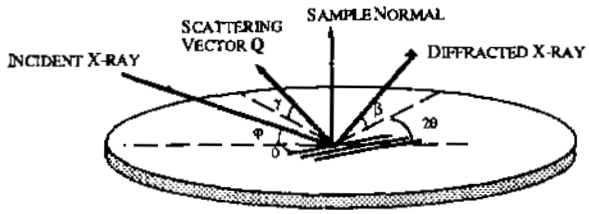

Figure 1: Schematic of GIXS geometry. Note that θ and 2θ are in the plane of the sample.

material and, hence, the depth in the material from which signal is detected, can thus be tailored by varying the incident angle. The scattering geometry used in the GIXS scans is shown in Figure 1. X-rays are incident at some small angle ϕ relative to the sample surface and θ relative to the diffracting planes. The scattered X-rays are detected at some angle β relative to the sample surface. The scattering vector **Q** is inclined slightly relative to the sample's surface. Since this inclination angle is less than a degree, the planes participating in the scattering event are essentially perpendicular to the sample surface.

III Results and Discussion

A Aluminum Uniform Films

In the present section, we provide a brief summary of the results of our study of aluminum alloy uniform films. Some of the results are published [2][13][4], and a journal paper summarizing the work is currently in press[14]. The results of the stress relaxation experiments are seen to be thickness dependent. As the films were heated to temperatures greater than 100°C stresses are compressive and relaxation is seen to occur uniformly at all levels in the film. For all films it was found that, below 200°C, the surface of the film maintained a slightly higher value of stress with respect to the bulk. In thicker films, this condition reverses during heating between 200°C and 300°C and the surface relaxes with respect to the bulk. The surface then remains relaxed at all temperatures during subsequent thermal cycles. This behavior was observed for 1.0m thick Al-1.0%Si and Al-0.5%Cu films. Different behavior was observed in films 0.6μm and thinner. The surface of thinner films is more stressed relative to the bulk of the film during heating and remains so throughout the thermal cycle. These results are similar to those reported by Doerner and Brennan [11] in that they observed relaxation at the top surface of the film for smaller film thicknesses, i.e. 0.26μm and 0.6μm. This could very well be due to the well-known sensitivity of the film characteristics to differing impurity levels caused by film deposition conditions. Also, their films were annealed for 30 minutes at a temperature (450°C), 50°C higher than our annealing temperature. In spite of the qualitative differences seen with respect to strain gradients between relatively thick and thin films, it is safe to generalize that there are no gross strain gradients in Al films on Si even at elevated temperatures.

B Unpassivated Aluminum Lines

Determining the strain state for a uniform film is straightforward since the uniform film is subject to an equal biaxial stress state. Measurement of the in-plane strain fully defines the stress state of the film. The stress state is different once the film is lithographically patterned to form lines. Samples with unpassivated lines are subject to an unequal, biaxial stress state. Two orientations are required to fully define the strain state of a line.[4] As shown in Figure 2A, the scattering vector **Q** is oriented along the width of the line in the Width Orientation, and crystal planes parallel to the length of the line participate in the diffraction process. In the Length Orientation (Figure 2B), planes normal to the length of the line are sampled during diffraction, as **Q** lies along the length of the line. ϵ_x and ϵ_y are thus determined directly and unambiguously by these orientations.

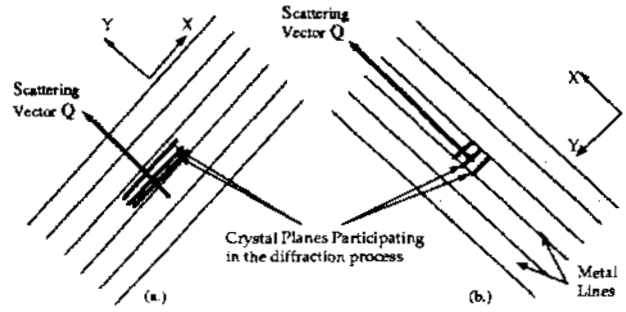

Figure 2: Scattering geometry for the two orientations (width and length of Al lines during GIXS.

Unpassivated metal lines were fabricated by lithographically patterning a sputter-deposited blanket film of 1.0 μm thick Al-0.5%Cu on a 1000 Å Ti barrier layer. The patterning produced arrays of parallel 1.25 μm wide lines and 1.25 μm wide spaces. The samples were thermally cycled from room temperature to 400°C. The stress relaxation was observed at several temperatures during heating and cooling. At room temperature, the stress at the surface of the film is 15% greater than the stress in the bulk of the film. As

with uniform films, the lines are in compression during heating and in tension upon cooling, and most of the stress relaxation occurs in the first few minutes of observation. This rapid relaxation was found both in heating and in cooling. At all temperatures during the thermal cycle, it was found that the width direction of the line supports essentially no stress. The surface of the film is relaxed relative to the bulk upon heating; however, upon cooling, the surface is in a higher state of stress relative to the bulk. This trend is still being investigated. The native oxide of Al is not believed to be responsible since it should be present at all temperatures. The formation of the intermetallic $TiAl_3$ (accompanied by a volume reduction of 0.22%[15]) was observed during the relaxation at 399°C using offset Bragg-Brentano X-ray scans. It remains during the cooling cycle. This formation, however, does not explain the stress behavior since the surface of the lines were at a higher state of stress than the bulk at room temperature before thermal cycling.

C Passivated Al Lines

Aluminum lines are typically passivated with SiO_2 or Si_3N_4 to provide electrical insulation. This passivation introduces a hydrostatic component to the stress state. This triaxial stress state necessitates using three orientations of the lines to fully define the strain state. As with uniform films and unpassivated lines, the {422} reflection is scanned in-plane and used to determine the strain in the X and Y directions of the line. In the final or height orientation, the scattering vector is orientated normal to the surface of the line (along the line height direction Z). The crystal planes participating in the diffraction process (the {222} reflection) are parallel to the surface to the sample. The SSRL results have been shown to be equivalent to conventional diffraction methods.[16] The strains have also been measured at SSRL during thermal cycling and compared with finite-element modeling methods.[17]

Figure 3 is a plot of stress as a function of temperature as measured at SSRL. The stress is given for the three directions (X, Y and Z). The stresses determined are much larger than those measured in uniform films and unpassivated lines. The stress behaves essentially linearly between room temperature and the passivation deposition temperature of 380°C. Above the passivation temperature the stress becomes compressive. At each temperature shown, the strain relaxation was measured and found to have a thermal dependence.[16] We are still analyzing this data, and plan more experiments on this and other samples to determine the activation energy for the relaxation.

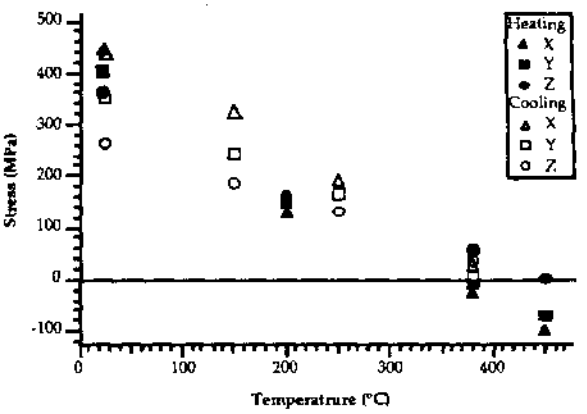

Figure 3: Initial and final values of stress for passivated Al-0.5%Cu lines during thermal cycling. Stress is shown for three directions: length (X), width (Y) and height (Z).

D Copper Uniform Films

Measurements of strain as a function of temperature for planar copper films have been carried out in the same manner as for planar Al films. The Cu was sputter-deposited (9000 Å) on thermally oxidized (100) Si with and without a 1000 Åunderlayer of W. A second set of films (1500 Å) was prepared by Chemical Vapor Deposition (CVD) at 150°C using a Cu^{+1} precursor. Three substrates were used: oxidized (100) Si, oxidized (100) Si with sputtered W (1000 Å), and oxidized (100) Si with sputtered TiW (1000 Å).

The Cu texture and microstructure was evaluated by x-ray methods and Transmission Electron Microscopy (TEM). Unlike the strong {111} texture seen in Al, the Cu {111} texture is weak and is influenced by the barrier material. For instance, Cu films on oxide were {111} textured with a {100} secondary component, while Cu films on W were more strongly {111} textured with only a few scattered {100} grains.

Average biaxial residual stress after sputter deposition, measured by wafer curvature and by GIXS scans, was found to be small and slightly compressive in the sputtered Cu films. In the CVD films, the biaxial residual stress after deposition of was small and slightly tensile. Thermal cycles to 400°C and back to room temperature were carried out while measuring the resulting Cu strain by GIXS (Figure 4). After one heating and cooling cycle, the bulk biaxial stress in all films was tensile. The biaxial stress in the Cu on W was larger than the Cu on oxide, and greater {100}-oriented grain growth was seen in the Cu on W.

Strain as a function of depth in the films was also measured before, during, and after the heating cycle. Before thermal cycling, the surface of the sputtered

copper was in tension while the bulk was in compression. Above 200-300°C and after heating, the surface was relaxed with respect to the bulk. This effect was more pronounced for the Cu deposited on W. The influence of film thickness on surface relaxation has not yet been investigated. Isothermal relaxation was also measured for the sputtered films. Most of the relaxation occured during the first 20 minutes after reaching temperature. This behavior is similar to that seen for Al films.

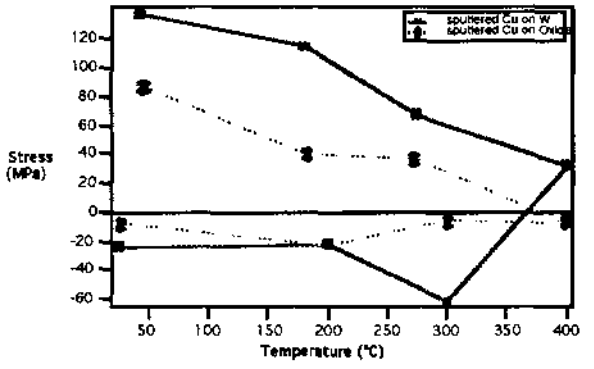

Figure 4: Stress as a function of temperature for sputtered Cu films.

IV Summary and Conclusions

GIXS was used to measure elastic strain and calculate stress as a function of film depth at different temperatures during thermal cycling in Al films of various thicknesses, Al lines, and Cu films. For thick Al films, the surface of the film relaxed with respect to the bulk during the first heating (at 200-300°C). For films 0.6μm and thinner, the surface always remained at a slightly higher value of stress than the bulk. However, it can be generalized that any deviation from a uniform stress through the film thickness takes place only near the very surface of the film. In the case of Al-0.5%Cu on Ti lines, the width direction of the line supports essentially no stress through the thermal cycle. Passivated Al-0.5%Cu lines support much larger stresses than their unpassivated counterparts and have a significant hydrostatic component. Initial studies of copper films indicate that the mechanical behavior of Cu is, in some ways, different from that of aluminum and deserves further investigation.

V Acknowledgements

The authors would like to acknowledge the support of the Semiconductor Research Corporation. Support for S. Brennan is provided by the Department of Energy (DOE) Office of Basic Energy Sciences. These experiments were performed at SSRL, which is supported by the DOE, Division of Chemical Sciences.

References

[1] R. Venkatraman et al. *J. Elec. Mat.*, 19:1231–1238, 1990.

[2] R. Venkatraman, P.R. Besser, S. Brennan, and J.C. Bravman, *MRS Symp. Proc. Vol. 239*, pages 227–232. MRS,1992.

[3] B. Greenbaum, A.I. Sauter, P.A. Flinn, and W.D. Nix. *Appl. Phys. Lett.*, 58(17):1845–1847, 1991.

[4] P.R. Besser, R. Venkatraman, S. Brennan, and J.C. Bravman, *MRS Symp. Proc. Vol. 239*, pages 233–238, MRS,1992.

[5] P. Borgesen, J.K. Lee, R. Gleixner, and C.-Y. Li. *Appl. Phys. Lett.*, 60(14):1706–1708, 1992.

[6] C.-K. Hu, X. Chang, M.B. Small, and J.E. Lewis, *VLSI Mult. Inter. Conf. Proc.*, pages 181–187, IEEE,1986.

[7] C.-A. Chang. *J. Appl. Phys.*, 67(10):6184–6188, 1992.

[8] P.A. Flinn. *J. of Mat. Res.*, 6(7):1498–1501, 1991.

[9] P.H. Fuoss and S. Brennan. *Ann. Rev. of Mat. Sci.*, 20:365–390, 1990.

[10] M.F. Toney, T.C. Huang, S. Brennan, and Rek. A. *J. of Mat. Res.*, 3:351–356, 1988.

[11] M.F. Doerner and S. Brennan. *J. Appl. Phys.*, 63:126–131, 1988.

[12] C.J. Shute and J.B. Cohen. *J. Appl. Phys.*, 70(4):2104–2110, 1991.

[13] R. Venkatraman. PhD thesis, Stanford University, 1992.

[14] R. Venkatraman, P.R. Besser, S. Brennan, and J.C. Bravman. *J. Appl. Phys.*, Submitted to, 1992.

[15] D.S. Gardner and P.A. Flinn. *J. Appl. Phys.*, 67:1831–1844, 1990.

[16] P.R. Besser, S. Brennan, and J.C. Bravman. Submitted to *J. of Mat. Res.*, 1993.

[17] P.R. Besser, A. Sauter Mack, D.B. Fraser, and J.C. Bravman. Accepted to *J. Elec. Soc.*, 1993.

FLUORESCENCE EXAFS STUDY OF HEAVILY-DOPED III-V AND II-VI COMPOUND SEMICONDUCTORS

Kin Man Yu, J. M. Jaklevic, Carolyn Rossington, and Wladyslaw Walukiewicz
Lawrence Berkeley Laboratory

Introduction

It had been recognized since the early stages of semiconductor research that, unlike elemental semiconductors which can be doped to very high levels, compound semiconductors in general exhibit lower dopant activation efficiency [1-4]. In the cases of group II-VI semiconductors, a certain type of doping, i.e. p-type in CdSe and n-type in ZnTe, cannot be realized at all. Understanding the mechanisms leading to this saturation of free carrier concentrations in compound semiconductors is an issue of great fundamental and practical importance. In the extreme case, when high concentration of the impurity atoms is introduced into the semiconductor (several atomic %), new alloys will be formed. In particular, when magnetic ions such as Mn and Fe are introduced into II-VI semiconductors, a new class of materials, magnetic semiconductors are formed[5].

The goal of our project is threefold: 1) to develop low energy x-ray detectors specialized for EXAFS measurements; 2) to investigate the relationship between the structure of the local environment of the impurity atoms and the macroscopic electrical properties of the compound semiconductor materials; and 3) to study the local environment of magnetic semiconductors synthesized by high dose ion implantation techniques(ion beam synthesis).

Experiment

Two types of samples were prepared for EXAFS measurements. For doping studies, ZnSe:Cl, CdTe:Cl and GaP:Mn samples were prepared by ion implantations followed by rapid thermal annealing. For ion beam synthesis of magnetic semiconductors, high dose Mn ions were implanted into CdTe substrates followed by rapid thermal annealing. As-grown bulk $Cd_{1-x}Mn_xTe$ crystals were also measured. The EXAFS experiments were performed in the fluorescence mode at beamline 4-3 using the x-ray spectrometer designed, built and tested at LBL.

Results and Discussion

During our first run on June 1992, we encountered several technical difficulties in obtaining Cl EXAFS spectrum. One of the main problems was inadequate beam flux at the low energy range for Cl. Moreover, the energy resolution of our spectrometer was not good enough to discriminate the Cl K x-ray and the elastically scattered x-ray peak. To overcome these difficulties, we are requesting beam time at another beamline which is more suitable for low energy work. Moreover, our spectrometer is being modified so that improved energy resolution can be achieved.

Due to the above mentioned problems, our experiments in 1992 concentrated on the study of ion beam synthesized magnetic semiconductors. High dose Mn ions (~2x1016 /cm2) were implanted into CdTe crystal to synthesize a thin layer of $Cd_{1-x}Mn_xTe$ alloy with maximum x~0.2. Fig. 1 (a) shows the Mn K edge EXAFS spectrum from the $Cd_{0.8}Mn_{0.2}Te$ bulk sample. The corresponding k^3-weighted EXAFS spectrum is shown in Fig. 1(b).

Fourier tranforms of the EXAFS data obtained from the ion beam synthesized samples, as-implanted and annealed and from the bulk alloy is shown in Fig. 2. The Fourier transformed data revealed that the local environment of Mn in the ion beam synthesized and annealed alloy is very similar to that of a bulk grown alloy.

Using $MnTe_2$ powders as the standard for the backscattering amplitude and phase shift, multiparameter curve fittings were performed on the back-transformed data. Table I shows the results from the fitted data. The results in Table I indicate that the nearest neighbor (nn) distance of the 20% bulk grown alloy (2.770Å) is significantly smaller than that extrapolated from Vegard's law for a 20% Mn alloy (2.794Å). On the other hand the nn distance of the bulk alloy is also larger than that of an extrapolated zinc-blende MnTe phase (2.746Å). The nn distance is however, very close to the value calculated (Vegard) for a $Cd_{0.3}Mn_{0.7}Te$ alloy which is the zinc blende phase with maximum Mn concentration.

The ion beam synthesized alloy has nn distance very similar to that of the bulk grown alloy. The unannealed sample, however, has a slighlty larger nn distance (2.786Å). The next nn distance for the as-implanted sample differs significantly from that of the annealed sample (and also of the bulk alloy). This is believed to be the result of radiation damage of the sample which is only

Table I Summary of the Mn EXAFS analysis on the ion beam synthesized and bulk grown CdMnTe alloys.

	NN(Mn-Te)			NNN(Mn-Cd)	
	R(Å) (±0.01)	CN	s^2(Å^2)	R(Å)	CN (±0.02)
alloy	2.770	3.8	0.001	4.53	
Unann.	2.786	3.3	0.004	4.612	12.1
Annealed	2.777	3.4	0.004	4.525	17
theoretical values: (Vegard)					
CdTe	2.806	4.0		4.583	12
MnTe: (extrapolated)	2.746	4.0		4.484	12
$Cd_{0.8}Mn_{0.2}Te$	2.794	4.0		4.566	12
$Cd_{0.3}Mn_{0.7}Te$	2.764	4.0		4.515	12

Acknowledgement

This work is supported by the Laboratory Directed Research and Development Program at the Lawrence Berkeley Laboratory. The authors wish to thank Britt Hedman for her assistance in performing the EXAFS experiments and for allowing us to use the XFPKG data analysis software. The cooperation of the SSRL staff is also acknowledged.

References

1. L.J. Vieland and I. Kudman, J. Phys. Chem. Solids **24**, 437 (1963); H. Ito and T. Ishibashi, Japan J. Appl. Phys. **26**, L1760 (1987).
2. Y. Yuba, K. Gamo, K. Masuda and S. Nambu, Japan. J. Appl. Phys. **13**, 641 (1974).
3. W.A. Sunder, R.L. Barns, T.Y. Kometani, J.M. Parsey, Jr. and R.A. Laudise, J. Cryst. Growth **78**, 9 (1986).
4. M.G. Astles, F.G.H. Smith and E.W. Williams, J. Electrochem. Soc. **120**, 1750 (1973).
5. J. K. Furdyna, J. Appl. Phys. **53**, 7637 (1982) and references therein.

partially repaired through dynamic annealing during implantation. The structural, electrical and optical properties of these samples are currently under investigation.

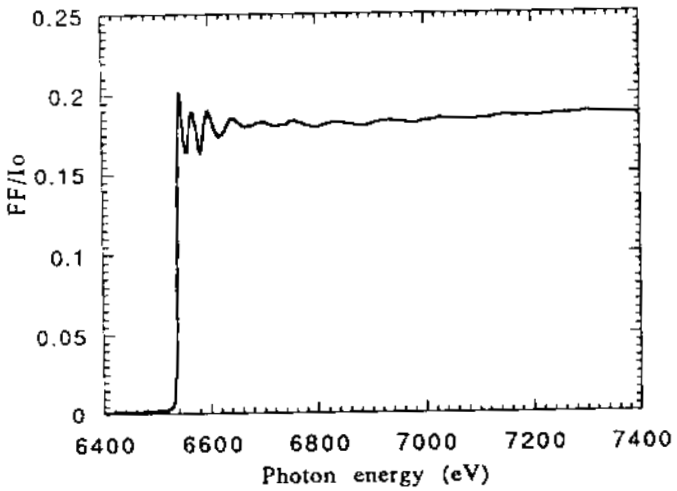

(a)

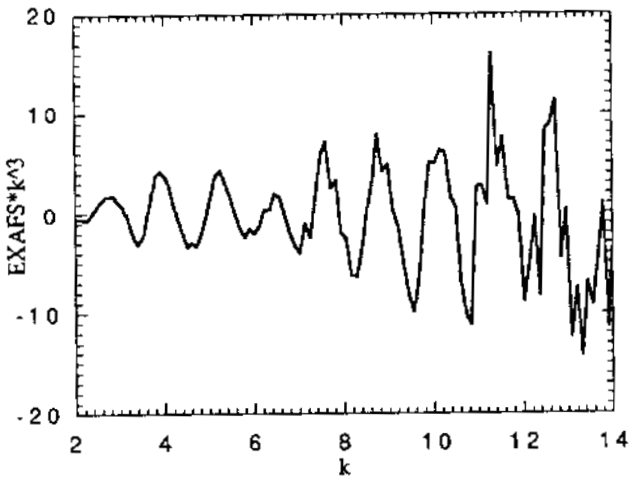

(b)

Fig. 1(a) Fluorescent intensity of the Mn K_α as a function of excitation photon energy from a $Cd_{0.8}Mn_{0.2}Te$ bulk crystal. (b) The corresponding k^3-weighed EXAFS spectrum.

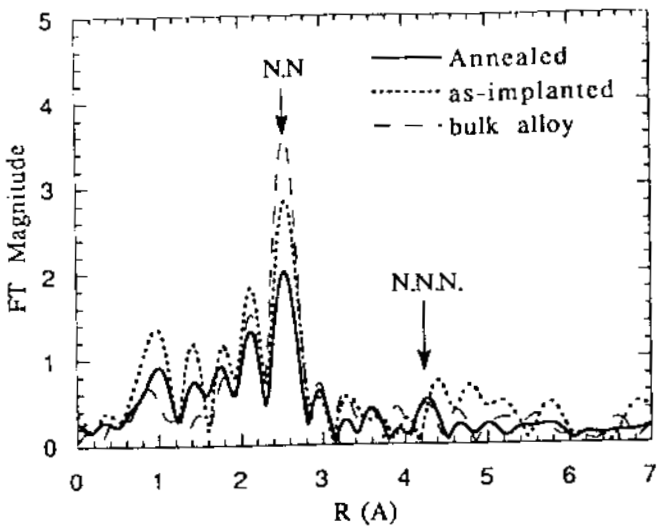

Fig. 2 Fourier tansforms of the EXAFS data from the bulk CdMnTe alloy and the ion beam synthesized layer as-implanted and annealed.

DETERMINATION OF THE OXIDATION STATES OF URANIUM AND THORIUM COMPOUNDS

David Shuh, Jerry Bucher, Norman Edelstein, Bernd Jung, and Wayne Lukens
Chemical Sciences Division, Lawrence Berkeley Laboratory

Heino Nitsche and Phillip Torretto
Earth Sciences Division, Lawrence Berkeley Laboratory

M.F. Lappert
Chemistry Department, University of Sussex, Brighton, England

In recent years, a number of new organometallic compounds of Th have been synthesized. One of these compounds has been shown to be Th in the tripositive oxidation state, a most unusual valence state for a molecular Th compound. Further synthetic efforts have resulted in the isolation of a compound which may have the Th ion in the dipositive state.

A number of thorium and uranium organometallic compounds were synthesized and dissolved in THF (tetrahydrofuran) or hexane. In addition solid thorium and uranium compounds were prepared along with aqueous solutions of UO_2Cl_2.

Near Edge X-ray Absorption Fine Structure (NEXAFS) spectroscopy data were collected on these samples on beam line 4-1. Preliminary examination of the data for the thorium compounds, such as ThI_2, ThI_3, Th metal, and Th(IV) organometallic compounds showed no systematic charge state shifts which can be attributed to different oxidation states. However it should be notedthat in general the metal ion concentrations of the samples were not ideal .

Examination of the uranium data shows significant shifts between U(VI) compounds and U(III) compounds.

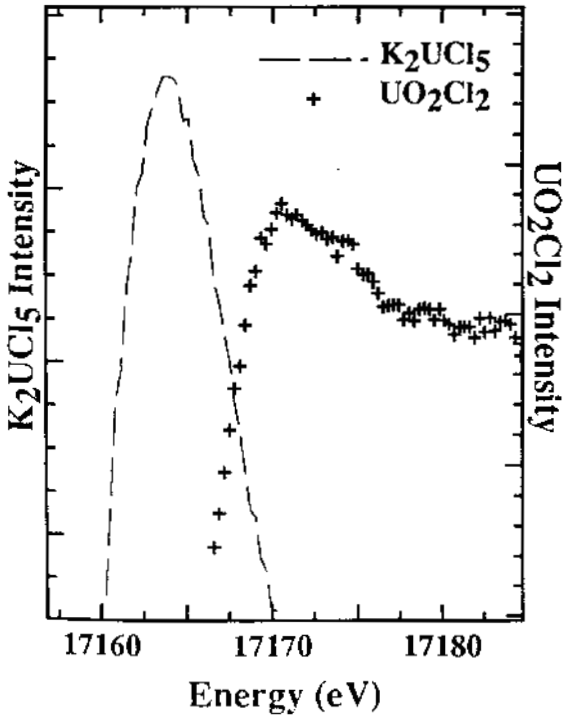

Figure 1. Comparison of the U edge positions between K_2UCl_5 and UO_2Cl_2 (Th084)

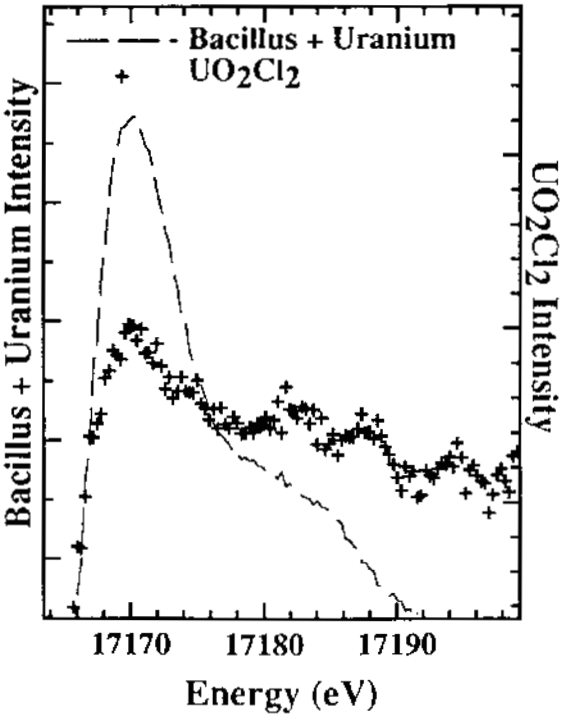

Figure 2. Comparison of the U edge positions between the Bacillus + Uranium and UO_2Cl_2.

The shift between aqueous UO_2Cl_2 (U(VI)) and K_2UCl_5 is shown in Figure 1.

The uptake of uranyl compounds (U(VI)) by microbial agents for bioremediation is being investigated. The organisms do bind the uranyl compounds, but the formal oxidation state of the bound U ions is unknown. Preliminary analysis of a sample of uranyl ions bound by the microbial agents indicate, that for this sample, the oxidation state of uranium is hexavalent. (See Figure 2.) Further work is underway to verify this result.

Acknowledgments

This work was done at SSRL which is operated by the Department of Energy, Division of Chemical Sciences. This work was supported by the Director, Office of Energy Research, Office of Basic Energy Sciences, Chemical Sciences Division of the U. S. Department of Energy under Contract No. DE-AC03-76SF00098.

A Nuclear Multilayer Monochromator for Synchrotron Radiation

A.I. Chumakov[1], G.V. Smirnov[1], A.Q.R. Baron[2], J. Arthur[2], D.E. Brown[2], S.L. Ruby[2], G.S. Brown[3], N.N. Salashchenko[4]

[1]Kurchatov Institute, 123182 Moscow, Russia

[2]Stanford Synchrotron Radiation Laboratory, PO Box 4349, Bin 69, Stanford, Ca 94309

[3]Dept. of Physics, University of California at Santa Cruz, Santa Cruz, Ca 95064

[4]Applied Physics Institute RAN, 603600 Nizhnii Novgorod, Russia

This report is from a collaboration between physicists at SSRL and UC Santa Cruz, and physicists from the Kurchatov Institute in Russia. The sample described below was one of several that were investigated during the timing mode operation of SPEAR from 25 June to 13 July, 1992. The text is an abbreviated version of an article recently submitted to Physical Review Letters.

We introduce a new class of materials to be used in nuclear diffraction of synchrotron radiation: synthetic multilayers. Until now, much of the progress in this field has been accomplished using perfect single crystals having a naturally occurring structure[1]. Multilayers [2-4] are attractive because the material parameters (e.g. layer composition, layer thickness, number of periods) may be easily varied over a broad range. In particular, the hyperfine structure of the nuclear resonance can be designed for a specific experiment by controlling the composition of the layers containing Mossbauer isotopes and the surrounding layers.

One important application of a multilayer structure is as an ultra-high resolution monochromator for synchrotron radiation. In particular, we used a 25 period sample (magnetron sputtered onto glass) where each period contained four layers: ^{57}Fe(22Å)/Sc(11Å)/Fe(22Å)/Sc(11Å). Radiation at energies near the nuclear resonance energy (14.413 keV) in ^{57}Fe then sees a 66 A period while radiation far from resonance will see only the 33A electronic period. Thus, the first Bragg peak for resonant radiation is electronically forbidden, so only nearly resonant radiation will be reflected.

The bandpass for such a structure, might be expected to be of order the nuclear linewidth, $\Gamma_0 = 4.7 \times 10^{-9}$ eV. However, the large d spacing and small Bragg angle at 14 keV, result in a wide rocking curve so that all the incident radiation is at the Bragg angle. In this case, the actual bandpass of the system is dominated by dynamical considerations, with the coherent response of the system at the Bragg angle being many times broader than the width of the resonance. This makes possible a monochromator with ~1 μeV bandpass and large angular acceptance.

This multilayer was investigated previously[4] using a conventional ^{57}Co(Cr) radioactive source at the Moscow Kurchatov Institute. The conversion electron spectrum of the multilayer was approximately an unresolved doublet with a total width of about 0.8 mm/sec or 8 Γ_0 (including a source width of 0.2 mm/sec). This important simplification of the hyperfine spectrum of ^{57}Fe is a result of partial diffusion of scandium atoms into the iron layers[5]. A pure nuclear reflection peak at a Bragg angle of 7 mrad was observed with incident radiation in resonance with the ^{57}Fe nuclear levels. A Mossbauer diffraction spectrum of the pure nuclear reflection showed remarkable coherent broadening of the resonance to a width of about 40 Γ_0 with an

average reflectivity of about 10% over this range.

The work described here was performed at SSRL, beamline 10-2, a 31 pole wiggler end station. Beamline optics included a platinum-coated toroidal mirror for focusing and a double-crystal Si(111) monochromator. Further monochromatization was accomplished using a channel cut Si(10 6 4) crystal[6], providing a source beam with a 60 meV bandwidth at the nuclear resonance energy, 14.413 keV. The synchrotron was run in timing mode, providing a pulse of x-rays (~1/2 ns duration) every 195 ns. The photons reflected by the multilayer were detected by an avalanche photodiode (APD) detector[7] with timing electronics synchronized to the storage ring.

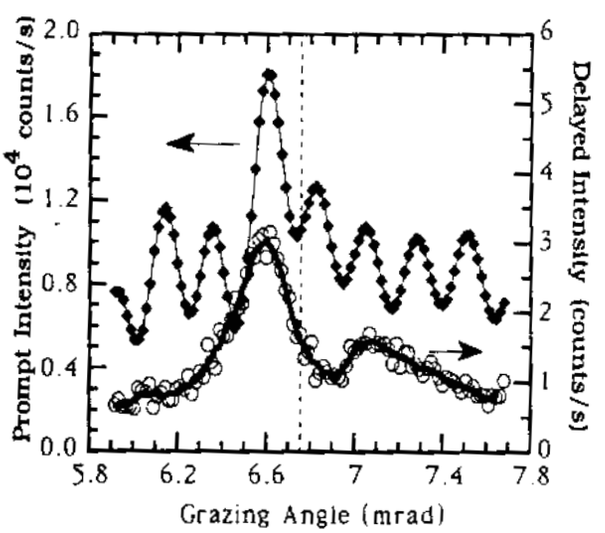

FIG. 1. Electronic (thin line) and nuclear (thick line) rocking curves near the pure nuclear reflection. The dashed line shows the nuclear Bragg position. Solid lines are to guide the eye.

Electronic and nuclear rocking curves for the multilayer were measured simultaneously in the vicinity of the pure nuclear reflection (Fig. 1). The nuclear curve was determined by integrating counts over the time interval between 17 and 150 ns after the synchrotron pulse. Delayed events before 17 ns were not counted due to the instrumental response to the prompt scattering. The prompt electronic scattering shows the Fresnel beat pattern due to interference between waves scattered by the top and bottom boundaries of the multilayer. The approximate angular position of the nuclear reflection, determined in studies discussed below (shown by the dashed line), coincided with one of the Fresnel minima. The prompt (electronic) reflectivity at this angular position was about 3×10^{-4}.

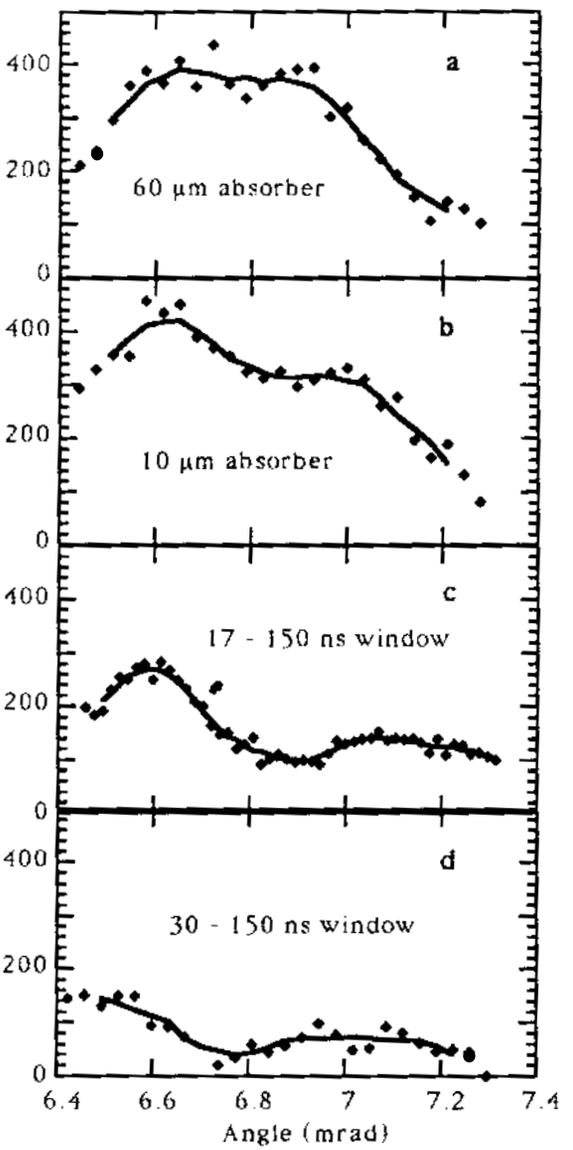

FIG. 2. Nuclear rocking curves progressing from a broad peak to a "volcano" shape, depending upon the counting window and the presence of absorbers. See text below. Solid lines are to guide the eye.

The "volcano" shape of the nuclear rocking curve (Fig. 1 or Fig. 2c) is significantly different from the rocking curve measured with a ^{57}Co source[4]. This is attributed to counts lost during the 17 ns dead time after the synchrotron pulse. As the

nuclear Bragg angle is approached, the speedup of the nuclear decay increases so that most of the reflected radiation is re-emitted in the first 17 ns. The volcano crater may be interpreted as the "shadow of the time gate". When the gate was set to only count from 30-150 ns, the shadow became more pronounced (Fig. 2d).

In order to shift the radiation emitted at early times into the counting window of 17-150 ns, resonant forward scatterers were placed after the multilayer. They provided additional time delay for the scattered radiation. Figure 2 shows the rocking curve when 95% enriched $^{57}FeBO_3$ crystal plates of 60 m (Fig. 2a) and 10 m (Fig. 2b) thickness were used. The rocking curve shape approaches the single broad peak measured with a radioactive source[4] . The rocking curves in Figure 2 enable one to estimate the nuclear Bragg position to be approximately 6.8 mrad, as is shown in Figure 1.

Figure 3 shows the time evolution of the radiation reflected from the multilayer near the nuclear Bragg position. Speedup of the nuclear decay is evident, with the strongest speedup observed near the nuclear Bragg position (Fig. 3a). The decay time constant during the interval 17-50 ns increased from 12 to 33 ns as the deviation from the Bragg position increased from 7 to 100 arc seconds. The slow beats visible in the time distribution are suspected to be the Bessel function oscillations characteristic of dynamical nuclear resonant diffraction[8].

The spectral properties of the radiation diffracted by the nuclear multilayer were investigated using forward scattering through a resonant $^{57}FeBO_3$ absorber. The $^{57}FeBO_3$ crystal plate was magnetized by an external magnetic field to orient the internal nuclear hyperfine magnetic field perpendicular to the photon propagation direction, and either parallel or perpendicular to its polarization. With the hyperfine field perpendicular to the photon polarization, selection rules insure only those hyperfine transitions in the iron borate with $\Delta m=0$ will be excited (lines 2 and 5), while in the parallel case transitions with $\Delta m=1$ will be excited (lines 1,3,4, and 6)[9] .

The time evolution of the diffracted radiation measured with a 60 m $^{57}FeBO_3$ absorber downstream of the multilayer is shown in Figure 4. In Fig. 4a, with the hyperfine field perpendicular to the polarization direction, a beat period of 14 ns is consistent with the data. This is the result of beating between lines 2 and 5, which are separated in energy by 67 Γ_0. The time response shown in Fig. 4b was observed with the hyperfine field parallel to the photon polarization, and is consistent with a beat pattern resulting from the simultaneous excitation of the four $\Delta m=1$ hyperfine transitions. The two strongest transitions (lines 1 and 6) have an energy separation of 115 Γ_0, causing an 8 ns beat period. However, interference from the weaker lines (3 and 4, separated by 18 Γ_0) modulates the beat pattern to give a 16 ns component which appears in Fig. 4b. Thus the bandwidth of radiation reflected by the mirror is sufficient to excite all six of the hyperfine

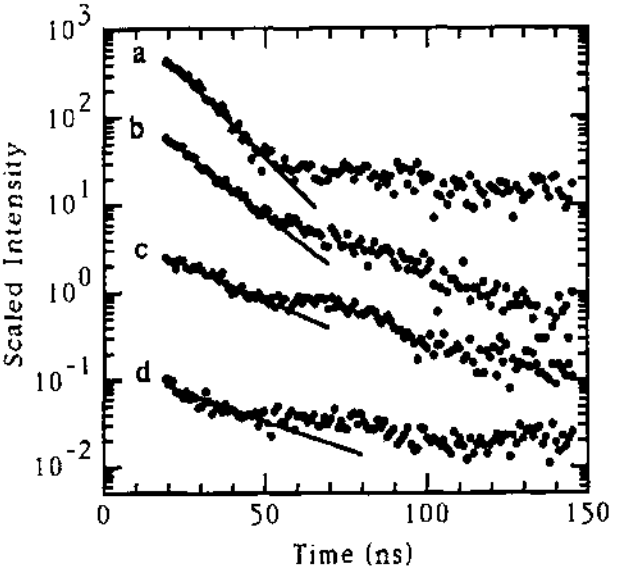

FIG. 3. Time response of the multilayer near the nuclear Bragg position. The vertical scale is correct for curve (a); each succeeding curve has been lowered one decade. Solid lines are $\exp(-t/\tau)$ fits to the interval of 17-50 ns. Deviation from the Bragg position was (a) -7 arc seconds, τ=12 ns; (b) -32 arc seconds, τ=15 ns; (c) -72 arc seconds, τ=27 ns; (d) -100 arc seconds, τ=33 ns.

transitions in iron borate, even the outer lines separated by the energy interval of $115\,\Gamma_0$.

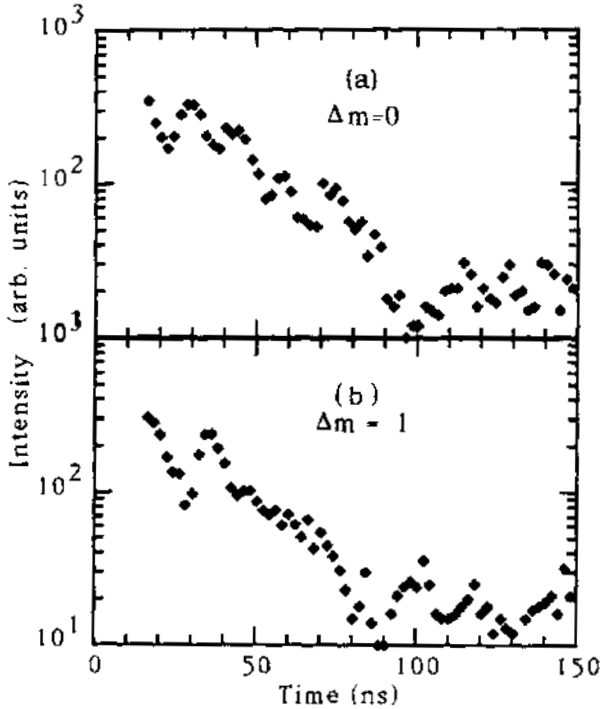

Fig. 4. Forward scattering through a 60 μm $^{57}FeBO_3$ absorber placed after the nuclear multilayer, with the multilayer at the Bragg position. In (a) the hyperfine magnetic field was perpendicular to the photon polarization direction (Δm=0 transitions excited) while in (b) the field was parallel (Δm = +-1 transitions).

Diffraction of synchrotron radiation by this nuclear multilayer showed a strong speedup of the nuclear decay and remarkable broadening of the resonance. The decay time of the coherent nuclear response of the multilayer was about 12 ns, measured in a 17-50 ns time interval, and is estimated to be less than 5 ns in the initial stage of decay. Studies of nuclear forward scattering in resonant absorbers downstream from the nuclear multilayer demonstrate that the energy bandwidth of the radiation reflected by the multilayer is sufficiently broad to excite all the nuclear resonant transitions in an $^{57}FeBO_3$ resonant absorber. The electronic reflectivity at the nuclear Bragg position was only 3×10^{-4}. The present work shows the nuclear multilayer to be a promising candidate for an extremely small bandpass monochromator for synchrotron radiation.

SSRL is operated by the US Department of Energy, Office of Basic Energy Sciences, Division of Chemical Sciences. Support for this research was provided by that Office's Division of Materials Sciences, and by the Kurchatov Institute in Moscow and the Institute of Applied Physics in Nizhnii Novgorod, Russia.

[1] E. Gerdau, R. Rüffer, H. Winkler, W. Tolksdorf, C. P. Klages, and J. P. Hannon, Phys. Rev. Lett. **54**, 835 (1985). U. van Bürck, R. L. Mössbauer, E. Gerdau, R. Rüffer, R. Hollatz, G. V. Smirnov, and J. P. Hannon, Phys. Rev. Lett. **59**, 355 (1987). A. I. Chumakov, M. V. Zelepukhin, G. V. Smirnov, U. van Burck, R. Rüffer, R. Hollatz, H. D. Rüter, and E. Gerdau, Phys. Rev. **B41**, 9545 (1990). W. Sturhahn, E. Gerdau, R. Hollatz, R. Rüffer, H. D. Rüter, and W. Tolksdorf, Europhys. Lett. **14**, 821 (1991). G. Faigel, D. P. Siddons, J. B. Hastings, P. E. Haustein, J. R. Grover, and L. E. Berman, Phys. Rev. Lett. **61**, 2794 (1988). J. Arthur, G. S. Brown, D. E. Brown, and S. L. Ruby, Phys. Rev. Lett. **63**, 1629 (1989). S. Kikuta, Y. Yoda, C. K. Suzuki, H. Ohno, H. Takei, K. Nakayama, X. W. Zhang, T. Matsushita, S. Kishimoto, and M. Ando, Jap. J. Appl. Phys. **30**, L1686 (1991).

[2] R. Röhlsberger, E. Witthoff, E. Leuken, and E. Gerdau, to be published.

[3] A. I. Chumakov and G. V. Smirnov, Pis'ma Zh. Eksp. Teor. Fiz. **53**, 258 (1991) [JETP Lett. **53**, 271 (1991)].

[4] A. I. Chumakov, G. V. Smirnov, S. S. Andreev, N. N. Salashchenko, and S. I. Shinkarev, Pis'ma Zh. Eksp. Teor. Fiz. **55**, 495 (1992) [JETP Lett. **55**, 509 (1992)].

[5] D. H. Ryan, J. O. Ström-Olson, W. B. Muir, J. M. Cadogen, and J. M. D. Coey, Phys. Rev. **B40**, 11208 (1989).

[6] G. Faigel, D. P. Siddons, J. B. Hastings, P. E. Haustein, J. R. Grover, J. P. Remeika, and A. S. Cooper, Phys. Rev. Lett. **58**, 2699 (1987).

[7] S. Kishimoto, Nucl. Instrum. Methods **A309**, 603 (1991). S. L. Ruby and A. Q. R. Baron, to be published.

[8] Y. Kagan, A. M. Afanas'ev, and V. G. Kohn, J. Phys. C. **12**, 615(1979).

[9] M. Eibschütz, and M. E. Lines, Phys. Rev. **B7**, 4907 (1973).

SI-TASI$_2$ *IN-SITU* COMPOSITES

S.R. Stock[1], Z.U. Rek[2], Y.H. Chung[1,3] and B.M. Ditchek[4]

[1]School of Materials Sci. & Eng., Georgia Institute of Technology, Atlanta, GA 30332-0245

[2]Stanford Synchrotron Radiation Laboratory, Stanford University, Stanford, CA 94309

[3]Currently at: Kimbo Color Laboratory, 430 Shotwell St., San Francisco, CA 94110

[4]GTE Laboratories, 40 Sylvan Road, Waltham, MA 02254 USA

Directional solidification of semiconductor-metal eutectic mixtures commonly yields aligned arrays of metallic rods in a single crystal semiconductor matrix, and Si-$TaSi_2$ composites are the most promising for device applications such as diodes. Rod diameters and spacings of the samples described below are on the order of one and ten micrometers, respectively. Wafers, cut transverse to the [111] growth direction of the boules, have thicknesses of 500 μm after polishing with colloidal silica. X-ray double axis diffractometry, with Cu Kα radiation, a 0.6 x 1.6 mm^2 spot focus, a 1 mm diameter collimator and a monochromator, produces [333]Si rocking curve widths (full width at half maximum or FWHM) ranging between 45 and 60 arc seconds. [1]

As the Si-$TaSi_2$ composite structures have dimensions which are near the spatial resolution limit of x-ray diffraction topography, it is not surprising that white beam projection and section topographs reveal little structure; the topographs do not, however, exhibit asterism. In addition to the sharply defined topographs, diffuse radial streaks are observed in transmission Laue patterns and reflect the symmetry of the Si matrix (Figure 1). Eighteen streaks are approximately equally spaced around the transmitted beam. There appear to be nine pairs of parallel streaks, one on either side of the incident beam and the intensity of each streak varies along its length. These streaks are not observed in Si crystals and are, therefore, related to the composite structure.

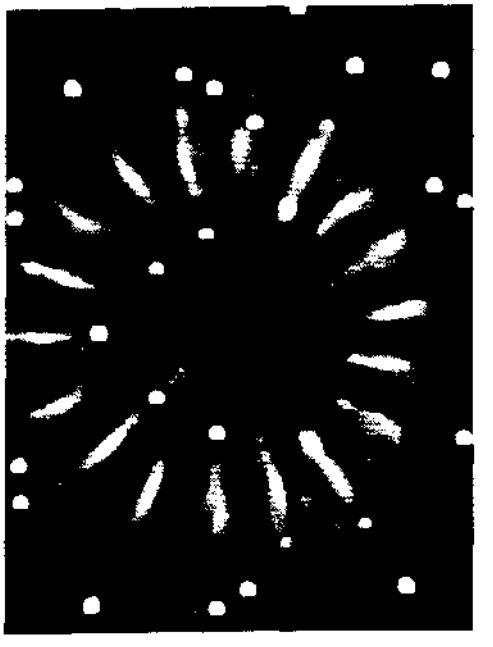

Fig. 1 Transmission synchrotron radiation Laue pattern of Si-$TaSi_2$ wafer. Topograph is printed in reversed contrast. White, well defined spots are from Si and radial diffused bands from $TaSi_2$

The length and arrangement of the diffuse streaks suggest a crystallographic/diffraction origin, specifically, diffraction by the $TaSi_2$ rods. This is verified by recording the Laue pattern with and without fil-

ters (in the beam) possessing absorption edges in the wavelength range expected in the streaks. The images of rods (i.e., topographs of the rods) diffracting wavelengths higher than that of the absorption edge suffer relatively little attenuation while those images produced with wavelengths just below the absorption edge are essentially eliminated. The result is a sharp change in intensity at the position where the rods are oriented to diffract the absorption edge wavelength.

The diffuse streaks are characterized by placing Zr, Mo and Ag filters in the incident beam. The thickness of the filters are 108 μm, 60 μm and 60 μm respectively, and the change in contrast occurs at wavelengths of 0.689Å, 0.620Å, and 0.486Å, respectively. Figure 2, from a Laue pattern recorded with a 4 mm diameter beam, shows a typical streak without a filter, with a Mo filter and with a Zr filter (top, middle and bottom, respectively). The d-spacing for the topographs of $TaSi_2$ rods comprising this streak is between 1.59Å and 1.60Å which corresponds to d_{113}. [2] Another set of crystallographically equivalent streaks, obscured by the beam stop in Figure 1, were investigated with and without a Mo filter; the average d-spacing of these six streaks was determined to be 4.11Å, i.e., these six streaks were produced by {100}.

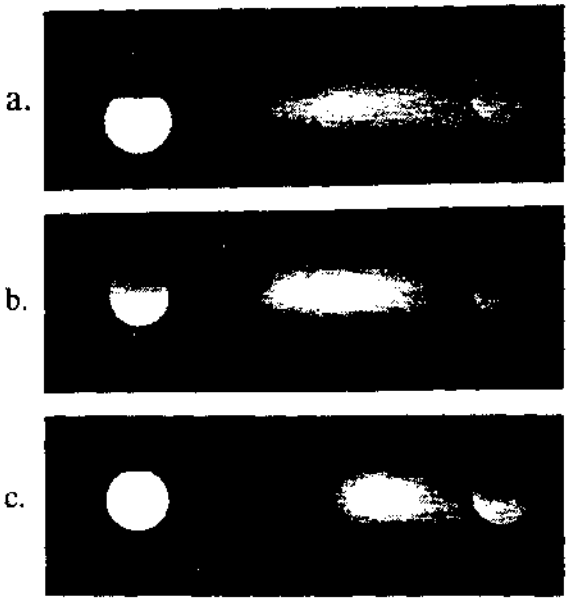

Fig. 2 Diffused streak imaged a) without filter, b) with Mo filter, c) with Zr filter. A 4mm diameter collimator is used, and the abrupt change in streak contrast is due to K absorption edge of the filter.

Demonstration that the streaks are diffraction from $TaSi_2$ is important because this shows that the rods have very strong preferred orientation relative to the Si matrix. Use of absorption edges from filters can, therefore, be used to study the texture in the $TaSi_2$/Si and other similar composite systems, texture which is difficult to study by conventional methods because of the very small volume fraction of the phase of interest.

References

1. S.R. Stock, Z.U. Rek, Y.H. Chung, P.C. Huang and B.M. Ditchek, to appear in J. Appl. Phys., February, 1993.

2. Card 38-483, Powder Diffraction File, Joint Committee for Powder Diffraction Standards, International Centre for Diffraction Data.

HARD X-RAY CHARACTERIZATION OF YB_{66} CRYSTALS

Z.U. Rek[1], Joe Wong[2], T. Tanaka[3], Y. Kamimura[3]

[1] Stanford Synchrotron Radiation Laboratory, Stanford, CA 94309
[2] Lawrence Livermore National Laboratory, Livermore, CA 94551
[3] National Institute for Inorganic Materials, Tsukuba, Ibaraki 305, Japan

YB_{66} semiconductor material with cubic structure, due to its large lattice constant of 23.44Å, absence of intrinsic absorption edges and its vacuum compatibility have been studied extensively for possible application as a soft X-ray monochromator in the 1-2 keV energy range [1]. Monochromator quality single crystals of YB_{66} have been grown by Tanaka et al. [2] by the indirect heating floating zone (IHFZ) method shown on fig. 1. The growth process consists of 3 basic steps: 1) pre-forming of a polycrystalline sintered feed rod from synthesized high purity raw powder; 2) a seeding and necking process that brings in contact seed and molten zone and starts the growth process; 3) a single or multiple-zone-pass of molten zone to densify the feed rod and improve the crystal quality. Systematic work on various unit-processes of the crystal growth combined with thorough characterization resulted in a number of process changes which were required to establish reproducible growth and high-quality crystals. Two major modifications of the technique introduce quite significant differences in crystal quality. These are: a) growth by upwards or downwards drive of the feed rod and the crystal in an attempt to control the interface shape to be convex, under congruent composition growth; b) growth under incongruent conditions [3]. An incongruent composition means that the composition of the feed rod and molten zone are different. In the case of the crystal discussed below, the [B]/[Y]≈56 for the feed rod and [B]/[Y]=40 for the molten zone. In congruent composition growth [B]/[Y]=62. The crystal characterization was accomplished using hard x-ray white beam topography in reflection and transmission mode and double-crystal rocking curve measurements using a conventional CuKα source. The crystals grown under congruent conditions were found to have high crystalline quality areas on the seed or zone end dependent on the particular growth process. These areas are on the order of several millimeters as reported in [3], but most of the crystal however, exhibits large and small grain boundaries, Fig. 2. Application of incongruent conditions seems to achieve more reproducible growth of high quality crystals compared with congruent growth. From several crystals obtained, all of them show similar behavior of defect structure through the length of the crystal. That is, many subgrains that appeared during the seeding process decrease progressively in number towards the zone end, thus yielding high crystal quality near the zone end. Another characteristic feature of these crystals is the high quality of the material in the center and fast deterioration at the edges of a boule as shown by reflection topography, fig. 3a. Fig. 3b displays the (400) double-crystal rocking curves, measured with

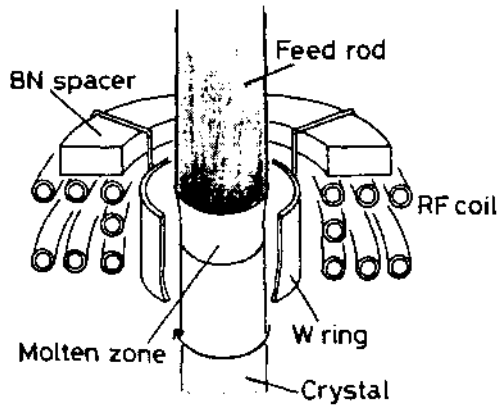

Fig. 1. Schematic diagram of the indirect heating floating zone method

CuKα radiation and asymmetric Si(333) monochromator at 3 points of the crystal indicated by the arrows. The FWHM of rocking curves measured for areas of *ca* 8mm from the central part of crystals were on the order of 120 to 130 arc sec. The reflectivity was ~3%. From the number of crystals studied, the best pair of crystals, cut along crystal growth direction from zone end of a boule, were selected for the first experiment on the JUMBO monochromator on beam line 3-3.

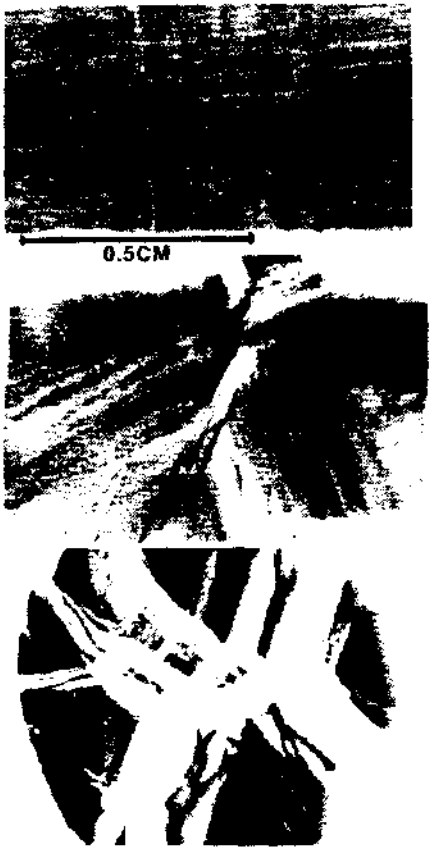

Fig. 2 Transmission white beam topography of YB_{66} samples cut perpendicular to [100] crystal growth direction at different parts of crystal: A.) seed end, B.) center C.) zone end

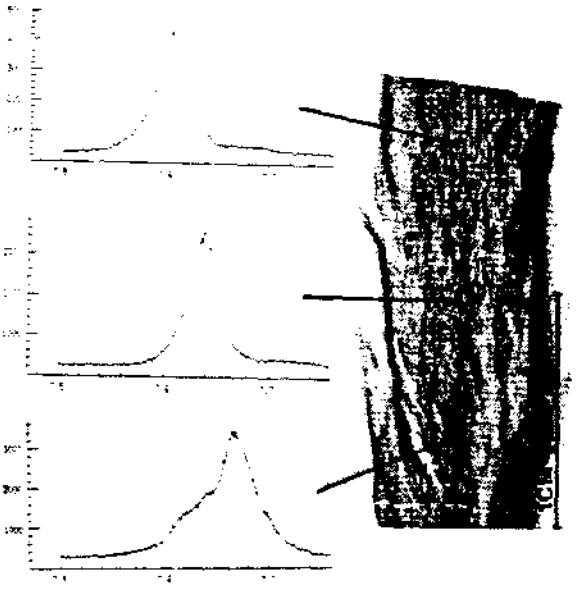

Fig. 3 Reflection topography of the zone end of YB_{66} grown under incongruent composition conditions and (400) double-crystal rocking curves measured with a CuKα conventional source for selected parts of this crystal. Crystal was cut parallel to [100] growth direction.

1. J. Wong, G. Shimkaveg, W. Goldstein, M. Eckart, T. Tanaka, Z. Rek, H. Tompkins, N.I. & M., A291, (1990), 243

2. T. Tanaka, S. Otani, Y. Ishizawa, J. Cryst. Growth, 73, (1985), 31

3. Z. Rek, J. Wong, T. Tanaka, Y. Kamimura, F. Schaefers, B. Muller, M. Krumrey, P. Muller, SPIE Proc., Vol. 1740, (1992), 173

Structural Evidence for Y Ions Trapped Inside C_{82}: An EXAFS Study

C.-H. Park, B. O. Wells, J. DiCarlo, Z.-X. Shen
Department of Applied Physics and Stanford Synchrotron Radiation Laboratory, Stanford University, Stanford, CA 94305,
J. R. Salem, D. S. Bethune, C. S. Yannoni, R. D. Johnson, M. S. de Vries,
Almaden Research Center, IBM Research Division, 650 Harry Road, San Jose, CA 95120
C. Booth, F. Bridges
Physics Department, University of California, Santa Cruz, CA 95064
P. Pianetta
Stanford Synchrotron Radiation Laboratory, Stanford University, Stanford, CA 94305

The suggestion of the possible existence of fullerene cages with atoms inside the cavity has generated intense interest, both because of potential new chemistry and because of potential new materials properties. Unfortunately, definitive structural tests of this possibility, such as X-ray crystallography, require material of higher purity, which is not available today. One way to circumvent this problem is the use of Extended X-Ray Absorption Fine Structure (EXAFS) spectroscopy. It is possible to tune the radiation to the absorption edge of the metal atom of interest and to obtain information about the metal atom neighbors from the fine structure of its absorption coefficient. Because the method is specific for the atom being probed, it is possible to perform such an experiment in relatively dilute samples.

We carried out EXAFS and K-edge absorption experiments to investigate the structural and chemical state information of metallofullerenes. For samples containing only YC_{82} and Y_2C_{82} in addition to bare fullerenes, yttrium K-edge EXAFS data can only be interpreted with yttrium being indohedral and a Y-C nearest neighbor bond length of about 2.4Å. The finding constitutes a direct structural evidence showing that yttrium is indeed trapped and strongly bonded inside the fullerene. The yttrium K-edge data suggest that the chemical state of yttrium is 3+, even for Y_2C_{82}.

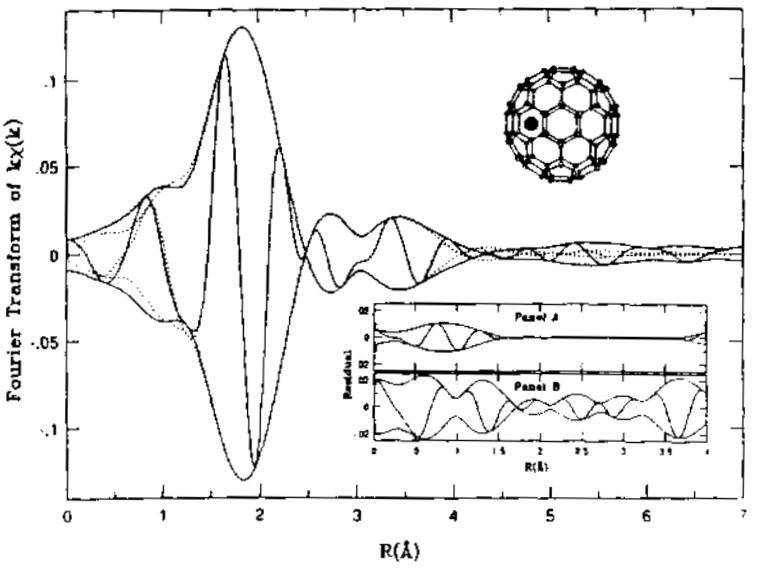

Fig. 1. R-space data (solid line) and a complete fit of indohedral geometry (dotted line). The fit is performed in R-space range from 1.5 to 3.8 Å. The graphical representation is shown in upper right corner. Panel A is the residual of the indohedral fit while Panel B is the residual of a typical exohedral fit. It is clear the indohedral fit is muc better.

FRACTAL SURFACE OF AMORPHOUS PLATINUM PYRIMIDINE COMPLEXES IN SOLID STATE AS REVEALED BY ANOMALOUS SMALL ANGLE SCATTERING

R. Serimaa,
Department of Physics, P. O. Box 9, 00014 University of Helsinki, Finland,
T. Laitalainen
Department of Chemistry, P. O. Box 6, 00014 University of Helsinki, Finland,
M. J. Regan and A. Bienenstock
Stanford Synchrotron Radiation Laboratory, Slac Bin 69, Stanford, P. O. Box 4349, Ca 94305, USA

INTRODUCTION

Platinum pyrimidine greens, which are synthesized from *cis*-diaquodiammineplatinum(II) and pyrimidine nucleosides, belong to a class of amorphous Pt-complexes, platinum blues.[1] These Pt-complexes are antitumor active[2,3] and their other interesting properties include an intense colour, termochromism and catalytic reaction with hydrogen peroxide.[4,3,5]

Results of our AWAXS study[6] indicate that the basic structural Pt-units of these amorphous Pt-complexes in the solid state are tetranuclear or dinuclear. Since these results provide only a short-range picture of the Pt-complexes, we report here a complementary study using anomalous small-angle x-ray scattering (ASAXS) which provides insight on a length scale from 5-500 Å and Pt-specific information by using the anomalous dispersion relations. From an earlier SAXS study[7], the Pt-complexes in aqueous solutions dissolved into dimers, which may then form aggregates. The sizes of the aggregates depend on the concentration. In a dilute solution (14 mg/ml) the radii of gyration varied between 4-7 Å.

EXPERIMENTAL

The samples chosen for study in this work are the following: Pt-uridine green nitrate (1), Pt-uridine green sulfate (2), Pt-uridine violet sulfate (3), Pt-5-bromouridine green sulfate (4), and Pt-ftorafur green sulfate (5). The main differences of the syntheses are as follows[4,3,7]. The Pt-complexes were synthesized from $Pt(NH_3)_2(H_2O)_2(NO_3)$ (1) or $Pt(NH_3)_2(H_2O)_2(SO_4)$ (2-5). The Pt-complexes (1), (2), (4) and (5) were synthesized by hydrogen peroxide oxidation. The reaction temperature was 70 °C for a time of 0.5–1 h. Pt-uridine violet (3) was synthesized without an oxidant in room temperature for 170 h. The main difference between Pt-uridine green (1) and (2) is a different counter ion. The green (2) and the violet (3) complexes are synthesized from the same starting materials, but with different reaction conditions. The Pt-complex (4) has Br in the position 5 of the uridine heterocycle instead of H. Ftorafur (5) has F in position 5 of uridine and lacks all OH-groups in the ribose part.

Data were taken at the eight-pole focused wiggler end-station 4-2 of the Stanford Synchrotron Radiation Laboratory (SSRL). The basic line consists of a bent cylindrical mirror and a double-crystal monochromator. For this experiment, we used Si(111) crystals and worked at several incident x-ray energies below the Pt L III edge (11.1, 11.2, 11.3, 11.4, and 11.5 keV) as well as at a single, lower energy (8 keV). All the Pt-complexes (1)-(5) were measured at 8 keV and Pt-uridine green (2) and Pt-5-bromouridine green (4) at 11.1-11.5 keV. Experiments at 8 keV are used to study the SAXS patterns at small scattering vectors that are otherwise obscured by parasitic scatter at the higher energies. That no fluorescence from Pt is obtained at 8 keV can be used to determine the background due to near-edge contributions of fluorescent processes at 11.1-11.5 keV.

The SAXS camera[8] is semi-permanently located at line 4-2 and is one of the results of the SSRL Biotechnology program. The samples were held in transmis-

sion and separated by an evacuated chamber approximately 2.7 m from a linear position-sensitive proportional counter. Miniature ionization chambers, placed directly before and after the sample, were used to normalize scattering data as well as calibrate the monochromator.

The data were corrected for absorption and any nonlinearities in the detector, scaled to the primary beam intensity, and background subtracted. The range of reciprocal space covered is from k =0.006 to 0.28 $Å^{-1}$ ($k = \frac{4\pi}{\lambda}\sin\theta$, where λ is the wavelength and θ is half of the scattering angle). Smearing effects due to finite beam size were considered but appear negligible due to the small spot size used.

RESULTS

The samples scatter strongly in the small-angle range and the intensity curves show a power-law dependence. The slopes are smaller than -4 (the classical Porod's law), thus the concept of fractal geometry is the key to understanding these scattering curves. A power law distribution of uniform pores would be another possible model. Because the materials are amorphous, it seems unlikely that the shapes of the pores would be uniform. The structural parameters that can be determined from SAXS data are the fractal dimension and the radius of gyration.

The slope was obtained from the intensity curve by fitting a line to pairs of points $(\ln(k), \ln(I(k))$. The fitting results are shown in Table 1. Figure 1 presents the power law fit for Pt-green (2). The slope α varies between 3.37 and 3.76, which indicates that the scattering units are surface fractals. The surface fractal dimension $D_s = 6 - \alpha$ varied between 2.25 and 2.63.

The intensity curves were in a reasonable agreement with Guinier's law only on a very short range $0.006 < k < 0.008$, only 5-7 data points. The radii of gyration (R_g) varied between 310 Å and 370 Å. It is conluded that the smallest reliable k was too large to obtain a full picture of the structure of the samples.

There is a change in SAXS at the Pt-edge, which excludes the possibility that the Pt is uniformly distributed in the sample. The differences of two intensity curves at two energies are largest at $k < 0.03$ $Å^{-1}$ (Figure 2). A reasonable model is one that accounts for the small angle scattering from aggregates of Pt-complexes. The Pt-complex was approximated as a two-component system of Pt's (component a) and other atoms C, N, O, S, and H (component b). To verify this model, the behaviour of the calculated and the experimental SAXS invariants, $Q = \int_0^\infty I(k)k^2dk$, as a function of energy were compared. The invariant Q of a system of

DISCUSSION

All the Pt-complexes studied form large aggregates in the solid state, which are quite compact yet have a rough surface. The surface fractal dimensions D_s vary between 2.24–2.63. The fractal dimensions for all the complexes (1)-(5) correspond to length scales of approximately 17-140 Å. The upper limit may be too low, because the corresponding k-value was very close to the first measuring point. The aggregates are much larger in the solid state than in solution, which implies that, when mixed with water, they decompose.

Pt-violet (3) exhibits the roughest surface. It also has the most prominent large angle maximum and might be slightly more ordered than the other complexes. The differences in the aggregates of Pt-violet (3) and Pt-green (2) may be related to intermolecular order of the two complexes, because according to our WAXS study they are both composed of tetranuclear Pt-units. Changing the counter ion from sulfate to nitrate might also increase the surface roughness, since D_s of Pt-green (1) was larger than D_s of (2). It also affects on the structure since the positions of 'the wide angle maximum' differs. However, our results are inconclusive at this point since a WAXS study of Pt-green (1) has not been performed, and hence we cannot identify Pt-complexes (1) and (2) as having the same primary Pt-units.

Pt-green (4) shows slightly increased surface irregularity compared to Pt-green (2). The results of our AWAXS study indicate that Pt-green (4) consist of dinuclear Pt-units, and that the shortest distance between two dinuclear units is larger than in the tetranuclear Pt-green (2).

Both Pt-green (2) and (5) show a relatively low degree of surface irregularity with the same surface fractal dimension D_s of about 2.2. The absence of the three OH-groups in the ligand seems to have no effect on the structure of the aggregates in the solid state. The same result has been obtained for H_2O-solutions: the particle sizes of all the complexes (2), (3), and (5) are about the same. This indicates that intermolecular hydrogen bonding is not the primary reason for the aggregate formation.

The aggregates may form during the reaction itself, during the precipitation after the addition of acetone, or even during drying. The model of irreversible aggregation[9] explains the appearance of surface fractality in colloids e.g. silica colloids. The surface fractal dimension from the simulations is 2.52,[9] which agrees well with our results for Pt-complexes (1) and (3). This suggests that one possible aggregation mechanism of Pt-complexes might be a slow cluster-cluster aggregation process in a dense system, where small clusters are more agitated than large ones. The small aggregates in dilute water solutions may be formed by a different mechanism.

ACKNOWLEDGEMENT

The financial support of The Finnish Academy, The University of Helsinki and Technology Development Centre is gratefully acknowledged. Support for MJR and AB was provided by the US Department of Energy (DOE), Office of Basic Energy Sciences. Part of this work was done at SSRL, which is supported by the DOE, Division of Chemical Sciences and the NIH, Biotechnology Resource Program, Division of Research Resources.

REFERENCES

(1) Farrell, N. Transition metal complexes as drugs and chemotherapeutic agents. **1989**. Kluwer Academic Publishers, The Netherlands.
(2) Davidson, J. P.; Faber, P. J; Fischer, R. G.; Mansy, S.; Peresie, H. J.; Rosenberg, B. and Van-Camp, L. Cancer Chemother. Rep., Part 1, **1975**, 59, 287.
(3) Shimura, T.; Tomohiro, T.; Laitalainen, T.; Moriyama, H.; Uemura, T. and Okuno, Y., Chem. Pharm. Bull. **1988**, 36, 448.
(4) Tomohiro, T.; Laitalainen, T.; Shimura, T.; Okuno, Y. Proceedings of an International Symposium on Activation of Dioxygen and Homogeneous Catalytic Oxidations, Tsukuba, Japan, 12-16 July 1987 Studies in Organic Chemistry, Vol. 33, pp. 557-562.
(5) Okada, T.; Shimura, T. and Okuno, H. Chem Pharm. Bull. 1992, 40, 264-266.
(6) Serimaa, R. et. al. in this book.
(7) Serimaa, R.; Laitalainen, T.; Vahvaselkä, S.; Paakkari, T. to be submitted for publication.
(8) Wakatsuki, S.; Hodgson, K.O.; Eliezer, D; Rice, M; Hubbard, S; Gillis, N; Doniach, S; Spann, U. Rev. Sci. Instrum. **1992**, 63 (2), 1736.
(9) Kolb M. and Herrmann H. J. Phys. Rev. Lett. **1987**, 59, 454.

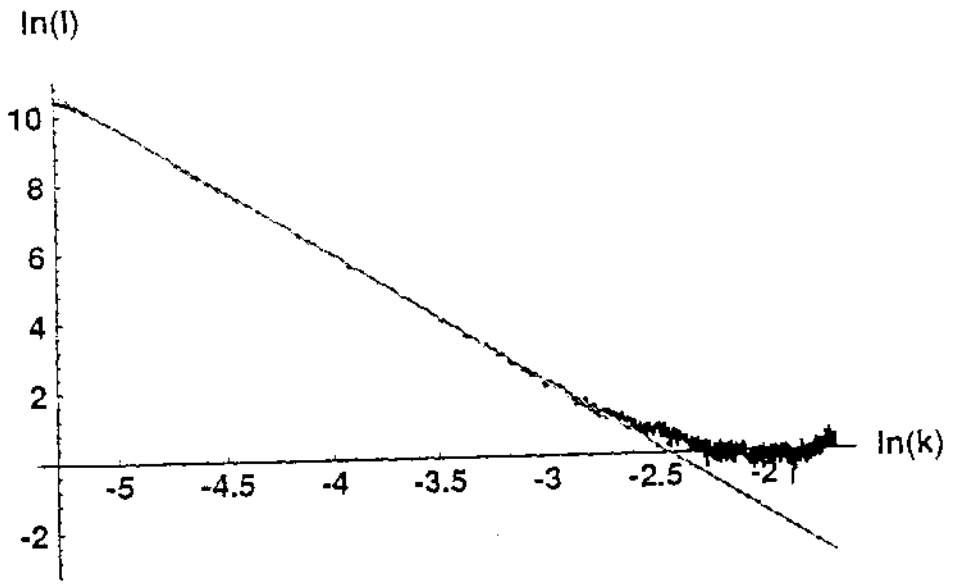

Figure 1. The fitted power law for Pt-green (2)

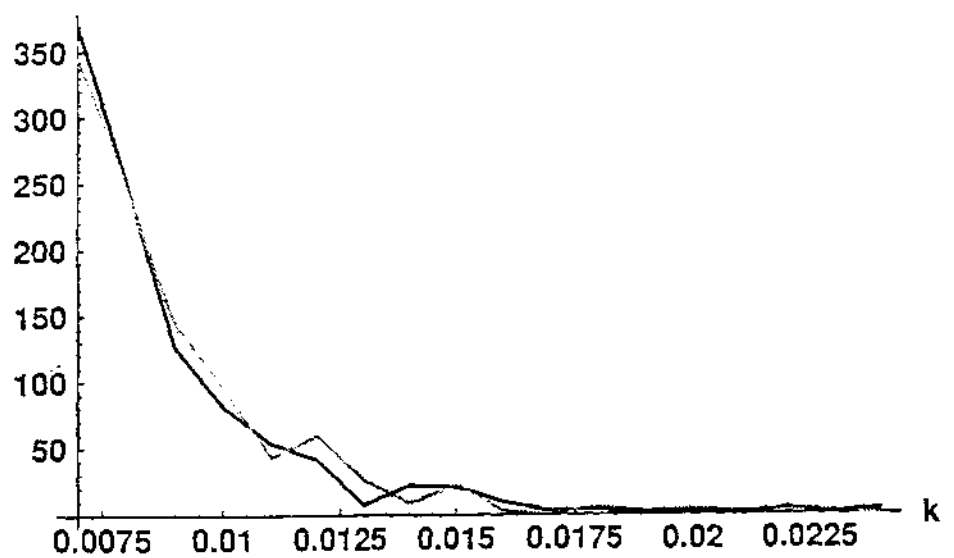

Figure 2. The differences of two intensity curves at two photon energies (11.1, 11.3 keV and 11.1, 11.5 keV) divided by the difference of real parts of the anomalous scattering factor f' of Pt at these energies.

AWAXS STUDY ON AMORPHOUS PLATINUM COMPLEXES

R. Serimaa, V. Eteläniemi, T. Paakkari
Department of Physics, P.O. Box 9, 00014 University of Helsinki, Finland
T. Laitalainen
Department of Chemistry, P.O. Box 6, 00014 University of Helsinki, Finland
A. Bienenstock
Stanford Synchrotron Radiation Laboratory, Slac Bin 69, Stanford, P. O. Box 4349, CA 94305, USA

INTRODUCTION

Platinum blues are amorphous Pt-complexes, which are of interest due to their antitumor activity. As a result of the pioneering work of Davidson et al.[1], and others referred to in ref. 2, it has become established that cis-$[Pt(NH_3)_2(H_2O)_2]SO_4$ reacts with pyrimidine bases and derivatives to give cytotoxic Pt-complexes with rich phenomenology. Methods to synthesize selectively platinum pyrimidine greens and blues have been developed.[3] It has also been shown that Pt-greens are decisively more active than Pt-blues.[4]

In this work the structures of amorphous platinum pyrimidine complexes are studied by means of anomalous wide angle x-ray scattering (AWAXS) and differential anomalous scattering (DAS) technique. Results of an earlier WAXS-study of Pt-uridine complexes[5] indicated that they all have a tetranuclear basic structure in solid state. In H_2O-solution the tetranuclear Pt-units dissociate into dinuclear Pt-units, which may undergo aggregation.[5]

EXPERIMENTAL

The samples chosen for this study are the following: Pt-uridine green (1), Pt-uridine green (2), Pt-uridine violet (3), Pt-uridine blue (4), Pt-uridine black (5), Pt-uracil-β-D-arabinofuranoside green (6), Pt-2'-deoxyuridine green (7), Pt-5-bromouridine green (8), Pt-5-fluorouridine green (9), Pt-6-azauridine green (10), Pt-ftorafur green (11), and Pt-thymidine-5'-monophosphate green (12). All Pt-greens have been synthesized from $Pt(NH_3)_2(H_2O)_2SO_4$ and pyrimidines by hydrogen peroxide oxidation between 50-80 °C. Pt-violet was synthesized at room temperature and Pt-blue under air at 80 °C and Pt-black by exhaustive hydration at room temperature from Pt-green. Pt-black (5) is formed from Pt-green by slow evaporation of water under air.

Pt-complexes (1-5) have the same ligand and the reaction conditions are varied, while for the Pt-complexes (6-12) the reaction conditions are comparable and the structure of the ligand is varied. The ligands in (1-5) and in (6) differ only in a configuration at C2'-atom and in (7) the OH-group has been replaced by H-atom at C2'-position, which is a strategic position in view of biological activity. The ligands of (8) and (9) contain Br and F instead of H in 5-position of uridine. The ligands in (9) and (11) are itself biologically active and (12) is a DNA-nucleotide.

The AWAXS measurements were carried out at the Stanford Synchrotron Radiation Laboratory on the wiggler beamline 4-3 utilizing a Si (111) two-crystal incident beam monochromator and a two-circle diffractometer on symmetrical reflection and transmission modes. The scattered intensity was measured in step-scan fashion with a high purity Ge solid state detector. The primary beam intensity was monitored by a scintillation crystal (NaI) and a photomultiplier detector. The intensity curve of the sample was measured in three parts increasing the measuring time at large k ($k = \frac{4\pi}{\lambda}\sin\theta$ is the magnitude of the scattering vector, θ is half of the scattering angle and λ is the wavelength) to collect at each point at least 100,000 counts. The range of k was 0.3-10 $Å^{-1}$ and the steps were 0.05 $Å^{-1}$. Each scan took about 7 hours. The photon energies were

chosen 60–960 eV below the Pt L_{III} absorption edge. In this energy range only the scattering factor of Pt changes significantly. The dispersion correction f'' is nearly constant but f' changes as a function of energy.

The experimental intensity curves were corrected for absorption and parasitic scattering using a measured non-sample scattering curve. The air scattering was quite prominent at $k < 2$ Å^{-1}, but diminished rapidly at larger k. The data were normalized to absolute scale with the large angle method. Normalization involved determination and subtraction of fluorescence in the data and subtraction of the calculated Compton intensity.[6] Because of the small k-range available (the photon energies were 10.6–11.5 keV) the normalization could not be done accurately. This specially affects the quality of the differential distribution functions.

RESULTS

The radial distribution functions (RDF), which represent a distribution of neighbouring atoms around an average atom in the sample, were determined from the intensity curves measured with one photon energy:

$$4\pi r^2\rho(r) = 4\pi r^2\rho_0 + \frac{2}{\pi}r\int_0^\infty ki(k)\sin kr\ dk,$$

where ρ_0 is the average atomic density and $i(k)$ the total structure function, which is calculated from the coherently scattered intensity per atom I_a by $i(k) = (I_a(k) - \langle f^2(k)\rangle)/\langle f(k)\rangle^2$. The differential distribution functions (DDF), which show the average environment of Pt atoms, were calculated from two intensity curves measured at two different photon energies. The DDF is related to the scattering via the differential structure factor (DSF), which is defined as follows:

$$\mathrm{DSF} = \frac{I(E_1) - I(E_2) - (\langle f(E_1)^2\rangle - \langle f(E_2)^2\rangle)}{\langle f(E_1)\rangle^2 - \langle f(E_2)\rangle^2},$$

where E_1 and E_2 are the two photon energies.

The intensity curves differ from each other most at $k < 2$ Å^{-1}. They all have a pronounced maximum at about 0.5 Å^{-1}, which corresponds to a Bragg distance of 12.6 Å. The RDF's contain a maximum in this position. The intensity curves of Pt-blue (4) and Pt-black (5) resemble each other closely. They have two broad maxima at $k < 2$ Å^{-1} and differ from the intensity curves of Pt-greens (1), (2), (6), (7) and (9) and Pt-violet (3), which all contain 3 broad maxima in this range of k. The first maximum of the intensity curve of Pt-green (2) is more pronounced than that of Pt-green (1).

The function, $4\pi r^2(\rho(r) - \rho_0)$ (ΔRDF) is convenient for estimation of atomic distances. The ΔRDF's of the majority of the complexes are very similar and have maxima at about 2.0–2.1, 2.9–3.1, 3.8–4.3, 5.0–6.0, and 7.4–8.6 Å (Table 1). The most intensive of them are located at 2.9–3.1, 5.0–6.0, and 7.4–8.6 Å. The ΔRDF of Pt-5-Br-green shows only two intensive maxima at 3 and 5.4 Å. The ΔRDF's of Pt-blue (4), Pt-black (5), and Pt-2'-deoxyuridine green (7) display two maxima between 5-6 Å while those of the rest of the Pt-complexes have only one maximum. The ΔRDF's of Pt-violet (3) and Pt-greens (1), (2), (6), (9), (10), and (11) are closely alike, except the positions of the maxima (Figure 1).

The ΔDDF's contain also pronounced maxima at 2.9–3.1, 5.0–6.0, and 7.4–8.6 Å, which indicates that these maxima arise partially from Pt-Pt distances. The ΔDDF's give better estimates for Pt-Pt-distances than the ΔRDF's. The position of the maximum at 2.9-3.1 Å is 2.86 Å for Pt-black (5) (2.86 Å), 2.96 Å for Pt-green (10), 3.0 Å for Pt-greens (1), (9), and (12), 3.03 Å for Pt-greens (7), (8), and (11), and 3.05 for Pt-uridine complexes (2–4).

The average coordination numbers (CN) at 2 Å from RDf's were between 3.8-4.0 for Pt-blue (4), Pt-black (5), and Pt-green (7), between 4.3–4.4 for Pt-greens (6), (8), (9), and (12), 4.6 for Pt-violet (3), and between 4.8–4.9 for Pt-green (1), (2), (10), and (11). The CN's at 3 Å were 8 (RDF) and 11 (DDF) for Pt-green (8), and between 10–11 (RDF's) and 15–22 (DDF's) for others. The precision of the CN's from RDF's and DDF's is only 20 %, since the maxima are not well resolved.

INTERPRETATION OF THE RESULTS

The interpretation of the experimental RDF's is based on the structures of similar crystalline model compounds.[2] These model Pt-complexes consist of the bridged dinuclear Pt-units, which may associate by hydrogen bonding into tetranuclear Pt-units, and these may further undergo oxidation into mixed-valent Pt-complexes. The model Pt-complexes's RDF's show the first maximum at 1.4 Å due to the shortest distance in the ligand. The maximum at 2 Å arises from Pt-N and Pt-O distances. The most intensive maximum at 2.8–3.2 Å is partially due to the shortest Pt-Pt distance. The RDF of a discrete te-

tranuclear Pt-unit contains two other intensive maxima at 5–6 Å and 7–9 Å due to the longer Pt-Pt-distances.[5]

That all the RDF's contain a maximum at about 3 Å indicates that the basic structural Pt-unit of the studied complexes is dinuclear. This is in agreement with our SAXS results, too. It is also reasonable since a bidentate ligand with a suitable bite-distance was used, which excludes mononuclearity. The RDF's of Pt-uridine complexes (3–5) have been be interpreted in terms of a tetranuclear model.[5] The maxima can arise from distances between Pt's belonging to two neighbouring tetranuclear Pt-units. The RDF's of Pt-uridine complexes resemble those of all other measured complexes excluding Pt-green (8). The RDF of Pt-green (8) may be interpreted in terms of a dinuclear model. The distance of 3 Å is the distance of Pt's belonging to the same dinuclear Pt-unit and the distance of 5.4 Å is the average shortest distance between Pt's of two neighbouring dinuclear Pt-units.

For interpretation of the average coordination numbers the Pt-complex is approximated as a two-component system of Pt-atoms (α) and the H-, C-, N-, O-, and S-atoms (β). The shares of the partial pair distribution functions $\rho_{\alpha\alpha}$, $\rho_{\alpha\beta}$, and $\rho_{\beta\beta}$ in the RDF's and DDF's may be estimated in terms of the atomic fractions x_α and x_β and charges of the components Z_α and Z_β.[9] For instance, in the case of Pt-violet (3) $x_{Pt} \approx 0.03$, $Z_{C,N,O,S} \approx 4.5$, and the shares are about

$$\begin{aligned} \text{RDF} &= 3.0\rho_{\alpha\alpha} + 0.4\rho_{\alpha\beta} + 0.5\rho_{\beta\beta} \\ \text{DDF} &= 11.1\rho_{\alpha\alpha} + 0.7\rho_{\alpha\beta}. \end{aligned}$$

Since the maximum of the RDF at 2 Å does not arise from Pt–Pt-distances, we may solve the numbers of atoms $n_{\alpha\beta}$ and $n_{\beta\beta}$ from the pair of equations above using the measured CN's and setting $n_{\alpha\alpha} = 0$. This calculation gives $n_{\alpha\beta}$ of 3.6-4.1 for the Pt-complexes (3–5), 4.3-4.5 for (1), (2), (7), (8), (9), (10), and (12), and 4.7-5.0 for (6) and (11) at 2 Å.

The nuclearity of the complexes cannot be concluded unambiguously from the CN's at 3 Å, since both dinuclear and tetranuclear models can give the same CN's. For instance, the CN's of 11 (RDF) and 22 (DDF) are obtained with the following numbers of atoms: $n_{\alpha\alpha} = 1.5$, $n_{\alpha\beta} = 8$, and $n_{\beta\beta} = 4$ (tetranuclear) and $n_{\alpha\alpha} = 1$, $n_{\alpha\beta} = 15$, and $n_{\beta\beta} = 4$ (dinuclear). The EXAFS-results for Pt-uridine complexes (1–5) indicate that the number of other atoms than Pt's at the distance of 3 Å is 4–7,[10], which excludes the dinuclear model.

DISCUSSION

The results of this study indicate that the Pt-complexes (1–12) all except Pt-green (8) consist of basic dinucler Pt-units, which are further clustered into tetranuclear either by hydrogen bonding or additionally further oxidation. Merely the color and paramagnetism observed with (1–5) verifies the oxidation and mixed-valency. The results for Pt-greens (1) and (2) are similar but not identical. The estimated intradimeric Pt-Pt-distance of Pt-green (1) is 3.0 Å and 3.05 Å for (2–5). The positions and the number of the maxima of the RDF's and DDF's of (1–5) differ at larger r indicating that there are differences in the order between the dinuclear units. Pt-violet (3) resembles more closely the green complexes (1) and (2) than Pt-blue (4) and Pt-black (5).

The heterocycles of the ligands of Pt-green (6) and (7) are the same, but the riboses differ slightly from that of uridine. The ΔRDF and ΔDDF are very similar to those of Pt-uridine greens (1,2). The estimated intradimeric Pt-Pt-distance of Pt-green (6) (3.05 Å) differ only slightly from that of (7) (3.03 Å), and is equal to those of Pt-uridine complexes (2–4). There are small differences also at $r > 4$ Å, which implies that also the interdimeric order of the Pt-complexes is similar.

Pt-greens (8–10) have different heterocycles but the same riboses. The DDF's of these complexes differ at both small and large r indicating that their structures are different. Our results indicate that Pt-5-Br-green does have a dinuclear basic structure. The RDF of Pt-5-F-uridine-green (9) agrees well the tetranuclear model. The intensity curve of Pt-green (10) shows unique features, and it's RDF does not agree as well with a tetranuclear model as that of (9).

Both the heterocycle and the ribose of the ligand of Pt-greens (11) and (12) differ from those of uridine. The ΔRDF and ΔDDF resemble closely those of Pt-uridine greens (1,2). The estimated intradimeric Pt–Pt-distance of (11) is nearly equal to that of Pt-green (1), thus the remote substituent with strong electronegativity does not affect much on the Pt–Pt bond length. Pt-green (11) has the smallest and Pt-green (12) the largest ligand among the studied. Since the Pt–Pt-distances both in the dinuclear Pt-complex and between two of them are comparable

in (1–12), it indicates that the remote substituents have little influence on the structure in the Pt-units.

ACKNOWLEDGEMENT

The financial support of The Finnish Academy, The University of Helsinki and Technology Development Centre is gratefully acknowledged. We are grateful to Sean Brennan and MaryBeth Rice for help in alignment of the diffractometer.

REFERENCES

(1) Davidson, J. P.; Faber, P. J; Fischer, R. G.; Mansy, S.; Peresie, H. J.; Rosenberg, B. and VanCamp, L. Cancer Chemother. Rep., Part 1, 1975, 59, 287–300.

(2) Farrell, N. Transition metal complexes as drugs and chemotherapeutic agents. 1989. Kluwer Academic Publishers, The Netherlands.

(3) Shimura, T.; Tomohiro, T.; Laitalainen, T.; Moriyama, H.; Uemura, T. and Okuno, Y., Chem. Pharm. Bull. 1988, 36, 448–451.

(4) Okuno, Y.; Inoue, T.; Yonemitsu, O.; Tomohiro, T. and Laitalainen, T. Chem. Pharm. Bull. 1987, 35, 3074–3077.

(5) (a) Serimaa, R.; Vahvaselkä, S.; Paakkari, T.; Laitalainen, T.; Sundberg, M.; and Oksanen, A. X-ray scattering studies on platinum uridine green. University of Helsinki, Report Series in Physics. HU-P-254, 1990, 17 s. (b) Serimaa et al. To be published.

(6) Fuoss P. H., Eisenberg P., Warburton W. K. and Bienenstock A. Phys. Rev. Lett. 1981, 46, 1537.

(9) Ding, K and Andersen, H. C. Phys. Rev. 1987, B 36, 2675–2686.

(10) Eteläniemi et al. To be published.

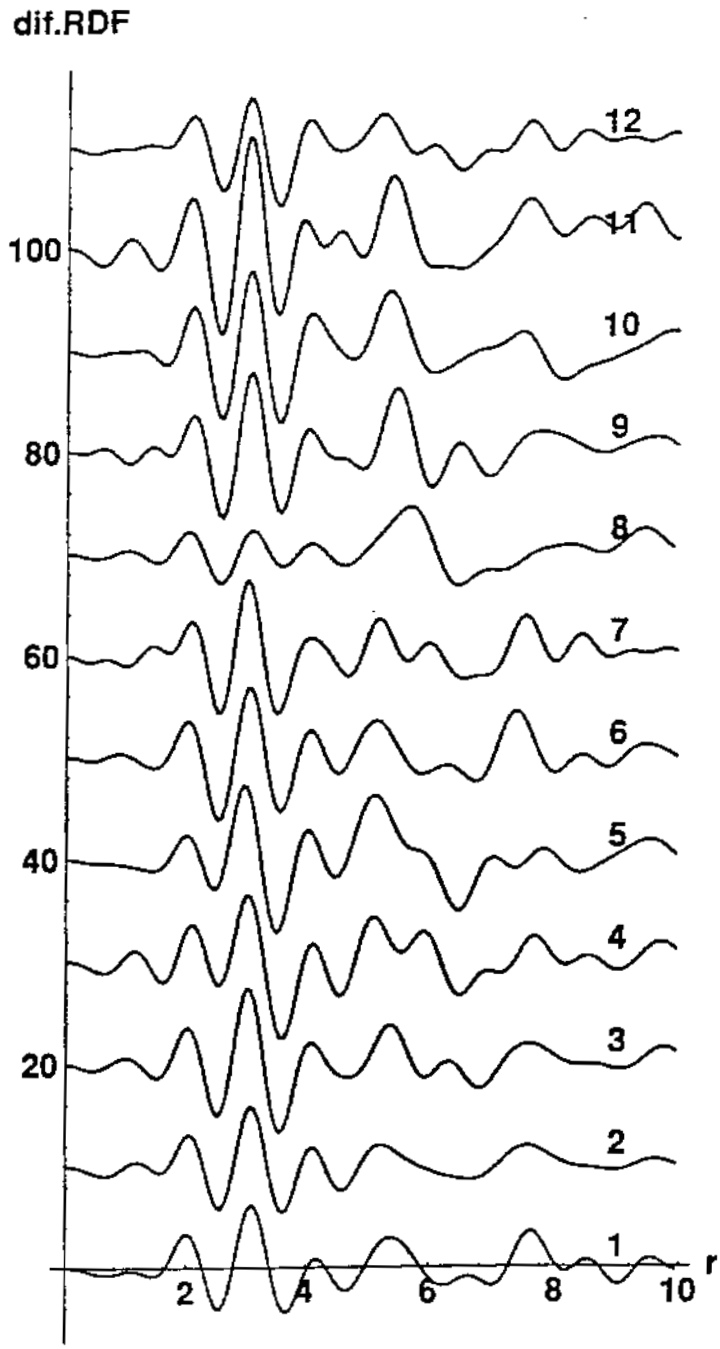

Figure 1. The RDF's of Pt-complexes (1-12).

X-RAY TOPOGRAPHIC STUDIES OF DEFECTS IN $K(D_xH_{1-x})PO_4$

Jim De Yoreo and Chris Ebbers
Lawrence Livermore National Laboratory, Livermore, Ca 94550

Zofia U. Rek
Stanford Synchrotron Radiation Laboratory, Stanford, Ca 94309

Introduction

Single crystals of the solid-solution grown $K(D_xH_{1-x})_2PO_4$ (DKDP) are used in a variety of electro-optic applications. Through the stress-optic effect, the presence of strain in these crystals generates optical inhomogeneities which degrades performance. We are pursuing an experimental program to answer the following questions: What is the magnitude and distribution of strain in DKDP crystals and how does it depend on the growth history; what are the defects which generate this strain; and how are these defects incorporated during growth? We are using optical techniques[1] to obtain profiles of the strain in crystals of DKDP but must rely on other methods to study structural defects. X-ray topography is a valuable tool for identifying crystalline defects and evaluating overall crystalline perfection. By combining the optical measurements with the X-ray topographs, we hope to answer the questions listed above.

Results and discussion

We performed X-ray topographic measurements using white beam reflection topography on 15 crystals of DKDP having a thickness of 10mm on beam line 2-2. Our results reveal three common defects: regions dense in dislocations emanating from (101) face of the seed cap, regular banding in (001) growth sectors and a multimodal distribution of domains. Examples of each are shown in Fig. 1 along with the illustration of the growth sector geometry of DKDP. The dislocation structure seen in Fig. 1 has been reported by others for KDP and ADP[2]. The two other features have not been previously reported and are discussed below.

a) Domains. Fig. 1c demonstrates the presence of domains in DKDP crystals. The boundaries of these domains often coincide with the pyramidal growth sector boundaries. Within a single sector the boundaries tend to lie along the [100] and [010] crystallographic directions. We have observed domains only in mixed crystals of DKDP. Crystals of pure KH_2PO_4 (DKP) are domain free. We do not know if this is a general result or an artifact of sampling a small population. The topographs show that these domain boundaries separate regions with either different crystallographic orientations or lattice spacings. Further X-ray topographic work using monochromatic X-rays is planned for 1993 to distinguish between these two possibilities and determine the magnitude of the differences. We suspect that these differences can be related to variations in the H or D ratio in these crystals.

b) Growth bands. The bands seen in Fig. 1b are parallel to the growth fronts of the (100) and (010) growth sectors. We hypothesize that they are due to changes in the lattice parameters caused by compositional variations. These variations may be impurity related, but are more likely a result of fluctuations in the H to D ratio. This hypothesis is supported by NMR determinations of the H to D ratio in this crystal which show that the D level varies by 0.5% from the seed cap to the tip of the crystal and is also consistent with thermodynamic analyses. We will use monochromatic topography to quantify the changes in lattice constants indicated by this banding.

Conclusion

We see no direct correlation between the locations of defects as seen by the X-ray topographic measurements and regions of high strain as determined optically. However there is a strong correlation between overall crystal homogeneity in the X-ray to-

pographs and the level of optical distortion. This is not surprising since the strain field is a complex function of defect type and orientation. In addition, the optical measurements integrate over the entire thickness of the crystal while the X-ray topographic measurements in reflection geometry are sensitive only to near-surface (a depth of ~100μm).

References

1. J.J. De Yoreo and B.W. Woods, A study of stress and the stress-optic effect in mixed crystals of $K(D_xH_{1-x})PO_4$, J. Appl. Phys., (in press)

2. A.A. Chernov, I.L. Smolskii, V.F. Parvov, Y.G. Kuznetsov and V.N. Rozhanskii, X-ray diffraction investigation of growth of ADP crystals. Sov. Phys. Cryst. 25, 469, (1980).

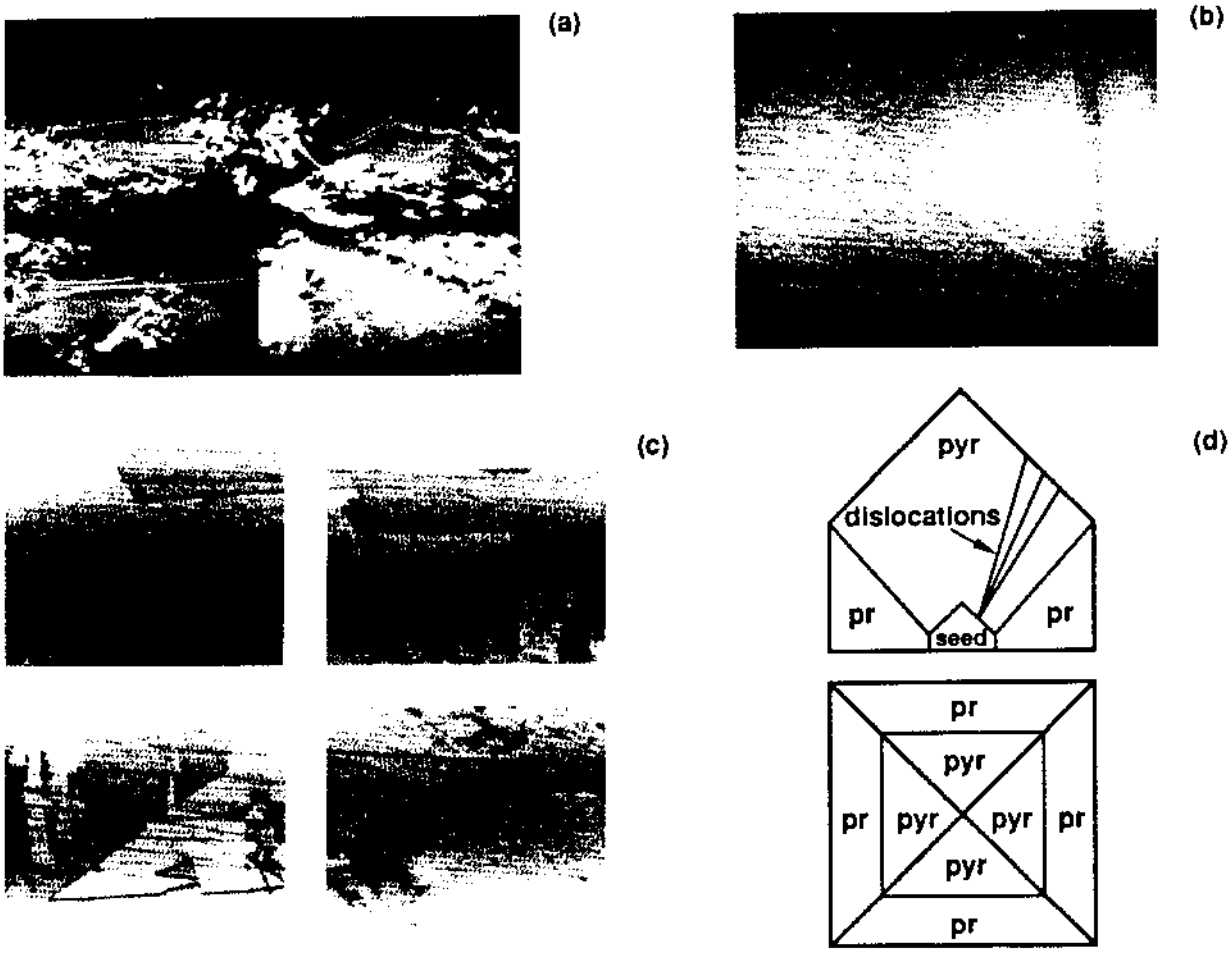

Fig. 1 Features seen in X-ray reflection topographs include: (a) dislocations emanating from the (101) face of the seed cap, (b) regular banding in (100) and (010) sectors, and (c) bimodal distribution of domains. (d) Growth sector geometry and dislocation bunches in DKDP. pyr=pyramidal or (101). pr=prismatic or (100) and (010). Note that the topographic technique foreshortening in one direction in a,b,c. The actual aspect of crystals is 1:1. Crystals of size 50mmx50mm were imaged in 4 section due to limited beam size.

STRUCTURE OF TiO_2 CLUSTERS

Robert J. Davis and Zhufang Liu
Department of Chemical Engineering
University of Virginia
Charlottesville, VA 22903

Isolated, nanophase semiconductors like titania (TiO_2) can be considered as zero- and one-dimensional quantum dots and quantum wires. Therefore, interest in using these systems as device components in quantum electronics and nonlinear optics is rapidly growing. In this work, we synthesized nanometer-sized titania clusters inside the constrained environment of a zeolite channel.

The challenge lies in the chemical synthesis of these systems. The materials synthesis, quantum size effects, and photophysical properties of nanometer-sized clusters have been recently reviewed [1]. One way to prepare small semiconductor clusters is to form them inside a zeolite framework. We have prepared titania inside the channels of large pore molecular sieve VPI-5 and inside the cage structure of zeolite Y. Since no crystalline titania phase was detected by x-ray diffraction, we subjected the samples to investigation by x-ray absorption spectroscopy at the Ti K edge. All of the XAS experiments described here were performed in the transmission mode of data collection on samples that were in air at room temperature at BL IV-1 SSRL.

The near edge spectra for bulk phase anatase and rutile powders, Ti/VPI-5, Ti/Y zeolite, and TS1 (a titanosilicate molecular sieve) are shown in Figure 1. The anatase and rutile near edge spectra show the well-known pre-edge features for Ti^{4+} in a slightly distorted octahedral coordination environment. Selection rules dictate that pre-edge resonances are not significant for Ti compounds having octahedral coordination (anatase and rutile), but a large pre-edge resonance is expected for Ti compounds having tetrahedral coordination [2,3]. A prominent pre-edge peak is present in Figure 1 for the zeolite supported titanium samples compared to the anatase and rutile powders which suggests that the occluded clusters do not have regular octahedral coordination, but rather a combination of octahedral, tetrahedral, and possibly square pyramidal geometries [3]. Our near edge results also suggest that the coordination environment of Ti in Y zeolite may be similar to that in TS1 (where Ti is speculated to be in the zeolite framework.)

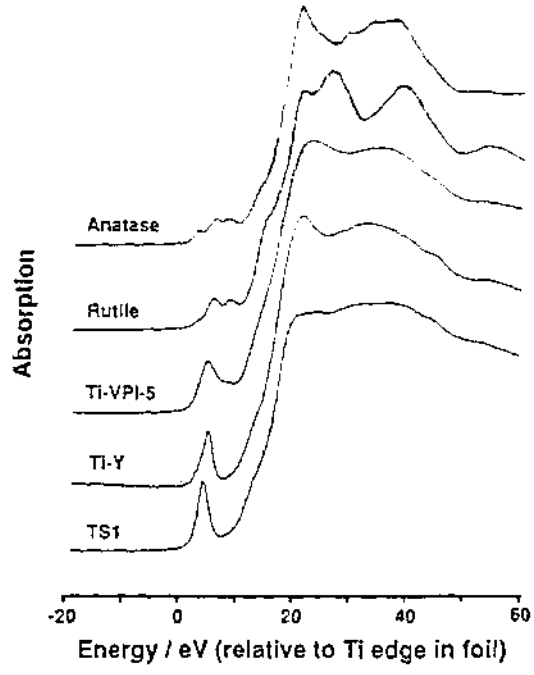

Figure 1. Ti K edge XANES results for materials containing titanium.

Figure 2 shows the radial structure functions (not corrected for phase shifts) around a Ti central atom derived from the Ti K edge EXAFS in anatase and Ti/Y. The anatase RSF reveals a peak in the first coordination sphere of Ti for the Ti-O bonds and a peak for the Ti-Ti scattering at a longer distance. Contributions from higher shells are also seen at distances greater than 3 Å. The RSF for the Ti-Y sample is completely different from anatase where the Ti-O bond distance (outlined in Figure 2) is shortened by about 0.1 Å and higher shell Ti-Ti contributions are not immediately evident. Curve fitting of the experimental x-ray spectra is extremely difficult for Ti zeolites [4] and we are still analyzing our spectra. In

summary, the near edge and EXAFS results are consistent with the formation of very small titania clusters, probably of nanometer size (consistent with our UV reflectance data), that may actually be molecular in nature.

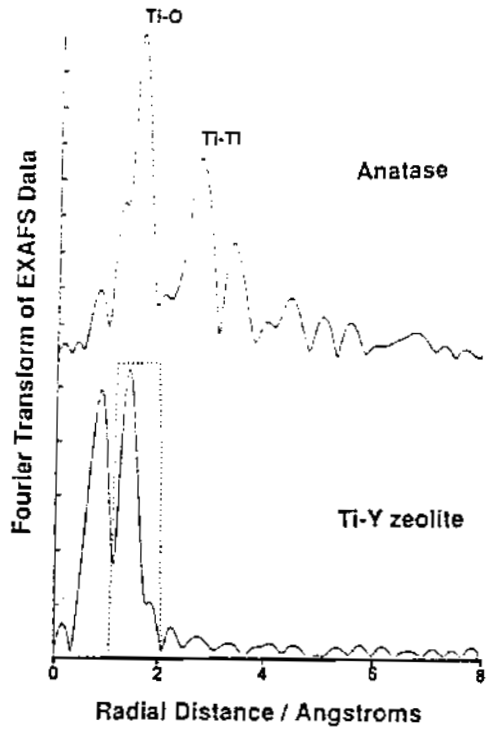

Figure 2. Fourier Transforms of Ti K edge EXAFS for titanium dioxide (anatase) and Ti/Y zeolite.

REFERENCES

1. Wang, Y.; Herron, N. *J. Phys. Chem.* **1991**, *95*, 525.
2. Waychunas, G.A. *Amer. Minerol.* **1987**, *72*, 89.
3. Behrens, P.; Felsche, J.; Vetter, S.; Schulz-Ekloff, G.; Jaeger, N.I.; Nieman, W. *J. Chem. Soc., Chem. Commun.* **1991**, 678.
4. Schultz, E.; Ferrini, C.; Prins, R. *Catal. Lett.* **1992**, *14*, 221.

In Situ X-ray Scattering from Single Crystal Electrode Surfaces.

I. M. Tidswell, N. M. Markovic and P. N. Ross

Lawrence Berkeley Laboratory, One Cyclotron Rd., Berkeley CA 94720

Although it has been well known for many years that the room temperature surfaces of the *5d* metals reconstruct *in vacuo* [1], [e.g. all three low index faces of gold and the Pt(001) and (011) faces] the structure of the solution interface has remained a mystery due to the technical difficulties associated with probing the liquid/solid interface. We have used x-ray diffraction (principally x-ray reflection and diffraction) to study the metal/solution interface while the metal is held under potential control. This technique was recently used to probe the low index faces of gold in contact with acidic and neutral electrolytes [2, 3, 4]. These studies found that at sufficiently negative potentials the solution interface of all three low index gold surfaces could be induced to reconstruct. These reconstructions occurred at potentials for which anion adsorption on the surface was largely eliminated. In general, the reconstructed surfaces had structures which were quite similar to the UHV reconstructions.

Our work at SSRL extended the study of the reconstruction of the Au(001)/solution interface to alkaline electrolyte. In addition, we studied the interface of Pt(001) and Pt(111) with both acid and alkaline electrolytes. The vacuum interface of Pt(001) has a similar reconstruction to the Au(001) surface. In electrolyte, however, at potentials just above hydrogen evolution, platinum surfaces are covered by an adsorbed state of hydrogen, a state which is not found on gold surfaces at similar potentials [5].

Gold Surface Reconstruction

Our studies of gold at SSRL have been used to contrast the reconstruction measured previously in acidic and neutral electrolytes with the reconstruction in alkaline electrolyte using x-ray reflectivity and grazing in-plane diffraction measurements.

In perchloric acid electrolyte (and vacuum) the (001) surface forms a distorted hexagonal overlayer rotated $\pm 0.8°$ degrees from the [110] direction. In alkaline electrolyte, however, the reconstruction forms in smaller domains and is aligned along the [110] direction. These changes appear to be a consequence of the faster kinetics of the reconstruction formation and lifting in alkaline electrolyte.

The reconstruction of the (111) surface appears to be very similar in acidic, neutral, and alkaline electrolytes, although again the reconstruction forms more rapidly in the latter. Faster reconstruction formation is also found for the (011) surface in alkaline electrolyte, where the (1×3) reconstruction is formed. In vacuum the (1×2) surface reconstruction is favored. A previous study of this surface in perchloric acid [4] found that the reconstruction is potential dependent, with the (1×2) formed initially, and a

more complicated structure which is a combination of (1×2) and (1×3) reconstructions, formed at more negative potentials. In salt solutions, however, the (1×3) reconstruction only is observed. The explanation for these differences is unknown, but is probably a consequence of the very similar surface energies of the two different reconstruction. The (1×3) reconstruction seems to be favored if adsorbing anions are present in the electrolyte.

Platinum Surface Relaxation

Although the Pt(001) surface reconstructs in vacuum, and the Pt(111) surface reconstructs at elevated temperatures, neither of these surfaces was found to be reconstructed when placed in contact with an electrolyte. The x-ray reflectivity profiles were, however, found to be reversibly dependent on the potential (at sufficiently positive potentials, irreversible roughening of the surface occurs, due to oxide formation). Fig. 1 shows the cyclic voltammetry and the normalized scattering intensity changes occurring at two different places on both the specular reflectivity rod and a non-specular reflectivity rod as a function of potential for the Pt(001) surface in contact with 0.1M KOH electrolyte. In both cases the scattering below the Bragg peaks [positioned at (002) and (111)] show a increase of the scattering intensity as the potential is reduced below 0.3 V, while the scattering intensity above the Bragg peak shows the opposite behavior. This suggests that the top layer of platinum atoms are expanding away from the second layer as the potential is reduced. This effect occurs in the potential region between hydrogen evolution and 0.3 V (versus Pd/H reference electrode), where hydrogen adsorption is known to occur [5]. Fig. 2 shows two full truncation rods at two fixed potentials, 0.35 V, and 0.0 V. In both cases the scattering intensity lies below

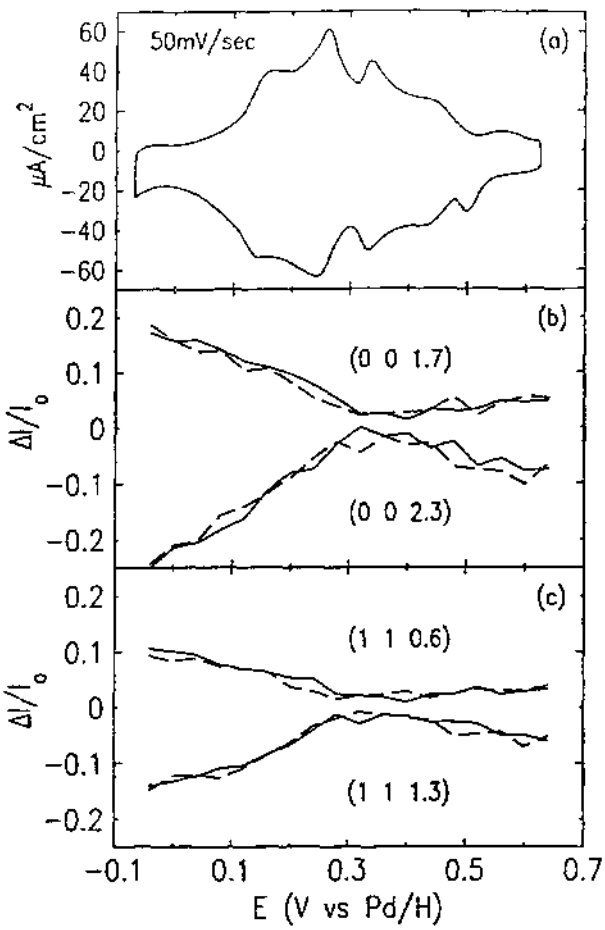

Figure 1: (a) Cyclic Voltammogram of the Pt(001) surface in 0.1M KOH electrolyte. The sweep rate was 50 mV/sec. (b) Changes in scattering intensity with potential at the (0 0 1.7) and (0 0 2.3) points on the specular rod. (c) Changes in scattering intensity with potential at the (1 1 0.6) and (1 1 1.3) points on the (1 1 L) non-specular rod. The solid(dashed) line shows the scattering on the positive(negative) sweep. The scan rate was approximately 4.5 mV/sec.

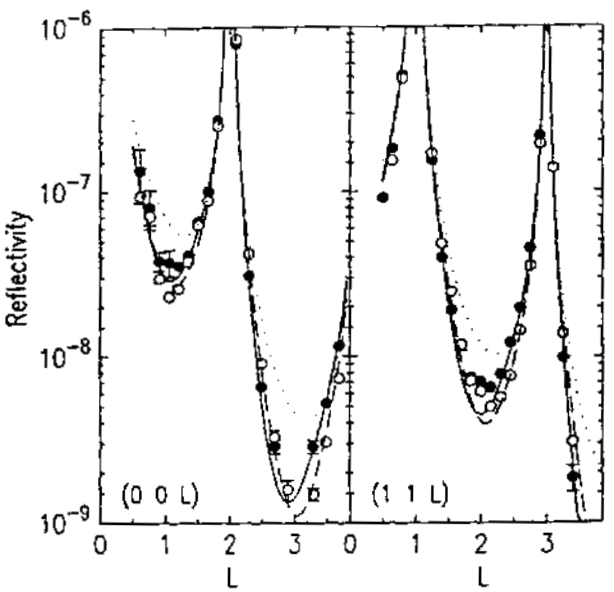

Figure 2: Scattering along the (0 0 L) rod (a) and (1 1 L) rod (b) at 0.0 V (closed circles) and 0.35 V (open circles). The dotted line shows the reflectivity expected from an ideal surface with bulk termination of the crystal. The solid and dashed lines show a model fit to the data at 0.0 V and 0.35 V respectively. The model is described in the text.

the expected scattering intensity for an ideal surface (dotted line), indicating that the surface is not sharp, most likely due to the presence of steps or islands of platinum on the surface. The model used to fit the data allowed the occupation and Debye-Waller-like disorder of the top metal layer to float, together with the top layer spacing (the distance between the first and second layers, d). The fits shown were obtained by using same parameters for the disorder and top layer occupation for both potentials and allowing d to float. For the surface at 0.35 V, the model indicates that d is $0.5 \pm 0.3\%$ larger than the bulk value. Previous vacuum studies of the (metastable) unreconstructed Pt(001) surface found d to be 0 - 0.2% larger than the bulk value [6]. On changing the potential to 0.0 V, the expansion increases to $2.8 \pm 0.3\%$ of the bulk layer spacing, which is equivalent to an expansion of approximately 0.05Å on changing the potential. We believe this is the firsted reported observation of this phenomenon. Unfortunately, no reliable studies of the structure of the H/Pt(001) surface in vacuum have been reported in the literature, so we are unable to determine whether this is a general effect or limited to the electrochemical interface. A similar change has also been observed for the Pt(001) interface with perchloric and sulfuric acids solutions, although the change in the top layer spacing was only about half the magnitude of the change in potassium hydroxide solution. The reason for the smaller change in acid electrolytes is unclear.

We have also studied the Pt(111) surface in contact with acid and alkaline electrolytes. Again the surface was not reconstructed in either electrolyte. The changes to the scattering in the hydrogen adsorption region were much smaller than found on the (001) surface, perhaps due to the much lower hydrogen coverage on this surface prior to hydrogen evolu-

tion. Reversible changes were also observed at higher potentials, in the potential region where the electrochemical "butterfly" feature is found (this electrochemical feature is characterized by a large pseudocapacitance of unknown origin). This change, however, cannot be associated with an expansion of the top layer spacing, and is probably due to the adsorption of anions. Studies of these and other related systems are ongoing.

Acknowledgments

This work was supported by the Director, Office of Energy Research, Office of Basic Energy Science, Materials Sciences Division of the U. S. Department of Energy under Contract Number DE-AC03-76SF00098.

References

[1] D. M. Kolb. In *Frontiers in Electrochemistry*, P. N. Ross and J. Lipkowski, editors, VCH Publishing, New York (1992). In press.

[2] B. M. Ocko, J. Wang, A. Davenport, and H. Isaacs. Phys. Rev. Lett. **65**, 1466 (1990).

[3] J. Wang, B. M. Ocko, A. Davenport, and H. Isaacs. Science **255**, 1416 (1992).

[4] B. M. Ocko, G. Helgesen, Bruce Schardt, and J. Wang A. Hamelin. Phys. Rev. Lett. **69**, 3350 (1992).

[5] R. Adžić. Adv. in Electrochem. and Electrochem. Eng. **13**, 163 (1984).

[6] M. A. Van Hove, S.-W. Wang, D. F. Ogletree, and G. A. Somorjai. Adv. Quantum Chem. **20**, 1 (1989).

Specular Reflectance and Diffuse Scattering Studies of Roughness at X-ray Mirror Surfaces and Interfaces

J.B. Kortright and T.D. Nguyen
Center for X-ray Optics
Lawrence Berkeley Laboratory
University of California
Berkeley, CA 94720

Interface roughness reduces specular reflectance and contributes to diffuse scattering, both of which are important in specifying the performance of x-ray mirrors. The effects of roughness are especially severe for x-ray multilayer mirrors because they operate at large scattering vector or momentum transfer compared to total reflection mirrors, where these effects are most pronounced. We study roughness of x-ray mirrors by measuring the specular reflectance and diffuse scattering from a variety of samples, including flat polished substrates, sputtered single films, and multilayer interference films. The surfaces are also measured by optical interferometry and atomic force microscopy to compare the roughness values obtained from these different techniques. Microstructural characterization using TEM and high-angle x-ray scattering are applied to multilayers and films in some cases.

In addition to providing fundamental data on x-ray mirror performance, these measurements allow us to test theoretical predictions of how interface roughness affects mirror performance. We are especially interested in studying how roughness evolves with polishing (in the case of mirror substrates) and with deposition (in the case of single or multilayer film deposition), and how thin film microstructure affects roughness.

Our first study investigates how roughness of glass substrates evolves with polishing, and how the different levels of substrate roughness affect the performance of multilayer mirrors deposited on those substrates.

Substrate polishing results

Fused-silica optical flats polished to four different levels of microroughness were obtained from an optical polisher [1]. Their rms roughness ranged from 0.2 to 10 Å as determined by optical interferometry at visible wavelength. This roughness spans the range typical of most well-polished x-ray mirrors, with the smoothest samples comparable to the best superpolished mirrors available.

The measured specular reflectance of these four optical flats, as well as fits to these data, are shown in Figure 1. Data were collected using the BL 6-2 Huber diffractometer, and have had the diffuse contribution subtracted to yield the true specular component. The oscillation in the specular reflectance for the smoothest two samples indicates an overlayer of different density than the substrate. Fits used a Fresnel reflectance model which incorporated a modified Debye-Waller factor [2,3] to account for scattering loss due to roughness. All but the roughest sample could be fit with a single overlayer model, in which the thickness and density of the overlayer and separate rms roughness values for the substrate-overlayer and overlayer-air interfaces were

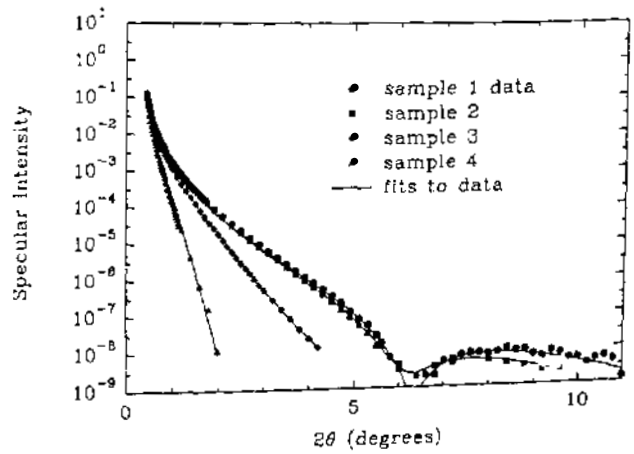

Figure 1. Specular reflectance data and fits for fused silica substrates polished to 4 different levels of roughness.

Table 1. Specular fit parameters.

sample	σ_{sub} (Å)	σ_{air} (Å)	t (Å)	ρ/ρ_{sub}
1	2.2	2.2	6.3	0.53
2	2.5	2.6	6.4	0.57
3	8.3	5.6	5.8	0.35
4	19.3	---	---	---

allowed to vary. Parameters used to fit the data are in Table 1, and are consistent with an overlayer roughly 6 Å thick having roughly the density of water. The range of rms roughness values obtained from the specular data is somewhat different from that obtained from visible interferometry.

In addition to the decrease in specular reflectance, roughness results directly in diffuse scattering, which is essentially small-angle scattering spread out over a large angular region compared to the specular peak. Various scan geometries can be used to measure the diffuse scattering along different directions in reciprocal space [4]. Rocking scans traverse reciprocal space in a direction mainly orthogonal to the specular direction, and are shown for the different samples in Figure 2. Three general features are observed in these data; a narrow specular peak at $q_x = 0$, a broad diffuse component, and Yoneda peaks in the tails of the diffuse intensity positioned where the incident and exit angles at the sample equal the critical angle. The Yoneda peaks indicate that the diffuse component results almost entirely from surface roughness, as opposed to bulk density fluctuations. Very large differences in the relative specular and diffuse components are evident among the different samples. While the specular intensities of samples 1 and 2 are nearly identical (Fig. 1), their diffuse components show greatly different intensity. Thus, diffuse scattering is a more sensitive measure of roughness than is specular reflectance for these smoothest samples. The roughest sample (4) shows no specular component at this momentum transfer.

The diffuse scattering is related to the power spectrum of the surface height distribution and to the Fourier transform of the height-height correlation function. We are investigating theories predicting the behavior of the diffuse scattering assuming some description of the surface roughness. Following Sinha et al. [3], a modified fractally rough, self-affine surface has a height-height correlation function of the form $C(R) = \sigma^2 \exp[-(R/\xi)^{2h}]$ where R is the in-plane separation, σ represents a roughness with units of length, ξ is a finite cut-off length, and h is the roughness exponent. The diffuse intensity is then related to the transform of a function including C(R), so that the parameters σ, ξ, and h can be varied in an attempt to fit the data. For results presented here σ is fixed at the values obtained from the specular scans.

Figure 3 shows preliminary fits using this modified fractal model to the corrected rocking curve data. This model can fit the data from the three roughest samples, but not from the smoothest sample. Table 2 shows the parameters used to fit the data. It is clear from

Table 2. Parameters to fit rocking scans.

sample	σ (Å)	h	ξ (Å)
1	---	---	---
2	2.5	0.23	5200
3	8.3	0.30	5800
4	19.1	0.13	6000

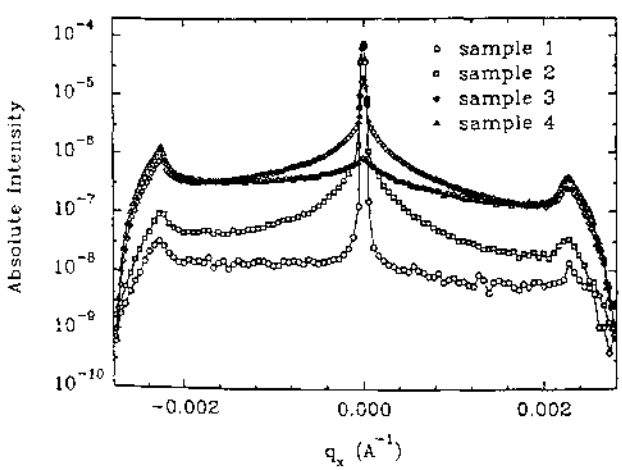

Figure 2. Rocking scans of the 4 samples at $2\theta = 2.0°$.

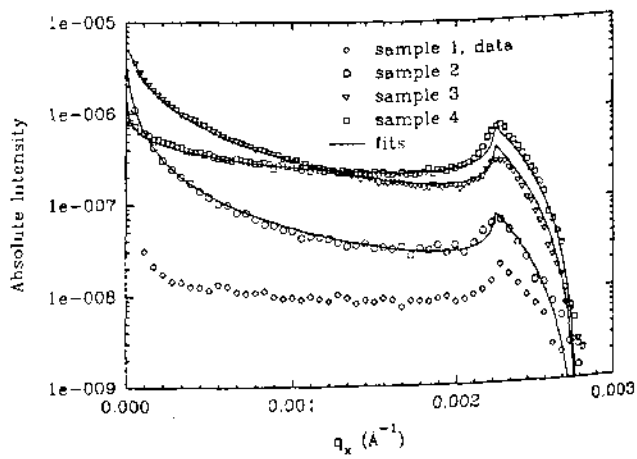

Figure 3. Fits to rocking scans using a modified fractal surface model.

the rocking scans and the fit parameters that the nature of the surface roughness depends sensitively on the degree of polishing. For the rougher samples which can be fit with the fractal model, the roughness exponent depends strongly on the degree of polishing, while the finite cutoff length ξ is roughly constant. This is consistent with the notion that the physical significance of ξ derives from a coherence length associated with the beam rather than from some characteristic length of the sample. For the smoothest sample (1), the diffuse intensity is roughly constant. The power spectrum of this surface looks like white noise over this range of frequencies.

Height-height correlation functions for the surfaces of the four samples are in Figure 4. For samples 2-4 the solid lines result from the analytical form of C(R) with parameters obtained from the fits in Fig. 3. For samples 1 and 2 the points are obtained from discrete Fourier transform of the diffuse component of the rocking scans, which is valid when $q_Z\sigma << 1$ [3]. The transformed C(R) are scaled to match the analytical calculation for sample 2. From both Figures 3 and 4 it is clear that the smoothest sample has a very different roughness spectrum than the rougher samples. Height-height correlations fall off relatively slowly for the rougher samples, but very fast for the smoothest sample.

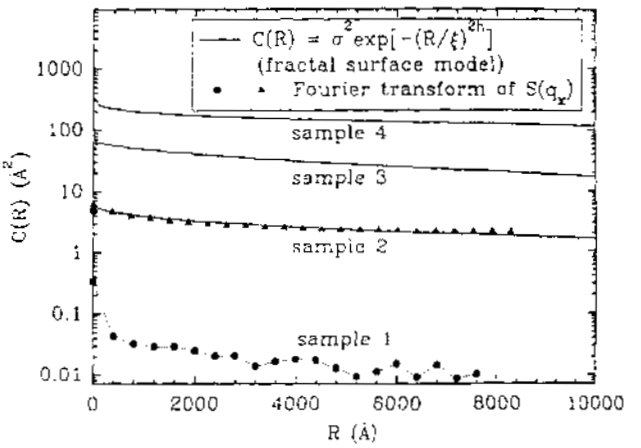

Figure 4. Height-height correlation functions derived from the rocking curve fits and data.

Multilayer results

Tungsten-carbon multilayers were sputter-deposited onto an identical set of substrates with different surface roughness. The trends in the specular and diffuse scans for the multilayer samples are very similar to those for the substrates. From the qualitative behavior of the specular and diffuse scans it is clear that the diffuse intensity contains vertical correlations of the multilayer and lateral correlations of the substrates. Thus we conclude that the roughness of the multilayers is dominated by conformal growth of each successive layer to the substrate roughness at least for frequencies $q_x <$ 0.003 $Å^{-1}$. This is not surprising since we know from extensive microstructural characterization of the W/C multilayer system that it forms very well defined and smooth layers [5-7]. These data are being analyzed using recent theoretical predictions of the effects of multilayer roughness on diffuse scattering [8].

Conclusions and future directions

Specular reflectance and diffuse scattering are together quite sensitive to the nature and details of surface and interface roughness. For the x-ray mirrors studied here, substrate polishing is seen to dramatically affect the specular and diffuse components. Further systemmatic studies are planned to investigate other aspects of roughness in x-ray mirrors, such as materials and processing dependence of roughness in single and multilayer films. More generally, the evolution of interface topography with deposition, etching, and processing can be studied for a wide variety of systems with these techniques.

Acknowledgments

We acknowledge I.M. Tidswell and C.A. Lucas for assistance in data collection and helpful discussions. This work is supported by the Director, Office of Basic Energy Sciences, Materials Sciences Division, of the U.S. Department of Energy under contract No AC03-76SF00098.

References

1. General Optics, Moorpark, California
2. L. Nevot and P. Croce, Rev. Phys. Appl., **15**, 761 (1980).
3. S.K. Sinha, E.B. Sirota, S. Garoff and H.B. Stanley, Phys. Rev. B, **38**, 2297 (1988).
4. J.B. Kortright, J. Appl. Phys., **70**, 3620, (1991).
5. T.D. Nguyen, R. Gronsky, and J.B. Kortright, Mat. Res. Soc. Proc., 139, 357 (1989).
6. T.D. Nguyen, R. Gronsky, and J.B. Kortright, Mat. Res. Soc. Proc, 187, 95 (1991).
7. T.D. Nguyen, M.S.Thesis, Dept. Mat. Sci. and Min. Eng., U.C. Berkeley, and Lawrence Berkeley Laboratory Report LBL-29206 (1990).
8. D.G. Stearns, J. Appl. Phys., 71, 4286 (1992).

DISTORTED LOCAL ENVIRONMENT AROUND ZN ON CU(2) SITES IN $YBA_2CU_3O_{7-\delta}$: AN X-RAY ABSORPTION STUDY

F. Bridges[1], G. G. Li[1], J. B. Boyce[2], T. Claeson[3]
[1]Physics Department, University of California, Santa Cruz, CA 95064
[2]Xerox Palo Alto Research Center, Palo Alto, CA 94304
[3]Chalmers Institute of Technology, Gothenburg, Sweden

I. INTRODUCTION

In most of the high T_c superconductors presently known, copper plays an important role. The compounds are all layered structures and the electrical conductivity is along layers of copper and oxygen. For $YBa_2Cu_3O_{7-\delta}$, there are two distinct Cu sites; the Cu(1) site is located on linear chains of alternating Cu + O atoms while the Cu(2) site is on a puckered square array of Cu + O atoms, on either side of the Y layer. Soon after the discovery of the 90 K superconductor, $YBa_2Cu_3O_{7-\delta}$, many investigators [1] began studying the properties of substituted samples, both to gain a further understanding of the relative roles of the Cu chains and planes and as a probe of the Cu site.

A surprising result of these studies is that Zn suppresses T_c more than most other elements. The amount of T_c suppression with Zn substitution varies considerably in the literature [2–8], particularly in early studies. Many investigations [2,4,6,8] indicate a nearly linear decrease of T_c with concentration, with $T_c \rightarrow 0$ near 10% Zn. One study [2] indicated a somewhat faster T_c suppression ($T_c \rightarrow 0$ at 7%) while a number of other studies [1,3,5,7] do not show a linear decrease of T_c with Zn concentration. We will show that this variation is likely due in part to the presence of ZnO in some samples.

The substitution site for Zn is widely taken to be the Cu(2) site [1,5,7,8] but there is still disagreement in the recent literature [4]. This is quite possibly the result of the presence of other phases but may be a real, sample preparation dependent effect. The apparent disagreement on the substitution site may also arise from large distortions about the Zn atom which are generally not included in data analyses. Our XAFS studies on samples containing no significant amounts of ZnO, support substitution of Zn mainly in a distorted Cu(2) site.

II. SAMPLES

Our samples were obtained from four sources. An early set of measurements were made in 1989 on a series of samples prepared by Tarascon [1] using standing sintering techniques with multiple grinding and resintering. These samples showed evidence of significant amount of ZnO. More recent measurements were made on a series of sintered samples obtained from H. Wuhl in Germany [9], and on two sets of samples prepared by sintering and by the sol-gel technique, from Chalmers institute of technology, Sweden [10]. The samples with the least contamination of ZnO particles were the Wuhl samples, and most of our more detailed analyses were carried out on these samples. For the other two sets of samples, the 10% Zn sample had a large fraction of ZnO present.

III. DATA COLLECTION AND REDUCTION

Copper and zinc K-edge data were collected in the transmission mode on beamline IV-1 at SSRL (on PRT time) using a Si (220) monochromator. For the Cu edge, we followed a basic procedure developed earlier [11,12]. For the Zn edge the situation is more complicated because a background oscillation from the high k, Cu-edge XAFS is present. However, for the low concentration YBCO:Zn samples investigated here, we find that the Cu XAFS signal is essentially the same as that of a good unsubstituted sample within the k-space range available for comparison. For the Cu edge of an unsubstituted sample, however, we have high quality data out to $k = 19$ Å^{-1}. We can therefore remove the remaining Cu edge XAFS in the region above the Zn K-edge using this Cu data, following a procedure similar to that which we developed to subtract the Pb L_{III} XAFS contribution from Bi L_{III}-edge data for $Ba(Bi,Pb)O_3$ samples [13]. In the pre-edge region below the Zn edge, we fit the Cu edge data of the pure, unsubstituted YBCO to the Cu XAFS

oscillations of the Zn substituted sample. This provides the correct amplitude of the Cu edge data for subtraction and eliminates the need to estimate this factor from step heights or the need of additional fitting parameters in the fits of the Zn spectra. An example is shown in Figure 1 for one of the 10% Zn doped samples.

The FT of $k\chi(k)$ at the Zn edge for the three Zn-substituted samples are compared with the Cu r-space XAFS of the pure sample in Figure 2. Here we show the real part of the transform and the envelope function $\pm\sqrt{(Im)^2+(Re)^2}$. Several points should be noted. First, the Zn r-space XAFS for the three concentrations are nearly identical. The equal amplitude of the first neighbor peak indicates that the background subtraction works very well. Second, the first shell O-peak for Zn is larger and shifted to higher r by nearly 0.1 Å compared to the Cu edge data. Third, the main Y/Ba peak which occurs at r=3.2 Å in the Cu-edge XAFS r-space spectra is shifted down in r by about 0.15 Å. Lastly, an oscillation in the real part of the FT of the Cu edge data at $r \simeq 2.8$ Å, which arises mainly from part of the Cu-Y component, is not observed in the Zn edge data. Either it is missing or the Zn-Y component has moved to a slightly longer distance. These observations clearly indicate that the Zn site is distorted and suggest possible starting parameters for the detailed fits.

Many of the Zn (and Ni) substituted samples have tiny particles of oxide, ZnO, (and NiO) present. We have compared the Zn-edge r-space data for four 10% Zn substituted samples with that for ZnO. The major feature of the ZnO data is a large Zn-Zn peak at r≃2.9 Å, which corresponds to 12 Zn neighbors. The structure of the real part of the FT from 2.8-3.0 Å is a clear signature of a Zn-Zn peak, and at this position is indicative of particles of ZnO. Three of the samples clearly show significant ZnO while the Wuhl sample has very little, if any, ZnO.

IV. DETAILED EXTRACTION OF PARAMETERS

We first considered the first O-shell about the Zn atom and used a sum of Zn-O standards to fit it. The main peak occurs at ≃2.02 Å with an amplitude corresponding to about 5 neighbors. No short bond, (expected for Cu(1) site), exists and no long bond near 2.3 Å occurs. The long Zn-O bond is either very close to the main peak (≃2.05 Å) or significantly larger, (≃2.7 Å).

We next included the possibility of Zn-Y, Zn-Ba and Zn-Cu/Zn peaks out to 4.0 Å starting with parameters and constrains corresponding to particular assumptions about the substitution site. No reasonable fits were obtained for substitutions at the Cu(1) site even allowing the Zn(1) to be displaced significantly along the c-axis. (Displacements in the a-b plane result in many Zn-Ba and Zn-Cu/Zn peaks and would result in a small multi-peak in the 2-4 Å region).

For substitution on the Cu(2) site, a good fit is obtained if the Zn(2) is displaced along the c-axis toward the Cu(1) by 0.2 to 0.25 Å. The Zn(2)-Ba and the Zn(2)-O(4) bonds are shortened, and the Zn(2)-Y and the Zn(2)-Cu(2)/Zn(2) bonds are lengthened. We note that a distortion along the c-axis for each Zn atom retains axial symmetry about the axis. Existing bonds are lengthened or shortened, but no additional bond lengths or a distribution of bond lengths is generated. The fits to the distorted Cu(2) site are shown as dotted lines on Figure 2.

We also carried out detailed fits on several samples containing significant amounts of ZnO. For these fits, two approaches were taken. First we fit these data to the sum of two spectra; the ZnO-free sample (Wuhl 10% Zn) and ZnO. It is not immediately obvious that such an approach is justified, particularly if the ZnO particles are small, as using the ZnO file to represent the very small ZnO particles, assume that the widths of the various bonds in the ZnO standard are the same as those in the tiny particles of this impurity phase. A second approach is to include a Zn-Zn peak at the correct distance for ZnO in the multipeak fit of the second and third neighbor r-space peak. Both approaches yield similar results; the amount of Zn in the Zn-O like environments is in the range of 40-50% for various samples.

V. DISCUSSION OF RESULTS

Our XAFS measurements indicate that substitution of Zn occurs primarily on distorted Zn(2) sites, with the Zn(2) displaced along the c-axis towards the Cu(1) site. This work illustrates further the tendency of $YBa_2Cu_3O_{7-\delta}$ to distort easily when modified. Each of the modifications we have investigated, O removal, Co, Ni, Fe and Zn substitution, have all resulted in a significant distortion of some part of the unit cell. We think this "softness" of the lattice, which may also be connected with the movement of the O(4) bridging oxygen partner, plays an important role in the superconductancy by controlling charge transfer or localizing electrons.

ACKNOWLEDGMENTS

This work was supported in part by NSF grant DMR-90-04325 and DMR-92-05204. The experiments were performed at the Stanford Synchrotron Radiation Laboratory, Which is supported by the U.S. Department of Energy, Office of Basic Sciences, and the National Institutes of Health, Biotechnology Division. These measurements were partially carried out on UC/National Laboratories PRT time. Support was also obtained from the Swedish National Science Research Council.

[1] J. M. Tarascon, P. Barboux, P. F. Miceli, L. H. Greene, G. W. Hull, M. Eibschutz, and S. A. Sunshine, Phys. Rev. B 37, 7458 (1988).
[2] B. Jayaram, S. K. Agarwal, C. V. Narasimha Rao, and A. V. Narlikar, Phys. Rev. B 38, 2903 (1988).
[3] R. S. Howland, T. H. Geballe, S. S. Laderman, A. Fischer-Colbrie, M. Scott, J. M. Tarascon and P. Barboux, Phys. Rev. B 39, 9017 (1989).
[4] K. Westerholt, H. J. Wuller, H. Bach, and P. Stauche, Phys. Rev. B 39, 11680 (1989).
[5] M. Kakihana, L. Borjesson and S. G. Eriksson, Physica C 162, 1251 (1989).
[6] C. Y. Yang, A. R. Moodenbaugh, Y. L. Wang, Youwen Xu, S. M. Heald, D. O. Welch, M. Suenaga, D. A. Fischer, J. E. Penner-Hahn, Phys. Rev. B 42, 2331 (1990).
[7] Y. Xu, R. L. Sabatini, A. R. Moodenbaugh, Y. Zhu, S.-G. Shyu, and M. Suenaga, Physica C 169, 205 (1990).
[8] Q. Song, B. P. Clayman, and S. Gygax, Physica C 165, 328 (1990).
[9] G. Roth, P. Adelmann, R. Ahrens, B. Blank, H. Borkle, F. Gompf, G. Gompf. G. Heger, M. Herview, M. Nindel, B. Obst, J. Pannetier, B. Renker, H. Rietschel, B. Rudolf, H. Wohl, Physica C 162-164, 518 (1989).
[10] M. Kakihana, L. Borjesson, S. Eriksson, P. Svedlindh, and P. Norling, Physica C 162, 931 (1989).
[11] F. Bridges, J. B. Boyce, T. Claeson, T. H. Geballe, and J. M. Tarascon, Phys. Rev. B 39, 11603 (1989).
[12] F. Bridges, J. B. Boyce, T. Claeson, T. H. Geballe, and J. M. Tarascon, Phys. Rev. B 42, 2137 (1990).
[13] J. Boyce, F. G. Bridges, T. Claeson, T. H. Geballe, G. G. Li, A. W. Sleight, Phys. Rev. B 44, 6961 (1991).

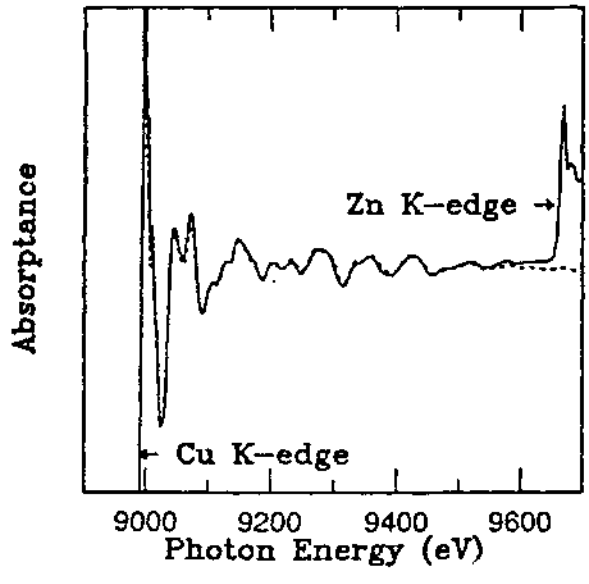

Figure 1. The x-ray absorption below the Zn K-edge for one of the 10% Zn doped YBCO. The dotted line show the Cu K-edge absorption data of pure YBCO sample; the amplitude of this trace has been adjusted to fit the Cu XAFS oscillations in the Zn substituted sample. The background corrected Zn data is obtained by subtracting this normalized Cu K-edge data from the Zn K-edge.

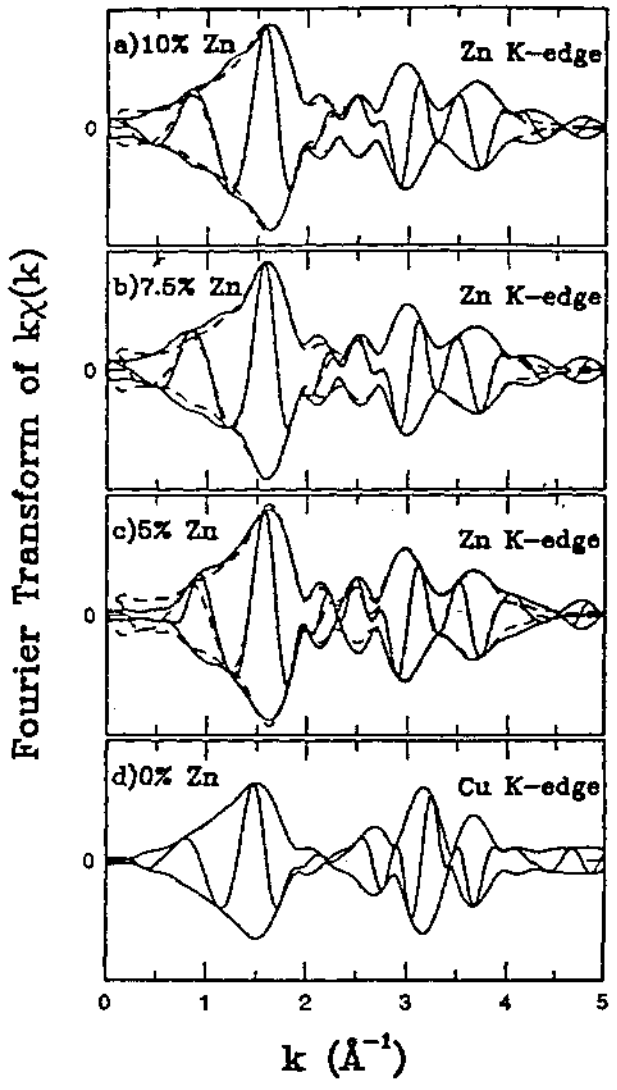

Figure 2. (a-c) The Fourier transforms of the Zn K-edge XAFS data over the range 3.2 to 12.5 $Å^{-1}$, with a 0.3 $Å^{-1}$ Gaussian window. (d)The bottom trace is the corresponding Cu K-edge data of pure YBCO, provided for comparison. The fast oscillations are the real part of the FT and the envelope is $\pm\sqrt{(Im)^2+(Re)^2}$. The dotted lines represent fits to the data for each composition.

Evidence for Disorder in the Oxygen Environment Around Praseodymium in $Y_{1-x}Pr_xBa_2Cu_3O_7$: A Progress Report

C. Booth†, F. Bridges†, P. Cervantes†, J. Boyce‡

†Department of Physics, University of California, Santa Cruz, CA 95064
‡Xerox Palo Alto Research Center, Palo Alto, CA 94304

An interesting property of $YBa_2Cu_3O_7$ (YBCO) is that one may replace the Yttrium atom with almost any rare earth and still obtain a high T_c superconductor [1,2], isostructural with YBCO. However, there are three rare earths that do not form a high T_c superconductor when attempts are made to dope them into the Y site: Cerium, Terbium, and Praseodymium [3,4]. Attempts to substitute with Ce or Tb have not produced the YBCO structure, even in small concentrations. Praseodymium, however, dopes readily onto the Y site, with T_c dropping monotonically with Pr concentration. A common denominator between these rare earths is that these are the only ones that can exist in either a +3 or +4 valent state. Since Y only exists in a +3 valent state, one explanation for the decrease in T_c with Pr concentration is that some fraction of the Pr exists in its +4 state, and thus fills a hole state in the Cu-O planes. There is some experimental evidence to support this view [5], but there are also convincing experiments that indicate that the Pr exists only in its +3 valent state [6]. Another possible mechanism for suppressing T_c in this material is that the $4f^2$ electrons are far enough extended to interfere with the conduction band [7]. There is also experimental evidence to show that the planar copper (Cu(2)) - axial oxygen (O(4)) distance is anomolously short [8].

Although neutron and X-Ray diffraction results show the nearest-neighbor Pr-O distance to be isostructural with YBCO, the possibility still exists that the oxygens be disordered about their mean positions. Such a change in the microstructure could produce some localization of electrons. Even if the Pr does exist in some mixed valent state, or the $4f^2$ electrons are interfering with the conduction band, changes in the Cu-O environment could be playing a role. Therefore, we have conducted X-Ray Absorption Fine Structure (XAFS) experiments on several concentrations of $Y_{1-x}Pr_xBa_2Cu_3O_7$, at the Cu, Y, and Pr K-edges (E_o = 8985 eV, 17035 eV, and 41133 eV respectively). These powder samples were prepared by Zhong-Xian Zhao (Institute of Physics, Chinese Academy of Sciences) , and characterized by resistivity and magnetic susceptibility measurements with Pr concentration and temperature. All XAFS experiments were performed at SSRL. Measurements of the incident and transmitted intensities were made with gas-ionization chambers. Si (111) crystals were used for

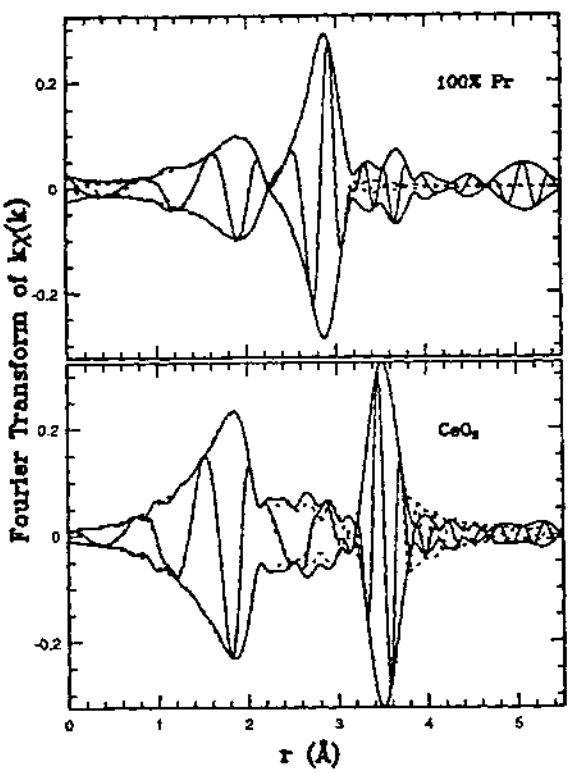

Figure 1: Fourier Transforms for kχ(k) for CeO_2 and $PrBa_2Cu_3O_7$, together with fits to the first two major peaks (dotted). The first peak in both cases is an eight-fold coordinated oxygen peak.

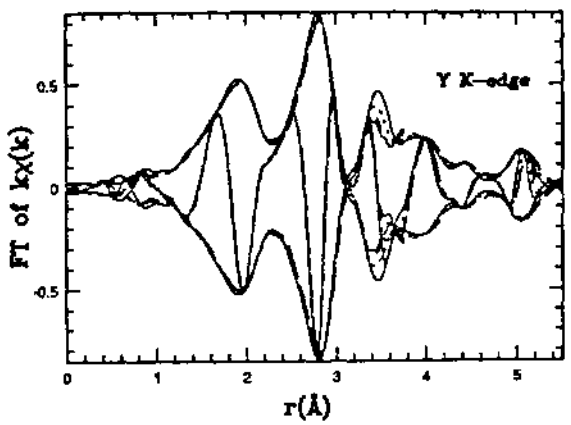

Figure 2: Fourier Transform of kχ(k) for Y K-edge data for 0% (solid), 30% (dotted), 50% (short dash), 60% (long dash) Pr concentrations.

the Cu and Y K-edge experiments, while Si (400) crystals were required for the Pr K-edge. Fits to the Pr K-edge data used theoretical standards calculated by FEFF5 [9]. Checks of the theoretical K-edge Xafs at high energy were carried out on CeO_2, with good agreement for the Ce-O peak.

We have compared the Pr K-edge XAFS for the first Pr-O peak to the first Ce-O peak in CeO_2 and found about a 30% drop in amplitude in the Pr-O peak (figure 1). Fits to the XAFS spectra indicate that either there are missing oxygens in the Cu-O planes or that one of the O sites is highly disordered and perhaps shifted ($\leq$ 0.1 Å) compared to the other one. Debye-Waller factors for the disordered site are typically 50% higher than for the "normal" site. Changes in the oxygen environment around the Yttrium in the Y K-edge XAFS, if any, are below the resolution of the experiment (figure 2). The copper K-edge XAFS show essentially no change in the planar oxygen environment, indicating that most of the planar oxygens should still be present.

Although these data and analysis show that disorder in the oxygen environment around the praseodymium clearly exists, the trends with Pr concentration are not clear. Additional data for a wider range of concentrations will be collected in our next run.

References

[1] (a) P.H. Hor, R.L. Meng, Y.Q. Wang, L.Gao, Z.J. Huang, J. Bechtold, K. Forster, and C. W. Chu, *Phys. Rev. Lett.* **58**, 1891 (1987); (b) S. E. Brown, J. D. Thompson, J. O. Willis, R, M, Aiken, E. Zirgniebl, J. L. Smith, Z. Fisk, and R. B. Schwarz, *Phys. Rev. B* **36**, 2298 (1987)

[2] L.F. Schneemeyer, J. V. Wasczak, S. M. Zahurak, R. B. Van Dover, and T. Siegrist, *Mater. Res. Bull.* **22**, 1467 (1987).

[3] D. W. Murphy, S. Sunshine, R. B. Van Dover, R. J. Cava, B. Batlogg, S. M. Zahurak, and L. F. Schneemeyer, *Phys. Rev. Lett.* **58**, 1888 (1987).

[4] L. Soderholm, K. Zhang, D. G. Hinks, M. A. Beno, J. D. Jorgensen, C. U. Segre, and Ivan K. Schuller, *Nature (London)* **328**, 604 (1987).

[6] For example, see A. Kebede, C. S. Jee, J. Schwegler, J. E. Crow, T. Mihalisin, G. H. Myer, R. E. Salomon, P. Schottmann, M. V. Kuric, S. H. Bloom, and R. P. Guertin, *Phys. Rev. B* **40**, 4453 (1989).

[7] L. Soderholm, C.-K. Loong, G.L Goodman, and B.D. Dabrowski, Phys. Rev. B. 43, 7923 (1991).

[8] C.K. Lowe and T.A. Vanderah, *Physica C* **201**, 233 (1992).

[9] J. Mustre de Leon, J.J. Rehr and S. I. Zabinsky, *Phys. Rev. B* **44**, 4146 (1991).

X-RAY ABSORPTION MEASUREMENTS OF THE RARE EARTH ORTHOPHOSPHATES

D. K. Shuh,[1] L. J. Terminello,[2] L. A. Boatner,[3] and M. M. Abraham[3]

[1]Chemical Sciences Division, Lawrence Berkeley Laboratory, Berkeley, CA 94720
[2]Lawrence Livermore National Laboratory, Livermore, CA 94550
[3]Oak Ridge National Laboratory, Oak Ridge, TN 37830

There is a rich history of rare earth (RE) 3d x-ray absorption measurements that has been augmented recently by improvements in both experimental and theoretical techniques.[1,2] X-ray Absorption Spectroscopy (XAS) of the RE $M_{4,5}$ edges (3d levels) yields sharp peaks near the edges as a result of strong quasiatomic $3d^{10}4f^{n} \rightarrow 3d^{9}4f^{n+1}$ transitions which exhibit a wealth of spectroscopic features. Although the purpose of XAS experiments is to obtain information on the RE ground state, the technique images the excited electronic final states. The total $3d^{9}4f^{n+1}$ multiplets for the RE's are quite complex and even with dipole selection rules limiting the allowed transitions from the ground state, gives rise to a large number of possible final states. The technique of total electron yield (TY) x-ray absorption spectroscopy has been shown to be a useful technique for investigation of 4f occupancy, 4f hybridization, and valence issues in RE materials since the TY measurements are known to be proportional to the x-ray absorption coefficient.

The electronic structures of the RE ions in the orthophosphates (La, Ce, Nd,...)PO_4 are of particular interest since the valence state is clearly defined as tripositive and are analogs of the corresponding actinide orthophosphates, which have been considered as materials for primary nuclear waste containment and disposal. Preliminary x-ray absorption measurements of the single crystal rare earth orthophosphates (RE = La, Ce, Pr, Nd, Sm, Eu, Tb, Er) at the $M_{4,5}$ edges were performed in the TY mode on the LLNL / UC PRT Beamline 8-2 SGM. The spectra were measured with the monochromatic x-ray beam (700-1300 eV) incident at ~45° to the surface normal, monitoring the photon flux with a Au grid, and by recording the total electron yield from a Channeltron.

Figure 1 shows the XAS spectra of the Ce 3d ($M_{4,5}$) edges in $CePO_4$ and is representative of the total electron yield spectra of the RE-PO_4's. The spin-orbit split (D_{SO}) Ce $3d_{5/2}$ and $3d_{3/2}$ peaks are the predominant features of the spectrum, whereas the exchange interaction provides the observed fine structure. The RE-PO_4 edges actually appear a few eV prior to the true RE edges, as a result of the strong

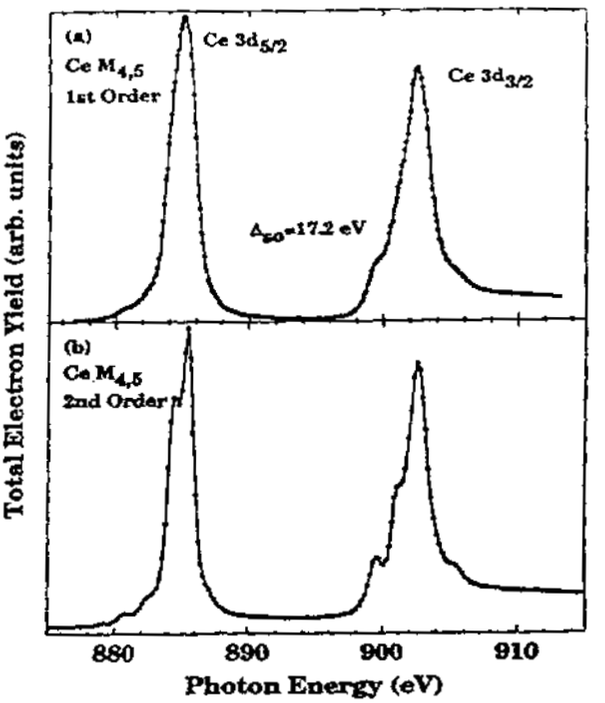

Figure 1. Representative XAS spectra of the Ce 3d edge ($M_{4,5}$) from single crystal $CePO_4$. Spectrum (a) was collected with the monochromator diffraction grating satisfying the n=1 condition, whereas (b) was recorded utilizing second order light (n=2) to improve spectral resolution.

core-hole/4f Coulomb interaction that lowers the energy of the final state. The intensity distribution between the spin-orbit pairs in the second order spectra are very slightly skewed, since the photon flux monitor primarily accounts for the distribution of first order light. Figure 2 presents the signal from the Nd 3d edges of $NdPO_4$ which is nearly identical to that calculated for Nd^{3+}.[2]

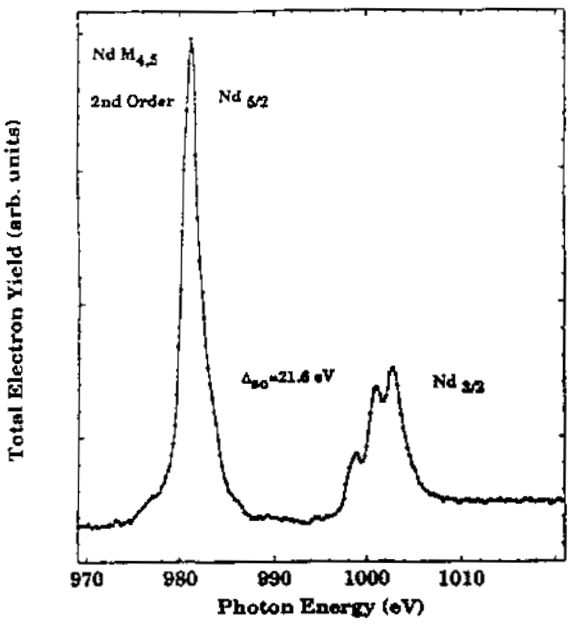

Figure 2. XAS spectrum of the Nd $M_{4,5}$ edges of $NdPO_4$. The spectrum was collected utilizing second order light from the 8-2 SGM.

The XAS spectra of the RE ions in the orthophosphate matrix generally resemble the XAS of the corresponding RE metal. This is not unexpected and emphasizes the major contribution of the trivalent state to the electronic transitions occurring at the RE 3d edges. These spectra unequivocally identify the transitions originating from well-characterized RE cores and correlate well with previous theoretical investigations. New features are observed in several of the RE-PO4 materials as a result of the high resolution measurements. The results of these measurements show that XAS of actinide and other active elements, safely contained in similar matrices, is feasible and will yield valuable electronic information.

Acknowledgements

This work was done at SSRL which is operated by the Department of Energy, Division of Chemical Sciences. This work was supported by the Director, Office of Energy Research, Office of Basic Energy Sciences, Chemical Sciences Division of the U. S. Department of Energy under Contract No. DE-AC03-76SF00098.

References

1. G. Kaindl, G. Kalkowski, W. D. Brewer, B. Perscheid, and F. Holtzberg, J. Appl. Phys. **55** 1910 (1984).

2. B. T. Thole, G. van der Laan, J. C. Fuggle, G. A. Sawatzky, R. C. Karnatak, and J.-M. Estera, Phys. Rev. **B32** 5107 (1985).

MEASUREMENT OF RESIDUAL STRESS AND PARTICLE SIZE USING SYNCHROTRON RADIATION

James F. Shackelford, Jun S. Park, and Li-Chi Liu
Department of Mechanical, Aeronautical, and Mechanical Engineering
University of California, Davis

and

Richard W. Ryon
Nondestructive Evaluation Section
Lawrence Livermore National Laboratory

Two, independent studies are reported here: 1) the measurement of the residual stress due to machining the surface of a ball-bearing steel and 2) the measurement of the particle size of silicon "quantum dots" in a glass matrix.

I. Residual Stress Measurement

This work was an extension of earlier LLNL-related efforts [1-3] to determine the most effective method for determining residual stress in metal components by non-destructive techniques. These activities have included neutron diffraction, x-ray diffraction, and ultrasonics. We have recognized that the UC/LLNL beam line at the Stanford Synchrotron Radiation Laboratory (SSRL) could be applied to determine lattice strains in a fashion helpful to our overall research goals. Pioneering work using synchrotron radiation for stress measurements had been reported in Japan.[4] Benefits of a synchrotron source to our studies include a highly intense and monochromatic beam, with variable energies (allowing significant sample penetration) and very low beam divergence.

A ground ball-bearing steel with a highly characterized surface stress state (from its role in an international round robin testing program [5,6]) was used in a run utilizing SSRL beam time available in early March 1989 [SSRL Proposal 9902]. Beam line 10-1 was used at that time, with the primary benefit of variable beam energies up to 24 keV. The follow-up studies under the current proposal were done on Beam line 7-2, a dedicated diffraction station with substantially more convenient specimen manipulation but with a fixed beam energy of 10.5 keV. The overall characterization of the stress state obtained from both SSRL runs will be summarized here.

Experimental measurements of the surface stress gradient were made with a limited number of beam energies. Most work was done using energies of either 10 or 12 keV. Useful data were taken using harmonics at 20 and 24 keV, respectively. Time did not permit obtaining useful results from other fundamental energies or from higher harmonics of the 10 and 12 keV beams.

Characterization of the outer surface stress was made using the conventional stress measuring technique of specimen tilting. Both forward (iso-) and side tilting were used. Side tilting has certain advantages, especially for higher beam energies and associated, smaller Bragg angles. ("Tilting" refers to producing a specimen orientation such that the specimen surface is not parallel to the crystal planes responsible for a given diffraction peak. This parallel orientation is maintained by conventional diffractometers in which the detector has twice the angular rotation rate as the specimen.)

Diffraction peaks for the (211) plane of the ferritic "round robin" specimen (ball bearing steel 100 Cr 6) were obtained at 10, 12, 20, and 24 keV beam energies. Peak intensity profiles were collected using the VAX system at SSRL. All data were transferred to a Macintosh diskette at SSRL, and data analysis was carried out at UC-Davis using a MacII personal computer. Peak intensity profiles were modified by the Lorentz factor.[7] Peak positions were determined by a second-order polynomial fit to intensity data above 85% of maximum peak intensity. This corresponds to a parabolic curve fit to the top of a given diffraction peak.

Noyan [8] has summarized a method by Hauk in which a precise value of the interplanar spacing for the unstressed material can be calculated theoretically from analysis of the dependence of the measured interplanar spacing on the isotilting angle in a stressed material. Using this technique for the "round robin" specimen, we have determined the unstressed interplanar spacing for the (211) planes in this alloy to be 0.117237 nm ± 0.000005 nm. The necessary tilting measurements were made in our laboratory using CrK-α1 radiation.

Figure 1 summarizes the experimental results for the "round robin" steel specimen. "Depth" refers to the penetration depth of x-rays associated with a given beam energy as given by:[7]

$$x = (\sin\theta)/(2\mu) \quad (1)$$

The vertical axis of Figure 1 is the average of the principal stresses in order to allow for a comparison to the surface stress values obtained in previous round robin tests conducting by the CIRP [5,6] in which the tilting method was used. (The CIRP results indicated that outer surface stresses were effectively equal in directions parallel and perpendicular to grinding, allowing a direct comparison to the average value in Figure 1.)

The values of surface stress in Figure 1 represent an average in terms of depth of surface sampled, following the method of Sasaki, et.al. [9]. The result is in close agreement with the near-surface portion of the full surface gradient obtained by Brinksmeier, et.al. using the conventional tilting technique and CrK-α radiation (E = 5.41 keV and a corresponding depth of penetration of 0.61 micrometers). It should be noted that their depth plot was obtained destructively using this low-penetration, "soft" x-ray by etching away the surface of the sample at a slight incline, so that different positions along the surface corresponded to different depths relative to the original surface position.

Figure 2 summarizes the measurement of the outer surface residual stress on the ground ball-bearing steel sample using the 10.5 keV beam. The x-ray energy was calibrated with a Si wafer using (111) and (400) diffraction lines. A beam size of 5 mm x 5 mm was used. For the steel specimen, the (420) diffration line was used. Side-tilting angles, ψ, of ± 20, ± 30, ± 40, and ± 50° were used in an orientation normal to the ground direction. Figure 2 is a plot of the diffraction angle, 2θ, versus $\sin^2\psi$. The slope of the plot is an indication of the sign and magnitude of the outer surface stress [7]. Using available elastic constants for this alloy [5], we obtain a value of residual stress of 1367 MPa (tensile), in good agreement with previous results [5].

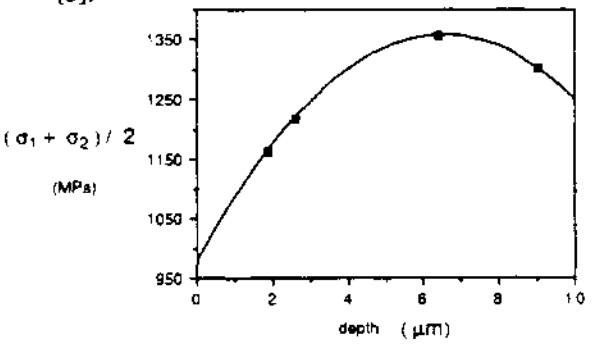

Fig. 1 Stress gradient at surface of ground ball-bearing steel.

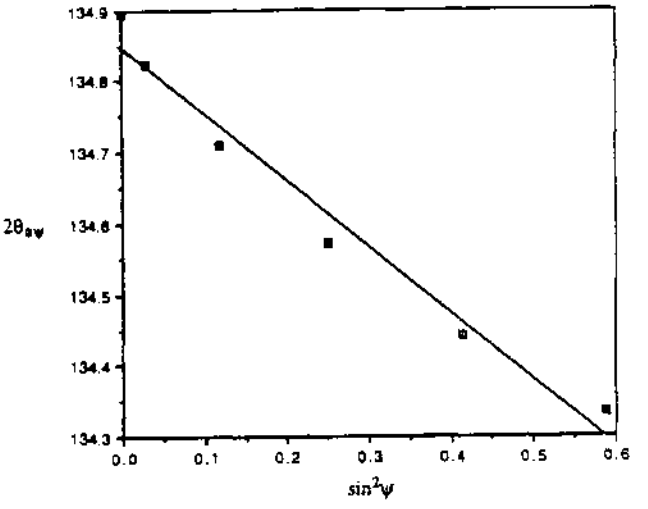

Fig. 2 A 2θ versus $\sin^2\psi$ plot for the ground ball-bearing steel sample. The slope of the plot indicates a residual stress of 1367 MPa (tensile).

II. Particle Size Measurement

The particle size of nanometer-scale silicon remnants sequestered in a silicate glass matrix was determined by a standard diffraction line broadening technique [7]. The advantage of the Synchrotron source was its high brightness, permitting a measureable diffraction profile from samples with low concentrations of Si particles. The interest in these materials is the luminescent behavior of the "quantum dot" silicon [11]. A well-defined Si (111) diffraction peak was observed at an angle 2θ = 21.66°. Figure 3 shows this peak corrected for background. The peak width at half-height indicates, in

conjunction with the Scherrer equation [7], an average particle size of 1.32 nm. Independent electron microscopy inspection of the samples indicates that this number may indicate a subgrain size, i.e., the Si particles are likely to be agglomerates or subgrains of Si powder from the original melt [11].

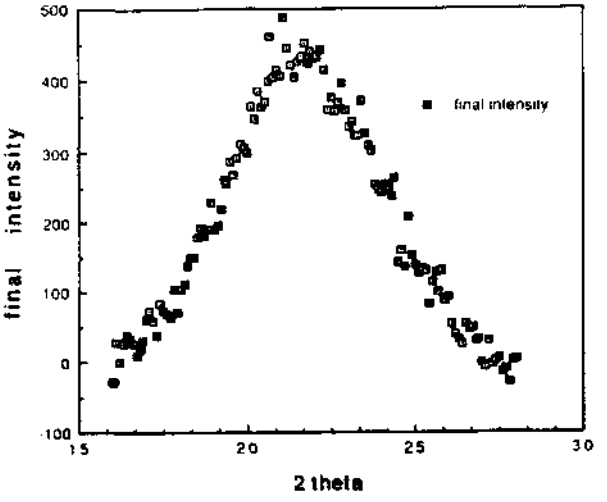

Fig. 3 Diffraction peak from (111) planes of Si "quantum dot" particles in glass matrix. Broadening indicates average crystallite size of 1.32 nm.

III. Acknowledgements

We want to thank Elane Flower, formerly of LLNL, for her enthusiastic and generous support of this and related studies of residual stress by x-ray diffraction techniques. A special acknowledgement is due to Lane Wilson for his management of the Beamline 10 activities and Sean Brennan for similar management of Beamline 7 work. Their patience and helpfulness under frequently grueling circumstances was a source of amazement to all of us.

IV. References

1. E.C. Flower, S.R. MacEwen, and T.M. Holden, "FEA Predictions of Residual Stress in Stainless Steel Compared to Neutron and X-ray Diffraction Measurements," UCRL-96643, August 1987.

2. J.F. Shackelford and B.D. Brown, "A Critical Review of Residual Stress Technology," Final Report, LLNL Intramural Order 5710705, September 1987.

3. J.F. Shackelford and B.D. Brown, "Analysis of Triaxial Residual Stress Measurement Using High-Energy X-ray Diffraction," Final Report, LLNL Intramural Order 2660503, January 1989.

4. Y. Yoshioka, et.al., "X-ray Residual Stress Analysis in Textured Steels by Use of Synchrotron Radiation Source," in Residual Stresses in Science and Technology, Vol. 1, pp. 369-76, E. Macherauch and V. Hauk, eds., Verlag, Germany (1987).

5. E. Brinksmeier, et.al., "Residual Stresses - Measurement and Causes in Machining Processes," Annals of the CIRP, 31 (2) 491-510 (1982)

6. J.F. Shackelford, "University of California Participation in the CIRP Round Robin of Residual Stress Measurement," UCID-19838, July 1983.

7. B.D. Cullity, Elements of X-Ray Diffraction, 2nd Ed., Addison-Wesley, Reading, Mass., 1978.

8. I.C. Noyan, "Determination of the Unstressed Lattice Parameter 'a-0' for (Triaxial) Residual Stress Determination by X-rays," in Advances in X-Ray Analysis, Vol. 28, ed. C.S. Barrett, P.K. Predecki, and D.E. Leyden, 1984, pp. 281-88.

9. T. Sasaki, M. Kuramoto, and Y. Yoshioka, "A Practical Phi-Method for the Evaluation of Stress on Materials with Stress-Gradient by X-rays," in Advances in X-Ray Analysis, Vol. 28, ed. C.S. Barrett, P.K. Predecki, and D.E. Layden, 1984, pp. 265-274.

10. I.C. Noyan and J.B. Cohen, Residual Stress, Springer-Verlag, New York, 1988.

11. S.H. Risbud, et.al., submitted to Nature.

Chemical Vapor Infiltration of Continuous Filament Ceramic Matrix Composites

J.H. Kinney, D.L. Haupt, and R.A. Saroyan
Lawrence Livermore National Laboratory
Livermore, CA 94550

T.M. Breunig and M.C. Nichols
Sandia National Laboratories, Livermore CA

T.L. Starr, S.R. Stock, and M.D. Butts
Georgia Insititue of Technology
Atlanta, GA

Introduction

Chemical vapor infiltration (CVI) is an important technology for fabricating SiC ceramic matrix composites[1]. In CVI, a vapor precursor of the matrix material—methyltrichlorosilane (MTS)—is passed through a network of reinforcing fibers at elevated temperature. The MTS dissociates, and the SiC matrix phase deposits on the fibers. As matrix growth progresses, avenues for gas transport become more tortuous and begin to close off, eventually stopping the infiltration process. Pore closure determines the final density of the composite.

CVI technology must be improved if continuous fiber ceramic composites are to realize their full potential. Fabrication costs must decrease, and residual porosity must be reduced and controlled. Achieving these goals will require a better understanding of how processing variables and fiber architecture ultimately control a composite's microstructure. Process models of CVI have been developed to economically search for optimum fiber architectures and processing variables.[2] Unfortunately, the development and validation of these models has been frustrated by a lack of good experimental data on the evolution of composite microstructure during CVI.[3] This lack of good microstructural data is due partly to naturally occurring sample to sample variations as well as to the difficulty in reconstructing three–dimensional pore networks from two–dimensional sections.

We have applied a new, noninvasive imaging method to volumetrically characterize the evolution of microstructure in a Nicalon fiber / SiC matrix composite during CVI. The method, called x–ray tomographic microscopy (XTM), is an ultra–high resolution form of x–ray computed tomography. Because characterization can be performed on the same sample during CVI, interpretation of microstructural changes is not clouded by sample to sample variability. Furthermore, because the technique is "truly" volumetric, there are none of the traditional difficulties encountered in interpreting pore structure or fiber orientation.

This paper reports the findings from an experiment where XTM was used for the first time to observe and quantify the consolidation of a composite during isothermal, forced–flow CVI. Specifically, we followed the time evolution of 1) V_V, the microporosity within the fiber tows 2) S_V, the surface area per unit volume available for matrix deposition, and 3) N_V, the number of isolated pores within the structure. The results are compared to theoretical models of CVI.

Materials and Methods

Experimental Design

For this experiment, preforms were made by stacking 20 layers of square–weave Nicalon (nanocrystalline SiC) cloth into a cylindrical graphite reaction chamber. The Nicalon fiber tows each contained approximately 500 fibers. Both $0^o/90^o$ and $0^o/45^o$ lay–up architectures were studied. The preform dimensions were approximately 6.2 mm in diameter by 6.0 mm high. These dimensions were chosen so as to optimize image quality while minimizing edge effects.

The chamber could be inserted and removed from a furnace maintained at 975°C. Reactant gas, consisting of H_2 bubbled through liquid MTS at laboratory ambient temperature, was forced through the graphite tube and fiber preform (isothermal, forced–flow CVI). The excess H2 and reaction by–products exited through the gas outlet.

XTM

Three–dimensional XTM images of the fiber preforms, while in their reaction chambers, were made prior to infiltration.[4] The XTM measurements were made on the 31–pole wiggler beam line (BL–

10) at Stanford Synchrotron Radiation Laboratory. A double crystal monochromator [Si(220) reflections] was used to select energies between 20 and 27 keV. High resolution radiographic images were acquired as the sample rotated in half–degree increments from 0 to 180^0. The radiographic images were normalized to the incident beam and reconstructed into three–dimensional images using Fourier–filtered back projection method. Radiation exposure times of approximately 4 minutes were required to image the entire sample volume.

After imaging, the samples were placed into the furnace and infiltrated for 3 hours. After the infiltration, XTM was repeated. This procedure of interrupted CVI followed by imaging was repeated at 3 hr intervals until vapor flow through the composite could no longer be achieved due to pore closure.

Data Analysis

The XTM data were converted into three–dimensional images of the samples at the various stages of consolidation. The volume elements (voxels) used to create the microstructural images were 15.8 μm in all three dimensions. Each measured volume element contains the linear x–ray attenuation coefficient a(cm^{-1}) for the local region within the sample. The linear attenuation coefficient is related to the materials density and chemistry through the relation

$$\alpha_i = \mu_i \rho_i \qquad (1)$$

where r is the density in volume element i and μ is the mass attenuation coefficient (cm^2/g) of the element. The chemical information is contained in μ. Chemical or density differences between phases leads to a contrast differences in the XTM images.

It is possible to write an expression which converts the XTM data for the uninfiltrated preform into the volume fraction of microporosity, V_v^{up}. In the uninfiltrated state, the preform is a two phase mixture of Nicalon fibers and pores. If μ_N and r_N are the mass attenuation coefficient and density for Nicalon (measured independently by other means), then

$$V_v^{up} = 1 - \frac{\langle \alpha \rangle}{\mu_N \rho_N} \qquad (2)$$

Using Equation 2 with tabulated values for the mass attenuation coefficient of Nicalon and a Nicalon density of 2.6 we have measured the initial pore density within the tows of both a 0/45 and a 0/90 weave preform at more than 200 locations in each specimen. The results indicated that the volume fraction of micropores within the tows was 0.45±0.02, in excellent agreement with optical microscopy on *post mortem* sections of nearly identical samples (0.44±0.07)[5]. Figure 1 shows the tow porosity averaged over locations within individual plies as a function of distance from the vapor inlet. There is no statistical difference in the micropore density for 0/45 and 0/90 architectures. This is as expected, and the close agreement between two different samples as well as to optical sectioning methods supports the validity of XTM for determining micropore density in woven fiber composites.

The surface area per unit volume, S_V, was determined by fitting a contour around the individual pores and measuring the length of the perimeter. The surface area was then calculated using the well known relationship from stereology $S_v = \frac{4}{\pi} B_A$ where B_A is the perimeter length per unit area of sample.[6] Because of resolution errors that are introduced in measuring the perimeters of small pores, only macropores (larger than 45 μm diameter) were measured using this method.

The number of pores per unit volume, N_V, is one of the most difficult parameters to measure with standard sectioning methods. We define a unique pore as a void which is not connected by any pathway to another void. Initially, all pores are interconnected within the preform. As infiltration proceeds, small pores are spawned when pathways become closedoff from vapor flow. Therefore, though total pore

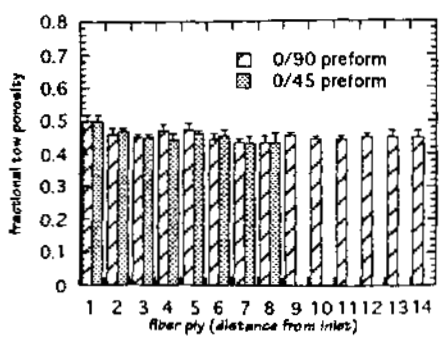

Figure 1: Measured values for the uninfiltrated tow porosity in both the 0/45 and 0/90 preforms. The values were calculated using equation 2

volume will decrease with infiltration, we expect to see a growth in the total number of pores due to pore closure.

XTM, because it is inherently three–dimensional, is the ideal technique for measuring N_V as a function of infiltration time. By using techniques from percolation theory, it is possible to identify unique pores within the imaged volume.[7] This is described in more detail in a companion paper in these proceedings.[5] Efficient computer algorithms enable relatively large volumes (400x400x400 voxels) to be percolated in a few hours on inexpensive work stations.[8] Once the XTM data set is percolated, it is possible to determine N_V as well as perform more exhaustive analyses on shapes, sizes, and distribution of pores within the structure.

Results and Discussion

Time Evolution of V_V

Figure 2 shows the microporosity remaining within the fiber tows of a 0/90 sample after 3 and 6 hours of consolidation, respectively. Consolidation within the first six layers appears to be complete after 3 hours. This is supported by the observation that there is no statistically significant consolidation in these layers after three additional hours of consolidation. In layers seven through fourteen, however, consolidation continues to completion between 3 and 6 hours of infiltration. The large surface area in the tows accounts for the rapid consolidation; whereas, the gradient in the infiltration is most likely a result of MTS depletion upstream.

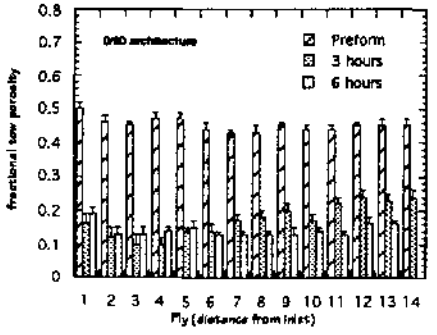

Figure 2: Tow porosity remaining in the 0/90 sample: uninfiltrated preform, 3 hours infiltration, and 6 hours infiltration. Tows are fully consolidated in the first 6–7 plies by the end of three hours of infiltration.

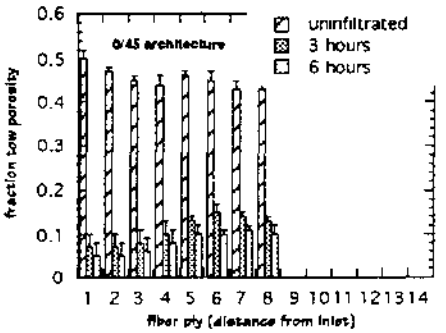

Figure 3: Tow porosity remaining in the 0/45 sample after 3 and 6 hours infiltration.

Figure 3 shows the microporosity remaining in the 0/45 sample after infiltration. Consolidation in the 0/45 architecture is similar to that of the 0/90 with the exception that slightly more consolidation occurs in the first two layers of the 0/45 during the first three hours of infiltration. This difference in the consolidation near the inlet may be due to slight differences in the fiber architecture or in slight irregularities of the packing. Nevertheless, there does not appear to be any pronounced difference in the tow consolidation between the two weaves. This is demonstrated in greater detail in Figure 4, where we chart the volume fraction of SiC after three hours of infiltration.

Time Evolution of S_V

Figure 5 shows the surface area per unit volume prediction of the uniform deposition model for woven preforms and the experimentally determined values for both the 0/45 and 0/90 fiber architectures after three hours of infiltration. Experimental results are nearly identical after six hours of infiltration. The data are in good agreement with the predictions of the uniform deposition model[9] of CVI between 0.7 and 1.0 fractional density. Deviations below 0.7 volume fraction are due to our inability to accurately measure the micropore surfaces. Nevertheless, no statistically meaningful differences exist between the measured surface areas for different two–dimensional fiber architectures.

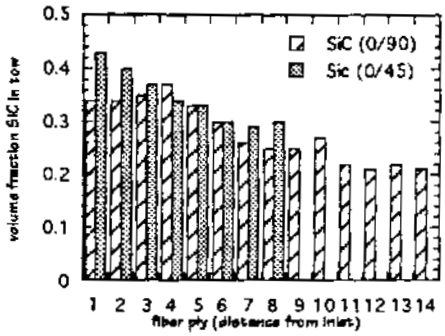

Figure 4: The volume fraction of SiC deposited within the fiber tows after three hours of infiltration for a 0/90 and 0/45 architecture.

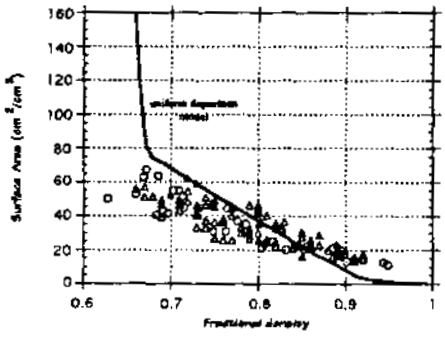

Figure 5: The surface areas measured for both 0/90 (open circles) and 0/45 (triangles) after 3 hours of CVI as a fraction of theoretical density.

Time Evolution of N_V

Percolation has been performed on the data sets from the 0/90 architecture samples after 3 hours and 6 hours of infiltration. After 3 hours, an abundance of microscopic pores have formed in addition to the vapor pathway (large pore). The vapor pathway after 3 hours is 13.6 mm^3, and one pore of 0.2mm^3 has sealed off. After 6 hours infiltration, the vapor pathway has continued to consolidate, but has also spawned two additional large pores. Now, the vapor pathway is 7.3mm^3 and the other pores are 0.48mm3 and 0.34mm^3. The 0.2mm^3 pore is still intact, and has not changed size–indicating that the pore was indeed sealed off from the vapor flow. A more detailed analysis of pore evolution is being performed.

Acknowledgements

This work is supported by the U.S. Department of Energy Advanced Industrial Concepts Materials Program ED38–02. We acknowledge the electronics engineering support of W.N. Massey (LLNL).

References

1. T.M. Besmann, B.W. Sheldon, R.A. Lowden, and D.P. Stinton, "Vapor–Phase Fabrication and Properties of Continuous–Filament Ceramic Composites", Science, Vol. 253, 1991, pp. 1104–1109

2. T.L. Starr, S.R. Stock, T.M. Besmann, and J.C. McLaughlin, "Model Validation for Isothermal Chemical Vapor Infiltration", elsewhere in these proceedings.

3. G.B. Freeman, T.L. Starr, and T.C. Elston, "Transport Properties of CVI Preforms and Composites", MRS Symposium Proceedings, Vol. 168, 1990, pp. 49–54

4. J.H. Kinney and M.C. Nichols, "X–ray Tomographic Microscopy (XTM) Using Synchrotron Radiation", Annual Reviews of Materials Science, Vol. 22, 1992, pp. 121–152.

5. T.M. Breunig, M.C. Nichols, J.H. Kinney, and D.L. Haupt, "Quantitative Microstructural Characterization of a Composite Material Using Destructive and Noninvasive Techniques", elsewhere in these proceedings.

6. E.R. Weibel, "Measuring Through the Microscope: Development and Evolution of Stereological Methods", Journal of Microscopy, Vol. 155, 1989, pp. 393–403.

7. D. Stauffer and A. Aharony, *Introduction to Percolation Theory*, 2nd Edition, Taylor and Francis, London, UK, 1991.

8. D.L. Haupt and J.H. Kinney, *Cluster_3D: A Three–Dimensional Percolation Routine for Porosity Analysis*, Lawrence Livermore National Laboratory (unpublished).

9. T.L. Starr, "Advances in Modeling of the Chemical Vapor Infiltration Process" in *Chemical Vapor Deposition of Refractory Metals and Ceramics*, T.M. Besmann, B.M. Gallois, and J.Warren, Eds. (Materials Research Society, Pittsburgh, PA), 1992, pp. 207–

X-RAY DIFFRACTION AT HIGH PRESSURE ON WIGGLER BEAM LINE 10-2

Malcolm F. Nicol, Susan E. Mustonen, Hyunchae Cynn,
Amy Martin, Michael Chan, and Richard Jacubinas
Department of Chemistry and Biochemistry
University of California, Los Angeles, CA 90024-1569, USA

During 1992, the UCLA contingent of the University of California-National Laboratories Participating Research Team installed a new, very flexible Huber multi-circle diffractometer in the rear hutch of beam line 10-2. Some capabilities of this diffractometer were demonstrated during a July run when x-ray diffraction patterns were collected from polycrystalline samples of Ni, $EuCo_2P_2$, and sulfur confined at pressures to 10 GPa (about 100,000 atmospheres).

The 10-2 diffractometer is designed to meet requirements of a wide variety of x-ray diffraction studies which have been proposed for this wiggler beam line. The heart of this instrument is a unique Huber multi-circle goniometer consisting of the typical 512 Eulerian Cradle with 520-mm χ circle and 63.5-mm offset ϕ circle and 511.1 X-Y cryostat carrier, a 430 θ goniometer. There are not one but two 440 2θ goniometers. Both 440's can be used to position x-ray detectors. During the summer, for example, a scintillation detector on one 440 was used in aligning samples in high pressure cells to the microcollimated beam; then, image plates on the second 440 were position to collect diffraction data from the entire 2θ cone. The second 440 also is designed for for positioning optics, light sources, and spectrometers that can monitor and/or excite samples while diffraction data are being collected.

The design of this diffractometer, associated optics, and detectors also takes into account the several ways the 10-2 source can be configured: as a white-light or monochromatic source, either focused or unfocused. Thus, scintillation and Ge(Li) detectors can be mounted on the 440 for conventional four-circle single-crystal studies. For powder work, the 440 can be operated in a 2θ-scanning mode with a scintillation or Ge(Li) detector; at fixed 2θ with a linear position-sensitive detector or, in an energy-dispersed mode, with a Ge(Li) detector; or at $2\theta = 0$ with image-plate detection. The 511.1 X-Y cryostat carrier on the large 512 cradle can accommodate Displex refrigerators or Schiferl furnaces so that samples, including those confined in Merrill-Bassett pressure cells, can be externally cooled nearly to liquid He temperature or heated to more than 1000 K.

Alignment of the monochromator is highly automated, and most alignment operations can be performed without opening the hutch. For example, the goniometer is mounted on a standard SSRL table with three stepper-motor driven axes, X-Z-α. Three sets of stepper-motor-driven 4-blade Huber slits and a dc-motor-drive 4-axis microcollimator are provided for defining the input and scattered x-ray beams. The beam on which the microcollimator and input slit are mounted also can be stepped in the x and z directions independently of the table. A motorized Huber 1003 sample goniometer head will be available during the 1993 run.

The diffractometer, detectors, and control electronics and beam line computer were connected together and aligned to the beam for the first time for a three-day shakedown run during May 1992. After several minor bugs (dimensional problems with the support table, signal levels in the motor control circuits, missing screws in a stepper-motor linkage) were found and solved, diffraction patterns of test MgO and NaCl samples were collected.

The May test run uncovered several minor problems which needed to be solved before the instrument could be made available to general users. Because the hutch was needed for other experiments from mid-May through early June, the diffractometer was removed while we solved these problems. The diffractometer was reinstalled in July for an 8-day experimental period.

Work during the July run emphasized demonstrating the capabilities for working with polycrystalling samples in

Merrill-Bassett diamond-anvil high pressure cells. The goals were to develop methods for rapidly aligning the samples and microcollimator to the monochromatic source and testing the Ge(Li), image-plate, and position-sensitive detectors. During the run, we developed the ability to align a new cell in well under an hour, using the Ge(Li) detector. After considerable trial-and-error experiments to determine the amount of shielding required for the Biochemistry Group's Hitachi image plates, we demonstrated the capability to collect very good diffraction patterns of samples of nickel (mixed with NaCl), sulfur, and $EuCO_2P_2$ (a compound prepared by Stacey's group at the University of California, Berkeley which may have a valence transition from Eu^{2+} to Eu^{3+} at high pressure). By the end of this run, we were collecting good diffraction patterns of sulfur at 7 GPa in between 5 and 20 minutes. Near the end of the run, we attempted quickly, without success, to test a position-sensitive detector from the Alivisatos group at Berkeley.

Acknowledgments: The $EuCo_2P_2$ sample was kindly provided by R. Bornick and S. Tolbert. Assistance provided by Hal Tompkins, Sean Brennan, Tony Tiscarino and other SSRL staff has been a great help during the installation process and is very gratefully acknowledged. This work was supported by grants from NSF (DMR 90-22076), IGPP-LANL (92-44), and the UCLA Academic Senate Research Committee.

BIOLOGY PROPOSALS

STRUCTURAL STUDIES OF THE DIIRON CENTER OF THE HYDROXYLASE OF METHANE MONOOXYGENASE IN THE PRESENCE OF SUBSTRATE AND COMPONENT B OF THE MMO ENZYME SYSTEM

Jane G. DeWitt,[1] Amy C. Rosenzweig,[2] Britt Hedman,[3] Stephen J. Lippard[2] and Keith O. Hodgson[1,3]

[1] Department of Chemistry, Stanford University, Stanford, CA 94305

[2] Department of Chemistry, Massachusetts Institute of Technology, Cambridge, MA 02139

[3] Stanford Synchrotron Radiation Laboratory, Stanford University, Stanford, CA 94309

Introduction

Soluble methane monooxygenase (MMO) is a multi-component enzyme system which catalyzes the NAD(P)H- and O_2- dependent hydroxylation of methane to methanol in methane-metabolizing bacteria [1]. MMO from Type I methanotroph *Methylococcus capsulatus* (Bath) [2] has been resolved into three components, consisting of a dinuclear non-heme iron enzyme [3] (hydroxylase, M_r 250 kDa), an Fe_2S_2-FAD electron transport protein [4] (reductase, M_r 39 kDa) which mediates the transfer of electrons from NAD(P)H to the hydroxylase, and a small regulatory protein (component B, M_r 16 kDa) which contains no metals or prosthetic groups [5]. Kinetic studies on the roles and interaction of the three components of the MMO system from *M. capsulatus* (Bath) [5,6] have suggested the formation of protein complexes during the catalytic cycle which have an effect on the oxygenase activity. Component B appears to serve a strict role in regulating the oxygenase activity of the *M. capsulatus* (Bath) system, preventing reduction of the hydroxylase by the reductase in the absence of substrate, and greatly increasing the electron transfer rate between the two components in the presence of substrate [6].

EXAFS studies of the hydroxylase [7] have shown that the first coordination sphere of the iron active site in the oxidized form of the *M. capsulatus* (Bath) hydroxylase consists of ~ 6 N/O at an average distance of 2.04 Å. The photoreduced semimet form has ~ 6 N/O at 2.08 Å for the *M. capsulatus* (Bath) hydroxylase. The reduced hydroxylase from *M. capsulatus* (Bath) has ~ 5 N/O at 2.15 Å in its first coordination sphere. The iron-iron distance for the oxidized and semimet forms of the hydroxylase was determined to be ~ 3.4 Å, and no iron-iron interaction was seen in the EXAFS of the reduced form of the protein, although EPR verified that the dinuclear iron center was intact after exposure to the beam.

Perturbations in the EPR spectra of the hydroxylase in the presence of component B and in the presence of small molecules have been documented, suggesting that complexation with the hydroxylase in some way affects the Fe site [8,9]. The effects of substrate, component B and the reductase on the redox potentials of the hydroxylase have also been investigated [10] and show that dramatic changes in the electron affinity of the hydroxylase core occur as a function of the presence of the other components. We have collected Fe K-edge EXAFS data on hydroxylase samples in a photoreduced semimet form in the presence of component B, bromopropene, and both component B and bromopropene to determine the nature of the change in the coordination environment of the iron atoms.

Experimental

The samples were run on unfocused 8-pole wiggler beamline 7-3 (18 kG) at the Stanford Synchrotron Radiation Laboratory (SSRL) operating at 3 GeV and 40 - 90 mA. A Si(220) double-crystal monochromator was used, detuned 45% at 7995 eV to reduce harmonic contamination in the incident beam. The data were measured in fluorescence mode at 10 K using a continuous-flow LHe cryostat (Oxford Instruments, model CF1208). The fluorescence signal was monitored with a 13-element Ge solid-state detector array[11] (Canberra) windowed on the Fe Kα signal (6840 eV). Total count rates of between 25,000 and 35,000 per second per channel (measured at 7997 eV detuned 45%) were maintained throughout the experiments. At these count rates, the detector was below saturation limits.

Results and Discussion

The EXAFS data for the semimet hydroxylase [7] is compared to the semimet hydroxylase EXAFS in the presence of component B, bromopropene and both B and bromopropene in Figure 1, and the Fourier transforms of

the data in Figure 2. Preliminary fit results do not show any significant difference in the iron coordination sphere due to the formation of hydroxylase complexes. The average first shell coordination of the complexed forms of the semimet hydroxylase was determined to be 5.3 - 6.4 N/O at 2.06 - 2.08 Å, similar to the average first shell coordination of the non-complexed semimet hydroxylase (5.6 N/O at 2.08 Å, ref. 7). The Fe-Fe distance for all of the semimet complexes is also very similar, varying from 3.39 Å to 3.41 Å. However, a change is seen in the relative coordination numbers of the long and short distance contributions to the first shell data for the B-hydroxylase samples.

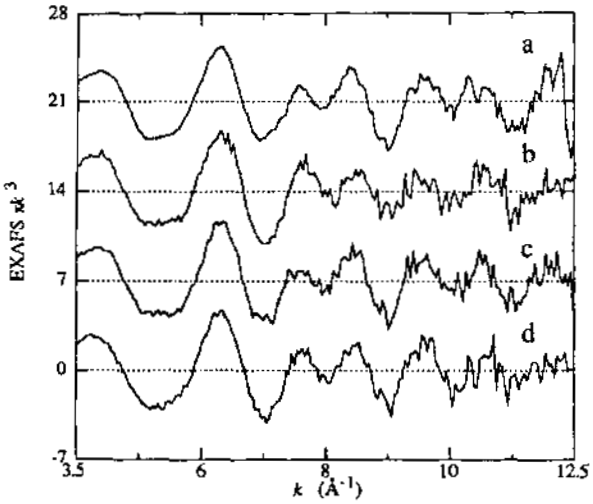

Figure 1. EXAFS of the semimet hydroxylase samples. (a) semimet hydroxylase sample, (b) with component B, (c) with bromopropene, (d) with B and bromopropene.

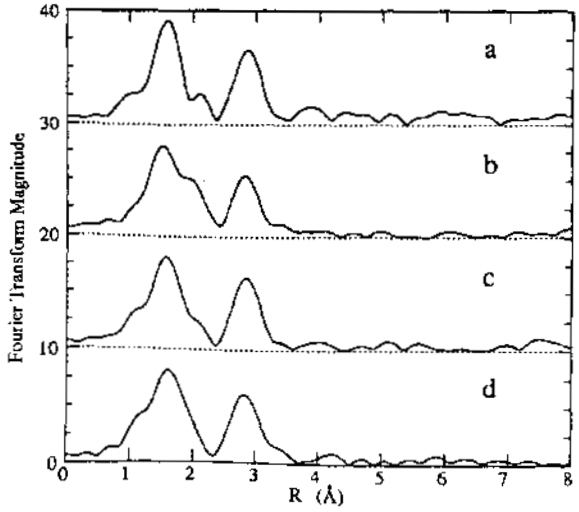

Figure 2. Fourier transforms of the semimet hydroxylase EXAFS (presented in Figure 1). (a) semimet hydroxylase sample, (b) with component B, (c) with bromopropene, (d) with B and bromopropene.

Although it is known that substrate interacts with the hydroxylase component, the location of the binding site has not been determined. A brominated substrate was used for the hydroxylase/substrate complex to provide information about the proximity of the substrate binding site to the iron center. Bromine is a stronger backscatterer than Fe, so an Fe-Br interaction should be detected if the substrate were to bind close enough to an iron atom in an ordered configuration (with little rotational or vibrational motion). To evaluate this, we have collected EXAFS data on a brominated derivative of Fe(acac)3, [tris-(3-bromo-2,4-pentanedionate)3 iron (III)] [12a] (or Fe(3-Br-acac)3) in which the Fe-Br distance is expected to be on the order of 5.2 Å [12b]. The contributions of the three bromine atoms at this distance are clearly seen in the Fourier transform of Fe(3-Br-acac)3 compared to Fe(acac)3 (Figure 3), suggesting that an Fe-Br interaction at a distance as long as 5 Å could be detectable by XAS. Inspection of the Fourier transforms of the semimet hydroxylase samples (Figure 2) shows no suggestion of a strong interaction above 3.5 Å, suggesting that substrate binds at a distance greater than 5 Å. Additionally, the second shell hydroxylase data can be well explained by only Fe and C contributions to the fits.

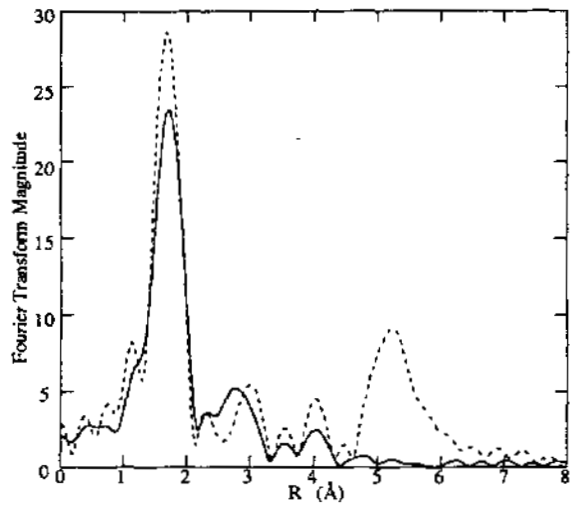

Figure 3. Fourier transforms of the EXAFS data for Fe(acac)3 (solid) and Fe(3-Br-acac)3 (dash). The peak at ~ 5 Å in the Fourier transform of Fe(3-Br-acac)3 is due to the Fe-Br interaction.

Conclusions

The Fe K-edge EXAFS showed only minor metrical changes in the coordination environment of the hydroxylase iron center due to the presence of substrate and component B, the regulatory protein of the MMO enzyme system. Preliminary results suggest that the presence of component B has an effect on the distance distribution of first shell atoms. Further analysis of the data is underway. No evidence of a Br contribution was seen in the EXAFS of the hydroxylase in the presence of a brominated substrate. This suggests that the site of

interaction between the hydroxylase and substrate is more than 4 Å from the iron center.

Acknowledgements

The data were collected at the Stanford Synchrotron Radiation Laboratory which is supported by the Department of Energy, Office of Basic Energy Sciences, Division of Chemical Sciences and Division of Materials Sciences and Office of Health and Environmental Research. SSRL is also supported by the National Institutes of Health, Biomedical Resource Technology Program, Division of Research Resources (RR-01209). Grant support was provided by the National Science Foundation (CHE 91-21576 to KOH).

References

1. Anthony, C. *The Biochemistry of the Methylotrophs*; Academic Press: London, 1982.
2. (a) Colby, J.; Dalton, H. *Biochem. J.* **1978**, *171*, 461-468. (b) Colby, J.; Dalton, H. *Biochem. J.* **1976**, *157*, 495-497.
3. (a) Woodland, M. P.; Dalton, H. *Anal. Biochem.* **1984**, *139*, 459-462. (b) Woodland, M. P.; Patil, D. S.; Cammack, R.; Dalton, H. *Biochim. Biophys. Acta* **1986**, *873*, 237-242. (c) Woodland, M. P.; Dalton, H. *J. Biol. Chem.* **1984**, *259*, 53-59.
4. Colby, J.; Dalton, H. *Biochem. J.* **1979**, *177*, 903-908. (b) Lund, J.; Dalton, H. *Eur. J. Biochem.* **1985**, *147*, 291-296.
5. Green, J.; Dalton, H. *J. Biol. Chem.* **1985**, *260*, 15795-15801.
6. (a) Lund, J.; Woodland, M. P.; Dalton, H. *Eur. J. Biochem.* **1985**, *147*, 297-305. (b) Green, H.; Dalton, H. *Biochem. J.* **1989**, *259*, 167-172.
7. DeWitt, J. G.; Bentsen, J. G.; Rosenzweig, A. C.; Hedman, B.; Green, J.; Pilkington, S.; Papaefthymiou, G. C.; Dalton, H.; Hodgson, K. O.; Lippard, S. J. *J. Am. Chem. Soc.* **1991**, *113*, 9219-9235.
8. (a) Fox. B. G.; Liu, Y.; Dege, J. E.; Lipscomb, J. D. *J. Biol. Chem.* **1991**, *266*, 540-550. (b) Hendrich, M. P.; Fox, B. G.; Andersson, K. K.; Debrunner, P. G.; Lipscomb, J. D. *J. Biol. Chem.* **1992**, *267*, 261-269.
9. (a) Dalton, H. *Adv. Appl. Microbiol.* **1980**, *26*, 71-87. (b) Dalton, H. *Microbial Growth on C1 Compounds*; Heyden Press: London, 1980, pp 1-10.
10. Liu, K. E.; Lippard, S. J. *J. Biol. Chem.*, **1991**, *266*, 12836-12839.
11. Cramer, S. P.; Tench, O.; Yocum, M.; George, G. N. *Nucl. Instrum. Methods Phys. Res.* **1988**, *A266*, 586-591.
12. (a) Kluiber, R. W. *J. Am. Chem. Soc.* **1960**, *82*, 4839-4842. (b) The crystal structure of the Fe complex has not been solved; the distance is based on the average Cr-Br distance for a crystallographically characterized Cr dimer of the same ligand. Estes, E. D.; Scaringe, R. P.; Hatfield, W. E.; Hodgson, D. J. *Inorg. Chem.* **1977**, *16*, 1605-1610. The sample of Fe(3-Br-acac)3 was diluted with BN powder, finely ground with a mortar and pestle, and pressed into a 1 mm Al spacer windowed with Mylar tape. The sample was run in transmission mode at SSRL on beamline 7-3 by using a Si(220) monochromator detuned 50% at 7997 eV. The incident and transmitted beam intensity were monitored by using N_2-filled ionization chambers of standard design. The data were collected at 10 K, maintained by a continuous-flow LHe cryostat (Oxford Instruments model CF1208).

X-Ray Absorption Near Edge Studies of Myoglobin, Cytochrome P-450-CAM, and Chloroperoxidase: Structural and Electronic Characterization of the Heme Active Site

Hongbin Isaac Liu[†], Britt Hedman[‡], Masanori Sono[§], Sally Kadkhodayan[§], John H. Dawson[§], Keith O. Hodgson[*†]

[†]Department of Chemistry, Stanford University, Stanford, CA 94305; [‡]Stanford Synchrotron Radiation Laboratory, Stanford University, CA 94309; [§]Department of Chemistry and Biochemistry, University of South Carolina, Columbia, SC 29208

Introduction

Since molecular structure dictates the spectroscopic and catalytic properties of the heme protein's active site, a thorough understanding of the unique spectral features of P-450 and chloroperoxidase have long been thought to be important for providing insight into its active-site structure, and therefore its catalytic mechanism. A question of central importance to the structures and catalytic activities of P-450 and chloroperoxidase have been the identity of the axial ligand to the heme iron. The ferric low spin, ferrous low spin and high spin forms of myoglobin, bacterial cytochrome P-450 CAM, and chloroperoxidase were examined by Fe-K X-ray absorption near edge spectroscopy. The electronic characterizations and structural correlation of the heme active sites are reported.

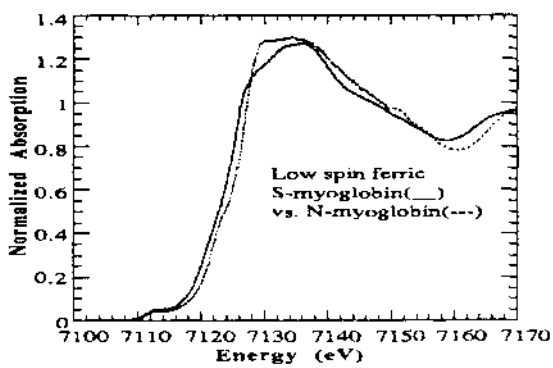

Figure 1: Consistent edge shifts are observed when a nitrogen-ligated myoglobin is compared with a sulfur-ligated myoglobin. A representative plot (above) is a comparison between N-methylimidazole and propanethiolate myoglobin.

Experimental

The spectra were measured at 10 K using a Oxford Instruments continuous-flowliquid He cryostat. The XAS data were collected at the Stanford Synchrotron Radiation Laboratory (SSRL) in 1990, 1991, and 1992. The data were collected as fluorescence excitation spectra on unfocused wiggler Beam Lines 7-3 and 4-2 using a Canberra 13 element Ge array detector.

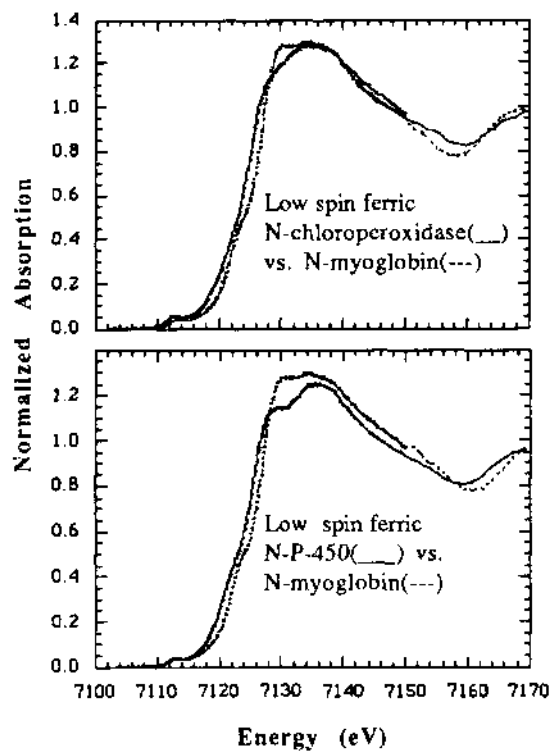

Figure 2: In the ferric and ferrous low spin state, the position of the absorption edge of imidazole-ligated chloroperoxidase and cytochrome P-450 were shifted in the direction of that of the ferrous state when compared with that of analogou myoglobin spectra.

The SPEAR storage ring was operated under dedicated conditions at 3.0 GeV and 35-95 mA.

Results and Discussion

A representative plot (Figure 1) shows a comparison between N-methylimidazole and propanethiolate myoglobin. The energy difference of the absorption edge of these two different myoglobins is 1.07±0.13 eV. The absorption edge of ferric propanethiolate myoglobin is shifted in the direction of lower energy and thus towards lower oxidation state.

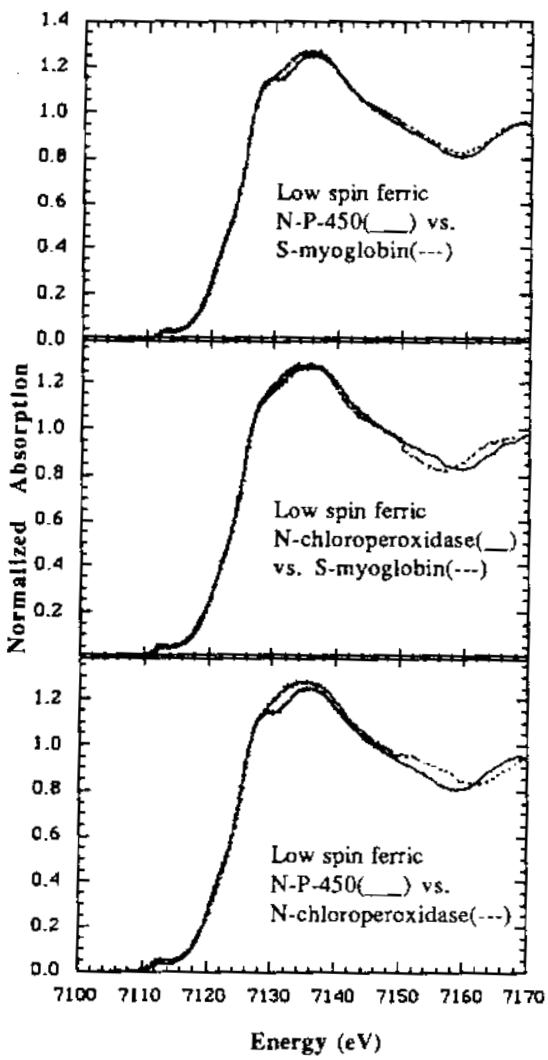

Figure 3: Both the positions of the absorption edge and the shapes of the preedge and edge spectra of imidazole-ligated chloroperoxidase and cytochrome P-450 are essentially the same as those of sulfur-ligated myoglobin.

The edge energy shift most likely derives from the distal sixth ligand: sulfur is a better π base than nitrogen, hence acts as an electron donor to the central iron atom. The difference in the spectral features of N-chloroperoxidase vs. N-myoglobin, and N-P-450 vs. N-myoglobin (Figure 2) thus are similar to those seen for S-myoglobin vs. N-myoglobin. Furthermore the preedge and edge shapes, and energy positions of N-chloroperoxidase and N-P-450 are very similar to that of S-myoglobin (Figure 3).

Since myoglobin has a distal His imidazole that has been proven by x-ray crystallography and many other optical methods, the XAS spectra reflect the similarities between the proximal ligand in N-chloroperoxidase, N-P-450 and the distal thiolate ligand in this myoglobin, and thus show that there is endogenous sulfur ligation of the central iron in chloroperoxidase and P-450.

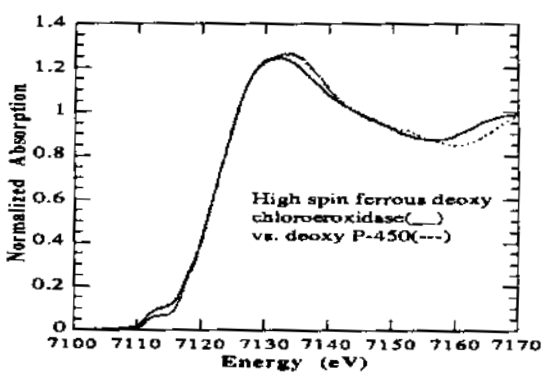

Figure 4 shows that in ferrous high spin states, chloroperoxidase and P-450 have very similar active sites. This finding is consistent with previous results obtained by EPR, UV, MCD measurements and recent DNA sequencing.

Conclusion

This XAS study has thus provided direct and compelling evidence for the presence of endogenous thiolate sulfur donor ligation to the central heme iron of chloroperoxidase and cytochrome P-450. This conclusion is strongly supported by recent EPR[1] study and DNA[2] sequence data of these proteins. X-ray crystallography[3,4] and previous EXAFS[5,6] studies of several P-450 ferric and ferrous states also support these conclusions.

Acknowledgments

This research is supported by Grants from NSF(CHE-9121576) to KOH and NSF(DMB86-05876) to JHD. The data were collected at SSRL which is supported by the U.S. DOE, Office of Basic Energy Science and in part by the NIH NCRR BRTP Program and by the DOE's Office of Health and Environmental Research.

References

1. Sono, M.; Hager, L.; Dawson, J. H. *Biochim. Biophys. Acta* **1078**, 351 (1991).
2. Blanke, S.; Hager, L. P. *J. Biol. Chem.* **263**, 18739 (1988).
3. Poulos, T. L.; Finzel, B. C.; Howard, A. J. *J. Mol. Biol.* **195**, 687 (1987).
4. Ragg, R.; Poulos, T. L. *Biochemistry* **30**, 2674 (1989).
5. Cramer, S. P.; Dawson, J. H.; Hodgson, K. O.; Hager, L. P. *J. Am. Chem. Soc.*, **100**, 7282 (1978).
6. Dawson, J. H.; Kau, L.; Penner-Hahn, J.; Sono, M.; Eble, K.; Bruce, G.; Hager, L.; Hodgson, K. O. *J. Am. Chem. Soc.* **108**, 8114 (1986).

SMALL-ANGLE X-RAY SCATTERING STUDIES OF THE IRON-MOLYBDENUM COFACTOR FROM *AZOTOBACTER VINELANDII* NITROGENASE

David Eliezer[a], Patrick Frank[b], Nanna Gillis[c], William E. Newton[d], Sebastian Doniach[c], and Keith O. Hodgson[b]

[a]Department of Physics, Stanford University, Stanford, CA 94305

[b]Department of Chemistry, Stanford University, Stanford, CA 94305

[c]Department of Applied Physics, Stanford University, Stanford, CA 94305

[d]Department of Biochemistry and Nutrition, Virginia Polytechnic Institute and State University, Blacksburg, VA 24061

Introduction:

Biological reduction of dinitrogen is catalyzed by the nitrogenase enzyme complex. The active site is a polynuclear metal cluster termed the iron-molybdenum cofactor (FeMoco)[1] (1,2,3). Until recently, the primary insights into the metrical details of FeMoco have come from x-ray absorption spectroscopy (edge and extended fine structure) (4,5), which clearly demonstrated the involvement of molybdenum in a polynuclear cluster bridged through a first shell of sulfides to a second shell of iron. The recent report of a preliminary crystal structure for the nitrogenase molybdenum-iron protein includes a proposed structural model of the FeMoco cluster bound within its protein matrix,

The inorganic complexes $((C_2H_5)_3NCH_2C_6H_5)_3[Mo_2Fe_6S_8(SC_2H_5)_9]$ and $((CH_3)_3NCH_2C_6H_5)_3[Mo_2Fe_7S_8(SC_2H_5)_{12}]$ were prepared by literature methods (9,10) and their identity and purity were established by elemental analyses and electronic spectra. The compound $((C_3H_7)_4N)_6Na_4[Fe_{18}S_{30}]$ was a kind gift of Professor Richard H. Holm of Harvard University, Department of Chemistry. Sample solutions of the molybdenum-containing dicubanes were prepared in *N,N*-dimethylformamide by dilution of a more concentrated stock solution. The sample solutions of the $[Na_2Fe_{18}S_{30}]^{(8-)}$ complex were prepared in similar fashion in acetonitrile.

SAXS data were collected and processed as

publication of the 18 Fe structure (13) is 6.4 Å, and the measured experimental value is 6.77 Å, again in good agreement. The excellent agreement between the experimental R_g values obtained for the model compounds and those calculated from the respective crystal structures is a good indication that the Guinier analysis used to extract the R_gs is valid, and that the effects of aggregation in these samples do not extend into the fitting range used. We believe it likely that the aggregation detected in these samples consists of only trace amounts of large aggregates.

The final average R_g value obtained for FeMoco is 6.96 Å. This value is surprisingly high, considering that its molecular weight, as calculated from its minimal composition, is significantly lower than that of any of the models involved, and that its shape in the protein is quite similar to that of the dicubane model compounds (6). In addition, the FeMoco data showed significantly stronger aggregation effects than the model compound data (Figure 1). These two observations lead us to hypothesize that unlike in the case of the model compounds, the aggregation effects observed in the FeMoco data are not caused merely by trace amounts of large aggregates. Instead we believe that a distribution of smaller FeMoco oligomers is most likely responsible for the observed R_g and for the large deviation of the data from a guassian shape in the smaller angle regions. The following discussion supports this hypothesis.

We applied a model using the analytical expression for the scattering from homogeneous spheres of specified R_g, first derived by Rayleigh (14).

$$I(S) \propto [(\sin(2\pi SR) - 2\pi SR\cos(2\pi SR))/(2\pi SR)^3]^2$$

where R is the sphere radius. Using this formula, the theoretical scattering pattern for a sample consisting of spheres of any single size can be calculated. If this pattern is then scaled so that it intersects the measured FeMoco SAXS data at one point, but does not exceed it at any point, it will then represent the maximum contribution that the presence, in the sample, of homogeneous spheres of that size could make to the measured data. Although the FeMoco aggregates are not known to be exactly spherical or entirely homogeneous, we believe that this model is still useful for gauging the contribution of aggregates to the data.

Using successively larger spheres, it is straight forward to estimate the maximum contribution that each particle size could make to the data (Figure 2). The contribution to the Guinier fitting region can then be calculated as the integrated intensity from the model normalized by the integrated intensity from the data. The results of the calculation show that according to this model the contribution from aggregates to the FeMoco data in the fitting region is limited to particles of less than about a 25 Å R_g. In fact the results suggest that the major contribution to the data comes from particles of a 6 to about 12 Å R_g. This bears out our expectation that the presence of smaller aggregates is necessary to explain the measured FeMoco R_g value.

In summary, the model compound data can be well explained by assuming a monomeric sample with trace amounts of large aggregates. In contrast, the large measured value of R_g for FeMoco cannot be explained in the same way. Our simple modeling analysis suggests that a significant presence of small FeMoco oligomers is necessary to explain the data. A unique distribution of particle sizes cannot be obtained from the data. However, we conclude with some confidence that in *N*-methylformamide solution, FeMoco largely exists in aggregated states of up to 25 Å in R_g. The average R_g value of the population is approximately 7 Å, a value significantly larger than what would be expected for a monomer.

Acknowledgments:

The critical interest and technical help of Dr. Michel Koch, Dr. Hirotsugu Tsuruta and Dr. Britt Hedman are gratefully acknowledged.

Support:

This work was supported by grants NIH RR01209 (to KOH), NIH DK37255 (to WEN) and by an NSF Graduate Fellowship (to DE). Data were collected at the Stanford Synchrotron Radiation Laboratory and the National Synchrotron Light Source which are supported by the US Department of Energy, Office of Basic Energy Sciences, Divisions of Materials and Chemical Sciences. SSRL is also supported by The National Institutes of Health, Biomedical Research Technology Program, and by the US Department of Energy, Office of Health and Environmental Research.

References:

1 Shah, V.K. and Brill, W.J. (1977) *Proc. Natl. Acad. Sci. USA* **74**, 3249-3253

2 Hawkes, T.R., McLean, P.A., and Smith, B.E. (1984) *Biochem. J.* **217**, 317-321

3 Scott, D.J., May, H.D., Newton, W.E., Brigle, K.E., and Dean, D.R. (1990) *Nature* **343**, 188-190

4 Conradson, S.D., Burgess, B.K., Newton, W.E., Mortenson, L.E., Hodgson, K.O. (1987) *J. Am. Chem. Soc.* **109**, 7507-7515

5 Conradson, S.D., Burgess, B.K., Newton, W.E., Hodgson, K.O., McDonald, J.W., Rubinson, J.F., Gheller, S.F., Mortenson, L.E., Adams, M.W.W., Mascharak, P.K., Armstrong, W.A., and Holm, R.H. (1985) *J. Am. Chem. Soc.* **107**, 7935-7940

6 Kim, J. and Rees, D.C. (1992) *Science* **257**, 1677-1682

7 Burgess, B.K., Jacobs, D.B., and Stiefel, E.I. (1980) *Biochim. Biophys. Acta* **614**, 196-209

8 Hedman, B., Frank, P., Gheller, S.F., Roe, A.L., Newton, W.E., and Hodgson, K.O. (1988) *J. Am. Chem. Soc.* **110**, 3798-3805 and references therein.

9 Wolff, T.E., Berg, J.M., Hodgson, K.O., Frankel, R.B., and Holm, R.H. (1979) *J. Am. Chem. Soc.* **101**, 4140-4150

10 Wolff, T.E., Power, P.P., Frankel, R.B., and Holm, R.H. (1980) *J. Am. Chem. Soc.* **102**, 4694-4703

11 Eliezer, D., Frank, P., Gillis, N., Chen, L., Tsuruta, H., Newton, W.E., Doniach, S., and Hodgson, K.O. (1991) *SSRL Activity Report* 142-144

12 Wakatsuki, S., Hodgson, K.O., Eliezer, D., Rice, M., Hubbard, S., Gillis, N., Doniach, S., and Spann, U. (1992) *Rev. Sci. Instrum.* **63**, 1736-1740

13 You, J.-F., Snyder, B.S., and Holm, R.H. (1988) *J. Am. Chem. Soc.* **110**, 6589-6591

14 Rayleigh, L. (1911) *Proc. Roy. Soc. (London)* **A-84**, 25-46

Figure 1: **Scattering data from equal concentrations of FeMoco and the $[Mo_2Fe_7S_8(SC_2H_5)_{12}]^{3-}$ model compound at angles smaller than those used for the Guinier fits.** The sharp rise of the scattering at small angles indicates the presence of trace amounts of large aggregates. The presence of more and/or larger aggregates in the FeMoco sample is readily apparent from the much stronger scattering at these low angles.

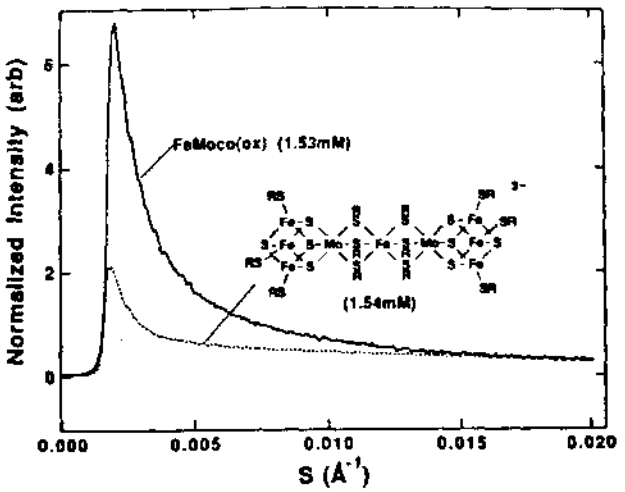

Figure 2: **Maximum possible contributions from homogeneous spheres of varying R_g to the measured intensity.** The scattering calculated for each sphere size may not exceed the measured scattering at any point.

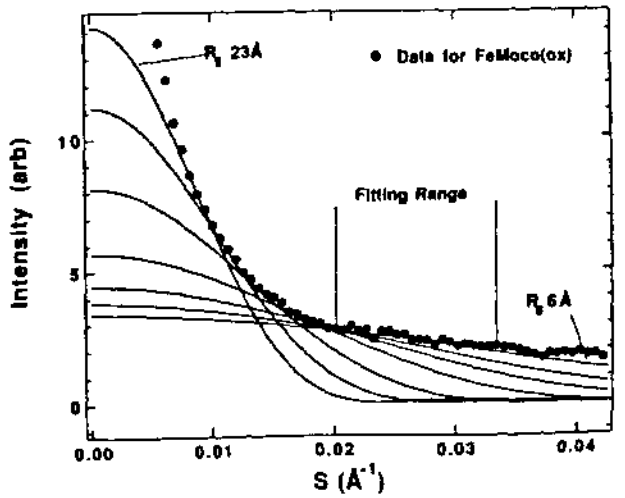

TIME-RESOLVED SAXS STUDIES OF THE MYOGLOBIN REFOLDING PATHWAY

David Eliezer[a], Kaori Chiba[b], Hirotsugu Tsuruta[c], Sebastian Doniach[d], Keith O. Hodgson[ce], and Hiroshi Kihara[f]

[a]Department of Physics, Stanford University, Stanford, CA 94305

[b]Department of Biological Sciences, Tokyo Institute of Technology, Yokohama, Kanagawa, Japan

[c]Stanford Synchrotron Radiation Laboratory, Stanford University, SLAC, Bin 69, P.O. Box 4349, Stanford, CA 94309

[d]Department of Applied Physics, Stanford University, Stanford, CA 94305

[e]Department of Chemistry, Stanford University, Stanford, CA 94305

[f]Department of Physics, Jichi Medical School, School of Nursing, Yakushiji, Tochigi, Japan

Introduction:

Recently the search for intermediates on the protein folding pathway has been advanced by techniques such as pulsed-labelling NMR and time-resolved CD spectroscopy. Information relating to the kinetics of secondary structure formation is now obtainable. In order to understand the forces driving the formation of the observed secondary structure and to understand its role in subsequent folding steps, it would be helpful to know the size of the protein at the times in question. However, a probe capable of measuring protein spatial dimensions during folding has been lacking.

Time-resolved small-angle x-ray scattering (SAXS), when combined with very high flux synchrotron sources, is capable of providing such physical information. Initial applications of this technique were performed using temperature as the denaturing agent and accessed a time scale of seconds (1). We describe herein a study using chemical denaturation and stopped-flow methods to investigate the refolding pathway of horse muscle myoglobin on a tens of milliseconds time scale from a physical perspective.

Methods:

Horse skeletal muscle myoglobin was purchased from the Sigma Chemical Company, St. Louis, MO (crystallized and lyophilized, salt-free, 95-100% pure) and stored frozen until use. The purchased protein was not purified further. 60 mg/ml protein samples were prepared in 7 M urea, 50 mM Bis-Tris-propane buffer at pH 9.1 with salt concentrations of 100 mM NaCl and 40 mM NaCN. No aggregation was observed in any of the protein samples, and upon spinning at 15000 rpm for up to an hour, no precipitate was observed. Protein-free dilution buffers were prepared at identical pH, NaCl, NaCN, and buffer concentrations, with urea concentrations of 0, 1, and 2 M.

For equilibrium studies 5 mg/ml protein samples were prepared at the same pH and salt concentrations, and at urea concentrations varying from 0 to 8 M in 1 M increments.

Data were collected in the angular range of $S=.002$ to $.025$ $Å^{-1}$ (where $S = 2\sin\theta/\lambda$, 2θ is the scattering angle, and λ is the x-ray wavelength). The x-ray stopped-flow rapid-mixer, developed in collaboration with T. Nagamura and Unisoku Inc. (Hirakata, Osaka, Japan) has been described in detail elsewhere (2), and has been successfully employed in time-resolved studies of quarternary structural changes of proteins. The machine is capable of mixing small sample volumes (20-100 μl) at various mixing ratios, at a controlled temperature ($\pm$0.1 °C), and with a mixing dead-time of 10 milliseconds. Beam-line data acquisition software allowed for the collection of data in a series of discrete time-intervals or frames. Frame duration was chosen to be between 20 and 200 milliseconds, depending on the rate of the observed process. In all cases a total of 94 frames were collected.

All time-resolved measurements were made using a 6:1 (dilution buffer:protein solution) mixing ratio. This resulted in final urea concentrations of 1.0, 1.9, and 2.7 M, and in a final protein concentration of 8.6 mg/ml. Data were accumulated for 5 mixing events at a time, and at least 10 separate accumulations were collected for each condition, for a minimum of 50 mixing events. Immediately following the time-resolved data collection, static data were measured from the mixed sample to record the final condition. Backgrounds were measured immediately before or after the time-resolved measurements.

Equilibrium data were collected at 15 °C in a flat 20 μm quartz window cell. Exposure times were from 300 to 600 seconds.

Analysis:

Reproducibility of the time-resolved data was verified by comparing different data sets collected under the same conditions, and was excellent in all cases. The processed data were fit using both non-linear least-squares and conventional Guinier fits in order to obtain the radius of gyration (R_g) and forward-scattered intensity (I_0) for each time-frame of data and for the static data. As previously observed in (3) I_0 showed a strong time-dependent signal (Figure 1).

Kratky plots for the initial state were obtained by averaging time-frames over one half-life of the observed time-course in I_0. In all cases, this average was found to overlay well onto the Kratky plot for the first time-frame alone. Kratky plots for the final state were obtained in a similar fashion, using the 40 final frames, during which no time-dependence was observed.

The equilibrium data were processed as above using Guinier fits to extract Rg and I_0. A calculation of the variation of I_0 with urea concentration shows that I_0 should decrease by about 50% in going from 0M to 8M urea. This agrees reasonably well with the observed decrease of I_0 in the equilibrium data. The decrease, then, is caused mostly or entirely by the change in solvent density. This result implies that if the background solvent remains the same during the unfolding or refolding of myoglobin, as in our time-resolved experiments, no change of I_0 should be observed as a result of the conformational change alone.

Results:

The R_g obtained from the initial time-frames (32±3 Å) is consistent with that of either a small oligomer or an unfolded state, but not with that of the native state (18±1 Å). The R_g from the final time-frames (20±2 Å) is in good agreement with the native state value.

Recently it has been shown that Kratky plots can be used to distinguish between coil-like and globular scatterers (4). Kratky plots of static data from unfolded myoglobin have a shape characteristic of coil-like scatterers, and different from the shape of Kratky plots of data from native myoglobin or other globular scatterers (Figure 2). Initial time-frame Kratky plots do not show the coil-like characteristic shape of unfolded myoglobin (Figure 3). Instead, they show a shape characteristic of a globular scatterer. This directly implies that immediately after the mixing of the solutions, the protein is no longer an unfolded monomer. This result, together with the high initial R_g value, leads us to conclude instead that the sample contains small globular protein oligomers. Under the initial conditions (before mixing) and under the final conditions (after equilibrium has been reached) no aggregation is detected in the samples. Therefore the oligomers detected in the initial frames of the experiment indicate the presence of an associative intermediate state.

After inital mixing, the background solvent remains the same throughout the ensuing measurements. As discussed above, under identical solvent conditions I_0 of unfolded myoglobin does not differ significantly from I_0 of the native state. It is most likely then that the decrease in I_0 is caused by a decrease in the volume and hence in the mass of the scatterer. We conclude, in agreement with the Kratky plot analysis, that dissociation of protein oligomers is responsible for the observed decrease in I_0.

In all of the time-resolved experiments, I_0 was observed to decrease by a factor of two, within the experimental error. This leads us to hypothesize that the signal we observe in I_0 is engendered by the dissociation of the entire intermediate population from dimers to monomers. If this were the case, the concentration of dimer in the sample at any time, normalized by the initial protein concentration, would be

$$[D](t)/[M](0) = (I_0(t)/I_0(\infty) - 1)/2$$

where [D] represents the dimer concentration and [M](0) the initial (before mixing) monomer concentration.

Far from being unprecedented, our results add to the growing body of evidence that transient association may be a commonly occurring process on protein folding pathways (5,6). Most notably, bovine carbonic anhydrase B was recently shown, using high-performance liquid chromatography, to undergo a dimerization process during refolding (5).

Because under our conditions the dimerizing species is not long lived we do not know its association equilibrium constant. We note, however, that this intermediate is possibly the same one detected by Phillips in a thermal denaturation study of myoglobin (1), and that therefore it may be possible to study its properties in equilibrium under those conditions, where a much longer lifetime was observed. In the meanwhile, we note that the dimerization of the protein appears to be completed within the dead-time of the rapid-mixer, which is 10 ms. We use this observation to set a lower limit of about 1 ms^{-1} mM^{-1} or 10^6 s^{-1} M^{-1} for the dimerization rate constant, k_d. If we assume that the measured apparent rate constant, k_{app}, is actually k'_d, the dissociation rate constant, then the equilibrium association constant $K = k_d/k'_d$ is in the vicinity of 10^6 M^{-1} under our various conditions. These values of k_d and K are similar in magnitude to values reported in the literature for similar processes in carbonic anhydrase B and bovine growth hormone (5,6). We emphasize however that the numeric K

value we obtain is only a rough estimate, because the presence of even a small amount of higher order oligomers or aggregates might have a significant effect on the magnitude of k_{app}.

Conclusion:

We believe that the demonstrated ability of time-resolved stopped-flow small-angle x-ray scattering to measure protein size as a function of time makes it uniquely applicable to studying the processes of compactization and association during protein refolding. Compactization is a necessary event in the folding pathway of every protein, and it is becoming evident that association is at least a potential event in folding pathways as well. Further applications of the method to a wider range of proteins should elucidate previously undetectable steps in their folding pathways, and provide critical constraints for future models of general protein folding pathways.

Acknowledgments:

We are grateful to Dr. G.V. Semisotnov for useful discussions and to Dr. Y. Amemiya for technical assistance. This work was supported by NIH grant RR01209 (to KOH) and by an NSF graduate fellowship (to DE). Data were collected at the Stanford Synchrotron Radiation Laboratory and at the Photon Factory, National Laboratory for High Energy Physics, Japan. SSRL is supported by the US Department of Energy, Office of Basic Energy Sciences, Divisions of Materials and Chemical Sciences, by the National Institutes of Health, Biomedical Research Technology Program, and by the US Department of Energy, Office of Health and Environmental Research.

References:

1) Phillips, J.C., A.D. LeGrand, and W.F. Lehnert. 1988. *Biophys. J.* 53:461-464.

2) Tsuruta, H., T. Nagamura, K. Kimura, Y. Igarashi, A. Kajita, Z.-X. Wang, K. Wakabayashi, Y. Amemiya, and H. Kihara. 1989. *Rev. Sci. Instrum.* 60:2356-2358.

3) Eliezer, D., K. Chiba, H. Tsuruta, R.L. Baldwin, S. Doniach, K.O. Hodgson, and H. Kihara. 1991. *SSRL Activity Report.* 145:146.

4) Kataoka, M., Y. Hagihara, K. Mihara, and Y. Goto. 1992. *J. Mol. Biol.* in press.

5) Cleland, J.L., and D.I.C. Wang. 1992. *Biotechnol. Prog.* 8:97-103.

6) Brems, D.N., S.M. Plaisted, H.A. Havel, and C.-S. C. Tomich. 1988. *Proc. Natl. Acad. Sci. USA.* 85:3367-3371.

Figure 1: **Kratky plots from urea-unfolded and native myoglobin.** The broad peak in the native data indicates that the scattering molecule is compact. The persistent linear rise of the unfolded data is characteristic of a random coil molecule.

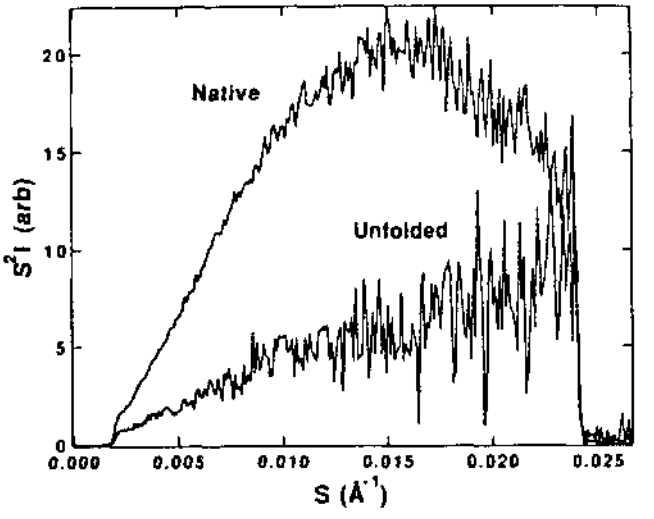

Figure 2: **Kratky plots averaged over the first 0.8 seconds and the last 4.4 seconds after mixing.** The plot for the last 4.4 seconds has been shifted arbitrarily along the ordinate for clarity of presentation. The final urea and protein concentrations were 1.0 M and 0.49 mM at 8 °C. The lack of the characteristic persistent linear rise in the initial time-frame plot indicates that the protein loses its random coil character within the mixing dead-time.

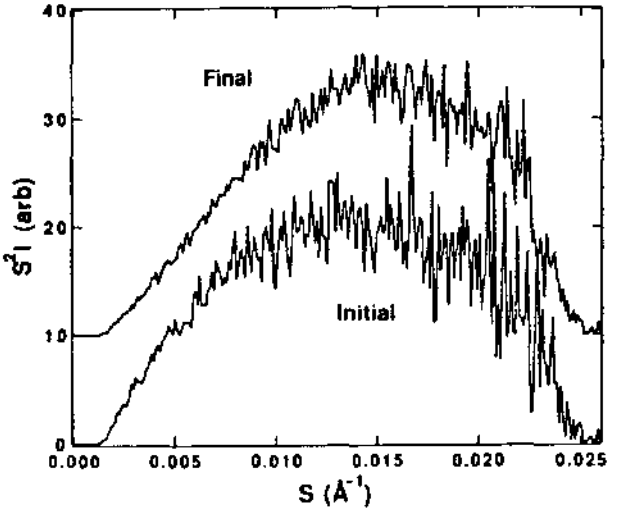

Figure 3: A representative plot of the forward-scattered intensity (I_0) vs. time after mixing.

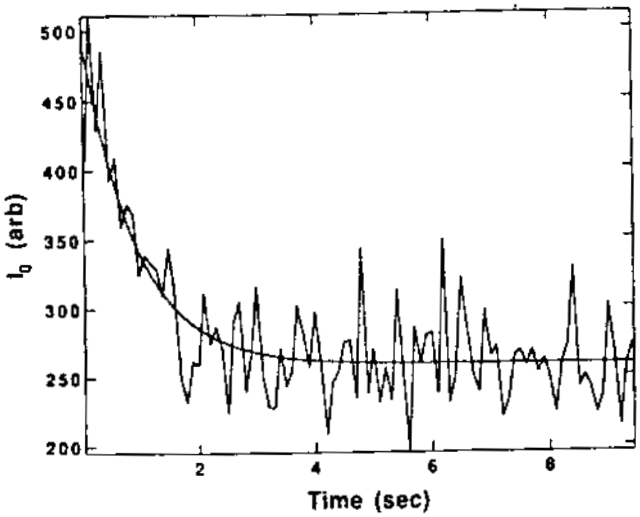

150 nSEC 2-D DETECTOR PROJECT - DESIGN ISSUES

W.K. Warburton and S.R. Russell
X-ray Instrumentation Associates
2513 Charleston Rd, Suite 207, Mountain View, CA 94043

We are currently developing a prototype 2-dimensional pixel detector for doing sub-microsecond time resolved protein crystallography or other x-ray diffraction studies. Our design uses the dark time between consecutive x-ray flashes to record the x-ray intensity striking the detector, provided the dark intervals exceed 150 nsec. Each detector pixel has an individual electronics processing chain consisting of a Si pixel, integrating preamplifier, amplifier, A/D converter and local memory buffer. Once per x-ray flash, the x-ray created charges in each pixel are thus collected, amplified and digitized and recorded in a local memory. This detector design is inherently massively parallel, since protein crystallography requires a detector resolution of between 512 x 512 to 1024 x 1024 pixels to be effective. The buffer memories will be 8K deep and provisions will be made to accommodate more slowly running experiments. In a full scale 10^6 pixel detector the maximum storage rate will be 6 Tbytes/sec for experiments lasting up to 1 msec and storing 6 Gbytes of data. The data will be unloaded to permanent storage in 10-15 minutes at video rates to allow an initial visual inspection. Because data storage is synchronous to arrival of the x-ray flashes, the detector can also be used in strobed measurements and achieve time resolutions limited only by the duration of the x-ray flashes themselves.

The resultant system design is shown in Figure 1. Several levels of gain will be required in the amplifier stages to accommodate variations in crystal scattering strength and SR intensity. We are currently at the stage of developing preamplifiers, whose conceptual operation is shown in Figure 2. Basically, the preamplifier integrates the charge created in a pixel by a single x-ray flash, waits long enough for the value to settle so that it can be measured, and then resets the integrator. Because the output is forced to zero between successive measurement, this is essentially a double sampling process.

Our principal research in 1992 was to determine that this approach was feasible before proceeding to the design and production of preamplifiers as integrated circuits. We therefore constructed a reset preamplifier using a discrete component design as shown in Figure 3. The detector capacitance is integrated on the detector capacitance. The resulting voltage is impedance transformed by FET follower LND150 and amplified by Op Amp CLC420. The voltage on the LND150's gate is reset by FET switch 5D210 once per x-ray flash.

This configuration was tested at SSRL in timing mode with the results shown in Figure 4. The charge collected from the x-rays can be clearly seen, showing that it is indeed possible to operate such a preamplifier synchronously with the x-ray beam as is required for our detector concept. However, as may also be seen, the voltage swings induced by the resets exceed those from the x-rays by a very large amount. This behavior is caused by

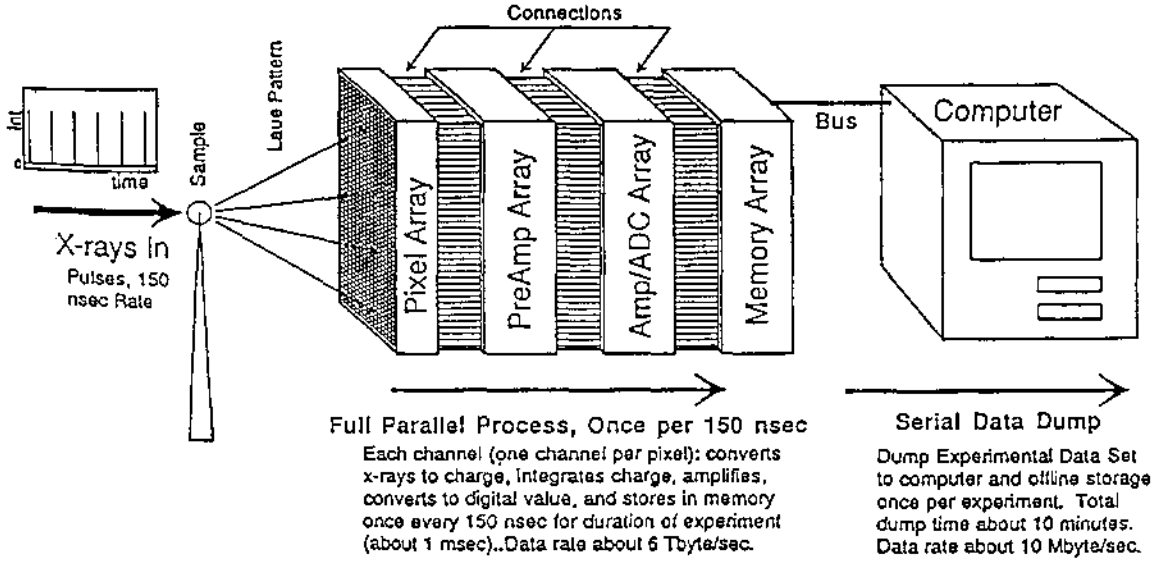

Figure 1: Schematic representation of time resolved protein crystallography detector showing massively parallel design.

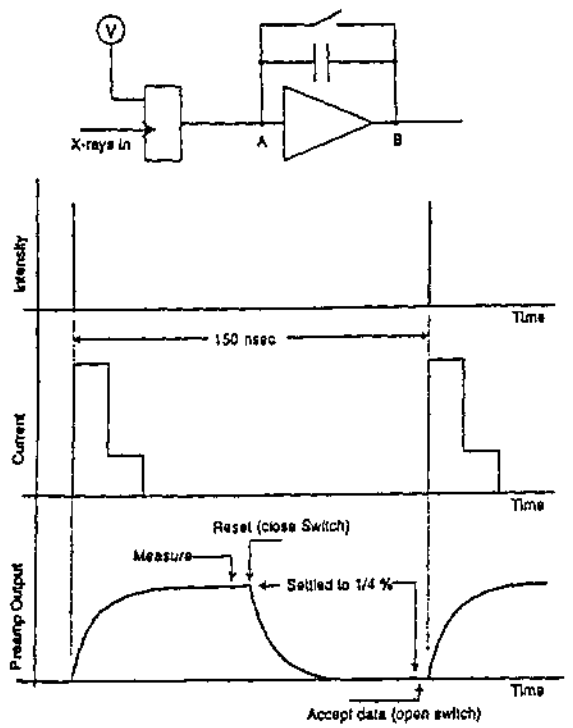

Charge flowing from detector is integrated on capacitor across preamplifier. When it has settled it is measured by the ADC after being amplified. The reset switch is then closed to prepare the preamplifier for the next current pulse. This cycle repeats once per x-ray flash for repetition periods of 150 nsec or longer.

Figure 2: The preamp's conceptual operating scheme.

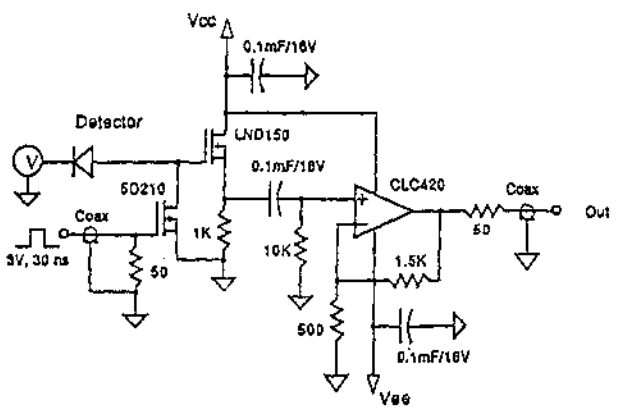

Figure 3: Reset test circuit with FET follower.

the gate-drain capacitance of the 5D210, which is too large and injects too much charge onto the integrating node during reset. This capacitance was the smallest commercially available and is purely an artifact arising from the connections between the FET, its package and the circuit board. These connections will be absent in an integrated preamplifier design, eliminating this problem.

Based on the success of these results, we have therefore proceeded with both the design and fabrication of a fully integrated CMOS preamplifier and the design and

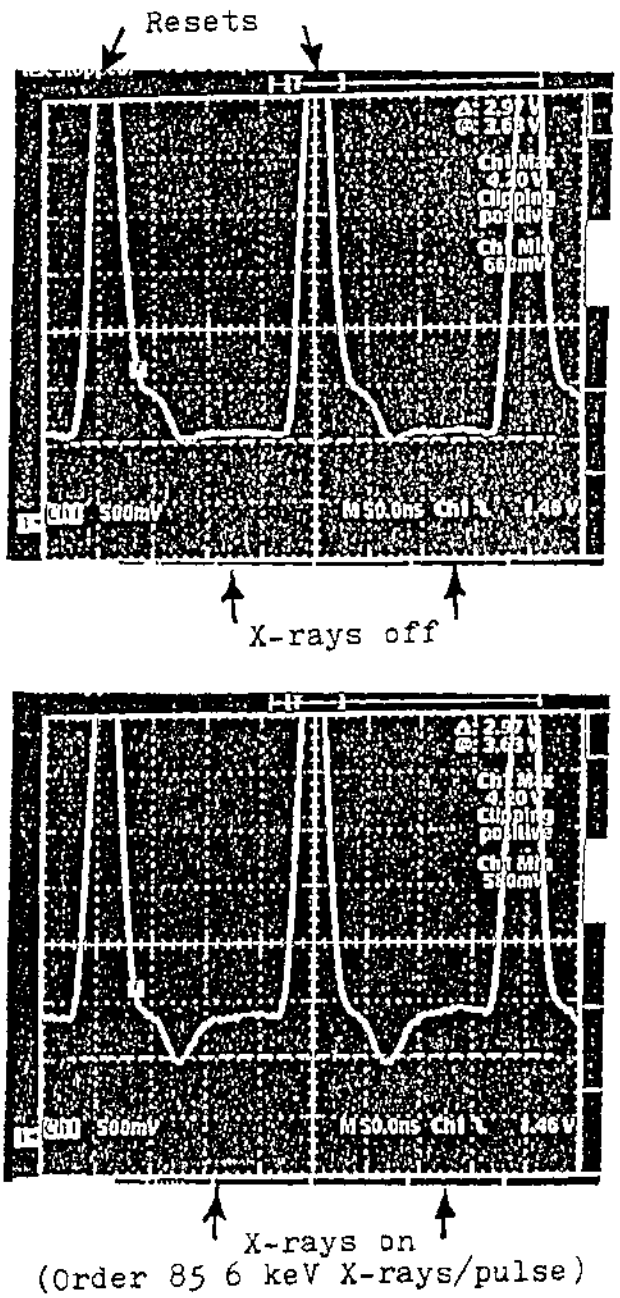

Figure 4: Showing the output of the amplifier both with x-rays turned off and turned on.

fabrication of test arrays of pixels. The preamplifiers will be built 64 to a chip, while the detectors are being designed in both 1-D arrays of 1x64 and 1x256 and a small test 2-D array of 8x8. We are also beginning the design of a prototype amplifier board so that in early 1993 we will be able to start assembling small 1-D and 2-D prototype versions of the full system shown in Figure 1. We expect to have these systems ready for experimental tests by late in the 1993 Spring run.

Funding for this research is being provided by the NIH through SBIR Grant #R44 GM43675.

pH DEPENDENCE OF THE ACTIVE SITE OF HORSERADISH PEROXIDASE COMPOUND II

C.-S. Chang, NCDMF, I. Yamazaki, NCDMF, R. Sinclair, NCDMF, S. Khalid, NSLS, and L. Powers, NCDMF

Using X-ray absorption spectroscopy, we investigated the active site of horseradish peroxidase (HRP) compound II at two different pH values. The results indicate that the bond length of the sixth coordinated ligand of the active site was 1.90 ± 0.02 Å at pH 7 decreasing to 1.72 ± 0.02 Å at pH 10. The average iron-to-pyrrole nitrogen and the proximal ligand bond lengths showed no significant changes. The position of higher coordination shells around the iron center changed, implying that some movement or deformation of nearby amino acid residues and/or of the heme occurred. Results of this study suggest that the decrease of the Fe–O bond length of HRP compound II at the higher pH might be attributed to the loss of a hydrogen bond which is present between the oxygen ligand and an amino acid residue in the heme pocket at pH 7.

AN EXAFS INVESTIGATION OF THE STRUCTURE OF THE ACTIVE SITE OF LACTOPEROXIDASE

C.-S. Chang, NCDMF, R. Sinclair, NCDMF, S. Khalid, NSLS, I. Yamazaki, NCDMF, S. Nakamura, Hirosaki U., and L. Powers, NCDMF

Native lactoperoxidase, compound III, and the reduced forms (at pH 6 and 9) were studied using X-ray absorption spectroscopy (XAS). Native lactoperoxidase has four pyrrole nitrogen ligands at an average distance of 2.04 ± 0.01 Å, a proximal ligand at 1.91 ± 0.02 Å, and a sixth (distal) ligand at 2.16 ± 0.03 Å. Lactoperoxidase native enzyme and compound III have first coordination shell structures that are similar to those of lignin peroxidase [Sinclair, R., Yamazaki, I.; Bumpus, J.; Brock, B., Chang, C.-S., Albo, A., and Powers, L. (1992) *Biochemistry* **31**, 4892–4900] and different from those of horseradish peroxidase [Chance, B., Powers, L., Ching, Y., Poulos, T., Schonbaum, G., Yamazaki, I., and Paul, K. (1984) *Arch. Biochem. Biophys.* **235**, 596–611]. The five-coordinated ferrous form was stable at pH 9, but at pH 6 was rapidly converted to the six-coordinated form with a distal ligand at 2.18 ± 0.03 Å. No evidence typical of changes in spin state was obtained at the different pH values.

THE STRUCTURE OF THE ACTIVE SITE OF LIGNIN PEROXIDASE ISOZYME H2: NATIVE ENZYME, COMPOUND III AND REDUCED FORM

R. Sinclair, NCDMF, I. Yamazaki, NCDMF, J. Bumpus, U. Notre Dame, B. Brock, Oregon Graduate Inst. Sci. and Tech., C.-S. Chang, NCDMF, A. Albo, Utah State U., and L. Powers, NCDMF

The wood degrading fungus *Phanerochaete chrysosporium* secretes a number of extracellular enzymes called lignin peroxidases which are involved in the degradation of both lignin and a number of persistent environmental pollutants. Lignin peroxidase isozyme H2, a glycosylated protein of approximately 40 Kd, contains a single heme. X-ray absorption spectroscopy (XAS) has been used to probe the local environment of the iron in the active site of resting enzyme, reduced enzyme and compound III. For the native and reduced forms respectively, the average Fe-pyrrole nitrogen distances are 2.055 Å and 2.02 Å($\pm$0.015 Å); the Fe-proximal nitrogen distance is 1.93 Å and 1.91 Å ($\pm$0.02 Å) while the Fe-distal ligand distance is 2.17 Å and 2.10 Å ($\pm$0.03 Å). Although the results are not as well defined, the active site structure of compound III is largely 2.02 0.015 for the average Fe-pyrolle nitrogen distance, 1.90 ± 0.02 Å for the Fe-proximal nitrogen and 1.74 ± 0.03 Å for the Fe-distal ligand distance. The heme iron pyrrole nitrogen distance is more expanded in ligninase H2 than in other peroxidases. The possible significance of this is discussed in relation to other heme proteins.

STRUCTURAL CHARACTERIZATION OF MERCURY METALLOPROTEINS USING XAS

Kimber Clark, Timothy Stemmler and James Penner-Hahn
Department of Chemistry
University of Michigan

Lisa Utschig and Thomas V. O'Halloran
Department of Chemistry
Northwestern University

Susan Miller
University of California, San Francisco
Department of Pharmecutical Chemistry

A central component of the bacterial mercury detoxification system is the cooperation between MerR, a metalloregulatory protein, and MerA, a mercuric reductase. MerR is an intercellular heavy metal sensor. It acts as a metal-responsive genetic switch, controlling production of the proteins which transport and reduce mercury. MerA catalyzes the actual two-electron reduction of Hg(II) to Hg(0) using NADPH and FAD. This project involves structural characterization of these proteins.

MerR

In the presence of mercuric ions, MerR is converted from a repressor to an activator of the prokaryotic mercury resistance genes. Cadmium and zinc adventiously activate transcription, but much higher concentrations of these metals are required. MerR is activated by 0.1 nM concentrations of mercuric ion, while Cd and Zn require concentrations ca. 100 and 1000 times higher, respectively[1]. Most other transition metals will not convert the protein to an activator conformation. Even at Cd and Zn concentrations high enough to activate MerR, the transcription levels are lower than for Hg-MerR, suggesting a binding site that is in some way different. This is somewhat surprising because of the similarities in Cd and Hg coordination chemistry. In order to obtain the structural information necessary to resolve the molecular basis of heavy metal recognition site in this metal-sensing protein, we have undertaken EXAFS studies of Zn and Cd substituted MerR.

We have previously reported EXAFS spectra for Hg-MerR. These data show a three-coordinate Hg environment with exclusively sulfur ligation. The average Hg-S distance is 2.43 A. [2] This tridentate coordination environment is in agreement with the thermodynamic stability of $[Hg(SR)_3]^-$ complexes. In contrast, other group IIB metals appear more likely to adopt tetrahedral environments with thiolate coordination. [2,3,4] An $Hg(S\text{-}Cys)_3$ binding site that is distinct from the Cd or Zn binding geometries thus suggests a structural rationale for the ability of MerR to both discriminate between Hg(II) and other group IIB ions while maintaining ultra sensitivity to mercuric ion.

X-ray absorption data for both Zn(II) and Cd(II) forms of MerR have provided further evidence for this proposed mechanism of

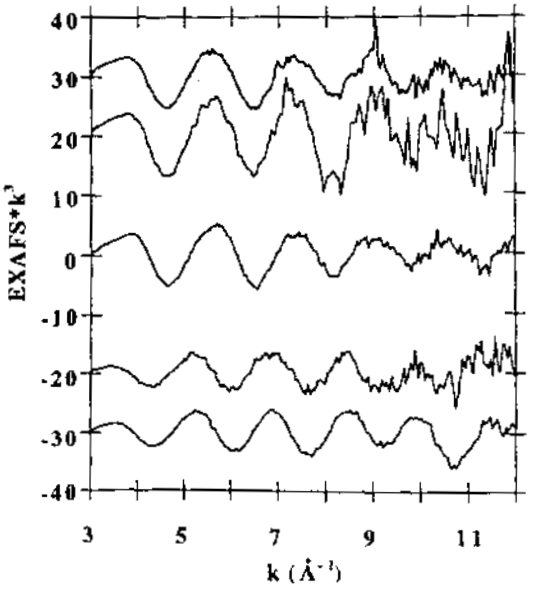

Figure 1. *Zn-Mer and Cd-MerR EXAFS data. From top: Zn(II)-MerR, # 1; Zn(II)-MerR, # 2; Zn(II)-MerR in Cl^- free buffer; Cd(II)-MerR, # 1: Cd(II)-MerR, # 2. Spectra offset vertically by +30, +20, 0, -20, and -30, respectively, for clarity.*

discrimination. The EXAFS are shown in Figure 1 and corresponding Fourier transforms are shown in Figure 2. The spectra for both the Cd(II) and the Zn(II) bound forms of MerR show only a single resolved shell of scatterers. The data are consistent with a four coordinate, primarily cystiene, environment with an average Zn-S distance of 2.3 Å. This distance is consistent with crystallographic data on four coordinate Zn-S complexes. [6] It is not possible, at present, to distinguish between a ZnS_4 structure and a ZnS_3N site. The fits to the Cd EXAFS suggests that the metal site is again four coordinate, with primarily thiolate environment. The average Cd-S distance of 2.5 Å is in agreement with distances of four coordinate Cd-S compounds. As with Zn, it is not at present possible to tell whether the additional ligand is sulfur or a low-Z ligand. Experiment to resolve this ambiguity are in progress.

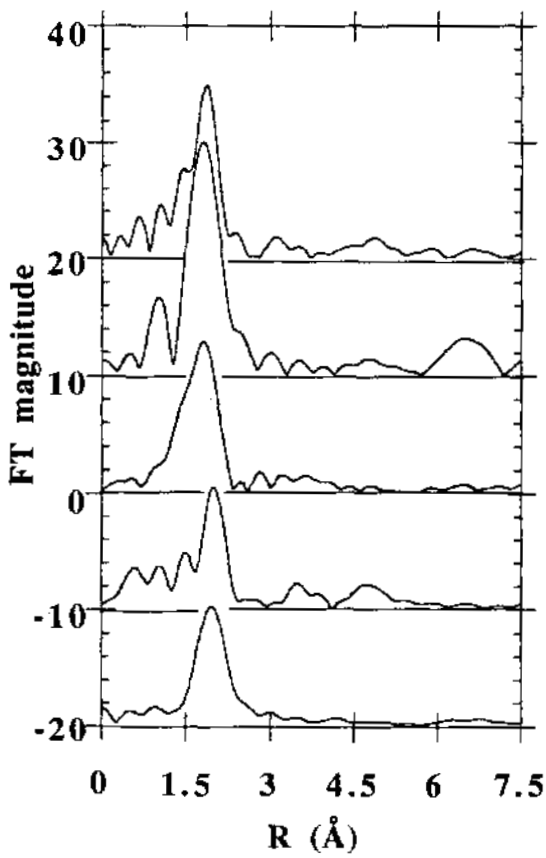

Figure 2. *Fourier transforms. From top: Zn(II)-MerR, sample 1; Zn(II)-MerR, sample 2; Zn(II)-MerR in Cl^- free buffer; Cd(II)-MerR, sample 1; Cd(II)-MerR, sample 2. Spectra offset vertically by 20, 10, 0, -10, -20, respectively, for clarity.*

MerA

The ultimate step in bacterial detoxification of mercuric ions is their two electron reduction to elemental mercury. This reaction is catalyzed by MerA. This enzyme is a dimer which contains FAD, a reducible active site disulfide, and a C-terminal pair of cysteines at each active site. Walsh and co-workers have found that all 4 cysteines are required for efficient Hg(II) reduction [7]. As noted previously [7], MerA must bind Hg tightly to prevent damage to other proteins, but this tight binding, by stabilizing Hg(II), is inconsistent with facile reduction of Hg(II) to elemental Hg. Recent data from pyridine nucleotide binding studies suggest that the dimeric enzyme is asymmetric when complexed to pyridine nucleotide substrates/products. EXAFS has been used to investigate evidence for the "alternating sites" hypothesis [8] which states that MerA dimers function asymmetrically, with one site within the dimer binding Hg(II) while the other catalyzes the reduction. Following reduction, the Hg(0) is released and the functional roles of the sites are switched.

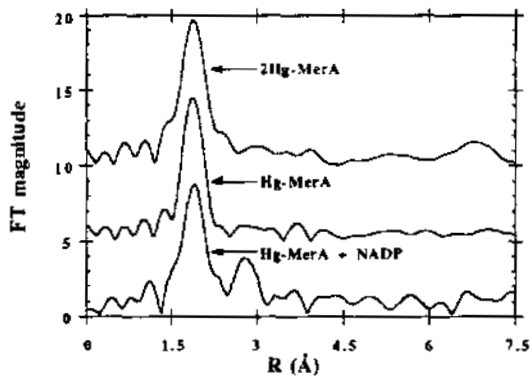

Figure 3. *Fourier transforms of MerA containing one equivilent Hg(II) per dimer in the presence and absence of NADP, and MerA containing two equivilents of Hg(II) per dimer in the absence of NADP.*

Previous EXAFS studies on the EH_2 form of MerA containing two Hg per dimer found an average Hg-S bond length of 2.30 Å, consistent with two-fold Hg-S coordination. [7] We have recently measured EXAFS data for MerA containing a single Hg(II) per dimer in the presence and absence of $NADP^+$, and for MerA with two Hg(II) ions per dimer in the absence of $NADP^+$. Curve fitting analysis of the EXAFS spectra show that there is no change in the Hg coordination sphere upon addition of a second Hg(II) per dimer, suggesting that there is no EXAFS detectable change in the Hg site when the Hg stoichiometry changes. However, the

addition of $NADP^+$ induces a structural change at ca. 3.0 Å from the Hg. All three data sets are consistent with Hg-S coordination and an average Hg-S distance of 2.34 Å. This distance is slightly, but probably significantly longer than the distance found previously by Walsh, et al.

Current absorbance and fluorescence emission spectra indicate that the enzyme undergoes a conformational change during its catalytic cycle [8]. The EXAFS data show that this change does not result in detectable changes in the local Hg environment. It is possible, however, that there are detectable changes in the Hg environment when NADH is present. Addition of nicotinamide dinucleotide substrates has been shown to induce a structural change in the *Bacillus* enzyme [9], promoting ligation between a tyrosine and the Cadmium bound derivative. This type of coordination could explain the long range interaction seen in the $NADP^+$ derivative. Experiments are in progress to definitively determine the source of this interaction.

The bond length we observed is ca. 0.04 Å longer than that described by Walsh[7]. This difference is significant since it is larger than the error boundaries (ca. 0.02 Å) inherent in EXAFS analysis. Since the protein can exist in three redox forms, we speculate that these differences may be due to Mercury-Sulfur coordination in different redox forms of the enzyme.[10]

Acknowledgements

This work was supported in part by the NIH (GM-38047 to JPH and GM-38784 to TVO).

References

1. D. M. Ralston and T. V. O'Halloran, *Proc. Natl. Acad. Sci. USA*, **1990**, *87*, 3846-3850.
2. J. G. Wright, H. T. Tsang, J. E. Penner-Hahn, and T. V. O'Halloran, *J. Am. Chem. Soc.*, **1990**, *112*, 2434-2435.
3. I. Persson and F. Zintl, *Inorg. Chim. Acta.*, **1987**, *129*, 21-26.
4. B. V. Cheesman, A. P. Arnold, D. L. Rabenstein, *J. Am. Chem. Soc.*, **1988**, *110*, 6359-6364.
5. D. L. Rehr and A. Zabinsky, *J. Am. Chem. Soc.*, **1991**, *113*, 5135.
6. E. S. Gruff and S. A. Koch, *J. Am. Chem. Soc.*, **1989**, *111*, 8762-8763.
7. M. Moore and C. Walsh, *Biochemistry*, **1989**, *28*, 1183-1194.
8. Miller,S.M.; Massey, V.; Williams, C. H.; Ballou, D.P.; Walsh, C.T. *Biochemistry*, **1991**, *30*, 2600-2612.
9. Schiering, N.; Kabsch, W.; Moore, M. J.; Distefano, M. D.; Walsh, C. T.; Pai, E. F. *Nature*, **1991**, *352*, 168-72
10. S. Miller, unpublished data.

STRUCTURAL AND DYNAMIC STUDIES OF ISOCITRATE DEHYDROGENASE USING LAUE X-RAY CRYSTALLOGRAPHY

Dr. Barry L. Stoddard *, Dr. Michael Soltis **, Dr. Paul Phizackerly **

* Hutchinson Cancer Research Center, Seattle Washington

** Stanford Synchrotron Radiation Laboratory, Stanford California

Using polychromatic crystallographic studies of isocitrate dehydrogenase, we have proposed to use this enzyme as a model system for the investigation and development of various techniques needed in four general areas important for kinetic crystallography:

(1) The triggering of turnover leading to the synchronized accumulation and decay of a transient intermediate species.

(2) Collection of data on a very fast timescale, while simultaneously garnering independent information on the rate and extent of turnover in the crystal, allowing us to relate crystallographic data to specific time points and chemical states in the catalytic pathway of the enzyme.

(3) Coverage of a significant portion of reciprocal space and calculation of accurate difference Fourier syntheses through several different data collection and processing strategies, and the development of alternative media for the recording of crystallographic data.

(4) Evaluation of the quality of structural information derived from polychromatic diffraction techniques with respect to related monochromatic techniques, and to the nature of the mechanistic questions being pursued through crystallographic studies of the enzyme

In the original proposal, we proposed a general experimental protocol which proceeded through three phases: initial studies of IDH in ternary complexes with substrate and cofactor using both Laue and monochromatic methods; structural studies of IDH site-directed mutants and their use in slow turnover experiments involving Laue data collection, and finally kinetic crystallographic analysis of wild type IDH using photolytically triggered single-turnover experiments. After a pair of highly successful runs in February and May-June of 1992, the first phase of this research project has largely been completed and we are set to pursue kinetic Laue experiments on both mutant and wild type enzyme.

Work Completed and Results

At the time that the original proposal for beamtime was submitted, crystals of IDH had never been exposed to the white x-ray beam. Since many crystals which yield reasonable monochromatic diffraction data often are found to possess too high a mosaic spread for the collection of Laue data, a careful survey and analysis of the diffraction characteristics of IDH was performed. Our results show that the crystals consistently diffract to 2.5 Å resolution and beyond, with extremely well ordered patterns. The crystals are quite stable to the x-ray beam both in the bound and unbound (apo) state. Using these initial images, we characterized the unfocused spectrum and the recovery of usable reflections over the entire range of the x-ray spectrum. We have experimented with crystal alignment, film or detector distance, and exposure times at various operative currents for maximum coverage of reciprocal space, recovery of data and maximization of signal to noise ratio. Approximately 22,000 individual spots, which reduce to over 9,000 unique reflections between 10 and 2.5 Å resolution, are recoverable from a single image collected in 50 msec on x-ray film. This represents approximately 1/3 of a complete data set. Using an optimum crystal orientation, approximately 85% of a complete data set may be collected from a single exposure.

Initial structural studies of IDH show that in the absence of substrate, the nicotinamide moiety of NADP is disordered and unobservable. In order to pursue kinetic Laue studies of turnover in IDH, the structure of the active site complexed with substrate and NADP(H) needed to be characterized. Crystals of the enzyme were grown and soaked in the presence of metal species which replace Mg structurally but prevent turnover, allowing studies of pseudo-Michaelis complex structures to proceed.

Data collection of the enzyme complexed to isocitrate, $NADP^+$, and Ca^{++} was performed using both the Laue station at SSRL and an R-axis area detector at Molecular Structure Corporation (Stoddard, et.al., in preparation). Both methods allowed full structural characterization of the active site of the enzyme in a completely bound state. The difference map generated with polychromatic data is of high quality and agrees with the monochromatic map in detail. However, the absence of low resolution terms from polychromatic data sets (caused by harmonic overlap of low resolution reflections) causes the Laue electron density to be more disjointed than the equivalent monochromatic data, producing a lower signal to noise ratio which is seen when contour levels are chosen which allow observation of the fully formed map of the ternary complex.

Collection of initial data showed that correction for the wavelength-dependent x-ray intensity is one of the major sources of error after data collection. We have used data from IDH to examine this effect and to pursue scaling strategies to reduce this effect, and also to design further experiments on IDH using flow cells to present substrate to the crystal in such a manner that data can be collected prior to and after substrate binding. This allows direct measurement of differences in intensities without a strict wavelength correction being performed.

During the second run in May and June, two experiments were performed: First, data was collected from the same crystals on x-ray film and on Fuji imaging plates in order to characterize exposure times, saturation levels on the different media, and techniques for kinetic experiments using both media. Similar patterns to those obtained on x-ray film have been collected from phosphor imaging plate media with exposure times of 1 to 2 milliseconds.

The second set of experiments are our first attempt at a true kinetic experiment. We used a site-directed mutant form of the enzyme (K230M) which is reduced in kcat by 10^5, but still binds isocitrate and NADP with Km's close to wild type. For this mutant, the half-life of the rate-limited oxalosuccinate intermediate in solution at optimal pH (8.0) is approximately 45 seconds. In the crystal at the pH used for crystallization and data collection, this half-life is extended to a minimum of 90 seconds and is probably considerably longer. For an intermediate chemical state with a life-time of this magnitude, direct diffusion is capable of efficiently delivering substrate throughout the crystal and acting as a trigger for catalytic turnover. Theories which account for competing processes of diffusion and chemical reaction (Moffat, 1990; Makinen and Fink, 1977) describe a critical diffusion length below which diffusion effects no longer contribute to a reaction rate for a given kcat/Km. In general, the intermediate of interest must possess a half life of 30 seconds to 10 minutes, depending on absolute kinetic and binding constants and diffusion rates For the K230M mutant, crystals of dimensions 0.5 x 0.4 x 0.2 mm (used in this study) with a solvent content of 65% should allow diffusion-driven reaction initiation.

Using a flow cell, data was collected from a crystal prior to presentation of substrate, and then 90 seconds after presentation of isocitrate, $NADP^+$, and Mg^{++} at concentrations approximately 100 X the Km of the enzyme in high ammonium sulfate. The experiment was performed independently on 8 crystals using the same strategy and time-course each time. Binding of isocitrate and reduction of the nicotinamide could be visualized in the crystal by the production of a yellow color (the crystals and the mother liquor containing $NADP^+$ are colorless, but NADPH produced in the active site after binding and hydride transfer from isocitrate is intensely yellow). Although various technical problems were encountered during presentation of substrate and collection of data, at least two crystals yielded diffraction patterns both before and after substrate binding with appear processable. This work is now in progress and might yield the first Laue result for a catalytic intermediate with a significantly short halflife. This would also be the first actual report of the combination of site-directed mutagenesis and Laue crystallography for structural studies of enzymatic function.

KINETIC CRYSTALLOGRAPHY OF CARBONMONXY MYOGLOBIN

Joel Berendzen, Ilme Schlichting[*], Paul Phizackerley[#] and Michael Soltis[#]

Los Alamos National Laboratory, [*]Max Planck Institut für Medizinische Forschung, and [#]SSRL.

How does the three–dimensional structure of a protein determine its biological activity? The answers to this question must be better determined before full use can be made of modern structural biology.

Proteins are complex molecular machines that perform tasks in precise coordination with other molecules, often simultaneously embodying a range of functions from transport to catalysis to control. Proteins are also flexible. Evidence from techniques such as fluorescence quenching, hydrogen exchange, kinetic studies, molecular dynamics, and X–ray crystallography says that proteins undergo rapid, continual, and significant fluctuations in structure, both in equilibrium and during function. The biological importance of these motions has been established for every protein in which they have been studied.

The details of how protein structure evolves during function constitutes one of the largest gaps in our knowledge of the structure-function relation. Although elements of these structural changes have been inferred through time–resolved spectroscopy, what is needed is precision of the sort that currently only crystallography can provide. Although technically challenging, kinetic X–ray crystallography holds the promise of revealing structural correlates of specific functional features that are shared by a wide class of proteins.

Take, for example, **myoglobin (Mb)**, which stores oxygen for use in the muscles. Mb is the prime model system for physical studies of the relation between molecular structure and biological function. Mb can reversibly bind O_2, CO, NO, and other small ligands at its heme iron. Absorption of a visible photon can cause the ligand to dissociate from the iron, and the subsequent rebinding reaction may be followed. Static X–ray diffraction measurements on Mb has shown that O_2 could not enter or leave the binding site without significant excursions from the average structures.

We are using kinetic X-ray Laue crystallography to attempt to measure the changes in protein structure that take place during the sequence of ligand rebinding after the CO bond is broken by a flash of visible light. Through these results, we hope to address a number of long–standing questions about the relation between protein structure and function in Mb: (*i*) What are the differences in the structures of the various conformational substates? (*ii*) What structural changes correspond to conformational relaxation? Could these changes also correspond to the mechanism of cooperative binding in hemoglobin? (*iii*) What is the structural nature of the solvent process? Specifically, are there well–defined channels in the protein through which the ligand travels? (*iv*) What is the role of the protein in the control of the binding of small molecules? How does the protein adjust barriers to rebinding at the heme and barriers to entrance to the heme pocket?

There are two differences in approach between the present proposal and earlier attempts. The first is the use of advanced kinetic techniques that simplify measurements through cooling the sample to liquid-helium temperatures, lengthening the shortest time scale required, and also by restricting measurement to a narrow range of rates over a wide range in temperature. The second is the use of the Laue method. This allows the experiment to be significantly simplified because three–circle goniometry of the cryogenics is not needed. Furthermore, exposure times may be reduced by perhaps a factor of 10^3 compared with monochromatic methods. Although the Laue method is as old as crystallography itself, it is only the availability of brilliant polychromatic synchrotron radiation in the last few years that has made it practical for use on proteins. Even more recently, Laue diffraction has been extended to kinetic studies on proteins.

In the last year, we have designed and constructed an X-ray diffraction camera for use with Laue diffrac-

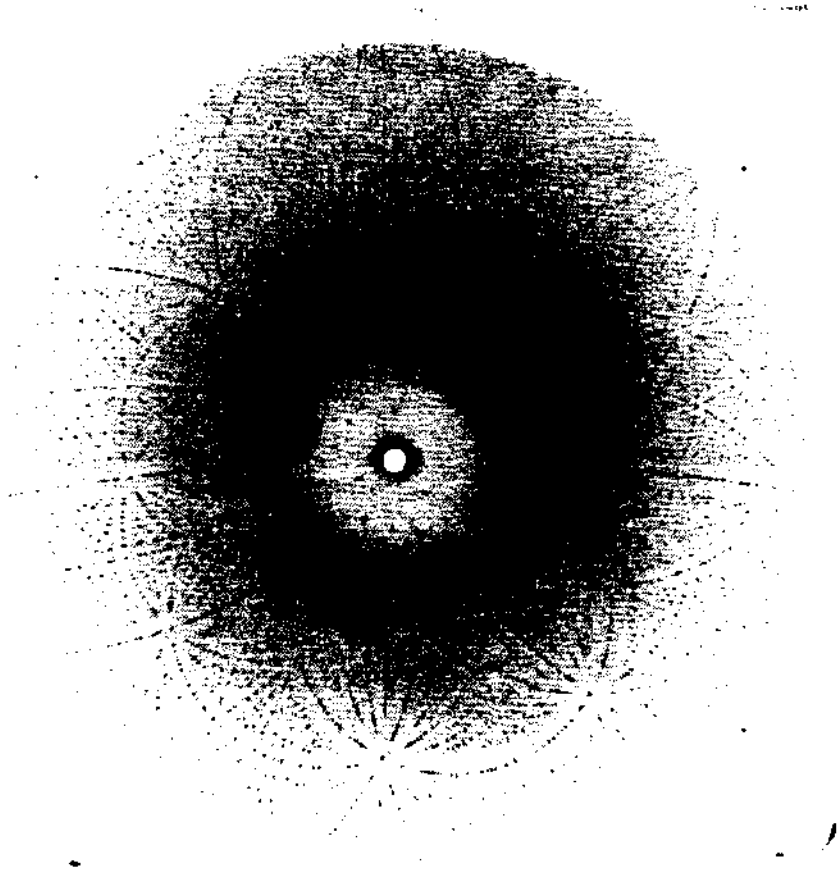

Fig. 1. Laue diffraction pattern from a high-symmetry (P_6) mutant (Asp122→Asn) sperm-whale met-myoglobin at 8 K. Analysis with the Daresbury LAUE software package shows that this crystal diffracts to better than 1.9 Å resolution, a result comparable to that obtained using monochromatic methods at room temperature.

tion at cryogenic temperatures. We tested the camera on beam line 10-2 and at X26-C at the NSLS. In the process, we obtained the first high-quality, high-resolution diffraction patterns of a protein crystal at liquid-helium temperatures. Analysis with the Daresbury LAUE program suite shows that the flash-frozen crystals diffract to better than 1.9 Å. A room-temperature Laue data set taken on a similar crystal at room temperature agreed with a diffractometer data set to an R-factor of 9%. In electron-density maps calculated from room-temperature Laue data set with phases taken from monochromatic data, the water coordinated to the heme may readily be seen. We hope soon to have similar data showing changes in Mb structure after photolysis of carbon monoxide ligands. Greg Petsko and Dagmar Ringe of Brandeis, and Bob Sweet of BNL are collaborators on this project.

LAUE STUDIES OF *RB. SPHAEROIDES* PHOTOSYNTHETIC REACTION CENTER

T.M. McPhillips[1], M.H.B. Stowell[1]; A.J. Chirino[1], J.P. Allen[2]; G. Feher[3], D.C. Rees[1]

[1]Department of Chemistry and Chemical Engineering,
California Institute of Technology, Pasadena CA 91125
[2]Department of Chemistry and Biochemistry,
Arizona State University, Tempe AZ 85287
[3]Department of Physics, University of California,
San Diego, La Jolla CA 92093

Crystals of the *Rb. sphaeroides* photosynthetic reaction center, both of the extensively studied orthorhombic form and of a recently discovered tetragonal form, were tested for suitability for Laue diffraction studies. The orthorhombic crystal form is of space group $P2_12_12_1$ (#19), cell parameters a=138.0 Å, b=77.5 Å,141.8 Å, and Z=4. Monochromatic diffraction patterns collected on these crystals extended to 2.85 Å but were characterized by considerable mosaicity. The tetragonal crystal form is of the space group $P4_32_12$ (#96), with unit cell parameters a=b=141.7 Å, c=281.8 Å, Z=16, and two molecules in the asymmetric unit. Monochromatic data sets collected on these crystals indicate a quality significantly higher than that of the orthorhombic form. Diffraction spots were not only observed well past 3 Å but were characterized by very low average spot widths, indicating relatively low crystal mosaicity.

Experimental station 10-2 was used for all experiments in an unfocused white radiation mode. A single lysozyme crystal (space group $P4_32_12$ (#96), a=79.1 Å, c=37.9 Å) was used as a control. Seven Laue photographs were taken on the lysozyme crystal. X-ray film was used to record the diffraction patterns in each case. Four different orientations of the crystal were used and effects of varying the crystal to film distance and film development times observed. The highest signal to noise was observed at a distance of 15 cm and a full dark room development time of 120 s. At 10 cm, the background was significantly higher and proper development of the photographs difficult. Exposure times of 40 ms were used for each shot.

The quality of the diffraction patterns observed with the lysozyme crystal was excellent. The first exposure is characterized by nearly circular spots well resolved from each other. Streaks are observed only near the center of the photograph. The quality of the spots steadily decreased with each exposure; the seventh photograph is characterized by spots that are either streaked or twinned.

The orthorhombic RC crystals were analyzed next. Two Laue shots were taken of the first crystal at a crystal to film distance of 15 cm and exposure times of 40 ms. No single spots were observed in the developed films; long arcs replaced diffraction spots in the Laue pattern. A second crystal was mounted on the goniometer and the effects of inserting 8 layers of Reynolds 667 Aluminum Foil in the beam before the collimator observed. Cutting off the long wavelengths in this way did not improve the Laue patterns; nor did reducing the exposure time to 5 ms. While fewer arcs were observed in these cases, no actual spots were ever seen for the orthorhombic RC crystals. It was concluded that the inherent mosaicities of these crystals precluded their usefulness in time-resolved crystallography.

Subsequent analysis of the tetragonal RC crystals yielded results that were more encouraging. While the first crystal exposed showed streaking similar to the orthorhombic Laue patterns, subsequent crystals displayed clear diffraction spots. A crystal to film distance of 20 cm was used for each shot. The best diffraction pattern obtained was from the first exposure of the second crystal used; a very clear pattern of spots is recorded by this photo. While the spot quality is not as high as that characterizing the first lysozyme shots, only minimal streaking is observed. The exposure time used for this shot was 40 ms; exposures of 10 ms were clearly too short for these crystals (using film) and longer exposures led to significant crystal damage. It is believed that with the shorter exposures needed for Laue data collection with imaging plates, interpretable Laue diffraction patterns may be obtained from tetragonal RC crystals.

The tetragonal crystals hold more promise than sufficiently clear diffraction patterns. With two molecules in the asymmetric unit, real-space averaging of maps calculated from Laue data should be possible. The improvements in the averages maps should make up for some of the quality lost to incomplete data sets and the low-resolution hole.

CRYSTALLOGRAPHIC STRUCTURE DETERMINATION OF SULFITE REDUCTASE HEMOPROTEIN USING MULTIWAVELENGTH ANOMALOUS DIFFRACTION (MAD)

Brian R. Crane, Duncan E. McRee, Henry Bellamy and Elizabeth D. Getzoff
Department of Molecular Biology
The Scripps Research Institute
La Jolla, California 92037

Introduction

The reduction of sulfite to sulfide is a critical step in the biosynthetic assimilation of sulfur. To gain insight into the enzymatic mechanism of this reaction we have undertaken crystallographic characterization of the *E.coli* sulfite reductase hemoprotein subunit (SiRHP). When provided with artificial electron donors SiRHP catalyzes the concerted six electron reduction of sulfite to sulfide [1]. The enzyme is also capable of reducing nitrite to ammonia and has similarities in size, sequence and cofactors with the nitrite reductases found in green plants. This 64 kD protein contains two prosthetic groups: a siroheme, and an Fe_4S_4 cluster. These co-factors participate intimately in electron transfer to the substrate. Although many spectroscopic studies have focused on these prosthetic groups, their electronic linkage and chemical association is contingent on crystallographic confirmation [2]. SiRHP can potentially serve as a model for understanding the novel multielectron reductive chemistry of low molecular weight inorganic compounds in biology. Derivatization of SiRHP crystals with heavy atom reagents has been difficult, resulting in less than adequate phasing information. In order to augment the accuracy of the structure factor phases we have relied on wavelength dependent anomalous scattering effects caused by the native iron atoms coupled with the ability to tune synchrotron radiation on the iron absorption edge. Sulfite reductase hemoprotein represents one of the largest systems to date studied by mutiwavelength anomalous diffraction.

Experimental

Crystals of SiRHP grow de novo from a vapor diffusion setup where the drop consists of 50 mM potassium phosphate pH 7.7, 7mg/mL of protein and is 12% PEG 8K [3]. A combination of micro and macroseeding is used to grow single crystals (1.3 mm X 0.20 mm X 0.15 mm). Multiwavelength diffraction data was collected at the Stanford Synchrotron Research Laboratory beam line 1-5AD on a Xuong/Hamlin area detector. Three wavelengths were chosen to maximize the measurement of both the anomalous and dispersive scattering contributions of hemoprotein iron (1.5418 Å, 1.7374 Å and 1.7412 Å; $d\lambda/\lambda = 10^{-4}$) [4]. Wavelength dependent anomalous scattering terms were determined specifically for SiRHP crystals by X-ray fluorescence spectroscopy. Data was collected on five crystals at 4 °C over a period of three weeks. An area detector frame was collected at each of the three wavelengths before progressing through reciprocal space. This strategy was chosen to limit the elapsed time for collecting all measurements needed to phase one reflection. The crystal space group symmetry ($P2_12_12_1$) allowed the majority of the data to be collected with a mirror plane across the detector face, thereby facilitating the concomitant measurement of Bijvoet pairs. The oscillation speed of the crystal was varied from frame to frame to account for saturation of the detector by intense reflections and to correct for coincidence loss. The data is at least 90% complete to 2.5 Å at all three wavelengths (Table 1.).

Data Analysis and Results

After integration of the reflection intensities, the data at each wavelength was separately binned by 5 degree increments in oscillation angle, and then put on an overall scale. Anisotropic local scaling was used to reduce noise in the Bijvoet difference anomalous signal. A similar procedure was followed to scale equivalent reflections taken at the different wavelengths to one another. A Bijvoet difference cross Fourier was calculated using Bijvoet differences from the 1.7374 Å data set and phases determined from previous multiple isomorphous replacement experiments. The initial iron positions were taken from the peaks in this map. For reflections that had four or more independent observations a least squares approach (MADLSQ) was used to extract phase information and the normal scattering contribution of the iron atoms (FA terms) [5]. The initial iron positions were refined against the MADLSQ calculated FA values while fixing the cluster as a rigid body. The orientation of the iron sulfur cluster that minimized the

lack of closure of the MAD phased reflections was found by a figure of merit based rotational search. The refined iron positions were then used to calculate FA values for reflections having only three independent observations relevant for phasing. With calculated FA terms , these reflections could be phased by a least squares treatment analagous to MADLSQ. The new MAD determined phases, when combined probabilistically with existing heavy atom phases [6], resulted in considerably improved electron density maps. Elements of secondary structure, the direction of the polypeptide chain and the architecture of the active site are now more clearly discernible.

Acknowledgements

We thank Paul Phizackerly of SSRL for his assistance in analyzing EXAFS data used to select the appropriate wavelengths and scattering factors for the MAD experiment. The crystals of SiRHP were grown from *E. coli* recombinant protein provided by Dr. L.M. Siegel of the Duke University Medical Center. This work is supported by NIH grant 37684.

References

1. Siegel, L.M., Rueger, D.C., Barber, M.J., Krueger, R.J., Orme-Johnson, N.R. and Orme-Johnson, W.H. (1982) *J. Biol. Chem.*, **257**, 6343-6350.

2. McRee, D.E., Richardson, D.C., Richardson, J.S. and Siegel, L.M. (1986) *J. Biol. Chem.*, **261**, 10277-10281.

3. McRee, D.E., and Richardson, D.C. (1982) *J. Mol. Biol.*, **154**, 179-180.

4. Hendrickson, W.A., Smith, J.L., and Sheriff, S., (1985) *Meth. Enzymol.*, **115**, 41-55.

5. Hendrickson, W.A., Smith J.L., Phizackerly, R.P., Merrit, E. (1988) *Proteins*, **4**, 77-88.

6. Pähler, A., Smith, J.L., and Hendrickson, W.A. (1990) *Acta Cryst*, **A46**, 537-540.

Table 1. Statistics for Sulfite Reductase Multiwavelength Data Reduction

Wavelength Å	% Complete (Total)	% Complete (2.7-2.5Å)	R (Total)	R (2.7-2.5Å)	% Data $I > 5\sigma$	$\langle I/\sigma I \rangle$ (at 2.5Å)
1.5418	93.0	88.0	6.4	11.0	84.7	5.5
1.7374	91.4	84.6	7.3	10.1	83.3	4.5
1.7412	90.0	82.8	5.9	10.6	85.4	5.2

$$R = \sum(\mathrm{abs}(\langle I \rangle - I_{obs}))/\sum(\langle I \rangle)$$

X-RAY ABSORPTION SPECTROSCOPY STUDIES OF MANGANESE REDOX ENZYMES

James E. Penner-Hahn, Pamela J. Riggs and David Tierney
Department of Chemistry
University of Michgian

Rui Mei and Charles F. Yocum
Department of Biology
University of Michigan

Martha Ludwig and Myoung Soo Lah
Biophysical Research Division and Department of Biological Chemistry
University of Michigan

The goal of this project is to characterize the local structural environments of the Mn in Mn redox proteins. The principal focus is on the mononuclear Mn site in Mn superoxide dismutase, the binuclear Mn site in Mn catalase, and the tetranuclear Mn site in the photosynthetic oxygen complex. Recent results for the superoxide dismutase and for the oxygen evolving complex are summarized here.

The Photosynthetic Oxygen Evolving Complex

Photosynthetic oxygen evolution requires Ca^{2+}, Cl^-, and a multinuclear Mn cluster. The Mn cluster cycles through 5 kinetically resolvable intermediates (S_0, S_1, S_2, S_3 and S_4) as it accumulates oxidizing equivalents for the oxidation of water to dioxygen.[1] Although it is generally[2] agreed that the cluster contains 4 Mn, the nuclearity of this cluster remains unclear. X-ray Absorption Spectroscopy can address two particularly important questions pertaining to this area of photosynthesis research: 1) Through which oxidation states does the Mn cluster cycle? 2) What is the geometry of the cluster in the various S states? We have focused our XANES and EXAFS studies on reduced and chemically substituted derivatives of the Mn cluster to gain insight on its structure in the native state.

We have recently shown that the Mn cluster can be reduced in the dark using either NH_2OH or hydroquinone.[3,4,5] Moreover, this reduction can be completely reversed by illuminating the sample with room light for several minutes (see Figure 1). These reduced states could represent intermediates in the poorly understood process of photoactivation in which destroyed samples reincorporate exogenous Mn^{2+}, ultimately reforming an oxidzed cluster.

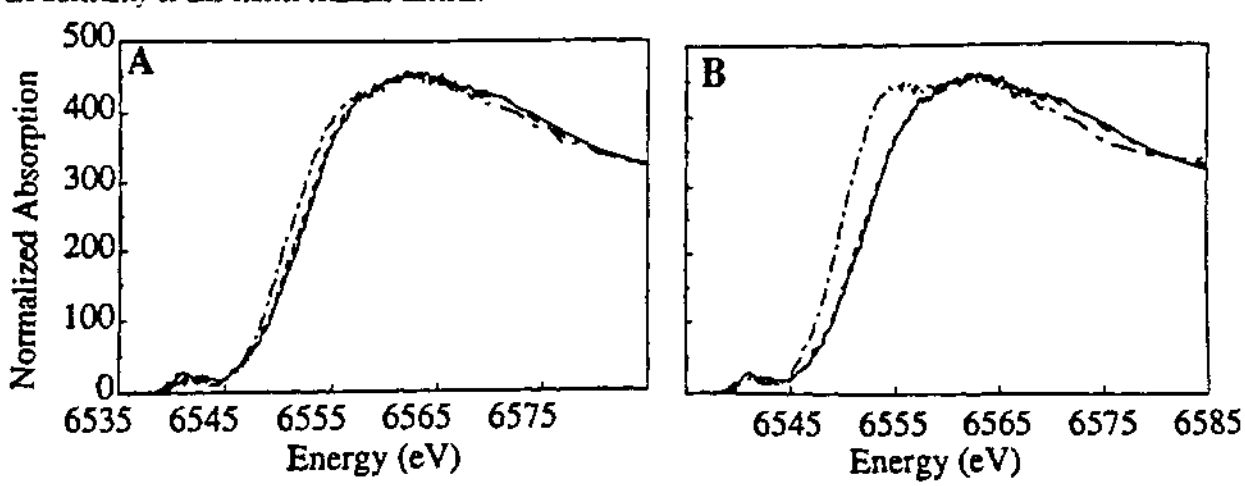

Figure 1: Normalized OEC XANES spectra. Solid = S_1 control; Dashed = reduced sample; Dotted-Dashed line = reduced sample followed by illumination and dark adaption. *Left*). NH_2OH (100μM, 3 minutes) reduced sample. *Right*). Hydroquinone (200μM, 30 minutes) reduced sample.

Figure 2 shows the effect of hydroquinone reduction and subsequent illumination and dark adaption. A new feature at circa 2.1Å appears that corresponds to longer Mn-O/N distances consistent with the presence of Mn(II). The amplitude of the 2.7Å peak is reduced to roughly one half of its size in the S_1 state. Interestingly, the 3.3Å peak is no longer discernible above the noise level.

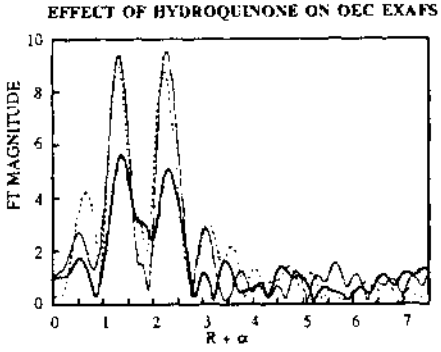

Figure 2 Effect of Hydroquinone Reduction on OEC EXAFS. Thin solid line = control S_1 state; bold solid line = reduced (200μM, 30 minutes); dashed line = reduced, illuminated, then dark adapted.

There is a Mn(II) six line EPR signal associated with this hydroquinone sample as well. The Mn giving rise to this signal cannot be removed with EDTA nor does it give rise to an NMR relaxation enhancement.[4] Even though the OEC is less reduced when treated with NH_2OH then when treated with hydroquinone (as judged by the XANES), NH_2OH reduced samples are very sensitive to EDTA addition. Mei and Yocum have interpreted this information as evidence for two distinct Mn sites. One site is quickly reduced by NH_2OH but not by hydroquinone. The other site is hydroquinone accessible and gives rise to a slower reduction of circa 2 Mn (determined quantitatively through XANES fits and EPR six line magnitude). NH_2OH will eventually attack this second site causing the release of 3 Mn. This can be seen in Figure 3 which shows the effect of increased NH_2OH concentration or incubation time. By varying these conditions, one can obtain a XANES spectra for a NH_2OH reduced sample that is the edge for a hydroquinone reduced sample. However, a NH_2OH treated sample that is reduced to this extent is inactive whereas the hydroquinone sample is still 80% active. Finally, Mei and Yocum have demonstrated a dramatic synergistic effect with these two reductants. A hydroquinone reduced sample treated with a normally non-lethal quantity of NH_2OH (20 μM) is quickly and irreversibly reduced.[4]

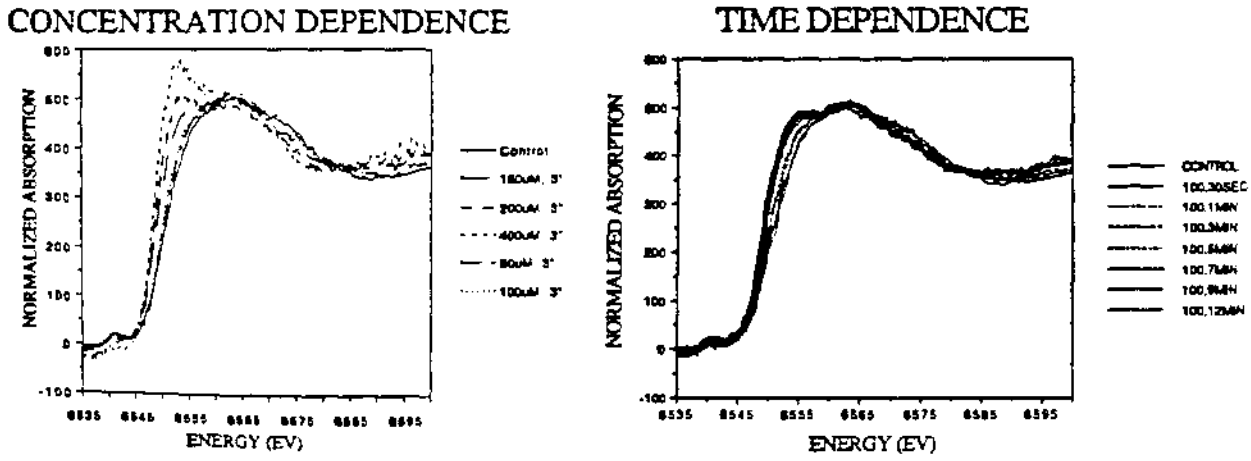

Figure 3 *Left.* Hydroxylamine Reduction at varying concentrations for 3 minutes *Right.* Hydroxylamine reduction at varying times at 100μM.

In light of these reactivity and structural studies, it is possible to speculate about the structure of the native Mn site. It must be organized in such a fashion as to either geographically or chemically separate two groups of Mn. The appearance of circa two Mn(II) in the hydroquinone reduced sample and the disappearance of half but not all of the 2.7Å features suggests that one 2.7Å dimer remains intact while another is reduced by hydroquinone. The disappearance of the 3.3Å feature could mean that the dimers are separated by 3.3Å in the native structure. This argument is strenghtened by our recent Ca substitution studies in which there is no observable change in the 3.3Å feature when Ca is replaced by Sr or Dy. Whether or not the original structure is a true dimer of dimers or an asymmetric tetranuclear structure with chemically distinct environments is still not unambiguously determined.

Superoxide Dismutase

Superoxide dismutase (SOD) catalyzes the disproportionation of superoxide to hydrogen peroxide and dioxygen. Three different forms of SOD are known; one prokaryotic and two eukaryotic forms. The prokaryotic form contains one copper and one zinc per monomer, while the two eukaryotic forms contain either one iron or one manganese[6-8]. This work is concerned with the two bacterial forms.

Azide is an inhibitor of SOD and is believed to bind analogously to superoxide. The structures of both the native enzyme and the azide derivative of iron SOD have been determined crystallographically by Ludwig, et al.[9], and Petsko, et al.[10]. The Ludwig structure shows a trigonal bipyramidal iron ligated by an equatorial plane of two histidines and one aspartate, with axially coordinated solvent and histidine. The Petsko structure shows a distorted tetrahedral iron, with little or no evidence for the inclusion of solvent. Neither structure shows a loss of protein ligands upon binding of azide. Two different structural schemes have been proposed for the azide complex. Stoddard, et. al. have put forth a five coordinate azide complex[11], while Ludwig, et. al. suggest a six coordinate iron. Both models suggest that there is no loss of solvent when azide binds[12].

EXAFS and XANES have been employed to distinguish between the proposed structural schemes for native Fe(III)SOD, and for its corresponding azide complex. The intensity of the 1s→3d transition in iron complexes and proteins has been shown to be directly correlated to coordination number[13]. The XANES spectra indicate a five coordinate environment for the native enzyme, going to six coordinate upon binding of azide (fig 1). Fits to the EXAFS also indicate a change in coordination from five to six (see Table 1). Fits were generated using theoretical models, with a scale factor of 0.9 and ΔE_0 of 8.8. Two parameters were allowed to vary (R and σ) per shell. The optimal values of R and σ were determined for all reasonable values of CN. Similar experiments are in progress for the Mn form of SOD.

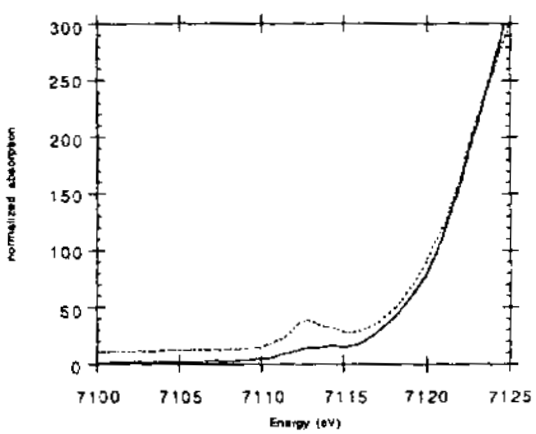

Figure 4 Expansion of the 1s→3d region of the XANES spectra for native FeSOD (dashed) and its azide complex (solid).

Table 1 Fits to protein EXAFS data for FeSOD and its azide complex.

Sample	CN	R (Å)	$\sigma \cdot 10^{-3}$	1s→3d area
native	5	2.00	11.0	14.8
azide complex	6	2.08	7.7	7.0

Acknowledgements

This work has been supported in part by grants from the NIH (GM-38047 to JEPH, GM-16429 to ML) and from the USDA, Competitive Research Grants Office, Photosynthesis Program (88-37130-3546 to CFY)

References

1. Kok, B.; Forbush, B.; McGloin, M. *Photochem. Photobiol.* **1970**, *11*, 457.
2. For a recent review, see Debus, R. *Biochim. Biophys. Acta* **1992**, *1102*, 269-352.
3. Mei, R.; Yocum, C. *Biochemistry* **1991**, *30*, 7836-7842.
4. Mei, R.; Yocum, C. *Biochemistry* **1992**, *31*, 8449-8454.
5. Riggs, P.; Mei, R.; Yocum, C.; Penner-Hahn, J. *J. Am. Chem. Soc.* **1992**, *114*, 10650-10651.
6. Michelson, A.M.; McCord, J.M.; Fridovich, I., eds. *Superoxide and Superoxide Dismutases*, 1977, Academic, New York.
7. Autor, A.P., J. Biol. Chem., **1982**, 257, 2713.
8. Sato, S.; Nakasawa, K., J. Biochem. (Tokyo), **1978**, 83, 1165.
9. Stallings, W.C.; Powers, T. B.; Pattridge, K.A.; Fee, J.A.; Ludwig, M.L., *Proc. Natl. Acad. Sci. USA*, **1983**, 80,3884.
10. Ringe, D.; Petsko, G.A.; Yamakura, F.; Suzuki, K.; Ohmori, D.; *Proc. Natl. Acad. Sci. USA*, **1983**, 80, 3879.
11. Stoddard, B.L.; Howell, P.L.; Ringe, D.; Petsko, G.A., *Biochemistry*, **1990**, 29, 8885.
12. Stallings, W.C.; Bull, C.; Fee, J.A.; Lah, M.S.; Ludwig, M.L.(1992), *Molecular Biology of Free Radical Scavenging Systems* (Scandalios, J.G., ed.), Cold Spring Harbor Lab Press.
13. Roe, A.L.; Schneider, D.J.; Mayer, R.J.; Pyrz, J.W.; Widom, J.; Que, L., Jr., *J. Am. Chem. Soc.*, **1984**, 106, 1676.

Conformational Changes in Aspartate Transcarbamylase Catalytic Subunit Studied with Small Angle X-Ray Scattering (SAXS)

Eric R. Johnson, Hirotsugu Tsuruta†, Bin-Bing Zhou*, H. K. Schachman**
** Department of Molecular and Cell Biology, University of California, Berkeley, CA*
† Stanford Synchrotron Radiation Laboratory, Stanford, CA.

We have collected small-angle x-ray scattering (SAXS) data on the catalytic subunit (CSU) of aspartate transcarbamylase (ATCase) from *E. coli*. Although substantial structural information exists for the holoenzyme form of ATCase, structural investigations of the isolated catalytic subunits have been few. We are interested in the relationship between substrate binding and conformational changes which may be important in understanding the functional mechanisms of catalysis. Our results so far are promising since we have observed a significant contraction of the trimeric catalytic subunits in the presence of a bisubstrate analog. This is in contrast to the net expansion which occurs in the holoenzyme form of ATCase under similar conditions. The results illustrate the complexity of conformational rearrangements which occur upon ligand binding to this regulatory enzyme.

Small-angle x-ray scattering study was performed on the wild-type and one mutant catalytic subunit in the presence of the bisubstrate analog, N-phosphonacetyl-L-aspartate (PALA). All experiments were conducted in 30mM Tris-acetate pH 8.2, 2mM beta-mercaptoethanol, 0.5mM EDTA. Satisfactory scattering data were obtained for the wild-type catalytic subunit in the concentration range of 1.0-14 mg/ml. The radius of gyration (R_G) for the unliganded catalytic subunit extrapolated to zero concentration was 34.8 Å, and R_G decreased to 32.4 Å upon saturation with PALA.

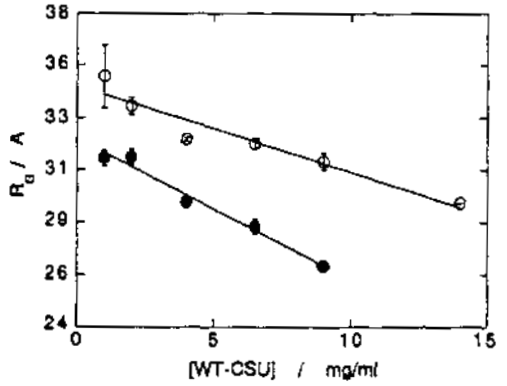

Radii of gyration of wild-type CSU in the absence (open circle) and in the presence (solid circle) of PALA.

Experiments were also performed on a defective, site-specific mutant catalytic subunit in which the normally occurring lysine residue at position 164 was changed to glutamic acid (Lys 164 -> Glu). This mutant has a greater than 60-fold higher K_m(aspartate) than that of wild-type. Since lysine 164 is not believed to participate in catalysis, the basis of inactivity of this mutant has been unclear. At an enzyme concentration of 2.5 mg/ml, the Lys 164 -> Glu mutant CSU shows little to no change in R_G upon saturation with PALA. R_G in the absence of PALA was 34.1 Å while R_G in the presence of PALA was 33.8 Å. Sedimentation velocity studies with wild-type and Lys 164 -> Glu catalytic subunit are in qualitative agreement with the x-ray scattering data. The sedimentation coefficient of the wild-type catalytic subunit increases by 1.5% upon saturation with PALA, while the Lys 164 -> Glu mutant shows no appreciable change in sedimentation coefficient under identical conditions.

The PALA-promoted decrease in R_G may reflect a contraction of the subunit which is important to the enzymatic mechanism. The lack of significant change in R_G for the Lys 164 -> Glu mutant subunit is consistent with such a conclusion. We are currently in the process of unravelling the relationship of the individual substrates, carbamoyl phosphate and aspartate, to this structural change. Furthermore, we are also performing analogous experiments with structurally similar transcarbamylases isolated from organisms other than *E. coli*.

Acknowledgements

The measurements were performed at SSRL which is supported by the Department of Energy, Office of Basic Energy Sciences, and in part by the NIH Biomedical Research Technology Program and by the DOE Office of Health and Environmental Research. E.R.J. was partially funded from a USPHS Molecular Biophysics Training Grant from the NIH.

The Structure of Theiler's Virus and Influenza Virus Neuraminidase

Ming Luo
University of Alabama at Birmingham

My research has been focused on studies of the atomic structure of intact viruses and isolated viral proteins by X-ray crystallography. Two of the major projects highlight the achievement in last year where X-ray diffraction data collected at SSRL were used for the experiments.

The first part is the atomic structure of Theiler's murine encephalomyelitis virus (TMEV). TMEV belongs to the picornavirus family and can be further divided into two subgroups. One is composed of highly virulent strains (e.g. FA and GDVII), which causes acute polioencephalomyelitis in mice, and the other consists of less virulent strains (e.g. BeAn and DA), which causes demyelination in mice after the establishment of a persistent infection. The less virulent strains have be used as an animal model to study human demyelination diseases such as multiple sclerosis. It has been shown that the virulency is related to the capsid protein, probably related to the mode of the virion attachment to the host receptor, host immune response and/or the capsid stability. The three dimensional structure of TMEV at 3.0 Å resolution reported by Luo et al. revealed the structural basis for the neural virulence of TMEV. Potential sites for virus attachment to the host receptor and dominant immunogen determinants distinguishing the two subgroups were mapped on the capsid. The result helps us a great deal in understanding the host receptor recognition, virion stability, and viral pathogenesis of TMEV. Our focus in last year's experiment was to determine the structure of a highly virulent TMEV strain, GDVII. Our group has been successful to crystallize the GDVII virus and the crystals were brought to SSRL to collect X-ray diffraction data. The data collection was performed at Station X7 using X-rays of 1.08 Å wavelength. The diffraction patterns were recorded on the newly installed image plate system made by Mar research. The image plate system is an additional factor which helped us in collecting high quality diffraction data at SSRL. A total of about 50 useful images were processed and the space group of the crystals was determined as C2, a=575.4Å, b=323.7Å, c=558.4Å, β=108.5°. There is a whole virus particle in the asymmetric unit, which results in a 60 fold noncrystallographic averaging in phase determination by the molecular replacement method. About 50% unique data were collected to 3.5Å resolution and the Rmerge was 11.5% for data with $I/\sigma>2.0$. A locked rotation function was calculated using data to 4.0 Å resolution and the virus orientation was clearly identified in the unit cell. Work is now continued on the translation of the virus particles in the unit cell. Once the position of the virus particles is known, phases could be first derived from the BeAn coordinates and improved by electron density averaging over the 60 fold noncrystallographic symmetry. The final structure of GDVII will reveal the differences between the highly-virulent group and the persistent group on the capsid. We shall learn more about the relationship between virus infection and demyelination and persistence infection.

The other major area of my research is the structure of influenza virus neuraminidase (NA). NA is one of the two surface antigens on influenza virus envelope and undergoes frequent antigenic

shifts (subtype replacement, only in type A influenza virus) and antigenic drift (accumulation of point mutations). This causes difficulties in using the surface glycoproteins as vaccines because it is impossible to predict what type of influenza virus would appear in the next epidemic and how much antigenic change. If a specific inhibitor to NA's sialylase activity could be found, however, it will serve as an effective anti-viral drug against all strains of influenza virus, because the active site of NA to which the inhibitor shall bind is highly conserved although the antigenic structure on the surface keeps changing. We have started rational designs of novel inhibitors based on the atomic structure of influenza virus neuraminidase. Our recent determination of the structure of B/Lee/40 neuraminidase complexed with sialic acid showed that an oxocarbonium ion was stabilized in the NA active site and proposed a completely new enzyme mechanism of this sialyl hydrolase in which the driving force of the enzyme catalyzed reaction is the stabilization of the intermediate in transition state rather than a nucleophile or a proton donor found in other enzyme structures. This piece of work not only proposed a logical mechanism which suits all the enzymatic and mutagenesis observations on influenza virus neuraminidase, but also provided new guide lines for design of anti-influenza drugs. In order to further confirmed the structural observation made at 2.4 Å resolution, diffraction data to 1.6Å resolution were collected at SSRL last year. The high resolution data will let us make precise measurement of the bond lengths and bond angles of the carbonium stabilized by the neuraminidase. A more detailed picture of the enzyme mechanism will be drawn when the refinement of high resolution structure is complete. In addition, several series of NA inhibitors have been designed based on the new mechanism and the atomic structure of NA, and synthesis is in progress. The high resolution structure will allow us to carry out more accurate energetic calculations in our design process.

CRYSTALLOGRAPHIC ANALYSIS OF MOLYBDENUM AND TUNGSTEN CONTAINING PROTEINS

D.C. Rees, M.K. Chan, J. Kim, M.M. Georgiadis
California Institute of Technology
Pasadena, CA 91125

NITROGENASE

The biological conversion of dinitrogen to ammonia is catalyzed by the nitrogenase enzyme system found in nitrogen-fixing bacteria. The conventional nitrogenase consists of two component proteins, the iron (Fe-) protein and the molybdenum-iron (MoFe-) protein, that together mediate the ATP dependent reduction of substrates such as dinitrogen and H^+ to products. Substrate reduction by nitrogenase involves three basic types of reactions: the reduction of Fe-protein by electron carriers such as flavodoxin; the ATP dependent transfer of single electrons from Fe-protein to MoFe-protein, with a minimal stoichiometry of two molecules of MgATP hydrolyzed per electron transferred; and electron and proton transfer to the substrate, which is almost certainly bound to the FeMo-cofactor of MoFe-protein. Because the active site of nitrogenase is provided by the MoFe-protein, the redox centers of this protein have attracted considerable attention. We have crystallographically determined the structures of the nitrogenase MoFe-protein and Fe-protein isolated from *A. vinelandii* (abbreviated Av1 and Av2, respectively), to determine the polypeptide and cofactor structures, and to provide a structural basis to address questions concerning the substrate reduction mechanism and assembly of nitrogenase.

Details of the Av1 and Av2 crystal structure determinations are described in Kim and Rees (1992a,b), Chan, Kim and Rees (1993), and Georgiadis,*et al* (1992)). Essentially, the two structures were solved by multiple isomorphous replacement and non-crystallographic symmetry averaging both within, and between, three different crystal forms. The averaging of electron density maps between three crystal forms was an essential aspect of this process. The Av1 and Av2 structures have been refined to current R-factors of 0.202 and 0.18 at 2.2Å and 2.9Å resolutions, respectively.

Synchrotron radiation data collection at SSRL has been an important component of the structure determinations, both for the Fe-protein structure at 2.9Å resolution and refinement of the MoFe-protein at 2.2Å resolution. During the past year, Av1 diffraction data was collected from two crystals at SSRL. The MAR imaging plate images were processed with MOSFLM and CCP4, yielding a final set of 95,078 reflections (90% complete to 2.2Å resolution) that were reduced from a total of 258,519 observations with an R-merge of 0.136. Data collection using the MAR Research imaging plate at SSRL permitted high resolution data acquisition that could not have been collected on conventional sources, and this has been invaluable for characterizing the detailed geometry of the MoFe-protein structure.

The MoFe-protein is an $\alpha_2\beta_2$ tetramer of total molecular weight ~240 kD, which contains two types of metal centers, termed the FeMo-cofactor and the P-cluster pair. The crystallographic analysis demonstrated that α and β subunits of the MoFe-protein exhibit similar polypeptide folds, consisting of three domains of the α/β type, with some extra helices. In each subunit, there is a cleft formed between the three domains; the FeMo-cofactor occupies the bottom of this cleft in the α subunit. The $\alpha_2\beta_2$ tetramer may be considered to be composed of a pair of $\alpha\beta$ dimers that does not exhibit overall 222 symmetry. Extensive contacts occur between the α and β subunits in an $\alpha\beta$ dimer; this is especially apparent in the location of the buried P-cluster pair at the $\alpha\beta$ dimer interface. The α and β subunits in this dimer are approximately related by a twofold axis that passes through the P-cluster pair. The tetramer twofold axis that relates pairs of α dimers is surrounded by α-helices from the β subunits that create a channel of ~10Å diameter.

The FeMo-cofactor consists of a pair of clusters of composition 4Fe:3S and 1Mo:3Fe:3S that are bridged by three non-protein ligands (Figure 1).

The Fe-Fe separation distance between bridged iron sites is ~2.5Å, whereas the separation distance is ~3.8Å between nonbridged iron sites on different cluster fragments. Based on electron density values, two of the bridging ligands are assigned as sulfur, while the third ligand (designated "Y") has lower electron density and may be either a well ordered O/N species, or a less well ordered S group. Homocitrate, which is an essential component of the FeMo-cofactor, coordinates the Mo through both hydroxyl and carboxyl groups. The entire cluster is coordinated to the α subunit through Cys α275 and His α442. An unusual feature of the FeMo-cofactor is the apparent trigonal coordination geometry of the six Fe that are bridged between the two cluster fragments. Although there may be some Fe--Fe bonding interactions that occur between these bridged Fe sites, neither protein groups nor solvent molecules that might possibly serve as fourth ligands have been observed within coordinating distance of any of these irons. The unusual coordination geometry of these irons may provide the site for substrate binding to FeMo-cofactor.

The P-cluster pair (Figure 2) contains two 4Fe:4S clusters that are bridged by an unusual disulfide bridge betwen two cluster sulfurs and two cysteine thiol ligands (from residues α88 and β95), with the four remaining Fe liganded by singly coordinating cysteine thiols (from residues α62, α154, β70 and β153). The coordination environment of Fe6 and Fe2 are distorted from ideal tetrahedral environment due to interactions with Ser β188 and the mainchain of Gly α185, respectively.

ALDEHYDE OXIDOREDUCTASE (AOR)

The tungsten containing protein aldehyde oxidoreductase (AOR) has been isolated from the extreme hyperthermophile *Pyrococcus furiosus*. AOR is believed to participate in a novel glycolytic pathway in this organism. The tungsten is associated with the protein as a tungstopterin that is analogous to the molybdenum-cofactor found in xanthine oxidase and other molybdoenzymes (except for nitrogenase). Several Fe:S clusters are also present in the protein. Crystals of this protein have been obtained (space group $P2_12_12_1$, a=107.9Å, b=80.5Å, c=158.9Å, with two monomers in the asymmetric unit) that diffract to at least 2.2Å resolution. In August, we collected 3Å resolution data at SSRL on the MAR imaging plate detector. A total of 22541 unique reflections were observed, reduced from a total number of 86751 reflections measured, with an R-merge of 0.086. At the wavelength of data collection, 1.08Å, $\Delta f''$ for the tungsten site should be greater than the Fe:S sites, while the opposite situation holds at 1.54Å resolution. Inspection of anomalous difference Patterson and Fourier maps at 5Å resolution have provided a tenative identification for these sites. Currently, efforts are underway to calculate higher resolution maps suitable for model building and refinement.

REFERENCES ACKNOWLEDGING SSRL SUPPORT

Georgiadis, M.M., Komiya, H., Chakrabarti, P., Woo, P., Kornuc, J.J., Rees, D.C. (1992) "Crystallographic Structure of the Nitrogenase Iron Protien from *Azotobacter vinelandii*" *Science* **257**, 1653-1659.

Chan, M.K., Kim, J. and Rees, D.C. (1993) "The Nitrogenase FeMo-cofactor and P-cluster pair: 2.2Å Resolution Structures" submitted.

ADDITIONAL REFERENCES

Kim, J. and Rees, D.C. (1992) "Structural Models for the Metal Centers in the Nitrogenase Molybdenum-Iron Protein" *Science* **257**, 1677-1682.

Kim, J. and Rees, D.C. (1992) "Crystallographic Structure and Functional Implications of the Nitrogenase Molybdenum-Iron Protein from *Azotobacter vinelandii*" *Nature* **360**, 553-560.

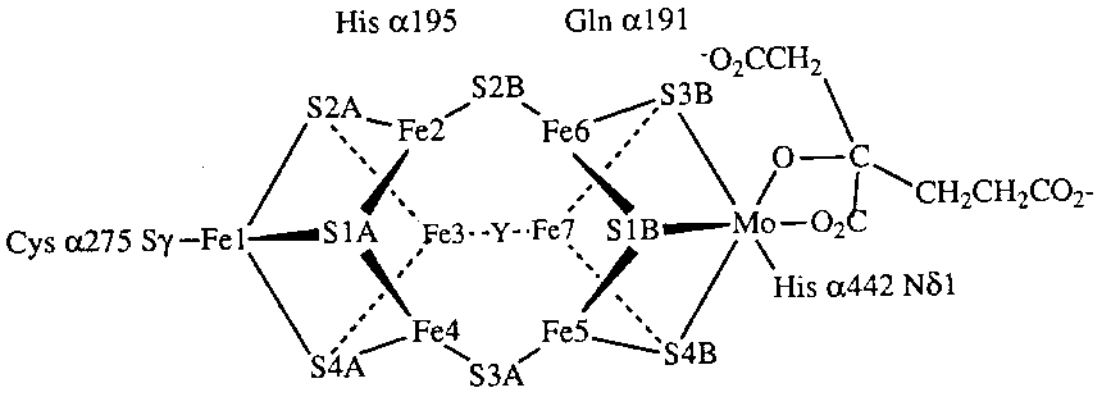

Figure 1. Structure of the FeMo-cofactor.

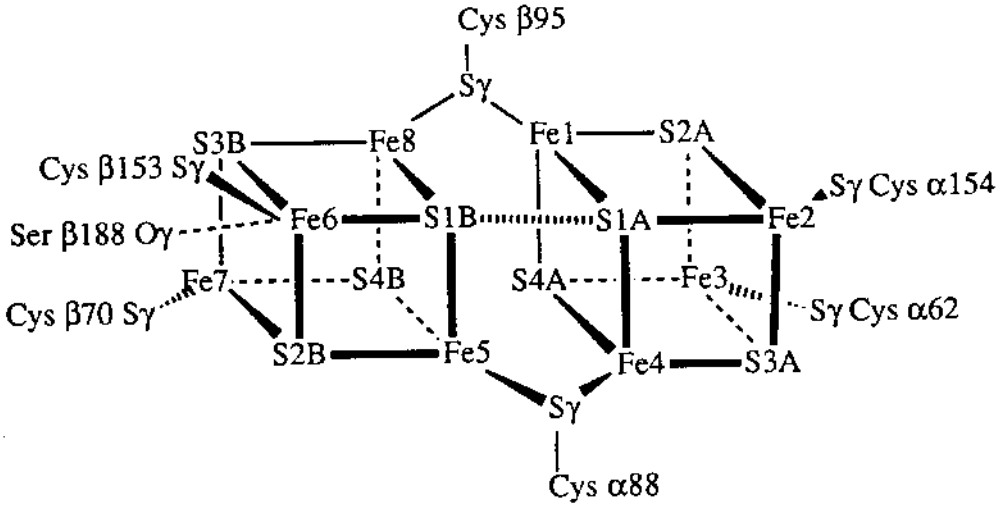

Figure 2. Structure of the P-cluster pair.

The Fe-Fe separation distance between bridged iron sites is ~2.5Å, whereas the separation distance is ~3.8Å between nonbridged iron sites on different cluster fragments. Based on electron density values, two of the bridging ligands are assigned as sulfur, while the third ligand (designated "Y") has lower electron density and may be either a well ordered O/N species, or a less well ordered S group. Homocitrate, which is an essential component of the FeMo-cofactor, coordinates the Mo through both hydroxyl and carboxyl groups. The entire cluster is coordinated to the α subunit through Cys α275 and His α442. An unusual feature of the FeMo-cofactor is the apparent trigonal coordination geometry of the six Fe that are bridged between the two cluster fragments. Although there may be some Fe--Fe bonding interactions that occur between these bridged Fe sites, neither protein groups nor solvent molecules that might possibly serve as fourth ligands have been observed within coordinating distance of any of these irons. The unusual coordination geometry of these irons may provide the site for substrate binding to FeMo-cofactor.

The P-cluster pair (Figure 2) contains two 4Fe:4S clusters that are bridged by an unusual disulfide bridge betwen two cluster sulfurs and two cysteine thiol ligands (from residues α88 and β95), with the four remaining Fe liganded by singly coordinating cysteine thiols (from residues α62, α154, β70 and β153). The coordination environment of Fe6 and Fe2 are distorted from ideal tetrahedral environment due to interactions with Ser β188 and the mainchain of Gly α185, respectively.

ALDEHYDE OXIDOREDUCTASE (AOR)

The tungsten containing protein aldehyde oxidoreductase (AOR) has been isolated from the extreme hyperthermophile *Pyrococcus furiosus*. AOR is believed to participate in a novel glycolytic pathway in this organism. The tungsten is associated with the protein as a tungstopterin that is analogous to the molybdenum-cofactor found in xanthine oxidase and other molybdoenzymes (except for nitrogenase). Several Fe:S clusters are also present in the protein. Crystals of this protein have been obtained (space group $P2_12_12_1$, a=107.9Å, b=80.5Å, c=158.9Å, with two monomers in the asymmetric unit) that diffract to at least 2.2Å resolution. In August, we collected 3Å resolution data at SSRL on the MAR imaging plate detector. A total of 22541 unique reflections were observed, reduced from a total number of 86751 reflections measured, with an R-merge of 0.086. At the wavelength of data collection, 1.08Å, Δf" for the tungsten site should be greater than the Fe:S sites, while the opposite situation holds at 1.54Å resolution. Inspection of anomalous difference Patterson and Fourier maps at 5Å resolution have provided a tenative identification for these sites. Currently, efforts are underway to calculate higher resolution maps suitable for model building and refinement.

REFERENCES ACKNOWLEDGING SSRL SUPPORT

Georgiadis, M.M., Komiya, H., Chakrabarti, P., Woo, P., Kornuc, J.J., Rees, D.C. (1992) "Crystallographic Structure of the Nitrogenase Iron Protien from *Azotobacter vinelandii*" *Science* **257**, 1653-1659.

Chan, M.K., Kim, J. and Rees, D.C. (1993) "The Nitrogenase FeMo-cofactor and P-cluster pair: 2.2Å Resolution Structures" submitted.

ADDITIONAL REFERENCES

Kim, J. and Rees, D.C. (1992) "Structural Models for the Metal Centers in the Nitrogenase Molybdenum-Iron Protein" *Science* **257**, 1677-1682.

Kim, J. and Rees, D.C. (1992) "Crystallographic Structure and Functional Implications of the Nitrogenase Molybdenum-Iron Protein from *Azotobacter vinelandii*" *Nature* **360**, 553-560.

MgATP-Induced Conformational Changes in the Iron Protein from *A.vinelandii* , as Studied by Small-Angle X-ray Scattering

Lingling Chen[1], Narasaiah Gavini[2], Hirotsugu Tsuruta[3], David Eliezer[4], Barbara K. Burgess[2], Sebastian Doniach[5], Keith O. Hodgson[1,3]

1. Department of Chemistry, Stanford University, Stanford, CA 94305
2. Department of Biochemistry and Molecular Biology, University of California, Irvine, CA 92717
3. Stanford Synchrotron Radiation Laboratory, Stanford University, Stanford, CA 94309
4. Department of Physics, Stanford University, Stanford, CA 94305
5. Department of Applied Physics, Stanford University, Stanford, CA 94305

The iron protein is one of the main components of nitrogenase(1,2). It is involved in the electron-transfer from reductants (ferredoxin *in vivo*) via its Fe-S cluster to the other main component, the molybdenum-iron protein(1,2). This electron transfer is coupled to the hydrolysis of MgATP within the iron protein. However, the details of the nucleotide binding site are still uncertain, as is the mechanism of coupling(1). On the other hand, EPR spectroscopy and electrochemical studies suggest that there is a local environmental change around the Fe-S cluster upon MgATP binding(1). Iron chelating studies also indirectly suggest that there is some gross conformational change upon MgATP binding(1,2).

Since small-angle x-ray scattering (SAXS) can provide direct information about the tertiary/quaternary structure of macromolecules under their physiological conditions, we performed SAXS experiments on the iron protein of nitrogenase from *Azotobacter vinelandii* in solution under anaerobic conditions in order to investigate the effect of MgATP binding on protein structure. We also studied this effect on one mutant of *A. vinelandii* iron protein (UW91). This strain is mutated at Ala158, which is not within the putative nucleotide binding sites(2). Its response to iron chelators differs from that of the wild type(2). The inactivation is thought due to either improper/no conformational change after binding MgATP, or the conformational change by the mutation(2).

SAXS data have been collected on a concentration series from 3 to 12mg/ml of the wild type protein and the mutant (UW91), both in the presence and absence of MgATP. Radii of gyration, R_g, were evaluated for each data set by Guinier approximation and extrapolated to zero concentration to exclude the effect of interparticle interference. The concentration dependence of radius of gyration is shown in Fig.1 and the extrapolated values are summarized in Table 1.

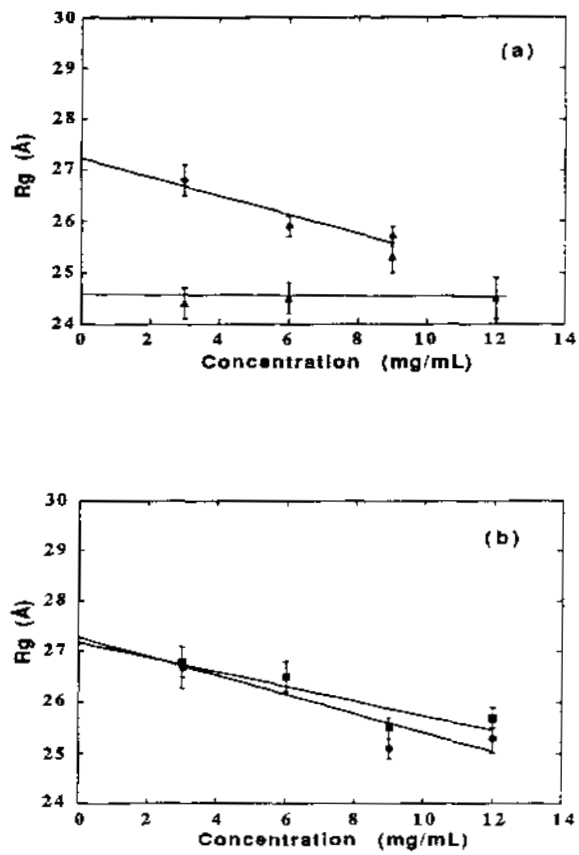

Fig. 1. Radii of gyration as a function of protein concentrations. (a) For the wild type in the absence (♦) and presence (▲) of MgATP. (b) For the mutant UW91 in the absence (●) and presence (■) of MgATP.

Table 1. Radii of gyration for the wild type and mutant UW91 Fe protein in the absence and presence of MgATP.

Fe protein	in the absence of MgATP (Å)	in the presence of MgATP (Å)
wild type	27.2 ± 0.4	24.6 ± 0.4
mutant UW91	27.3 ± 0.4	27.2 ± 0.4

Pair distribution functions generated for the wild type proteins in the presence and absence of MgATP by indirect transform method are presented in Fig. 2.

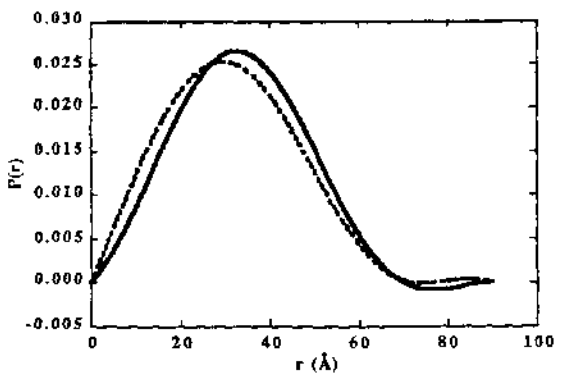

Fig. 2. Pair distribution function P(r). Solid line is for the wild type Fe protein in the absence of MgATP and dashed line is for the wild type in the presence of MgATP. The data of 6 mg/mL concentration were used to generate P(r) functions.

Preliminary results show that for the wild type protein R_g decreased about 2 Å upon MgATP binding, suggesting that MgATP induces protein contraction. Under the same conditions, R_g values for the mutant remained unchanged. Fig.2 shows that upon the binding of MgATP, the whole distribution curve was shifted to the left with the maximum of the P(r) function moving from 32.0 Å to 30.0 Å, and the maximum also diminished. These results show that the binding of MgATP induces a significant electron-transfer-favored conformation of the wild type protein, a conformation that does not exist in the mutant. The invariance of R_g between the wild type and mutant proteins in the absence of MgATP may rule out the possibility that some different conformation caused by mutation might be responsible for the mutant's inability to transfer electrons. It further agrees with the assumption that the proper MgATP-induced conformational change may be prerequisite for the nitrogen reduction(2).

Acknowledgment:

The authors thank Dr. Dmitri Svergun at EMBL for providing software GNOM for indirect transform performance. This research was supported by NIH Grant RR-01209 (to KOH) and NIH Grant GM 43144 (to BKB). Data were collected at beam line 4-2 at SSRL which is supported by the U.S. DOE, Office of Basic Energy Sciences, and in part by the NIH NCRR PRTP Program and by the DOE's Office of Health and Environmental Research.

References:

1) M.M. Georgiadis. (1990) Ph.D. thesis, UCLA.
2) N. Gavini, B. Burgess. (1992) *J. Bio. Chem.* 267, 21179-21186.

USING XAS TO PROBE THE ELECTRONIC STRUCTURE OF {FeNO}^{7} COMPOUNDS

Tami E. Westre,[1] Britt Hedman,[2] Keith O. Hodgson[1,2] and Edward I. Solomon[1]

[1] Department of Chemistry, Stanford University, Stanford, CA 94305
[2] Stanford Synchrotron Radiation Laboratory, Stanford University, Stanford, CA 94309

Introduction

Non-heme iron centers are present in the catalytic active sites of a large number of enzymes which are involved in the binding and activation of dioxygen [1]. Nitric oxide complexes of non-heme iron enzymes serve as stable analogues of possible dioxygen intermediates involved in catalysis. These enzyme-NO complexes exhibit an unusual S=3/2 EPR signal [2]. The S= 3/2 spin state has also been observed in various {FeNO}^{7} [3] model complexes [4]. {FeNO}^{7} complexes have been described as having different electronic structures for different geometric structures, linear Fe-N-O being viewed as NO^+ and bent Fe-N-O as NO^-. A wide range of bonding descriptions [5] have appeared for these complexes which include [Fe^+d^7(S=3/2) - NO^+(S=0)], [$Fe^{2+}d^6$(S=2) - NO^o(S=1/2)] antiferromagnetically coupled, [$Fe^{3+}d^5$(S=1/2) - NO^-(S=1)] ferromagnetically coupled, and [$Fe^{3+}d^5$(S=3/2) - NO^-(S=0)]. In order for the NO derivative of the non-heme iron enzymes to be used as a probe of electron distribution related to dioxygen reactivity, a clear understanding of the electronic and geometric structure of the {FeNO}^{7} unit is required.

XAS Fe K-edge spectra of Fe^{2+}EDTA, Fe^{3+}EDTA , and FeEDTA-NO have been used to elucidate the oxidation state of Fe in these {FeNO}^{7} systems. The XAS spectra indicate that the iron in FeEDTA-NO is in the Fe^{3+} oxidation state. A combination of this data and other spectral and theoretical methods have recently been used to generate a new electronic structure description of the S=3/2 {FeNO}^{7} unit which describes the complex as a high spin Fe^{3+}(S=5/2) which is antiferromagnetically coupled to an NO^-(S=1) to produce the S=3/2 ground state [6].

Experimental

The liquid samples (Fe^{3+}EDTA, Fe^{2+}EDTA, and FeEDTA-NO) for the x-ray absorption experiments were prepared by adding 50% (by volume) of glycerol to previously prepared Fe-EDTA solutions to produce 50 mM Fe solutions. These samples were then loaded into 140 µL lucite EXAFS cells (23x2x3mm) with 37 µm kapton windows in an anaerobic box under nitrogen. All three samples were frozen in liquid nitrogen to yield high quality glasses that were subsequently stored in a liquid nitrogen refrigerator until use.

The X-ray absorption spectra were recorded at the Stanford Synchrotron Radiation Laboratory on unfocused beamline 7-3 during dedicated conditions (3 GeV, 25-65 mA). The radiation was monochromatized using a Si(220) double crystal monochromator detuned 50% at 7474 eV to minimize harmonic contamination. An Oxford Instruments continuous-flow liquid helium CF 1208 cryostat was used to maintain a constant temperature of 85 K. The liquid samples were collected in fluorescence mode. The fluorescence signal was collected by an argon-filled ionization chamber , equipped with Soller slits and a Mn filter. Data were measured to k = 9.5 Å^{-1} with 1 mm high pre-monochromator beam defining slits. The spectrometer energy resolution was approximately 1 eV with reproducibility of edge position determination of < 0.2 eV. Energies were calibrated using an internal Fe foil standard, assigning the first inflection point to 7111.2 eV. Calibrated scans were inspected individually and rejected if the signal-to-noise ratio was too high compared to the other scans due to beam instabilities. Five to nine scans were averaged for each EDTA solution. A smooth pre-edge background was removed from the averaged spectra by fitting a first or second order polynomial to the pre-edge region and subtracting this polynomial from the entire spectrum. A one-segment spline of order one was fit to the EXAFS region and the data normalized to an edge jump of one.

Results and Discussion

The XAS edge spectra for the three EDTA solutions are shown in Figures 1 and 2. The lowest energy transitions are the weak 1s->3d pre-edge peaks at approximately 7112 eV (Figure 1,2). The 1s->3d transition of Fe^{2+}EDTA is a low-intensity split peak

located at 7111.1 eV and 7113.2 eV. The Fe^{3+}EDTA 1s->3d transition consists of a single feature at 7112.5 eV. FeEDTA-NO has a single pre-edge peak at 7112.3 eV, but the transition is more intense than the Fe^{3+}EDTA 1s->3d pre-edge feature. The Fe^{2+}EDTA spectrum exhibits an intense transition superimposed on the rising edge at 7124 eV which is approximately 10 eV higher than the pre-edge peaks. The intensity of this peak drops off rapidly in the multiple scattering region. The first transition after the 1s->3d pre-edge feature occurs at 7127 eV in Fe^{3+}EDTA and at 7125.5 eV in FeEDTA-NO.

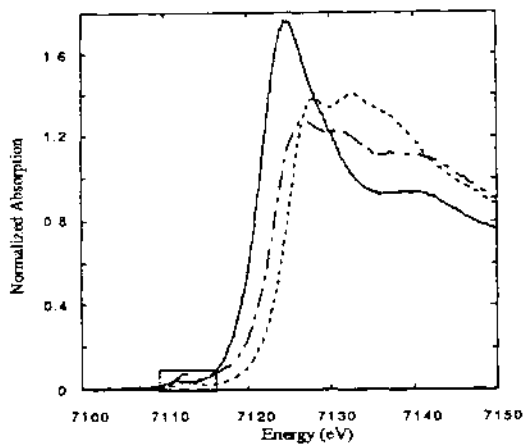

Figure 1. The Fe K-edge absorption spectra of Fe^{2+}EDTA (——), Fe^{3+}EDTA (-----), and FeEDTA-NO (— – —). The boxed region denotes the 1s->3d pre-edge region which is expanded and shown in Figure 2.

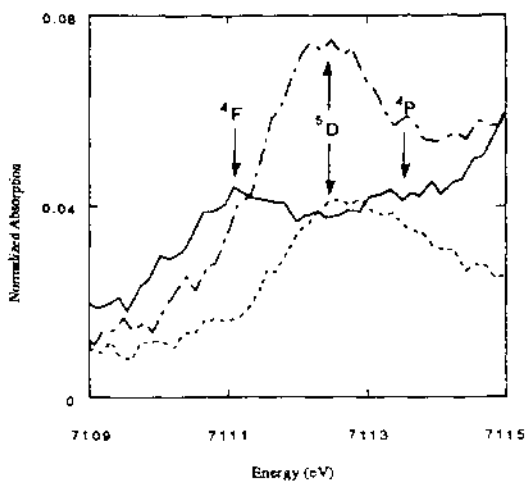

Figure 2. The 1s->3d pre-edge region of the Fe K-edge absorption spectra of Fe^{2+}EDTA (——), Fe^{3+}EDTA (-----), and FeEDTA-NO (— – —).

The 1s->3d pre-edge feature can be used to probe the iron oxidation state in $\{FeNO\}^7$ systems. FeEDTA-NO and Fe^{3+}EDTA exhibit single pre-edge features while the pre-edge of Fe^{2+}EDTA is split. The splitting of the pre-edge in Fe^{2+}EDTA is attributed to the free ion splitting of approximately 2 eV [7b]. Since the initial states of these iron systems are of maximum spin multiplicity, two final states can be reached in the ferrous case, ^4F and ^4P (where ^4F is at lower energy), while only one state of maximum spin multiplicity can be reached in the ferric case, ^5D (Figure 2). The lack of splitting in the 1s->3d pre-edge peak of FeEDTA-NO indicates that the iron in $\{FeNO\}^7$ systems is ferric. The pre-edge feature of FeEDTA-NO is more intense than that of Fe^{3+}EDTA. Empirically, the strength of the pre-edge transition is found to be dependent on the size of the "molecular cage". The molecular cage is defined by the nearest-neighbor ligands coordinating to the x-ray absorbing metal center [7d]. A cage which breaks inversion symmetry at the metal site can enable dipolar 1s->nd transitions which are normally dipole forbidden. In the case of FeEDTA-NO, the short Fe-N(O) bond lowers the symmetry around the Fe resulting in an increase in the intensity of the 1s->3d pre-edge feature.

The energy of the edge position is dependent upon the effective nuclear charge of the absorbing metal atom. The effective nuclear charge of the metal atom is governed by a combination of effects including the formal oxidation state of the metal, the number and type of ligating atoms and the coordination geometry [7]. Therefore, the oxidation state of a metal atom cannot be determined by the edge position without careful consideration of ligation effects on the effective nuclear charge of the metal atom. In the case of the three EDTA solutions, differences between the types of ligating atoms and the coordination spheres are minimized so that the increase in the edge energy in FeEDTA-NO compared to Fe^{2+}EDTA is mainly due to an increase in the oxidation state of the iron. The energy of the FeEDTA-NO edge lies between the reduced and oxidized iron-EDTA edges. However, the FeEDTA-NO spectrum is similar in intensity and shape to the Fe^{3+}EDTA spectrum. The FeEDTA-NO edge is lower in energy than in Fe^{3+}EDTA due to NO^- participation in ligand to metal σ donor bondng. This donation of electron density from NO^- to the iron in FeEDTA-NO reduces the effective nuclear charge of the iron and causes the FeEDTA-NO edge to be at a lower energy.

Conclusions

The XAS spectra indicate that the iron in FeEDTA-NO is best described as in its ferric oxidation state. Normal coordinate anaylsis of resonance Raman data indicate that the NO in FeEDTA-NO is in a form between NO and NO^- [6]. Together the XAS and rR data predict that upon NO binding to Fe^{2+}EDTA the

Fe^{2+} has transferred an electron to NO, producing a ferric-NO^- complex which has significant delocalization. Spin-unrestricted Xα calculations on an S=3/2 $\{FeNO\}^7$ compound describe the electronic structure of the complex as a high spin Fe^{3+}(S=5/2) which is antiferromagnetically coupled to an NO^- (S=1) to produce the S=3/2 ground state. Thus, an experimentally and theoretically consistent electronic structure has been generated for the $\{FeNO\}^7$ S=3/2 system. This new bonding description provides a general understanding of the interaction of NO with the high-spin ferrous site, and the spectral features can be quantitated to provide insight into differences in bonding and electron distribution which can be related to dioxygen activation by non-heme iron enzymes.

Acknowledgements

This research was supported by grants from the NIH (GM40392, E.I.S.) and NSF (CHE91-21576, K.O.H.). Stanford Synchrotron Radiation Laboratory is supported by the Department of Energy, Office of Basic Energy Science, Division of Chemical Science and Division of Material Science, and in part by the NIH NCRR BRTP Program (RR-01209) and DOE's Office of Health and Environmental Research.

References

1. Solomon, E. I.; Zhang, Y. *Acc. Chem. Res.* **1992**, *25*, 343.

2. (a) Nelson, M. J.; *J. Biol. Chem.* **1987**, *262*, 12137. (b) Rich, P. R.; Salerno, J. C.; Leigh, J. S.; Bonner, W. D. *FEBS Lett.* **1978**, *93*, 323. (c) Arciero, D. M.; Lipscomb, J. D. *J. Biol. Chem.* **1986**, *261*, 2170. (d) Arciero, D. M.; Orville, A. M.; Lipscomb, J. D. *J. Biol. Chem.* **1985**, *260*, 14035. (e) Twilfer, H.; Bernhardt, F. H.; Gersonde, K. *Eur. J. Biochem.* **1985**, *147*, 171. (f) Chen, V. I.; Orville, A. M.; Harpel, M. R.; Frolik, C. A.; Surerus, K. K.; Münch, E.; Lipscomb, J. D. *J. Biol. Chem.* **1989**, *264*, 21677.

3. (a) The Enemark-Feltham[3b] formalism for $\{MNO\}^x$ complexes is used here, in which x is the number of d-type electrons in the system when the nitrosyl ligand is formally considered as NO^+. (b) Enemark, J. H.; Feltham, R. D. *Coord. Chem. Rev.* **1974**, *13*, 339.

4. Bonner, W. D.; Blum, H.; Rich, P. R.; Salerno, J. C. *In Frontiers of Biological Energetics*; Academic Press: New York, 1978; Vol. II. p 997.

5. (a) Bill, E.; Bernhardt, F. H.; Trautwein, A. X.; Winkler, H. Eur. *J. Biochem.* **1985**,*147*, 171. (b) Wells, F. V.; McCann, S. W.; Wickman, H. H.; Kessel, S. L.; Hendrickson, D. N.; Feltham, R. D. *Inorg. Chem.* **1982**, *21*,2306. (c) Earnshaw, A.; King, E. A.; Larkworthy, L. F. *J. Chem. Soc. A.* **1969**, 2459. (d) Salerno, J. C.; Siedow, J. N. *Biochem. Biophys. Acta* **1979**, 579, 246. (e) Pohl, K.; Weighardt, K.; Nuber, B.; Weiss, J. *J. Chem. Soc., Dalton Trans.* **1987**, 187.

6. Zhang, Y.; Pavlosky, M. A.; Brown, C. A.; Westre, T. E.; Hedman, B.; Hodgson, K. O.; Solomon, E. I. *J. Am. Chem. Soc.* **1992**, *114*, 9189.

7. (a) Srivastave, U. C.; Nigam, H. L. *Coord. Chem. Rev.* **1973**, *9*, 275 and references therein. (b) Shulman, R. G.; Yafet, Y.; Eisenberger, P.; Blumberg, W. E. *Proc. Natl. Acad. Sci.*, **1976**, *73*, 1384. (c) Cramer, S. P.; Eccles, T. K; Kutzler, F. W.; Hodgson, K.O.; *J. Am. Chem. Soc.* **1976**, *98*, 1287. (d) Kutzler, F. W.; Natoli, C. R.; Misemer, D. K.; Doniach, S.; Hodgson, K. O.; *J. Chem. Phys.* **1980**, *73*, 3274. (e) Wong J.; Lytle, F. W.; Messmer, R. P.; Maylotte, D. H.; *Phys. Rev. B.* **1984**, *30*, 5596. (f) Roe, A. L.;Schneider, D. J.; Mayer, R. L.; Pyrz, J. W.; Widom, J.; Que, L., Jr. *J. Am. Chem. Soc.* **1984**, *106*, 1676. (g) Kau, L. S.; Spira-Solomon, D. J.; Penner-Hahn, J. E.; Hodgson, K. O.; Solomon, E. I.; *J. Am. Chem. Soc.* **1987**, *109*, 6433.

The Mo K-Edge EXAFS Studies of *A. vinelandii* and *C. pasteurianum* MoFe-Proteins

J. Chen (LBL), J. Christiansen (UCD), R. C. Tittsworth and B. J. Hales (LSU), N. Campobasso and J. T. Bolin (Purdue U.), S. P. Cramer (UCD)

Biological reduction of dinitrogen to ammonia is catalyzed by the enzyme system nitrogenase. The nitrogenase system contains two proteins, a large (~240 kD) protein referred to as the MoFe-protein (1), and a smaller ~55 kD protein known as the Fe protein. The MoFe-protein is an $\alpha_2\beta_2$ tetramer which contains ~30 Fe atoms and 2 Mo atoms, and the Fe-protein is a γ_2 dimer which has one 4Fe-4S cluster (2). In the MoFe-protein, a fraction of the metals are grouped in an extractable iron-molybdenum cofactor (FeMo-co), a complex of approximate composition $MoFe_7S_8$, which is thought to contain the active site (3). The remaining irons are grouped in so-called P-clusters, generally thought to contain two 4Fe-4S clusters (4). A crystal structure for the *C. pasteurianum* and *A. vinelandii* MoFe-protein is in progress (5). During the past decade, many structural details about the FeMo-co have been derived from EXAFS spectroscopy (6). The Mo EXAFS of both solutions and crystals of nitrogenase found characteristic Mo-S and Mo-Fe distances of 2.4 Å and 2.7 Å, respectively, Based on these early results a Mo-substuted cube fragment in the M center was proposed (7). The Fe EXAFS of isolated FeMo-co reveals not only 2.7 Å Fe-Fe interactions characteristic of Fe-S clusters, but a 3.7 Å Fe-Fe distance typical of prismanes (8). In the recent Fe *K*-edge EXAFS studies, the 3.8 Å Fe-Fe interaction and a new 4.3 Å Fe-S feature are observed for the first time in the intact proteins, and a variety of structure models for the M center are examined (9). Most recently, a structure model for the FeMo-co in *A. vinelandii* MoFe-protein has been proposed based on crystallographic analysis at 2.7 Å resolution (10). In here, we report the first time seeing longer Mo-Fe (~5 Å) interaction, which is observed in both solution and crystal MoFe-proteins EXAFS. The distance obtained from the fitting is consistent with recently proposed crystallographic models for the M center.

Nitrogenase solution samples were extracted from appropriate strains of *A. vinelandii* at LSU by methods previously described (11). Specific activities were 1800 nmol C_2H_2 reduced $min^{-1}mg^{-1}$ protein for both reduced and oxidized proteins. MoFe-protein crystals from *C. pasteurianum* were purified and crystallized at Purdue University (12). The crystals are in space group $P2_1$ with unit cell parameters a = 69.9 Å, b = 151.2 Å, c = 121.8 Å, and β = 110.3°. The Mo *K*-edge x-ray absorption spectra were recorded at 4 K using a Si(220) double crystal monochromator at 7-3 and 10-2 beamlines of SSRL, SLAC, Stanford. The protein samples were measured in the fluorescence excitation mode using a 13-element Ge solid state array detector (13).

The Fourier transforms of Mo *K*-edge EXAFS for reduced and oxidized *A. vinelandii* MoFe proteins, as well as *C. pasteurianum* crystal, are shown in Figure 1. For the reduced MoFe protein, the 1-3 Å region spectrum is dominated by Mo-S and Mo-Fe interactions at 2.33 and 2.70 Å. In addition a component at 2.08 Å is identified as a Mo-O(N) feature. The amplitudes of these features derived from the fittings are 4.8, 3.0, and 0.9 respectively (14). These values are in good agreement with early results on isolated cofactors and single crystals nitrogenase (7). In the 3-5 Å region, a ~4.9 Å Mo-Fe feature with an amplitude of almost 3 is observed, which by any means, is the first time reported in nitrogenase. The results are summarized in Table 1.

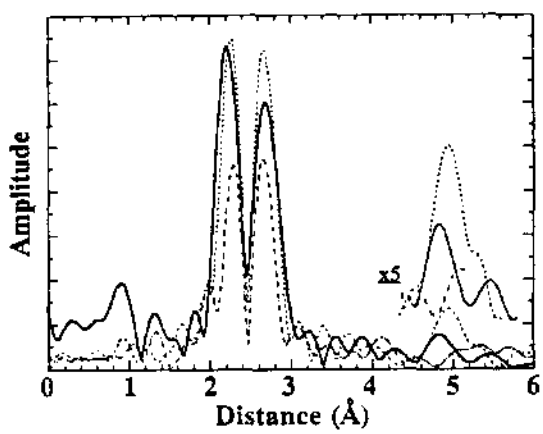

Figure 1. Comparison of Mo EXAFS Fourier transforms for nitrogenase. *Av1* solution, reduced (___) and oxidized (- - -), and *Cp1* crystal (. . .). Long range features have been multiplied by 5 in inset to enhance visibility.

All the features in the 1-3 Å region of the reduced EXAFS are also observed in the oxidized spectrum. The observed first shell Mo-S and Mo-Fe distances are almost unchanged upon thionine-oxidation, as well as Mo-O(N) distance (Table 1). Although the appearance of the Fourier transform changes, the optimized coordination numbers of Mo-S and Mo-Fe interactions only change ~20%, from 4.8 and 3.0 in reduced sample to 3.8 and 2.4 in oxidized sample. However, the 4.9 Å Mo-Fe feature becomes much weaker in the oxized spectrum. This change should be treat with caution. Since the EXAFS is only sensitive to the averaged distance over all

Fe atoms, the small change in each Mo-Fe distance can smear out the feature at this long range.

Table 1. Interatomic distances in Nitrogenase MoFe protein and $(CO)_3MoFe_6S_6Mo(CO)_3$ found in the Mo EXAFS curve-fitting.

			Mo-O	Mo-S	Mo-Fe	Mo--Fe
Solution	Red.	N [a]	0.9	4.8	3.0	3.0
		R (Å)	2.08	2.33	2.70	4.87
	Ox.	N [a]	1.2	3.8	2.4	1.4
		R (Å)	2.09	2.33	2.71	4.94
Crystal		N	1.0	5.7	3.8	4.2
		R (Å)	2.08	2.33	2.70	4.87
$MoFe_6S_6Mo$		N	3	3	3	3
		R (Å)	2.01	2.60	2.99	4.11
		$\sigma^2 x10^5$	209	318	270	597
		R [b] (Å)	2.020	2.582	2.930	4.24

a The coordination number found by optimization with fixed mean-square deviation values found in the model compound fit.
b The crystallographic value. Reference (14).

As expected, the *C. pasteurianum* crystal spectrum is similar to that of *A. vinelandii* proteins for distances (Figure 1). The found distances for Mo-O, MO-S, Mo-Fe, and longer Mo-Fe features are 2.08 , 2.33, 2.70, and 4.87 Å respectively (Table 1). However the amplitudes of these interactions vary with the crystal orientations. Especially the longer Mo-Fe interaction. For example, the amplitude of this feature changes from 3 to 4.2 in the crystal spectrum shown in Fig. 1 (the spectrum was taken by setting the crystal so that the synchrotron radiation polarization vector **E** is in the *ac* plane of the crystal and 35° away from the **a** axis).

During the past decade, many spectroscopic techniques have been used to study FeMo-co structure (16). In late 70's, a Mo-substituted cube fragment model was proposed by Cramer *et. al.* based on their EXAFS studies on FeMo-co (2.3 Å Fe-S, 2.6 Å Fe-Fe, 2.4 Å Mo-S and 2.7 Å Mo-Fe) (7). Since then, a wide variety of models have been proposed and synthized (9,16). Recently, a new crystallographic model has been proposed based on a 2.7 Å resolution x-ray diffraction result (10). Examination of this model shows that there should be three longer Mo-Fe interactions beyond the 2.7 Å shell, and their distances are very close to our EXAFS analysis, namely ~5 Å. The distance assignment is displayed in Scheme 1.

In conclusion, the structure of the intact MoFe-protein has been studied by the Mo *K*-edge EXAFS spectroscopy. We observed not only 'well known' 2.33 Å Mo-S and 2.7 Å Mo-Fe interactions, but also a ~5 Å Mo-Fe distance, which is reported for the first time in nitrogenase. Both this result and our earlier Fe *K*-edge EXAFS studies are consistent with recently proposed crystallographic models. This study also demonstrates that the EXAFS technique is capable of obtaining the structural information up to 5 Å in an unknown system.

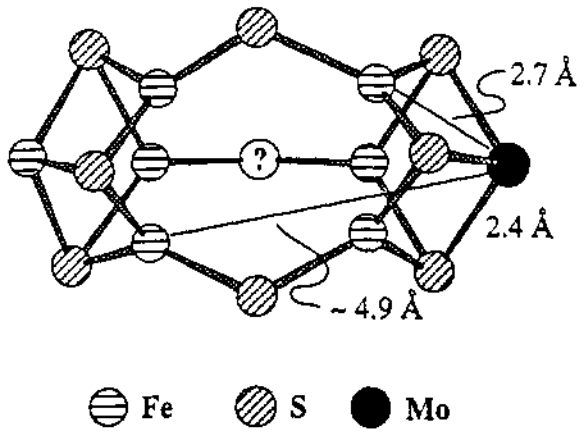

Scheme 1. An assignment for the long Mo-Fe distance in the M center.

ACKNOWLEDGMENTS. We thank Prof. Coucouvanis for providing the prismane samples. We also thank the staff of SSRL for their assistance in making this work possible. SSRL is supported by the Department of Energy, Office of Basic Energy Science. Support from the Department of Agriculture through grand DOA-91-37305-6514 (to SPC) and the NIH through GM-44380-2 (to SPC) and GM-33965 (to BJH) are gratefully acknowledged.

REFERENCES

1) Hageman, R. V.; Burris, R. H. *Proc. Nat. Acad. Sci. USA* **1978**, 75, 2699-2702.

2) a) Orme-Johnson, W. H. Ann. Rev. *Biophys. Biophys. Chem.* **1985**, 14, 419-459. b) Eady, R. R. *Adv. Inorg. Chem.* **1991**, 36, 77-102.

3) McLean, P. A.; Wink, D. A.; Chapman, S. K.; Hickman, A. B.; McKillop, D. M.; Orme-Johnson, W. H. *Biochemistry* **1989**, 28, 9402-9406.

4) Zimmerman, R.; Munck, E.; Brill, W. J.; Shah, V. K.; Henzl, M. T.; Rawlings, J.; Orme-Johnson, W. H. *Biochem. Biophys. Acta*, **1978**, 537, 185-207.

5) a) Bolin, J. T.; Ronco, A. E.; Mortenson, L. E.; Morgan, T. V.; Williamson, M.; Xuong, N.-H. in "Nitrogen Fixation: Achievements and Objectives" Gresshoff, Roth, Stacey, Newton, eds. Chapman and Hall, New York (1990) pp. 111-116. b) Georgiadis, M.; Chakrabarti, P.; Rees, D. C. in "Nitrogen Fixation: Achievements and Objectives" Gresshoff, Roth, Stacey, Newton, eds. Chapman and Hall, New York (1990) pp. 111-116.

6) Cramer, S. P. in "Extended X-ray Absorption Fine Structure", Konigsberger and Prins, eds. Plenum, New York (1988) pp. 257-320.

7) a) Cramer, S. P.; Hodgson, K. O.; Gillum, W. O.; Mortenson, L. E. *J. Am. Chem. Soc.* **1978**, 100, 3398-3407. b) Flank, A. M.; Weininger, M.; Mortenson, L. E.; Cramer, S. P. *J. Am. Chem. Soc.* **1986**, 108, 1049-1055.

8) Arber, J. M.; Flood, A. C.; Garner, C. D.; Gormal, C. A.; Hasnain, S. S.; Smith, B. E. *Biochem. J.* **1988**, 252,

VUV PROPOSALS

HIGH-RESOLUTION CORE-LEVEL PHOTOABSORPTION OF ALKALI HALIDES

E. Hudson, E. Moler, Y. Zheng, S. Kellar

Department of Chemistry, University of California and Chemical Sciences Division, Lawrence Berkeley Laboratory, Berkeley, California 94720

P. Heimann, Z. Hussain

Accelerator and Fusion Research Division, Lawrence Berkeley Laboratory, Berkeley CA 94720

D. A. Shirley

Departments of Chemistry and Physics, Pennsylvania State University, University Park PA 16802

Core-level photoabsorption spectra of single-crystal alkali halide salts have been measured at low temperature (T=80 K) using high-resolution soft X-rays from the LBL Spherical Grating Monochromator (SGM) on Beam Line VI-1. By employing the electron partial-yield detection technique, spectra of NaF, NaCl, and NaBr were obtained at the sodium K-edge (Fig. 1) and spectra of LiF, NaF, and KF were obtained at the fluorine K-edge (Fig. 2). All spectra showed sharp absorption features near the absorption threshold and broader absorption features extending 60-90eV above threshold.

The high resolution of the SGM allowed the detection of previously unobserved structure, particularly in the near-edge region. These narrow lines below and just above threshold are attributed to core-level excitons. The broader peaks above threshold are assigned to a combination of multi-electron excitations and photoelectron multiple-scattering resonances. A multi-electron excitation is the result of the simultaneous promotion of a core electron and one or more valence electrons to a bound final state. These excitations are observed in many systems but are generally less intense than the features observed here. Strong features are expected when a single electron is promoted to an unbound state which is resonantly enhanced by multiple scattering from the surrounding ions. This process is probably responsible for most of the above-threshold structure observed. A detailed analysis is underway which will include a comparison of the data to the results of a state-of-the-art multiple-scattering calculation. At the present time, a few qualitative conclusions are possible.

NaF fluorine K-edge spectra were taken at two different temperatures. Comparison shows that the features of the lower-temperature spectrum are sharper. This difference demonstrates the dependence of the resonance energies upon the position of ions in the lattice. At higher temperatures, the larger variation in the local lattice structure broadens the absorption features. This result supports the assignment of these features as core-level excitons and multiple-scattering resonances, rather than multi-electron excitations.

Spectra were also measured with different orientations of the x-ray polarization vector with respect to the crystal lattice. Surprisingly, the spectral features showed no dependence upon this change in experimental geometry. Such a dependence was expected, in particular, for the core-level excitons. The lack of a polarization effect suggests that the excitons observed in each individual spectrum share the same symmetry.

Work supported by the Director, Office of Energy Research, Office of Basic Energy Sciences, Chemical Sciences Division of the U.S. Department of Energy under Contract No. DE-AC03-76SF00098.

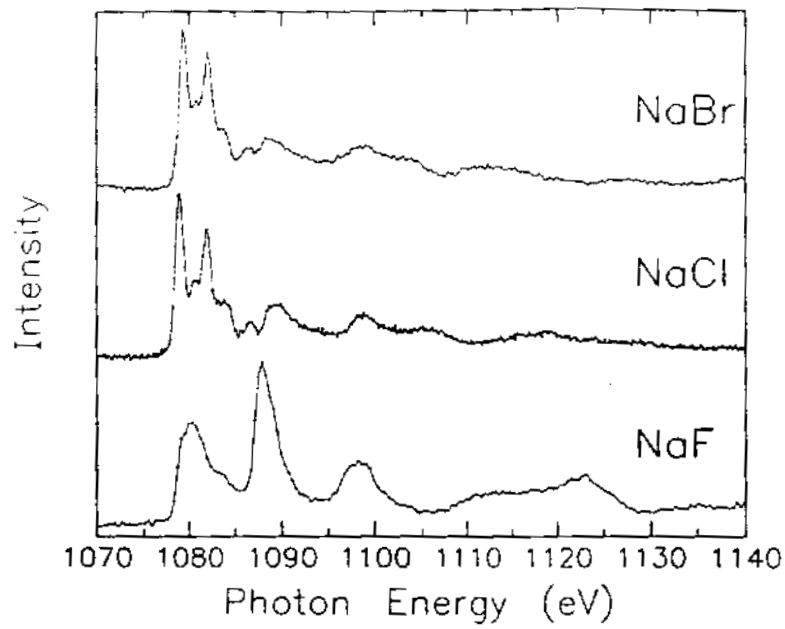

Figure 1: Photoabsorption spectra of sodium halide salts near the sodium K-edge. The results qualitatively reflect the relative crystal ionic radii of the halide ions; bromide and chloride have similar ionic radii, while that of fluoride is much smaller.

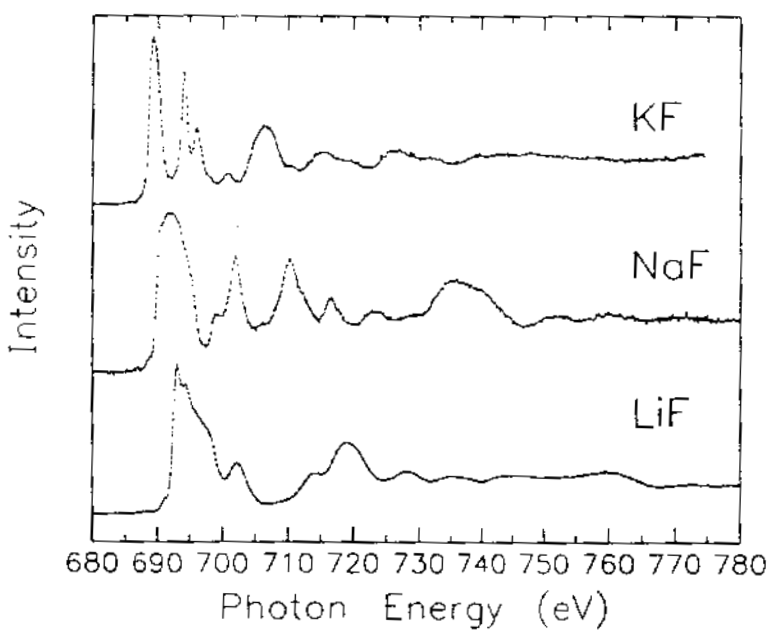

Figure 2: Photoabsorption spectra of alkali fluoride salts near the fluorine K-edge. The high throughput of the monochromator in this energy range allowed the rapid collection of high-resolution data.

CORE SATELLITE INTENSITIES IN CO

T.Reich[1,2], P.A.Heimann[1], B.L.Petersen[1], E.Hudson[1], Z.Hussain[1], and D.A.Shirley[2]

1 Lawrence Berkeley Laboratory, Berkeley, CA
2 Pennsylvania State University, University Park, PA

High-resolution photoelectron spectra and zero electron kinetic energy (ZEKE) spectra near the K edges in CO were measured to study the threshold behavior of the photoelectron satellite branching ratios. The measurements were performed on beam line 6-1 using the high-resolution SGM during the 4x1 timing mode of SPEAR. The electron time-of-flight (TOF) spectra were recorded at the magic angle for different kinetic energies from zero up to 45 eV.

The ZEKE spectra in Fig. 1 show remarkable differences in the shake-up energy and the intensity distribution between C1s and O1s satellites in CO. This features can be discussed on the basis of the equivalent core model, potential theory, and charge transfer effects [1].

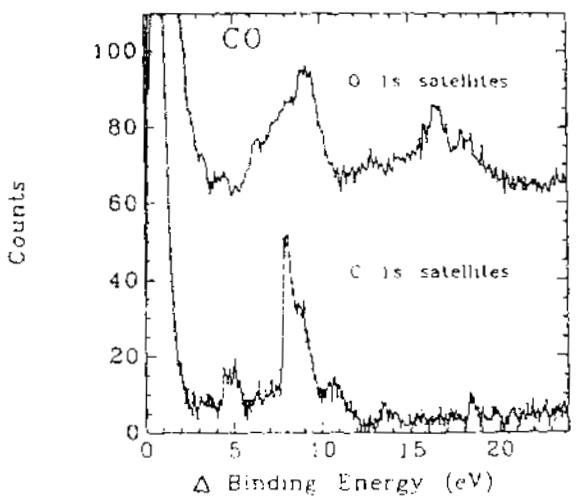

Figure 1. ZEKE scans of CO above the C1s and O1s thresholds.

We re-investigated the branching ratios of the singlet (S'=0) and triplet (S'=1) coupled $\pi\pi^*$ satellite states above the C1s edge. In the region of the S'=1 satellite, we were able to resolve three components (see Fig. 2) that show a variation in the branching ratios as a function of photon energies. The energy dependency of the branching ratios of the singlet and triplet $\pi\pi^*$ satellites are in qualitative agreement with calculations using the relaxed-core Hartree-Fock approximation [2].

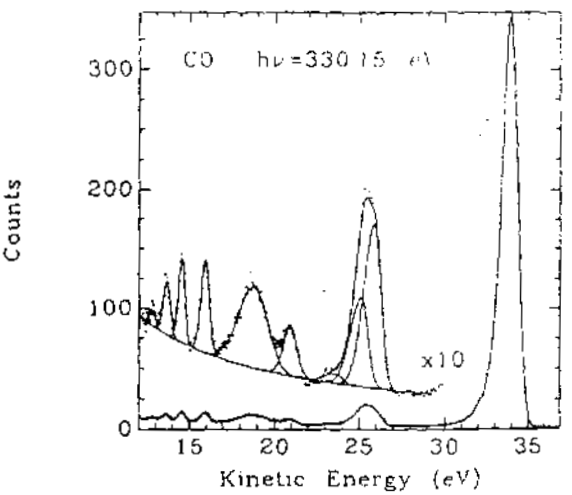

Figure 2. TOF photoelectron spectrum taken in the near-threshold region of the C1s satellites. The solid line is a least-square fit to the experimental data.

1) J.Feldhaus, A.Reimer, J.Schirmer, A.M.Bradshaw, U.Becker, H.G.Kerkhoff, B.Langer, D.Szostak, R.Wehlitz, and W.Braun, J.Physique, **C9**-773 (1987).
2) J.Schirmer, M.Braunstein, and V.McKoy, Phys.Rev.A, **44**, 5762 (1991).

The work was done at SSRL which is operated by the Department of Energy, Division of Chemical Sciences. This work was supported by the Director, Office of Energy Research, Office of Basic Energy Sciences, Chemical Sciences Division of the U. S. Department of Energy, LBL under Contract No. DE-AC03-76SF00098. T. R. thanks the Alexander von Humboldt Foundation for support through a Feodor Lynen Fellowship.

STRUCTURAL DETERMINATION OF NH_3 ADSORBED ON Ni(001) USING ANGLE-RESOLVED PHOTOEMISSION EXTENDED FINE STRUCTURE

Y. Zheng,[1,2] E. Moler,[2] E. Hudson,[2] Z. Hussain,[2] and D. A. Shirley[1]
[1] Departments of Chemistry and Physics, Pennsylvania State University, University Park, PA 16802
[2] Chemical Sciences Divison, Lawrence Berkeley Laboratory, Berkeley, CA 94720

The structure of NH_3 adsorbed on the Ni(001) surface has been studied using the angle-resolved photoemission extended fine structure (ARPEFS) technique. The N 1s ARPEFS data were taken along the surface normal and at 100 K, using the SGM on beamline 6-1. Figure 1 and Figure 2 show the experimental ARPEFS data and the corresponding Fourier transform, respectively.

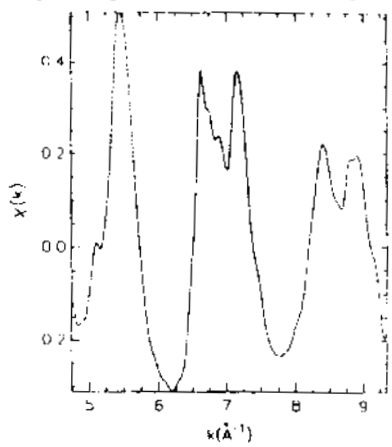

Figure 1. Experimental ARPEFS data.

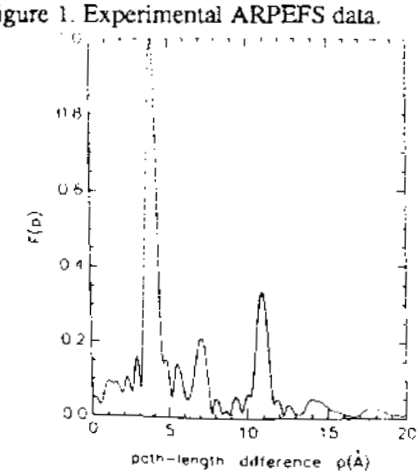

Figure 2. Fourier transform of the experimental ARPEFS data shown in Figure 1.

By qualitative and quantitative comparisons of the experimental ARPEFS data to the multiple-scattering spherical-wave (MSSW) calculations, it has been determined that NH_3 adsorbs at the atop site of the Ni(001) surface with a N-Ni bond length of 2.01 A and a 2.8% expansion of the topmost Ni-Ni interlayer spacing. The best fit of the MSSW calculation to the experimental data is shown in Figure 3.

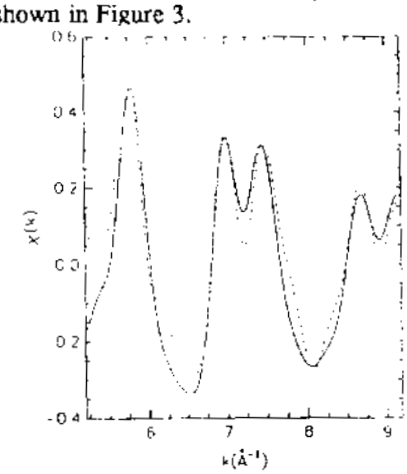

Figure 3. Best fit of the theory (dash line) to the experiment (solid line).

The experiments were performed at SSRL, which is supported by the U. S. Department of Energy's Office of Basic Energy Sceinces. This work was supported by the Director, Office of Energy Research, Office of Basic Energy Sciences, Chemical Sciences Division of the U. S. Department of Energy under Contract No. DE-AC03-76SF00098.

SITE-SPECIFIC SURFACE STRUCTURE DETERMINATION OF C(2X2) N_2/Ni(100) BY ANGLE-RESOLVED PHOTOEMISSION EXTENDED FINE STRUCTURE

E. Moler, E. Hudson, Y. Zheng

Department of Chemistry, University of California and Chemical Sciences Division, Lawrence Berkeley Laboratory, Berkeley, CA 94720

Z. Hussain

Accelerator and Fusion Research Division, Lawrence Berkeley Laboratory, Berkeley, CA 94720

D. A. Shirley

Departments of Chemistry and Physics, Pennsylvania State University, University Park, PA 16802

Energy-scanned Angle-Resolved Photoelectron Extended Fine Structure (ARPEFS) from nitrogen core-levels was used to determine the surface structure of molecular nitrogen C(2x2) physisorbed on Ni(100). We used the high resolution soft X-rays from the LBL Spherical Grating Monochromator (SGM) on Beam Line VI-1 to collect photoemission spectra of the chemically shifted nitrogen core levels. The measurements were made at low temperature (~60 K) in both normal and off-normal electron emission directions using a hemispherical electron energy analyzer.

The resolution of Beam-Line VI-1 and our angle-resolving analyzer and the chemical shifts of the core levels of the two nitrogen atoms allowed the collection of two diffraction curves simultaneously: one from the "inner" nitrogen atom, bound to the nickel substrate, and one from the "outer" nitrogen, bound to the inner nitrogen. The soft X-ray light passed by the SGM monochromator was of sufficient intensity and resolution to allow collection of core-level spectra over a photon energy range of 480-735 eV, the most useful range for ARPEFS measurements of the nitrogen core level. The core level intensities were thus measured over an electron kinetic energy range of 75-330 eV, corresponding to wave numbers of 5-9.5 $Å^{-1}$.

Analysis of these diffraction curves are underway using full Multiple Scattering Spherical Wave (MSSW) calculations. Preliminary results show the nitrogen molecule to be standing up on the surface on atop sites [Figs. 1,2]. Fourier transforms of the curves show bond lengths of approximately 1.1 Å for the N-N bond and 1.9 Å N-Ni bond. However, the full analysis is still in progress, and consideration of multiple scattering and phase-shift effects will yield more precise values for these bond lengths.

One interesting feature of the ARPEFS curves collected is the behavior of the 6 eV satellite peak, which is believed to originate in part from each of the core level peaks. Comparison of the satellite peak intensity oscillations and the oscillations of the sum of the two main line peaks shows a nearly identical curves, only shifted by 6 eV [Fig 3]. This demonstrates that the origin of the satellite peak is an intrinsic loss peak and not a result of some extrinsic loss process.

Work supported by the Director, Office of Energy Research, Office of Basic Energy Sciences, Chemical Sciences Division of the U. S. Department of Energy under Contract No. DE-AC03-76SF00098.

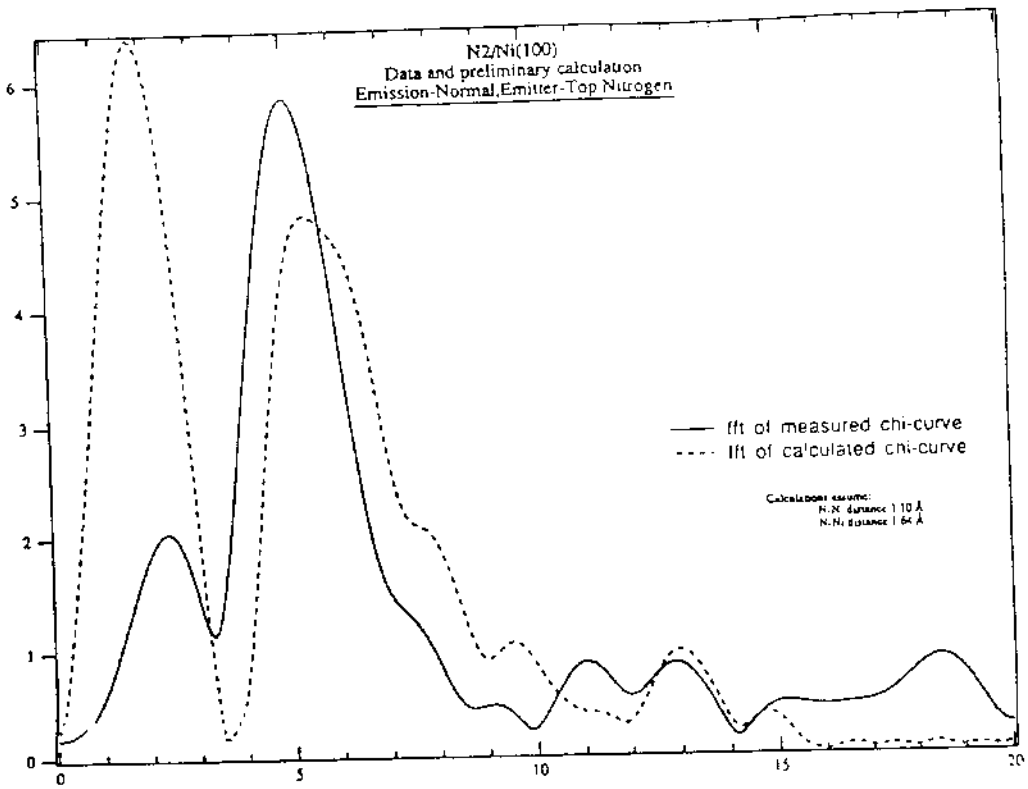

Fig. 1 Fourier Transform of the "outer" Nitrogen ARPEFS Curve and a Preliminary Calculation

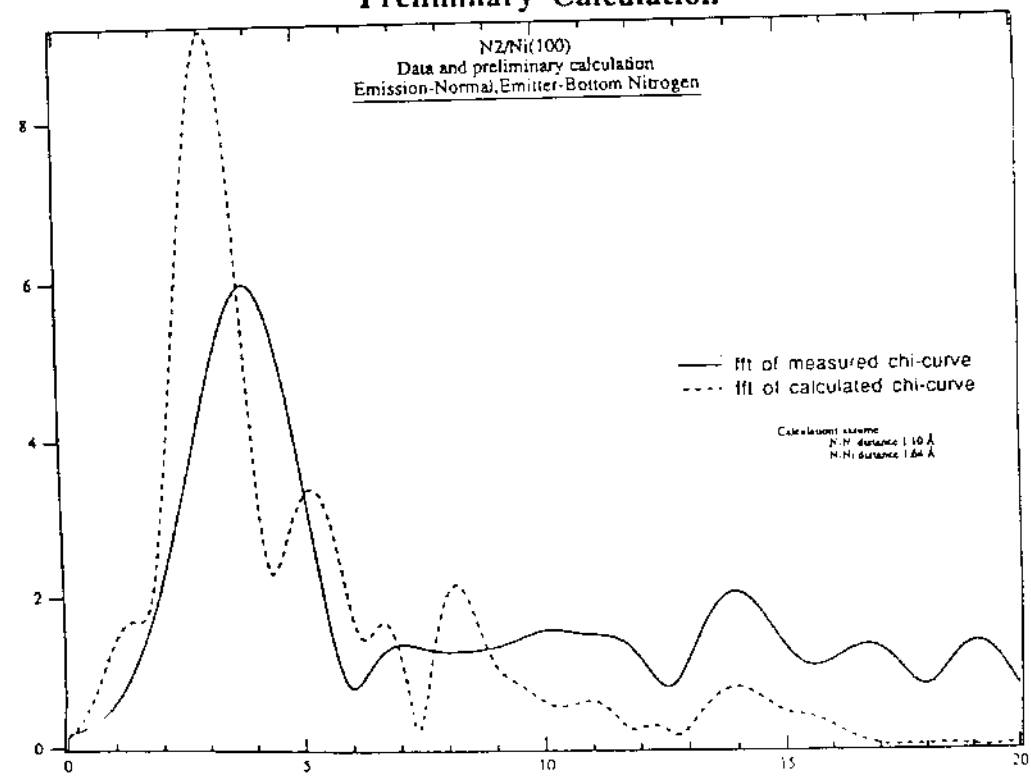

Fig. 2 Fourier Transform of the "inner" Nitrogen ARPEFS Curve and a Preliminary Calculation

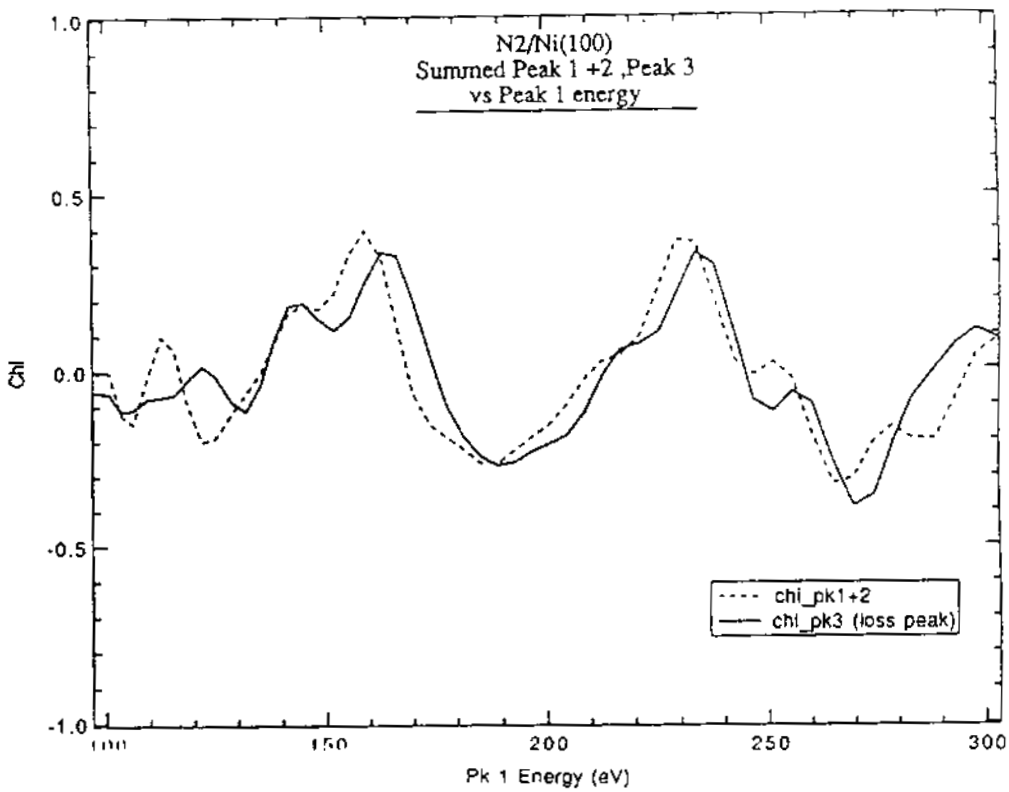

Fig. 3 ARPEFS Intensity of Peaks 1+2 (main line core levels) and Peak 3 (satellite peak) as a Function of Kinetic Energy.

HIGH RESOLUTION IN THE SOFT X-RAY RANGE FROM A TOROIDAL GRATING MONOCHROMATOR

T. Reich 1,2), Z. Hussain 1), E. Moler 1), M. Blackwell 1), G. Kaindl 1,3), D. A. Shirley 2), and M. R. Howells 1)

1) Lawrence Berkeley Laboratory, University of California, Berkeley, CA 94720, USA
2) Pennsylvania State University, University Park, PA 16802, USA
3) Institut für Experimentalphysik, Freie Universität Berlin, Arnimallee 14, W-1000 Berlin 33, Germany

Abstract

A resolving power, $E/\Delta E$, of $\geq$ 13,000 has been achieved with the modified 6m/160° Toroidal Grating Monochromator (TGM) installed on the Beam Line 8-1 at the Stanford Synchrotron Radiation Laboratory (SSRL). The resolving power of the TGM was increased by replacing the entrance and exit slits with high-precision slits, masking the horizontal part (short radius) of the grating, and improving the TGM scanning mechanisms. To determine the performance of the monochromator, we measured the dependencies of resolution and photon flux on the entrance and exit slit widths, the exit slit position, and the masking of the grating [1].

Introduction

Toroidal Grating Monochromators (TGM's) have been extensively used in various synchrotron radiation facilities. The TGM is generally known to have a moderate energy resolution with a high throughput [2]. The performance of TGM 8-1 has been improved by replacing the old entrance and exit slits by high-precision slits based on a flexural design which is used for the Lawrence Berkeley Laboratory Spherical Grating Monochromator on BL 6-1 at SSRL [3]. Both vertical and horizontal apertures are continuously adjustable from a few microns to 2 mm and 4 mm, respectively. A new micro-stepping motor (100,000 steps per revolution) controlled by a Mitutoyo linear encoder (Laser Holoscale with a resolution of 10 nm) drives the sine bar which moves the grating. This enabled us to sweep the photon energy in steps of less than one meV.

Experimental

The monochromator resolution in the energy range of 25 - 65 eV was derived from photoionization measurements of extremely narrow core-excitation resonances in He and Ne with natural linewidths that are much smaller than the value of the monochromator resolution. The photonflux was measured with a Si n-on-p photodiode.

Results

With 10 micron vertical entrance and exit slit widths and 32 % mask opening of the grating, the monochromator has a resolution (FWHM) of 5.0±0.7 meV at a photon energy of 64.5 eV and a flux of $2x10^7$ photons/sec/100 mA (see Fig. 1).

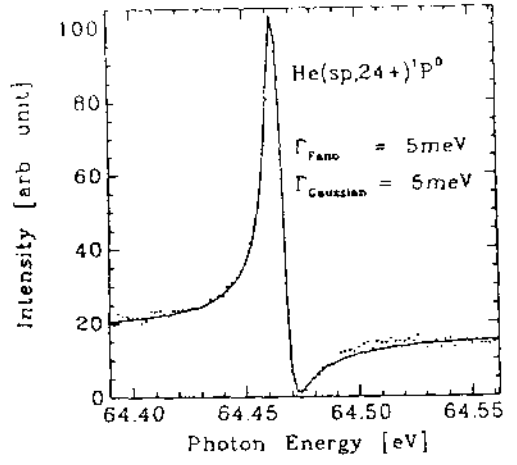

Figure 1. Photoionization spectrum from He gas showing the autoionizing double-excitation state of He $(sp,24+)^1P^0$. The solid curve is a fit with G_{Fano} = 5.0 meV and $G_{Gaussian}$ = 5.0 meV.

Fig. 2 shows a scan of the monochromator output over the energy range covered by the 823 l/mm grating.

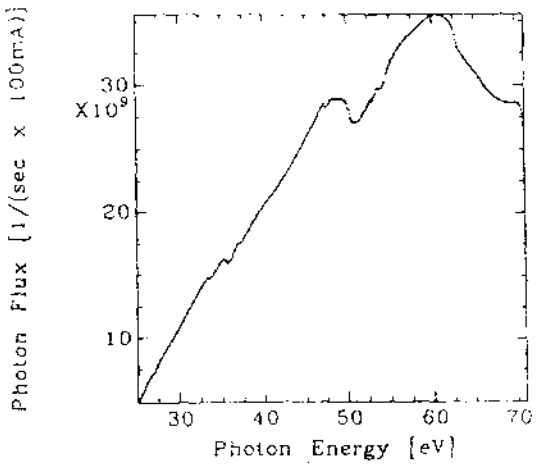

Figure 2. The monochromator output from the 823 l/mm grating detected with a Si photodiode and normalized to 100 mA ring current. The horizontal/vertical opening of the entrance and exit slits were 3 mm/200 μm and 1.5 mm/200 μm, respectively.

Fig. 3 shows the importance of a movable exit slit for achieving a high resolution over the available energy range.

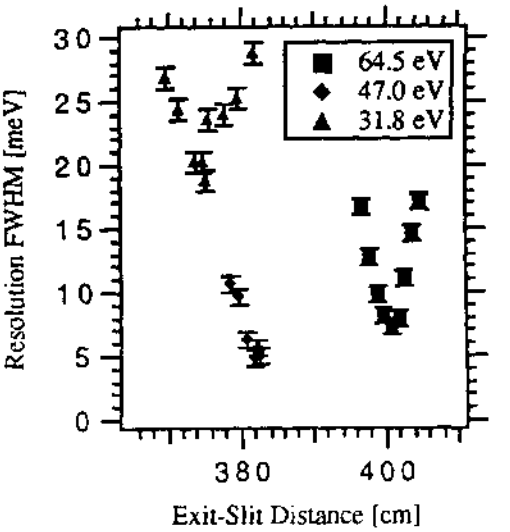

Figure 3. The measured monochromator linewidth (FWHM) as a function of the exit-slit distance. Entrance and exit slits vertical openings were kept at 20 μm with 48% mask opening of the grating. The 47 eV curve is incomplete, with the data extending barely through the minimum.

The effect of masking a part of the grating to reduce aberrations and thus improve the resolving power of the monochromator is shown in Fig. 4. Because without masking the monochromator resolution is the same for 10 μm

and 20 μm slit width, the resolution is not slit-width limited but determined by the aberrations of the grating. As can be seen from Fig. 4, the aberration decreases with increased masking of the grating.

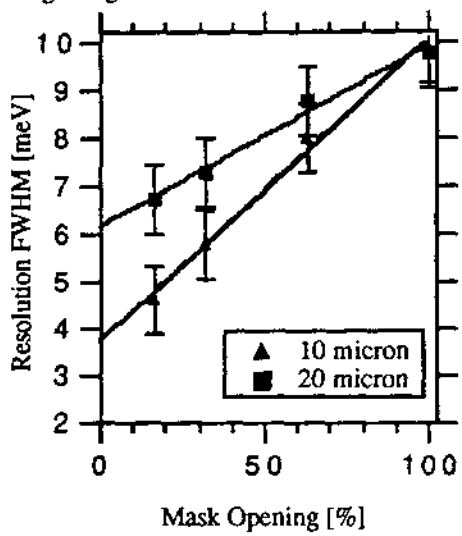

Figure 4. The measured monochromator linewidth (FWHM) at 64.5 eV plotted versus horizontal mask opening for vertical entrance and exit-slit openings of 10 μm and 20 μm. The horizontal entrance/exit aperture was kept at 3 mm/2 mm. The solid line is a linear least-square fit to the data.

Conclusion

We have shown that it is possible to achieve ultrahigh resolution, at the expense of the flux, in the soft x-ray energy range from a conventional, moderate-resolution Toroidal Grating Monochromator with a movable exit slit. An ultimate resolving power of 13,000 was obtained by improving the accuracy of the entrance and exit slits as well as the driving mechanism, and by horizontally masking about half of the grating.

Acknowledgment

We thank P. Pianetta and M. Weber for their help in the development of the slits and G. Husek for fabricating the slits and mounting of the encoder. We appreciate the efforts of M. Rowen and the SSRL vacuum group. This work was supported by the Director, Office of Energy Research, Office of Basic Energy Sciences, Chemical Sciences Division of the U. S. Department of Energy, LBL under Contract No. DE-AC03-76SF00098, LLNL under contract number W-7405-ENG-48. G. K. was supported by the Bundesminister für Forschung und Technologie, Project No. 05-5KEAXI3/TP03. T. R. thanks the Alexander von Humboldt Foundation for support through a Feodor Lynen Fellowship, and Penn State University for additional support.

References

1. T. Reich, Z. Hussain, E. Moler, M. Blackwell, G. Kaindl, D. A. Shirley, and M. R. Howells, submitted to Rev.Sci.Instr.

2. K. G Tirsell and V. P. Karpenko, Nucl. Instr. and Meth. **A291** (1990)511 and references therein.

3. P. A. Heimann, F. Senf, W. R. McKinney, M. R. Howells, R. D. van Zee, L. J. Medhurst, T. Lauritzen, J. Chin, J. Meneghetti, W. Gath, H. Hogrefe, and D. A. Shirley, Phys. Scr., **T31** (1990)127.

SPIN POLARIZED 4f PHOTOEMISSION STUDIES OF EPITAXIAL Gd(0001) FILMS ON W(110)

H. Tang [1], D. Weller[2], T.G. Walker[1], J. C. Scott[2], C. Chappert[2], H. Hopster[1], A.W. Pang[2], D.S. Dessau[3] and D. P. Pappas[2]

[1]Department of Physics and Institute for Surface and Interface Science, University of California, Irvine, Irvine, CA 92717-4575
[2]IBM Research Division, Almaden Research Center, 650 Harry Road San Jose, CA 95120
[3]Stanford Electronics Laboratory, Stanford University, Stanford, CA 94309

One of the most intriguing phenomena in surface magnetism is a situation in which the surface behaves differently from the bulk. Magnetic surface reconstruction (MSR) refers to a situation where the spin orientation at the surface is different from the bulk. Surface enhanced magnetic order (SEMO) corresponds to a situation in which the surface orders magnetically above the bulk Curie temperature. Most of the studies to date on surface magnetic behavior have been directed toward surfaces and ultrathin films of 3 d transition metals (Fe, Ni, Co). While the surface magnetic properties of these systems have been found to be different, *e.g.* altered surface moments, no indications of MSR or SEMO have been observed. Rare earth systems, on the other hand, exhibit a great variety of bulk ordering phenomena and can be expected to show interesting surface ordering. Early electron capture experiments on polycrystalline Gd films showed evidence for SEMO [1]. Spin polarized electron diffraction (SPLEED) on single crystal Gd(0001) films confirmed the existence of SEMO [2]. Spin polarized photoemission experiments showed small 4f polarizations, unexpected for a ferromagnetically ordered surface. The small 4f polarizations were ascribed to an antiferromagnetic alignment of the surface layer with respect to the bulk. Recent all-electron first-principles electronic structure calculations on Gd(0001) indeed favor an antiferromagnetic surface alignment [3]. The calculations also predict an outward surface relaxation, which was not confirmed in I - V LEED studies on bulk Gd(0001) samples [4].

In the present experiments we measured the temperature dependent spin polarization of photoemitted electrons from the Gd 4f levels. Epitaxial Gd(0001) films approximately 400 Å thick were grown in-situ on W(110) at a rate of 0.7 Å/s. The substrate was either at room temperature or at 650 K during growth. The room temperature growth promotes layer-by-layer growth, however with initially a large amount of disorder as judged by diffuse LEED patterns. Annealing to 825 K for a few minutes results in sharp (1x1) LEED patterns. The high-temperature grown films, although of good structural quality as inferred from LEED, exhibit more surface roughness since Gd grows as 3-dimensional islands on W(110) at elevated temperature.

Besides the sample characterization by Auger and LEED the magnetic properties were measured by magneto-optic Kerr effect (MOKE) hysteresis loops [5] and spin polarized secondary electron emission spectroscopy [6]. Subsequent quantitative I - V LEED analysis [7] confirmed the surface contraction as found on bulk Gd(0001) samples [4]. Thus, our thick Gd epitaxial films on W(110) can be expected to resemble the intrinsic surface magnetic behavior of the free Gd(0001) surface.

The spin polarization of the Gd 4f levels was measured in a spin polarized electron spectrometer based on a medium-energy (20-30kV) retarding-field Mott detector. In this apparatus the in-plane and out-of-plane spin polarization components can be measured. The photoemission experiments we performed at 149 eV photon energy. At this energy photoemission of the Gd 4f electrons occurs through a 4d-4f resonant excitation channel as well as the direct photoionization process. Control experiments at lower photon energy showed that identical spin polarization values are obtained for the resonant and direct processes. The increased intensity of the

resonant process allowed us to perform temperature sweeps in the range 140-350 K within about one hour. This is important due to the extreme sensitivity of the Gd surface to contamination from the residual gas. Figure 1 shows a comparison of the temperature dependent 4f polarization for two films prepared under different conditions. The films grown at room temperature(and subsequently annealed) show a larger spin polarization than the films grown at elevated temperature. At 140 K we find polarization values of 65% on the films grown at room temperature. An extrapolation to T=0 yields values close to 100%, which is the expected value for completely aligned 4f moments.

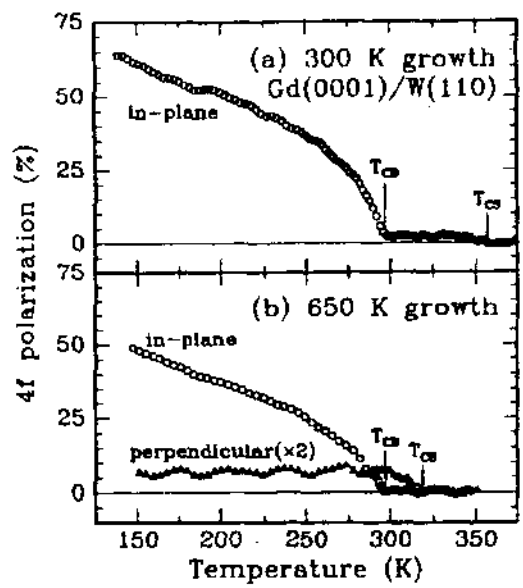

Fig. 1 *Temperature dependence of the 4f spin polarization from Gd(0001) films grown on W(110) at room temperature (upper panel) and 650K (lower panel)*

On the films grown at elevated temperatures the polarization values are consistently lower (about 50% at 140K). We attribute this to the surface roughness on these films which alter their magnetic behavior. The observed high values of the 4f spin polarization rule out an antiferromagnetic surface coupling which was inferred from previous photoemission experiments. The surface layer clearly couples predominantly ferromagnetically to the bulk. Upon heating the polarization decreases. However, a small but finite polarization persists above the bulk Curie Temperature T_{Cb} until the polarization vanishes at the surface Curie temperature T_{Cs}. The surface Curie temperature enhancement was found to be in the range of 20-50 K, depending very critically on the cleanliness and structural perfection of the film. The surface enhanced Curie temperature is especially apparent in the occurrence of an out-of plane spin polarization component as shown in the lower panel of Fig. 1. This perpendicular component is unaffected by the bulk transition and only vanishes at the surface transition temperature T_{Cs}. Thus, the surface layer behaves almost as an independent entity from the bulk, save for the ferromagnetic alignment of the in-plane component below T_{Cb}. The rather abrupt decrease at T_{Cs} is indicative of two-dimensional critical behavior.

In summary, we have shown the existence of surface enhanced magnetic order on Gd(0001) surfaces. while the surface-to-bulk coupling is predominantly ferromagnetic the surface layer has a canted spin configuration as evidenced by an out-of-plane polarization component.

1. C. Rau and S. Eicher, in Nuclear Methods in Materials Research edited by K. Bethge, H. Baumann, H. Jex, and F. Ranch (Vieweg Braunschweig, 1980)
2. D. Weller, S. F. Alvarado, W. Gudat, K. Schröder, and M. Campagna, Phys. Rev. Lett. 54, 1555 (1985)
3. R. Wu, C. Li, A. J. Freeman, and C. L. Fu, Phys. Rev. B44, 9400 (1991)
4. J. Quinn, Y. S. Li, F. Jona, and D. Fort, Phys. Rev. B46, 9694 (1992)
5. C. Chappert, D. Weller, H. Tang, J. C. Scott, H. Hopster, D. P. Pappas, to be published.
6. H. Tang, T. G. Walker, H. Hopster, D. P. Pappas, D. Weller, and J. C. Scott, Phys. Rev. B47, (1993); in press.
7. G. Giergel, A. W. Pang, H. Hopster, J. M. Lawrence, J. C. Hemminger, to be published.

Chemisorption of Methanol and Methyl Mercaptan on Zinc Oxide and Cuprous Oxide Single Crystal Surfaces

Paul Jones, Jeff Guckert, Jennifer May, Brad Reitz, Edward I. Solomon*

Department of Chemistry, Stanford University, Stanford, CA 94305

INTRODUCTION

Understanding the chemisorption properties of methanol and methyl mercaptan on cuprous and zinc oxide surfaces is of critical importance from both heterogenous and biological catalytic perspectives. First, ZnO is the methanol synthesis catalyst ($CO + 2H_2 \leftrightarrow CH_3OH$) and is promoted by Cu(I) substituted into the Zn(II) sites on the surface. It has been suggested that one of the promoter effects of the copper could involve activating different reaction mechanisms with different intermediates on the two surfaces and in particular that a hydroxy-methyl mechanism occurs on ZnO as compared to a methoxide intermediate on Cu/ZnO. One would expect different chemisorbed species from methanol deprotonation on the cuprous oxide as compared to the zinc oxide surfaces if this role for the promotion effect is correct. Further the ZnO($10\bar{1}0$) and (0001) surfaces have different surface stochiometries (coordinatively unsaturated $Zn^{+2} + O^{2-}$ dimer sites on the former vs Zn^{+2} sites on the latter) and it is important to understand their relative effectiveness with respect to deprotonation of chemisorbed species as this relates to the heterolytic cleavage of dihydrogen. Also, the copper promoted surface is much more sensitive to poisoning by sulfur containing species and the methyl mercaptan reactivity on ZnO and Cu_2O probes the electronic origin of this poisoning effect in parallel with our earlier research on the decomposition of H_2S. Finally, the blue copper sites in electron transfer proteins involve a copper-thiolate bond. Much is known about the oxidized sites in these proteins from traditional spectroscopic methods as these involve an open shell d^9 metal ion. However, there is essentially no experimental data on the thiolate-Cu(I) bond in the reduced sites. If the methyl mercaptan deprotonates on the Cu_2O surface, the resultant thiolate-Cu(I) surface species would provide a critically important model to experimentally define this bonding interaction in bioinorganic chemistry and would also allow one to calibrate and evalute self consistent field-Xα-scattered wave electronic structure calculations on the blue copper site.

EXPERIMENTAL

Experiments were performed on beamline III-1 at the Stanford Synchrotron Radiation Laboratory using a grasshopper monochrometer. The surfaces were cleaned in UHV by a series of Ar^+ ion

sputtering/annealing cycles. Variable inlet and exit slits on the monochrometer were maintained at a constant photon energy resolution of 0.2 eV, and the pass energy on the double pass CMA was held at 10 eV resulting in a constant instrument resolution of 0.2 eV. Mallinckrodt absolute, low acetone CH_3OH (99.9%) purified by freeze, pump, thaw cycles and research grade (Matheson, 99.5%) CH_3SH were used. Gas was introduced to the experimental chamber via a seperate UHV line through a Varian leak valve. The gas pressure was monitored using an ionization gauge. All experiments were carried out at a sample temperature of 130K, and no sample charging was observed, thus all data is referenced to the sample Fermi level.

RESULTS AND DISCUSSION

Low coverages of methanol result in similar 4 peak difference spectra (Figure 1) on $Cu_2O(111)$ and $ZnO(10\bar{1}0)$ and (0001). This chemisorbed species has been assigned to methoxide; no evidence is observed for the hydroxy-methyl species on ZnO surfaces. These results indicate that the difference in reactivity of Cu(I) vesus Zn(II) surface sites in methanol synthesis is not due to a difference in reaction mechanism or intermediate, but must relate to a difference in bonding in an earlier rate determining step of the catalytic reaction. Further, deprotonation of methanol is observed on both the polar and non-polar,dimer surfaces of ZnO. Therefore, the oxide must be available for reaction on the (0001)-zinc surface, and we are now looking for quantatative differences on the two ZnO surfaces through variable energy PES.

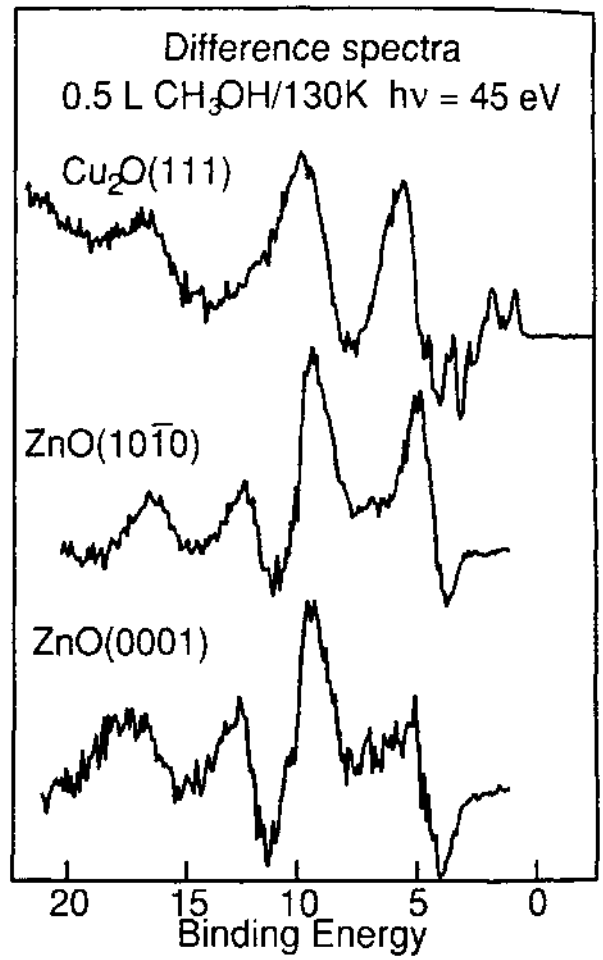

FIGURE 1: Difference (exposed minus clean) valence band PES spectra of CH_3OH (0.5 L) on $Cu_2O(111)$ and $ZnO(10\bar{1}0)$ and (0001). Taken at hv = 45eV at 130K.

Exposure of $Cu_2O(111)$ to CH_3SH at 130K results in the 3 peak difference spectra presented in Figure 2. These spectra are characteristic of a thiolate (CH_3SH^-) chemisorbed adsorbate at the Cu(I) surface site. Variable energy valence band spectra in Figure 2 allow the assignments of the peaks as indicated and show from photoionization cross sections that the S $3p_\pi$ level has little Cu(I) d contribution as there is no evidence of a delayed maximum in the hv =40 to 50 eV region. This is quite different from the oxidized

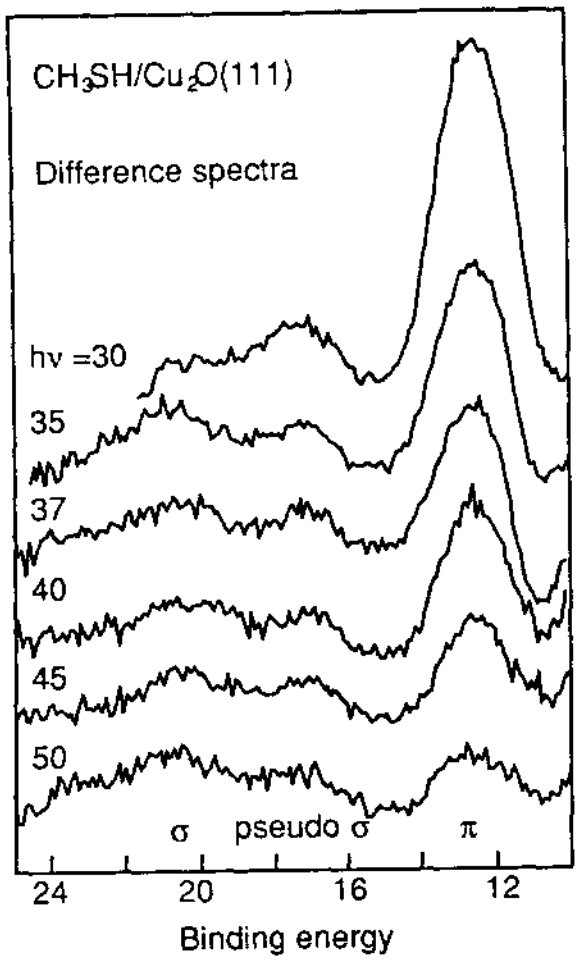

FIGURE 2: Difference spectra of .6 L CH_3SH on $Cu_2O(111)$ at 130K taken at the indicated photon energies.

Cu(II) site where the $d_{x^2-y^2}$-cysteine π bonding dominates the electronic structure. Thus there is a large change in electronic structure on reduction of these sites which can make a significant contribution to biological reactivity.

Structure of Sb monolayers on Ge(111)2x1: An X-ray standing waves study.

T. Kendelewicz (1), J. C. Woicik (2), . Herrera-Gomez (1), P. Pianetta (1), and W. E. Spicer (1).

(1) Stanford Electronics Laboratory, Stanford University, Stanford CA 94305

(2) National Institute of Standards and Technology, Gaithersburg MD 20899

We report results of an X-ray standing waves (XSW) structural study of annealed monolayers of Sb on cleaved surfaces of Ge(111)(2x1). Sb monolayers on Si or Ge are technologically important due to applications like delta doped structures in which a two dimensional thin layer of donors is confined inside a semiconductor. More recently, Sb interlayers were also successfully applied as surfactants to improve epitaxial growth of Si/Ge strained heterojunctions. The epitaxy of III-V semicinductors on Si or Ge is yet another application where understanding of group V (or III) elemental chemisorption is of great practical importance. From a fundamental point of view Sb and other column V overlayers on elemental semiconductor surfaces are of interest because of well ordered and thus calculable structures they form.

For the (1 monolayer of Sb)/Ge(111) interface, which is the subject of our investigation, only recently did structural information become available. Specifically, van Silfhout et al [1] demonstrated with X-ray diffraction the formation of Sb zig-zag chains on the c(2x8) reconstructed wafer surface, while Wan et al [2] using LEED proposed a substitutional geometry on an annealed cleaved single crystal with a 1x1 initial surface reconstruction. Our results, although taken on surface with different intial relaxation, are very similar to that of van Silfhout et al [1]. The substitutional geometry for the 2x1 initial surface can be ruled out all together.

The interfaces used in this study were prepared by evaporating 1ML of Sb on cleaved Ge(111) and annealing to 500 °C. The XSW data were taken on the "Jumbo" double crystal monochromator equipped with a pair of InSb(111) crystals by monitoring the intensity of the Sb 3d photoemission peak in the constant initial state (CIS) mode.

Fig. 1 shows the Ge(111) reflection and the Sb 3d yield together with the best fits. From the fit we obtain coherent distance of D=3.00(±0.05) Å and coherent fraction F=0.85. The value F supports a single site chemisorption with some structural disorder. The measured distance rules out the possibility of substitutional geometry in which Sb replaces the upper half of the Ge double layer and for which a distance of 3.68 Å is expected. The results of this study show that Sb atoms are located almost directly on top of the surface Ge atoms on an ideal (unreconstructed) Ge(111) surface in only very slightly tilted Saiwatz chains or trimers.

The work was performed under ONR contract N00014-92-J-1280 and was additionally supported by the National Institute of Standards and Technology.

References

1. R. G. van Silfhout, M. Lohmeier, S. Zaima, J. F. van der Veen, P. B. Howes, C. Norris, J. M. C. Thornton, and A. A. Williams ;Structure determination of the Ge(111)-2x1-Sb surface using X-ray diffraction. Surf. Sci. **271**, 32 (1992).

2. K. J. Wan, W. K. Ford, and J. C. Hermanson; Observation of LEED I-V analysis of the Ge(111)-1x1-Sb system. Surf. Sci. Lett. **268**, L253 (1992).

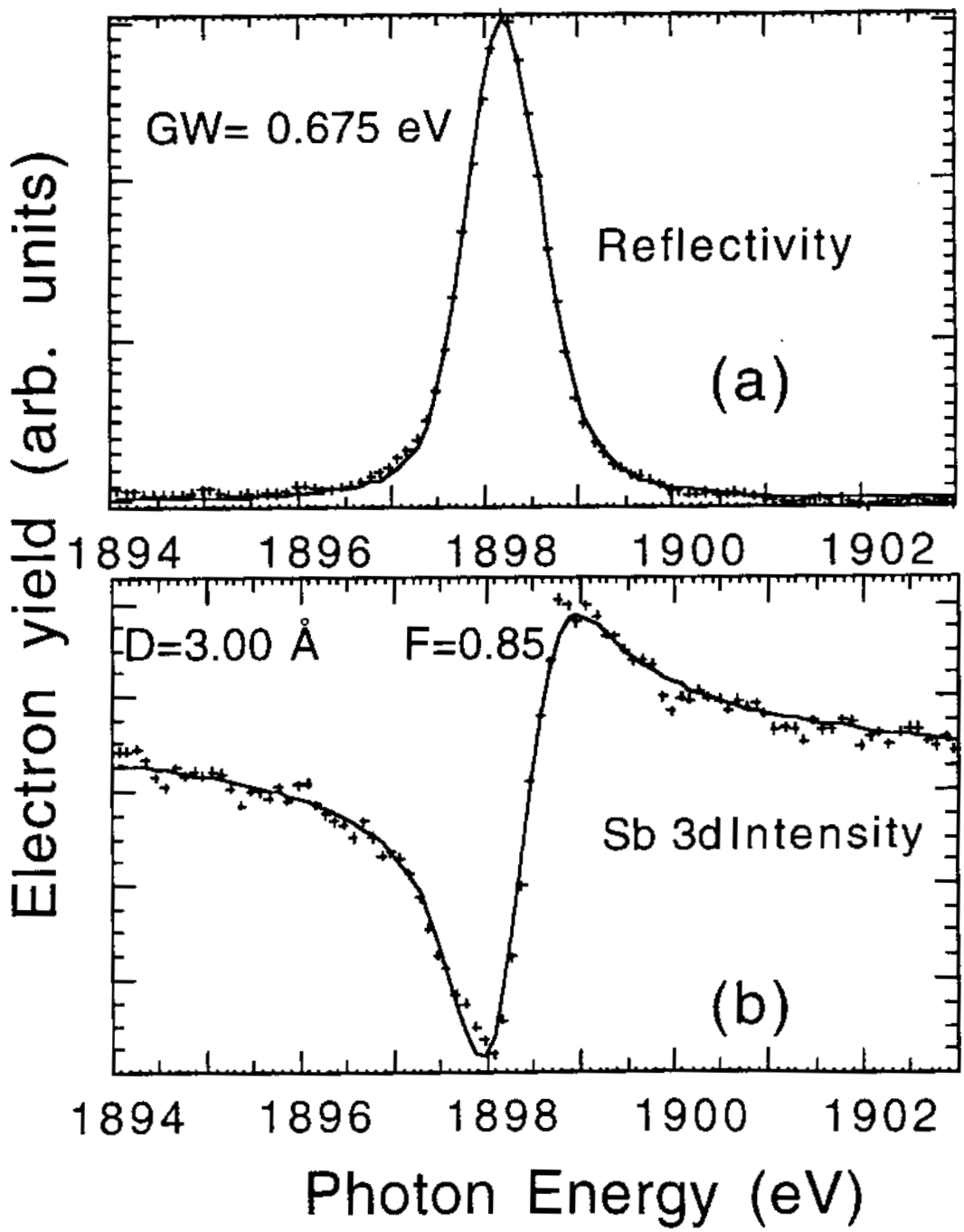

The Si(111) √3x√3-In surface: An unrelaxed T_4 geometry

J.C. Woicik[1], T. Kendelewicz[2], Alberto Herrera-Gomez[2], K.E. Miyano[3], P.L. Cowan[4], C.E. Bouldin[1], P. Pianetta[2], and W.E. Spicer[2]

1) National Institute of Standards and Technology, Gaithersburg MD 20899

2) Stanford Electronics Laboratory, Stanford CA 94305

3) Department of Physics, Tulane University, New Orleans LA 70118

4) Argonne National Laboratory, Argonne IL 60439

Abstract

Back reflection x-ray standing waves (BRXSW) and surface extended x-ray absorption fine structure (SEXAFS) have determined the atomic coordinates (the perpendicular displacement and the near-neighbor bond lengths) at the Si(111) √3x√3-In interface. Although the In adatoms are found to reside at a single position, 2.11 ± 0.04 Å above the first Si bilayer, amphoteric first-neighbor bonds to the substrate are found: 2.73 ± 0.02 Å to the first- and 2.49 ± 0.03 Å to the second-layer Si atoms, respectively. Because we have independently measured both the perpendicular distance of the adatoms to the bulk diffracting planes and the near-neighbor bond lengths of the adatoms to the first- and second-layer Si atoms, we have also determined the amount of substrate relaxation. Contrary to the accepted model, the T_4 geometry is not relaxed; i.e., the first- and second-layer Si atoms are in their ideal undistorted bulk-like geometry.

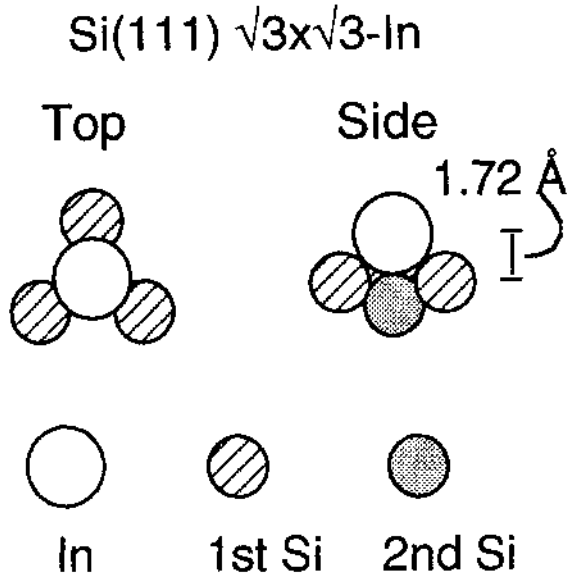

Extended x-ray absorption fine structure determination of bond-length conservation at the clean InP(110) surface

J.C. Woicik[1], T. Kendelewicz[2], K.E. Miyano[2], M. Richter[3],

C.E. Bouldin[1], P. Pianetta[2], and W.E. Spicer[2]

1) National Institute of Standards and Technology, Gaithersburg MD 20899

2) Stanford Electronics Laboratory, Stanford University, Stanford CA 94305

3) Department of Applied Physics, Stanford University, Stanford CA 94305

Abstract

Surface sensitive P LVV Auger yield extended x-ray absorption fine structure (EXAFS) has determined the near-neighbor bond lengths at the clean InP(110) surface. The surface sensitive data show no change in the first-neighbor P-In bond length but a measurable, ~ 0.1 Å, expansion of the average P-P second-neighbor distance over bulk sensitive total electron yield data recorded simultaneously. Together with recent surface sensitive x-ray standing wave (XSW) results [Woicik et al., Phys. Rev. Lett. **68**, 341 (1992)], these data establish the bond-length conserving rotation model for the non-polar III-V semiconductor cleavage surfaces.

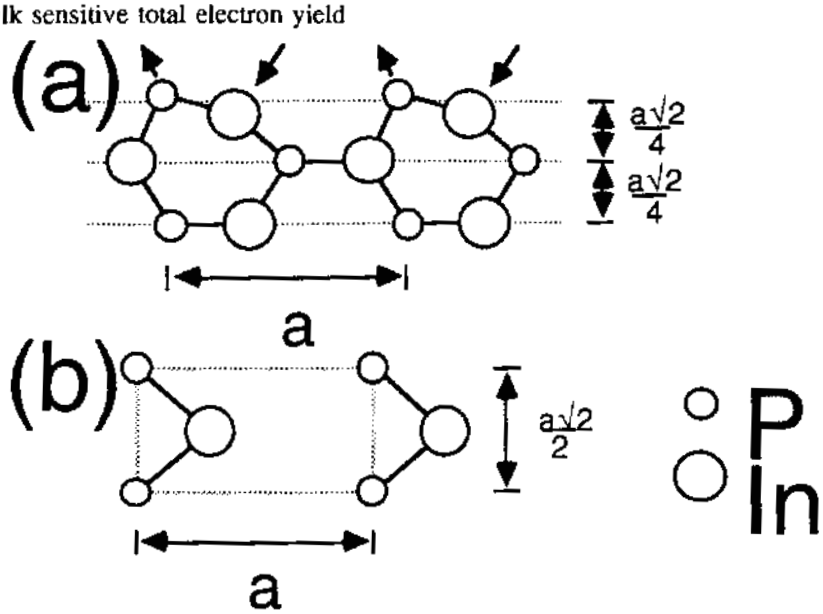

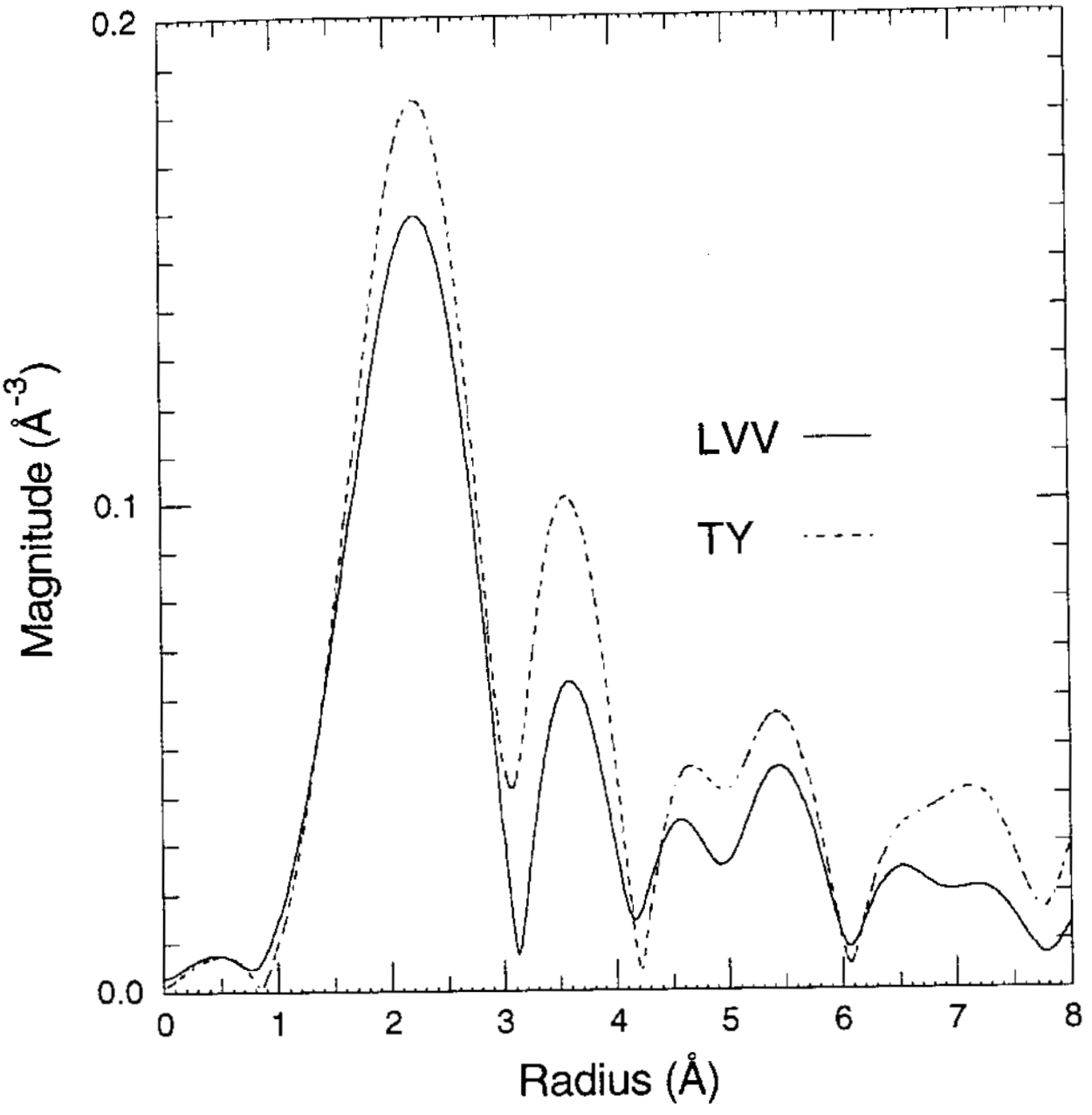

Determination of the Geometrical Configuration of Bi on GaAs (110) by X-Ray Standing Wave Triangulation

Alberto Herrera-Gómez[1], T. Kendelewicz[1], J.C. Woicik[2], K.E. Miyano[3], P. Pianetta[1], S. Southworth[2], P.L. Cowan[4], B.A. Karlin[2], W.E. Spicer[1].

(1) Stanford Electronics Laboratory. Stanford, California 94305.
(2) National Institute of Standards and Technology. Gaitherburg, Maryland 20899.
(3) Department of Physics, Tulane University, New Orleans, LA 70118.
(4) Argonne National Laboratory. Argonne, IL 60439.

We report results from a X-Ray Standing Wave (XSW) Triangulation study of the structure of epitaxial Bi overlayers on GaAs (110). This system was investigated by low energy electron diffraction (LEED) and scanning tunneling microscopy (STM) by McLean et al[1]. Their results indicate that Bi forms an ordered 1×1 monolayer with two Bi atoms per substrate surface unit cell. Results from core level photoemission[2] (PES) show two chemical species of the same intensity, which are associated with each of two Bi atoms. Tight-binding total-energy (TBTE) calculations[4] found two possible structures: the Epitaxial Continued Layer Structure (ECLS), and the Epitaxial on Top Structure (EOTS). Ford et al[5] tested both ECLS and EOTS models for Bi/GaAs using dynamical LEED. They found the most likely structure to be ECLS, although the discrimination is not as clear as in the Sb/GaAs case[3].

The X-Ray Standing Wave method (XSW) can unambiguously provide atomic geometries. The Bragg planes used in our study were (111), (11-1), and (220). Our results are consistent only with the Epitaxial Continued Layer Structure model. Our analysis is based on the prior experimental results that indicate two equally populated Bi sites.

The experiments were performed on the "Jumbo" beamline at the Stanford Synchrotron Radiation Laboratory (SSRL) and the X-24A beam line at the National Synchrotron Light Source (NSLS). Figure 1 shows the experimental data together with the fits to the reflectivity and standing wave yield spectra for each of the three reflections.

Our value for the order parameter ϕ is 0.32±0.01. This means that 32% of the Bi atoms are in one site and 32% are in the other; the remaining 36% are at incoherent positions. This value of disorder is larger than that obtained for Sb/GaAs[7], which is ~10%. This is as expected because there is a larger mismatch between the Bi chains and the GaAs substrate. An even larger disorder of 42% is found for the Sb/GaP system[6].

To facilitate comparison with previous work, the structural results displayed in table 1 are given in the usual terminology, which is defined in figure 2. This figure shows the position of the Bi sites according to

our results. The Bi positions are close to those of the next layer of bulk GaAs, so our results determine that the structure of the Bi overlayer is given by ECLS. Therefore, our comparison is made with the ECLS results of LEED[5] and TBTE[4].

The larger discrepancy between the XSW and LEED results is in the displacement parallel to the surface, where the sensitivity of LEED is smaller. For displacements perpendicular to the surface, the agreement is excellent. The overall comparison with the theoretical approach (TBTE) is poorer.

REFERENCES

1) A.B. McLean, R.M. Feenstra, A. Taleb-Ibrahimi, and R. Ludeke. Phys. Rev. B **39**, No. 17, p 12925 (1989).

2) J.J. Joyce, J. Anderson, M.M. Nelson, and G.J. Lapeyre. Phys. Rev. B **40**, No. 15, p 10412 (1989).

3) C.B. Duke, A. Paton, W.K. Ford, A. Kahn and J. Carelli. Phys. Rev. B **26**, No. 2, p 803 (1982).

4) A.M. Bowler, J.C. Hermanson, J.P. LaFemina, C.B. Duke. J. Vac. Sci. Technol. B **10**, No. 4, p. 1953 (1992).

5) W.K. Ford, T. Guo, D.L Lessor, C.B. Duke. Phys. Rev. B **42**, No. 14, p 8952 (1990).

6) K.E. Miyano, T. Kendelewicz, J.C. Woicik, P.L. Cowan, C.E. Bouldin, B.A. Karlin, P. Pianetta and W.E. Spicer. Phys. Rev. B **46**, No. 11, p. 6869 (1992).

7) T. Kendelewicz, J.C. Woicik, K.E. Miyano, A. Herrera-Gómez, P.L. Cowan, B.A. Karlin, C.E. Bouldin, P. Pianetta and W.E. Spicer. Phys. Rev. B **46**, No. 11, p. 7276 (1992).

Table 1. Comparison of the results of this work (XSW) to other techniques. The definition of the terms is in figure 2.

	$\Delta_{1,\perp}$	$\Delta_{1,y}$	$d_{12,\perp}$	$d_{12,y}$
TBTE	0.11±0.2	2.49±0.2	2.56±0.2	3.37±0.2
LEED	0.09	1.98	2.52	4.62
XSW	0.14±0.1	2.0±0.2	2.5±0.08	3.85 ±0.2

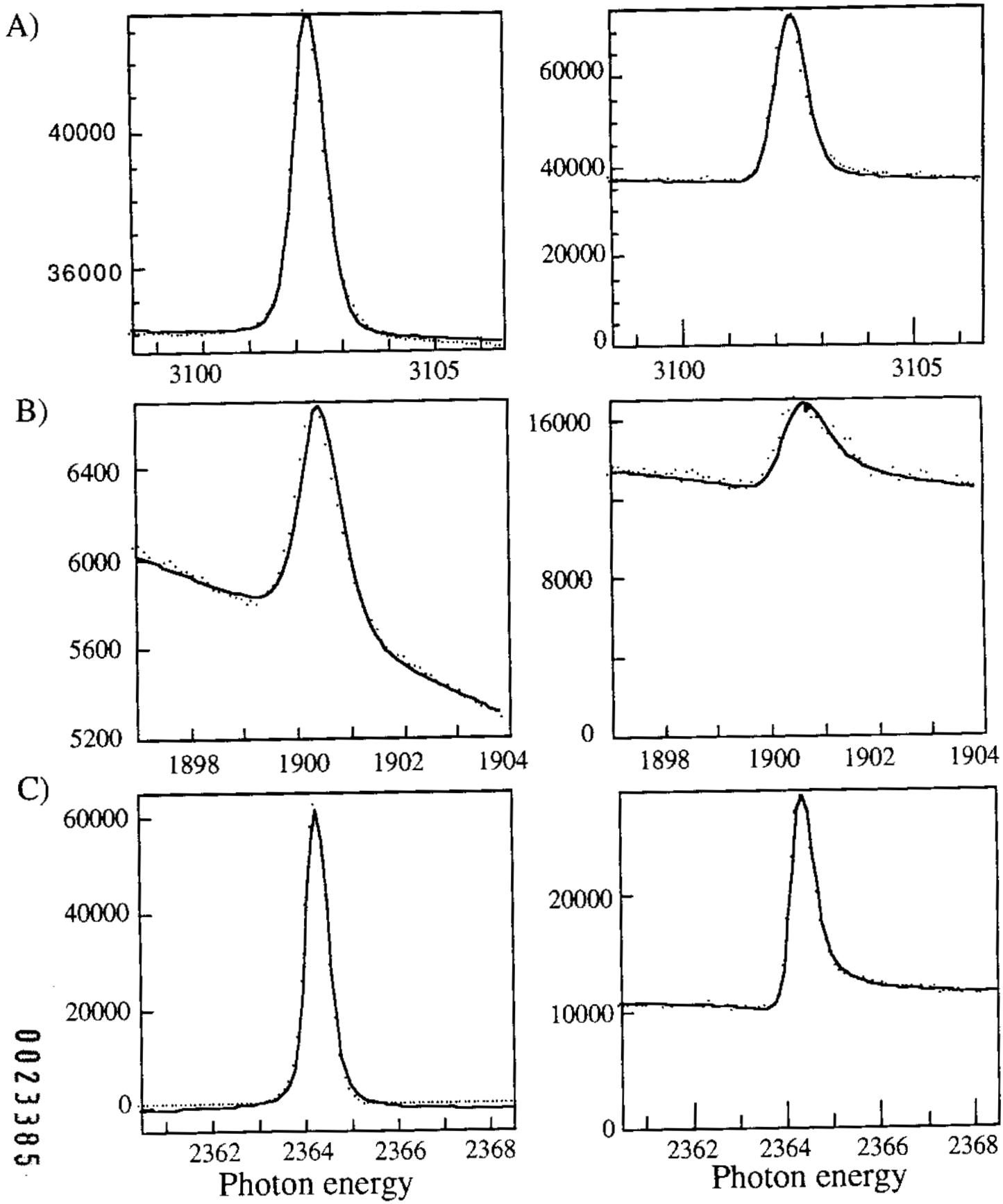

Figure 1. a) Reflectivity and fit for the (220) back reflection diffraction and Bi yield spectrum. b) Same for the (11) back reflection diffraction. c) Same for the (111) off-normal reflection.

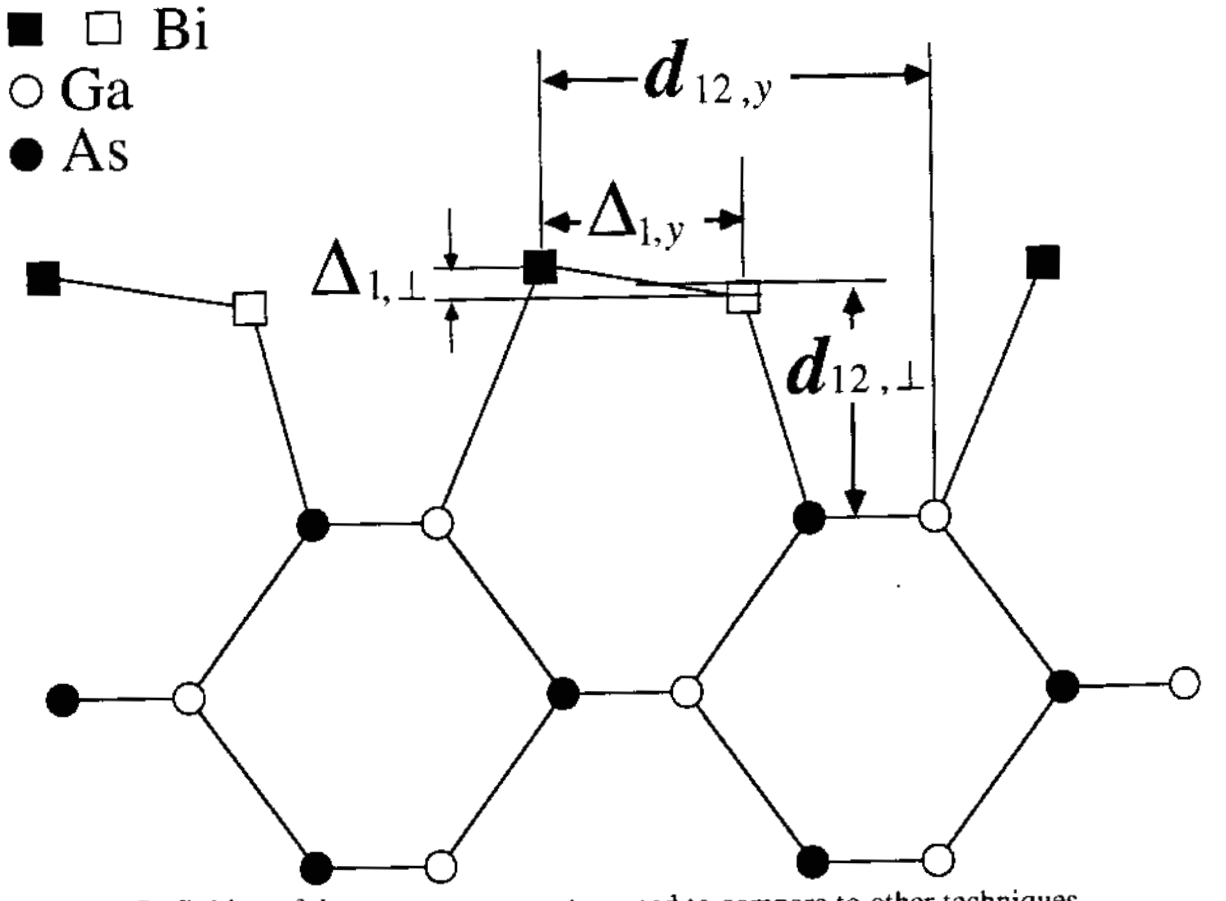

Figure 2. Definition of the structure parameters used to compare to other techniques.

FIRST TEST OF YB_{66} IN THE JUMBO MONOCHROMATOR

M. Rowen, Z. U. Rek

SSRL, P.O. Box 4349, Stanford Ca, 94309

In August the first successful operation of a double crystal monochromator with a pair of YB_{66} crystals was done at SSRL on Beam Line 3-3. YB_{66} has been singled out as a potential high resolution diffracting element in the energy range 1-2 keV[1] which includes the K edges of the important elements Mg at 1303 eV, Al at 1559 eV and Si at 1839 eV. Previously three different crystals Beryl $(10\bar{1}0)$, Quartz $(10\bar{1}0)$ and InSb (111) were used to cover these edges. Both Beryl and Quartz are insulating oxide crystals that damage readily in the intense x-ray beams from synchrotrons. YB_{66} is a semiconductor with a cubic structure and lattice parameter of 23.44Å. Large good quality single crystals were grown by Tanaka and Kamimura using a indirect heating floating zone method[2]. The crystals were carefully characterized using white beam X-ray topography and rocking curve measurements with Cu K_α[3,4]. The area of lowest strain and defect density were observed at the float zone end along the core of one boule.

A pair of crystals, approximately 18mm x 10mm, were selected from this boule and installed in the JUMBO monochromator. The crystals were oriented with the (400) planes (2d = 11.72Å) in a parallel non-dispersive geometry. Rocking curves were made by rotating the second crystal. Variations in rocking curve width and symmetry were observed by moving the beam across the crystals. The FWHM of the rocking curves were 0.23 eV at 1100 eV to 2.0 eV at 2500 eV, figure 1. Using filters to reduce the power on to the first crystal to maximum of 1 watt, and then limiting the vertical beam divergence generally improved resolution, but this was not always observed, possibly due to not aligning the beam on to the least strained parts of the crystals. When sampling a small area in the highest quality part of the crystals, a resolving power close to theoretical was measured, FWHM 0.16 eV at 1100 eV and 0.55 eV at 1500 eV.

The output of the monochromator was measured from 1100 eV to 2500 eV with a Au diode, figure 2. The large decrease in flux from 1700 to 2000 eV is due to absorption from the Y L_3 edge at 2080 and the Pt M_5 edge at 2122 eV.

The maximum power on the first crystal was 15 watts. With un-cooled crystals the heating of the first crystal is significant. Even with filters inserted before the monochromator to reduce the power to less than 1 watt the heating is observable. Further evaluation of thermal heating, reflectivity and energy resolution are planned.

The project has been performed in collaboration with Joe Wong from LLNL, T. Tanaka from NIRIM in Japan.

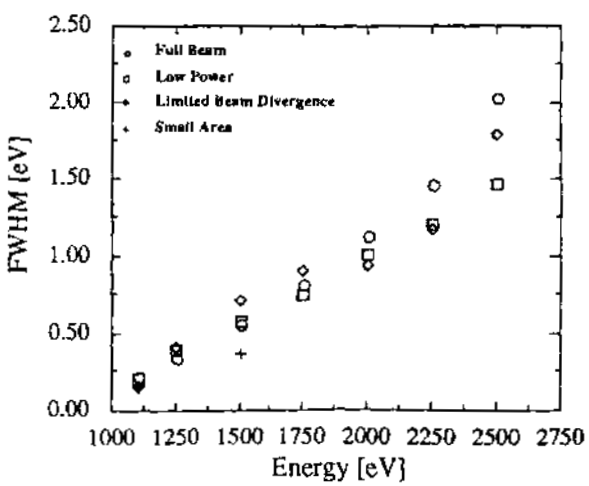

Figure 1. Double crystal rocking curves taken on JUMBO monochromator. Full Beam, ≤ 15 watts. Low power ≤ 1 watt. Limited Beam Divergence, vertical divergence ≈ .05 mrad. Small Area, ≈ 625 x 50 microns.

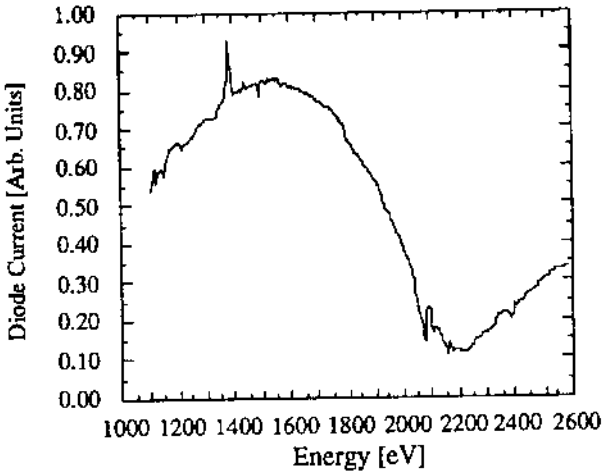

Figure 2. Throughput of Jumbo monochromator with YB_{66} crystals.

References:

1. J. Wong, G. Shimkaveg, W. Goldstein, M. Eckart, T. Tanaka, Z. Rek, H. Tompkins, Nucl. Instr. & Meth., A291, (1990), 243
2. Y. Kamimura, T. Tanaka, S. Otani, Y. Ishizawa, Z. Rek, J. Wong, J. Cryst. Growth, 128, (1993) 429
3. Z. Rek, J.Wong, T. Tanaka, Y. Kamimura, F. Schaefers, B. Muller, M. Krumrey, P. Muller, SPIE Proc., Vol. 1740, (1992), 173
4. Z. Rek, J.Wong, T. Tanaka, Y. Kamimura, SSRL Activity Report 1992

Anomalously Large Gap Anisotropy in the a-b Plane of Bi2212

Z.-X. Shen[1,2], D.S. Dessau[1,2], B.O. Wells[1,2], D.M. King[2], W.E. Spicer[2], A.J. Arko[3], D. Marshall[2], L.W. Lombardo[1], A. Kapitulnik[1], P. Dickinson[1], S. Doniach[1], J. DiCarlo[1,2], T. Loeser[1,2] and C.H. Park[1,2]
1. Department of Applied Physics, Stanford University, Stanford, CA 94305
2. Stanford Electronics Laboratory and Stanford Synchrotron Radiation Laboratory, Stanford University, Stanford, CA 94305
3. Los Alamos National Laboratory, Los Alamos, NM87545

A key to understanding the mechanism of high-T_c superconductivity is the symmetry of the superconducting order parameter. The conventional BCS theory has an s-wave order parameter, reflecting the spherically symmetric nature of the pair wave function. For the high-T_c cuprates, theoretical analysis on the crucial CuO_2 plane with consideration of the strong on-site Coulomb interaction leads to order parameter with other symmetries(e.g., d-wave or the extended s-wave). The symmetry of the order parameter is the central issue of the high-temperature superconductivity research.

Because the superconducting gap reflects the magnitude of the order parameter, the unique capability of angle-resolved photoemission measuring the gap as a function of crystal momentum provides an opportunity to probe this issue. We measured the gap of Bi2212 in **k**-space. Our data reveals a gap anisotropy in the a-b plane that is at least an order of magnitude larger than that of the conventional superconductors. In addition, we have observed spectra that is indicative of a node in the gap within the experimental limitation. The experimental data is qualitative imcompatible with angle the extended s-wave scenario. On the other hand, all aspects of the data (the anomalously large gap anisotropy, the specific **k**-dependence of the anisotropy, and the possible presence of the node along Γ-Y) can be well understood if we assume Bi2212 is a superconductor with the d_{x2-y2} order parameter.

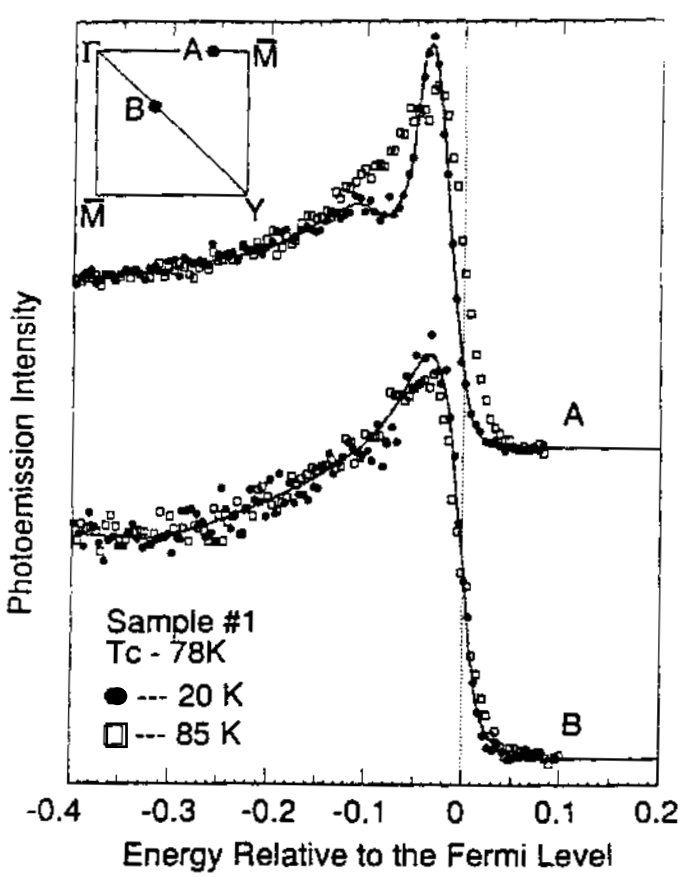

Fig.1 presents normal (open squares) and superconducting state (filled circles) ARPES spectra at **k**-space locations A and B. The spectral changes above and below T_c are caused by the opening of the superconducting gap. The change at A is quite visible, yielding a larger gap. The change at B is hardly visible, suggesting a very small or null gap.

Fermi Surface and Electronic Structure of $Nd_{2-x}Ce_xCuO_{4-\delta}$

D.M. King,[1] Z.-X. Shen,[1, 2] D.S. Dessau,[1,2] B.O. Wells,[1, 2] W.E. Spicer,[1] A.J. Arko,[3] D.S. Marshall,[1]
J. DiCarlo, [2] A.G. Loeser,[2] C.H. Park,[2] E.R. Ratner,[2] J.L. Peng,[4] Z.Y. Li,[4] and R.L. Greene [4]

[1]*Stanford Electronics Laboratory and Stanford Synchrotron Radiation Laboratory,*

[2]*Department of Applied Physics, Stanford University, Stanford, California 94305*

[3]*Los Alamos National Laboratory, Los Alamos, New Mexico 87545*

[4]*Center for Superconducting Research, Department of Physics, University of Maryland, College Park, Maryland 20742*

Using angle-resolved photoemission, we have succeeded in measuring the Fermi surface (FS) of $Nd_{1.85}Ce_{0.15}CuO_{4-\delta}$, a n-type high-$T_c$ superconductor, and overdoped metallic $Nd_{1.78}Ce_{0.22}CuO_4$. The observed FS is in good agreement with the predictions of local density (LDA) band calculations despite its failure to predict the insulating behavior of its parent compound, Nd_2CuO_4. In addition, it appears that the FS gets smaller with increased electron doping, in agreement with LDA calculations using a rigid-band picture. The observed simple electronic structure may be responsible for the more conventional physical properties of $Nd_{2-x}Ce_xCuO_{4-\delta}$ when compared to the other high-T_c cuprates. These findings are particularly important since this is the first time the FS of a one-layer compound has been studied, allowing us to unambiguously investigate the electronic structure of the essential CuO_2 plane.

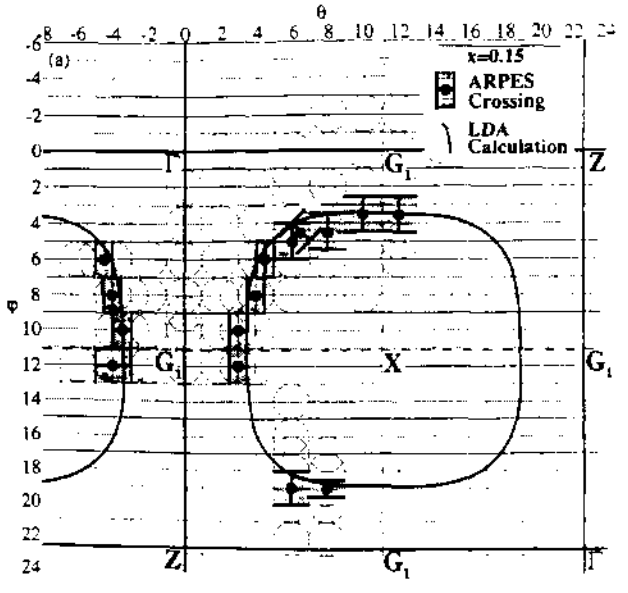

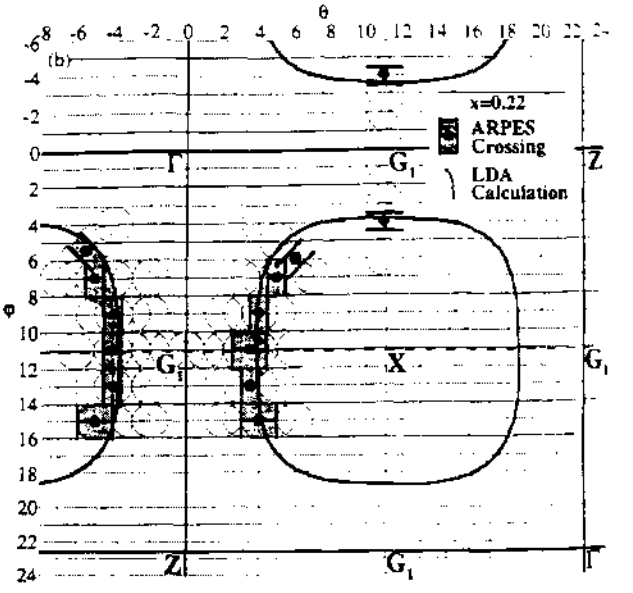

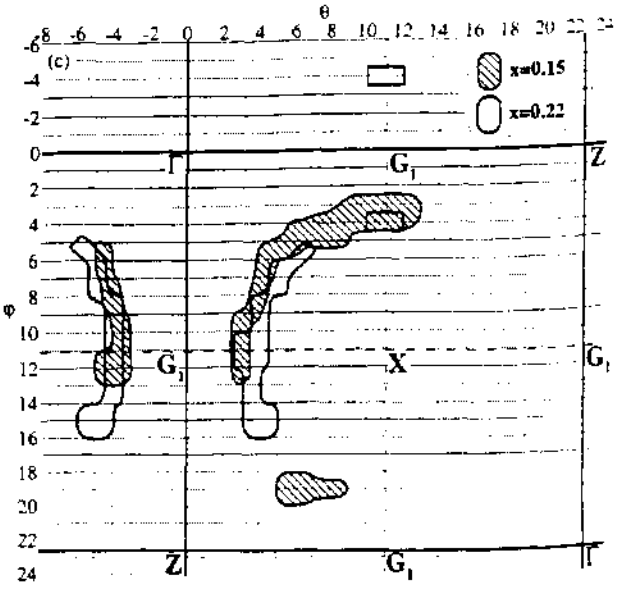

Fig. Experimental FS compared with results from LDA calculations for (a) x=0.15 and (b) x=0.22. In panel (c), the experimental FS from panels (a) and (b) are overlaid. The points with error bars show the experimental FS. The solid line represents the LDA calculated FS with k_z integration included in the line width. The empty circles show k-space locations where ARPES experiments have been performed. The data show remarkable symmetry with respect to Γ-G_1-Z high symmetry direction.

A Complete Mapping of the Fermi Surface of $Bi_2Sr_2CaCu_2O_8$

D.S. Dessau,[1,2] Z.-X. Shen,[1,2] D.M. King,[1] D.S. Marshall,[1] J. DiCarlo,[1,2] A.G. Loeser,[1] C.H. Park,[1]
W.E. Spicer,[1] L.W. Lombardo,[2] and A. Kapitulnik[2]

[1]*Stanford Electronics Laboratory and Stanford Synchrotron Radiation Laboratory,*
[2]*Department of Applied Physics, Stanford University, Stanford, California 94305*

We have used high energy resolution ARPES to measure the Fermi surface over the entire 2D Brillouin zone of single crystals of $Bi_2Sr_2CaCu_2O_8$ (Bi2212). Fig. 1 presents selected angle resolved spectra from the near E_F region taken at 100K (in the normal state). Sharp features corresponding to energy bands (and denoted by the triangles) are observed to disperse in energy as the emission angle (**k**) is varied. On the basis of data such as those in figure 1, we obtained the experimental Fermi surface as shown in Fig.2. The various circles represent the **k**-space locations sampled. The black circles represent the locations where a band is observed to cross E_F, with the solid lines through the black dots representing the experimental Fermi surface. This experimental Fermi surface can be well described by LDA [1] or tight-binding calculations considering only the two CuO_2 planes per unit cell. The grey circles represent the **k**-space location (near $\bar{M}$)where a flat band very close to E_F has been observed (see for example the top portions of cut 2 and the bottom portion of cut 5). These flat bands arrise from a saddle-point in the band structure which happens to lie very near E_F for Bi2212, and will lead to a strongly anisotropic $N(E_F)$ which will be strongly weighted near M. This may have important implications for understanding many of the anomolous normal state [e.g. Hall effect, susceptibility, thermopower] as well as superconducting state properties [e.g. gap anisotropy [2], magnitude of the T_c] exhibited by most of the HTSC's. This saddle point is observed at E_F at the corresponding **k**-space location of YBCO [3,4], though is found to be a few hundred meV below E_F in the n-type superconductor NCCO.[5]

Fig.2. A grid representing the energy position of the dispersive peak for each measurement location throughout the Brillouin zone. Dark circles are experimentally determined FS crossings, and the striped circles represent locations where the peak is very close to E_F, suggesting very flat bands and a high $N(E_F)$ contribution.

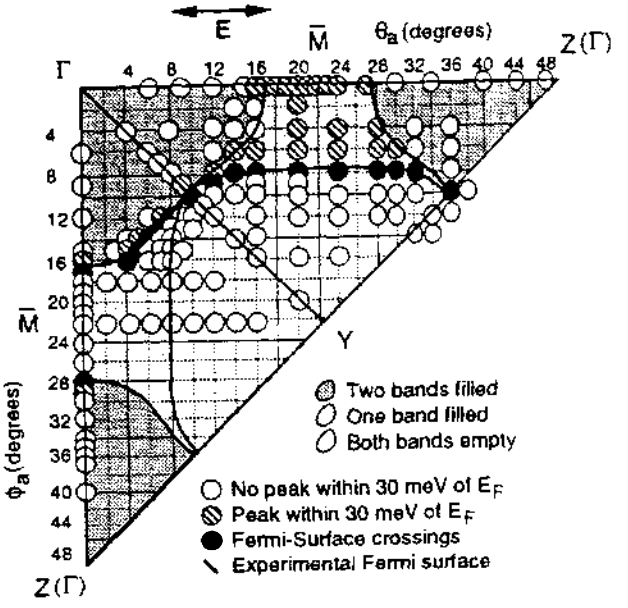

1. S. Massidda et al., Physica C **152**, 251 (1988)
2. B.O. Wells et al., Phys. Rev. B **46**, 11830 (1992)
3. R. Liu et al., Phys. Rev. B **45**, 5614 (1992)
4. J. Tobin et al., Phys. Rev. B **45**, 5563 (1992)
5. D. King et al, Submitted to Phys, Rev. Lett.

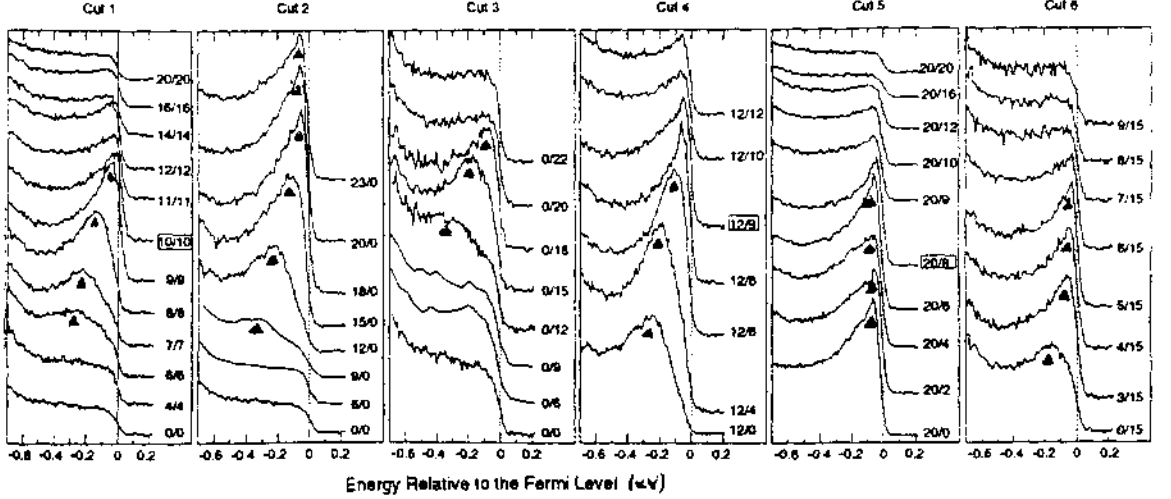

Fig.1 High energy resolution ARPES data from a $T_c = 85K$ Bi2212 single crystal taken at 100K. The numbers marked beside each spectra are angles θ and ϕ, as marked in the grid of Fig.2.

Imaging of A Surface Alloy with Energy-Dependent Photoelectron Holography

J.G. Tobin[A], G.D. Waddill[A], Hua Li[B], and S.Y. Tong[B]

[A]Chemistry & Materials Science Dept., Lawrence Livermore National Laboratory, Livermore, CA 94550

[B]Laboratory for Surface Studies & Dept of Physics, University of Wisconsin-Milwaukee, WI 53201

ABSTRACT

Fourier transformation of experimental energy-dependent photoelectron diffraction data has been used to produce an essentially artifact-free image of a surface alloy. This direct method, based upon the intersection of contour arcs associated with each measurement direction, can provide vectorial atomic positions with atomic resolution. A rapid data collection mode was introduced. Surface structural sensitivity was confirmed by comparison with multiple-scattering simulations. The previously ambiguous surface geometry of c(2x2) Au/Cu(001) has been determined, with clear, non-model-dependent discrimination of the surface alloy over the overlayer structure.

DISCUSSION

An elusive goal of surface crystallography is the development of a reliable direct method which reveals surface geometry with atomic resolution and chemical selectivity. An interesting idea, originally proposed by Szoke[1] and extended by Barton[2], was to apply a Fourier transformation (FT) to Auger- or photo-electron diffraction intensities over a wide angular range at a fixed kinetic energy. Early experimental work[3] seemed to confirm the validity of this approach. More recent investigations, based on simulated[4,5] and measured[6,7] diffraction spectra, have pointed out severe limitations of the single-energy transformation[8,9] . These limitations are due to the presence of artifacts in the reconstructed image in the form of bright spots or streaks at non-atomic positions. While simplified procedures[10] requiring more explicit prior knowledge of the structure have been suggested, the most promising method of resolution improvement, twin image suppression and artifact removal in electron holography appears to be the utilization of multiple energies[4,11,12]. It is this necessity of using multiple energies that leads us to consider a variant of photoelectron imaging in which sampling over a wide energy range is utilized.

Here we present a combined experimental and computational study that demonstrates direct wave-front reconstruction to obtain surface structure with atomic resolution using spatially-resolved imaging of energy-dependent photoelectron diffraction (SRI-EDPD). The theory behind this method has been presented earlier[13], but this is the first experimental investigation utilizing this particular approach. Moreover, while Fourier-transformation (FT) of experimental data provides a direct image of the surface structure, detailed multiple-scattering simulations and transformation of calculated intensities are used to verify the analysis. The crucial results are shown in Figure 1. Both the first in-plane nearest neighbors (Cu) and second in-plane nearest neighbors (Au) are imaged with atomic resolution, *without the intrusion of artifact peaks*. The system studied, 1/2-monolayer, c(2x2) Au/Cu(001),[14–18] is a particularly severe test of this imaging technique, because of the complexity of this system which exhibits competing growth modes involving surface-alloying, bulk-alloying and overlayer formation. It is shown that the c(2x2) surface alloy is clearly observed, and that the surface alloy is easily differentiated from a c(2x2) overlayer. It should be pointed out that such a non-model-dependent discrimination of a surface alloy from an overlayer is impossible using more-conventional diffraction techniques.

Although multiple-energy wave-front reconstruction had been carried out using experimental data[19,20], the previous works were done on bulk emission systems in which the structural information was averaged over many layers (i.e., the surface and bulk interlayer spacings mixed together). The present study is the first experimental demonstration of data inversion in which single-layer information is obtained. The atomic structure within the surface plane of the c(2x2) Au/Cu(001) system is directly imaged. This system contains strongly scattering Au and Cu potentials. Therefore, multiple wave-number phase-locking is essential to the success of the reconstruction process.

While this is the first demonstration of SRI-EDPD, structural studies with energy-dependent photoelectron diffraction (EDPD) have been done for quite some time[21,22]. Fourier transformation of the data has also been pursued: Early works[23-25], done on a fairly empirical basis, suggested that there was some validity to this method for determining *scalar* distances with normal emission. Subsequent attempts at improvement used energy variations along a few high symmetry directions[26,27]. But again, in these early works the goal was to extract *scalar* distances between the emitter and surrounding scatterers. The present approach involves inverting energy variation curves (over a 200 eV range) at a large number (48) of angular positions, and the idea is to extract *vector* (i.e., direction and distance) information relating an emitter and its neighbors. It is only because of our improved data collection mode that a full data set could be collected in a reasonable amount of time (approximately 12 hours total). The experiments were performed at the Stanford Synchrotron Radiation Laboratory using Beamline 8–2. This is a spherical grating monochromator beamline[28,29] which is part of the UC/National Laboratories Participating Research Team (PRT) facilities.

Although some peak distortion and shifting relative to the true positions can be observed in Figure 1, all of this is easily within 1Å. This observation can be discussed more effectively by comparison to the simulation of theoretical spectra. Also shown in Figure 1 are two Fourier transformations of calculated EDPD curves, generated by applying multiple scattering theory to the c(2x2) Au/Cu(001) surface alloy and overlayer models. (Again, note the strong agreement between the experimental results and those of the alloy model.) Even in images obtained from the theoretical curves, some peak position shifting occurs. The shifts are due to anisotropic factors (both in phase and magnitude) of the Au and Cu scattering factors[30]. The salient result in Figure 1 is that the FT of both the surface alloy and overlayer simulations recover the essence of each real space model, without the addition of artifact peaks. However, it appears that peak position shifting becomes progressively worse moving away from the central emitter. Thus only first and second nearest neighbor positions can be determined accurately with this database. (The data ranges used in the theoretical and experimental inversions are identical.) In the case of the overlayer, a less arealy dense structure, the second nearest neighbors are 5.1Å away, but in the surface alloy these atoms are now third nearest neighbors and exhibiting greater shifting as well as peak splitting[13]. The lateral distortion of the nearest neighbor Cu peaks in the experimental FT is absent in the surface alloy simulation: This appears to be related to surface vibrations in the real sample as well as systematic uncertainties in the data acquisition, such as sample alignment.

In summary, the reconstruction formula for inverting EDPD spectra has been applied to experimental data. First results for the c(2x2) Au/Cu(001) system are encouraging, demonstrating two-dimensional vectorial imaging. By achieving atomic resolution of less than 1Å, the reconstruction image shows directly and conclusively that the Au/Cu(001) system involves alloying in the surface layer. Further work is in progress using both regular photoemission spectra and spin-dependent photoemission with circularly-polarized x-ray beams[31].

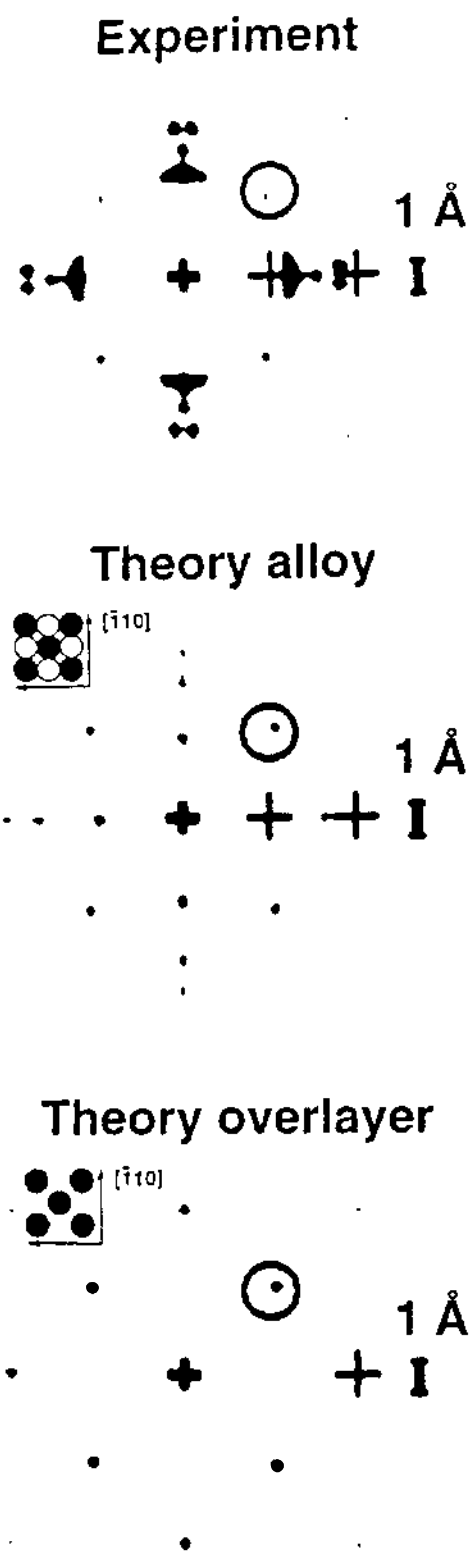

Figure 1. Images reconstructed from experimental spectra (top), calculated spectra for the surface alloy model (middle) and overlayer model (bottom). In each picture, the thick cross marks the Au emitter's position, thin crosses and the circle mark the expected atom positions of neighbors in a $\Pi/4$ sector.. The plane-of-view passes through the nuclei of surface layer atoms, see insets for surface models. [Au=solid circle, and Cu=hollow circle.] The experiment clearly agrees with the surface alloy model.

REFERENCES

1. A. Szoke, in "Short Wavelength Coherent Radiation Generation and Applications," ed. D.T. Attwood and J. Boker, AIP Conf. Proc. 142 (Am. Inst. Phys., New York, 1986)
2. J.J. Barton, Phys. Rev. Lett., 61, 1356 (1988).
3. G.K. Harp, et. al., Phys. Rev. Lett., 65, 1012 (1990).
4. H. Huang, Hua Li, and S.Y. Tong, Phys. Rev. B, 44, 3240 (1991).
5. S. Thevuthasan, et. al., Phys. Rev. Lett., 67, 469 (1991).
6. S.A. Chambers, V.A. Loebs, Hua Li, and S.Y. Tong, J. Vac. Sci. Technol., B10, 2092 (1992).
7. A. Stuck, et. al., Surf. Sci., 264, 380 (1992); A. Stuck, et. al., Surf. Sci., 274, 441 (1992).
8. L.J. Terminello and J.J. Barton, Science, 251, 1218 (1991).
9. S.A. Chambers, Adv. In Physics, 40, 357 (1991) and references therein; Surf Sci. Reports, 16, 261 (1992), and references therein.
10. R. Dippel, et. al., Phys. Rev. Lett., 68, 1543 (1992).
11. J.J. Barton and L.J. Terminello, in "The Structure of Surfaces–III," eds. S.Y. Tong, M.A. Van Hove, X. Xie, and J. Takayanagi, Springer, Berlin (1991); J.J. Barton, Phys. Rev. Lett., 67, 3106 (1991).
12. S.Y. Tong, Hua Li, and H. Huang, Phys. Rev. Lett. 67, 3102 (1991).
13. S.Y. Tong, H. Huang, and C.M. Wei, Phys. Rev. B, 46, 2452 (1992).
14. P.W. Palmberg and T.N. Rhodin, J. Chem. Phys., 49, 134 (1968); 49, 147 (1968).
15. Z.Q. Wang, et. al., Solid State Comm., 62, 181 (1987).
16. J.C. Hansen, et. al., Phys. Rev. B 36, 6186 (1987); J.C. Hansen and J.G. Tobin, J. Vac. Sci. Tech., A7, 2475 (1989); J.G. Tobin, et. al., J. Vac. Sci. Tech., A8, 2494 (1990); J.C. Hansen, et. al., Solid-State Comm. 72, 319 (1989).
17. D. Naumovic, et. al., Surf. Sci., 269/270, 719 (1992); Surf. Sci., XXX, (199X).
18. D.D. Chambliss, et. al., J. Vac. Sci. Tech., A10, 1993 (1992).
19. L.J. Terminello, et. al., J. Vac. Sci. Technol. B, 10, 2088 (1992).
20. H. Li, S.Y. Tong, D. Naumovic, A. Stuck, and J. Osterwalder, Phys. Rev. B, XX, XXXX (1993).
21. S.Y. Tong and C.H. Li, Bull. Am. Phys. Soc., 23, 417 (1978); C.H. Li, and S.Y. Tong, Phys. Rev. B 19, 1769 (1979); Ibid, Phys. Rev. Lett. 42, 901 (1979); Ibid. Phys. Rev. Lett. 43, 526 (1979).
22. S.D. Kevan, D.H. Rosenblatt, D. Denley, B.-C. Lus, and D.A. Shirley, Phys. Rev. Lett. 41, 1565 (1978).
23. Z. Hussain, D.A. Shirley, C.H. Li, and S.Y. Tong, Proc. Nat. Acad. Sci. 78, 5293 (1981).
24. D.H. Rosenblatt, et. al., Phys. Rev. B 23, 3828 (1981).
25. J.G. Tobin, et. al., Phys. Rev. B 26, 7076 (1982); S.Y. Tong, et. al., Phys. Rev. B 27, 4632 (1983).
26. J.J. Barton, C.C. Bahr, Z. Hussain, S.W. Robey, J.G. Tobin, L.E. Klebanderf and D.A. Shirley, Phys. Rev. Lett. 51, 272 (1983).
27. C.C. Bahr, J.J. Barton, Z. Hussain, S.W. Robey, J.G. Tobin, and D.A. Shirley, Phys. Rev. B 35, 3773 (1987).
28. K.G. Tersell, and V.P. Karpenko, Nucl. Inst. Meth. A291, 511 (1990).
29. L.J. Terminello, G.D. Waddill, and J.G. Tobin, Nuc. Instrum. Methods A319, 271 (1992).
30. S.Y. Tong, C.M. Wei, T.C. Zhao, H. Huang, and Hua Li, Phys. Rev. Lett. 66, 60 (1991).
31. J.G. Tobin, G.D. Waddill, and D.P. Pappas, Phys. Rev. Lett. 68, 3642 (1992); G.D. Waddill, J.G. Tobin, and D.P. Pappas, Phys. Rev. B, 46, 552 (1992).

ACKNOWLEDGMENTS

This work was conducted in part under the auspices of the U.S. Department of Energy by LLNL under contract no. W–7405–ENG–48. The SSRL is supported by DOE/BES. The work at the University of Wisconsin-Milwaukee was supported by NSF Grant No. DMR–9214054. Karen Clark provided clerical support for this work at LLNL.

VII ACTIVE PROPOSALS

SSRL accepts a variety of proposal types. These include a) full peer-reviewed proposals, b) letters of intent, c) rapid turnaround EXAFS proposals and d) rotation camera proposals for protein crystallography. Beam time is also assigned by the Participating Research Teams on their beam lines based on application to the PRT. As of December 31, 1992 there were 150 active proposals: 89 peer-reviewed, 4 rapid turnaround EXAFS, 28 rotation camera proposals, 23 letters of intent and 6 PRTs. The letter suffix appended to the proposal number indicates the Proposal Review Panel to which the proposal is assigned: Materials (M), Biology (B) or Vacuum Ultraviolet (VUV). The small "p" denotes a program propsal. The date is the original date of receipt. Peer-reviewed single project proposals remain active for two years after their initial rating, while program proposals can be renewed for an additional two years. The first person under each proposal is the proposal spokesperson and the institution listed is that of the spokesperson.

1021Mp 3/03/86 **Synchrotron X-ray Polycrystalline Diffractometry**
George Castro
Maurizio Bellotto
Curt Erickson
Michael Hart
Ting C Huang
George Will
(IBM RESEARCH LABORATORY)

2091Mp 3/15/89 **Strain Mapping and Crystal Characterization Using Synchrotron Radiation Polychromatic Topography**
S R Stock
Y H Chung
T S Gross
A B Lee
J D Plummer
Zofia U Rek
(GEORGIA INSTITUTE OF TECHNOLOGY)

2103Vp 9/10/89 **Photoemission Study of High T_c Superconductors and Related Materials**
Z. X. Shen
W.E. Spicer
I. Lindau
(STANFORD UNIVERSITY)

2105Mp 9/19/89 **Damage and Crack Closure in Composite and Monolithic Materials**
S R Stock
M D Butts
A Guvenilir
Sang B Lee
Zofia U Rek
(GEORGIA INSTITUTE OF TECHNOLOGY)

2111Vp 3/01/90 **Structural Studies of Thiols and Alcohols on Mo and Rh Surfaces**
C M Friend
Joachim Stöhr
Benjamin C Wiegand
Xueping Xu
(HARVARD UNIVERSITY)

2114Bp 3/01/90 **Structural Interactions in Respiratory Proteins**
James O Alben
Craig F Hemann
John Hill
Kimerly Powell
Jianhong Pu
Zhouhong Shi
(OHIO STATE UNIVERSITY)

2115Mp 3/21/90 ***In-Situ* Determination of Surface and Interface Structure of Sputter Deposited Films**
Bruce M Clemens
Sean Brennan
(STANFORD UNIVERSITY)

2117Bp 3/21/90 **Kinetic Intermediates on the Pathway of Protein Folding: SAXS Studies**
Keith O Hodgson
Robert L Baldwin
Sebastian Doniach
David Eliezer
A Robertson
(STANFORD UNIVERSITY)

2118Mp 3/21/90 **Anomalous X-Ray Diffraction Studies of Crystal Structure and Valence Ordering**
George Kwei
Joyce A Goldstone
Jon M Lawrence
Andrew C Lawson
Robert B Von Dreele
(LOS ALAMOS NATIONAL LABORATORY)

2121Vp 8/28/90 **Spin Polarized Photoemission Studies of Magnetic Surfaces and Ultra-Thin Films**
Herbert Hopster
C R Brundle
D E Fowler
A C Luntz
D P Pappas
Z X Shen
(UNIVERSITY OF CALIFORNIA at IRVINE)

2123Vp 9/04/90 **Growth, Structure and Electrical Properties of Large Bandgap Materials**
Don Kania
Lawrence Pan
Brad Pate
Piero Pianetta
(LAWRENCE LIVERMORE NATIONAL LABORATORY)

2128Bp 9/11/90 **Technetium and Rhenium Imaging Agents and Therapeutic Radiopharmaceuticals**
Richard C Elder
Edward A Deutsch
(UNIVERSITY OF CINCINNATI)

2129Bp 9/14/90 **Synchrotron Radiation Detector Development Program**
William K Warburton
J S Iwanczyk
Stephen R Russell
(X-RAY INSTRUMENTATION ASSOCIATES)

2133Mp 9/19/90 **Determination of Local Epitaxy and Strain in Sputter-Deposited Films**
Bruce M Clemens
Sean Brennan
(STANFORD UNIVERSITY)

2134V 4/11/91 **Determination of the Ellipsoidal Polarization Parameters of VUV Radiation**
S V Bobashev
O S Vasyutinskii
(A F IOFFE INSTITUTE)

2135Mp 2/06/91 **Structure/Activity Relationships in the Vanadium-Phosphorous-Oxide System**
Robert M Friedman
Farrel W Lytle
Michael Thompson
(MONSANTO COMPANY)

2136Mp 2/06/91 **Investigation of the Structure and Chemistry of Surface Layers for Corrosion Protection**
Robert B Greegor
Farrel W Lytle
(BOEING COMPANY)

2137Bp 2/18/91 **X-Ray Absorption Spectroscopic Studies of Nickel-Containing Metalloenzymes**
Robert A Scott
Mitchell C Brenner
Li Ma
(UNIVERSITY OF GEORGIA)

2138Mp 2/27/91 **Local Atomic Structure of High-T_c Superconductors**
James B Boyce
Frank Bridges
Tord Claeson
Theodore H Geballe
(XEROX)

2139Mp 2/25/91 **Chemical Vapor Infiltration of Ceramic Matrix Composites**
John H Kinney
C A Lundgren
Monte Nichols
T L Starr
S R Stock
(LAWRENCE LIVERMORE NATIONAL LABORATORY)

2140Mp 2/28/91 **X-Ray Diffraction Studies on AX_2 Compounds: Example BeH_2**
J Akella
L C Ming
G S Smith
S T Weir
(LAWRENCE LIVERMORE NATIONAL LABORATORY)

2141M 3/01/91 **High Pressure Transition Mechanisms in Iron via EXAFS**
Robert L Ingalls
Daryl Crozier
Fuming Wang
(UNIVERSITY OF WASHINGTON)

2142Mp 3/04/91 **Anomalous Scattering of X-Rays**
David H Templeton
Lieselotte K Templeton
(LAWRENCE BERKELEY LABORATORY)

2143Mp 3/12/91 **XAS Study of Cation Chemisorption at Oxide-Water Interfaces**
Gordon E Brown
John R Bargar
Singfoong Cheah
Farrel W Lytle
Peggy O'Day
George A Parks
Per Persson
Steve Towle
N Xu
(STANFORD UNIVERSITY)

2144M 3/02/91 **X-Ray Absorption Study of Metal Ion Reactions at Semiconductor Surfaces**
Nathan S Lewis
(CALIFORNIA INSTITUTE OF TECHNOLOGY)

2145Vp 3/02/91 **Photoelectron Spectroscopic Studies of Inorganic Materials as Active Sites in Catalysis**
Edward I Solomon
Jeff Guckert
Paul Jones
Jennifer A May
(STANFORD UNIVERSITY)

2146Bp 3/14/91 **XAS K-Edge Studies of Ligands Bound to Open-Shell Metal Ions in Proteins and Model Compounds**
Keith O Hodgson
Britt Hedman
Susan Shadle
Edward I Solomon
(STANFORD UNIVERSITY)

2147M 3/14/91 **Small Angle X-Ray Scattering Studies of Microvoids in Amorphous Semiconductors**
D L Williamson
Yan Chen
Richard Crandall
G David Mooney
(COLORADO SCHOOL OF MINES)

2148Bp 3/15/91 **Structure↔Function Studies of the Intrinsic Metal Sites in RNA Polymerase from *E. coli***
Linda S Powers
Gunther L Eichhorn
Robert Sinclair
(UTAH STATE UNIVERSITY)

2149Bp	3/15/91	**Structure↔Function Studies of the Active Sites of Lignin Peroxidase, Peroxidases, and Models** Linda S Powers Robert Sinclair (UTAH STATE UNIVERSITY)
2150B	3/15/91	**X-Ray Absorption Studies of the Structure of Cytochrome-c Oxidase** James E Penner-Hahn Kimber Clark Timothy Dawes Olof Einarsdottir Katy Georgiadis Pamela Riggs Timothy Stemmler (UNIVERSITY OF MICHIGAN)
2151Bp	3/15/91	**Structural Characterization of Mercury Metalloproteins Using XAS** James E Penner-Hahn Kimber Clark Susan Miller Thomas V O'Halloran Pamela Riggs Timothy Stemmler (UNIVERSITY OF MICHIGAN)
2152Mp	3/15/91	**XAS Study of Metal Ion Partitioning at Water/Mineral Interfaces** Kim F Hayes Lynn E Katz James E Penner-Hahn (UNIVERSITY OF MICHIGAN)
2153Mp	3/15/91	**Composition Fluctuations in Amorphous Films** Michael Regan Arthur Bienenstock (STANFORD UNIVERSITY)
2154V	3/15/91	**Photoelectron Microscopy** Piero Pianetta Changyoung Kim Paul King Ingolf Lindau (STANFORD SYNCHROTRON RADIATION LABORATORY)
2155M	3/15/91	**EXAFS Study of Cordierite Crystallization in Presence of Bi_2O_3 Flux** Gordon E Brown K B Schwartz Glenn A Waychunas (STANFORD UNIVERSITY)
2156Vp	3/15/91	**Passivation of GaAs and InP by Sb Interlayers** Tom Kendelewicz Al Green Alberto Herrera William E Spicer Masao Yamada (STANFORD UNIVERSITY)

2157M	3/15/91	**Structural Characterization of Ferrihydrite Surface Sites, Structure, and Absorbate Geometries** Glenn A Waychunas James A Davis C.C. Fuller Brigid A Rea (STANFORD UNIVERSITY)
2158M	3/15/91	**Structures for Silver(I)-Crown Complexes in Liquid and Solid Phases** Nolan Mangelson Robert B Greegor Max W Hill Farrel W Lytle Lawrence B Rees (BRIGHAM YOUNG UNIVERSITY)
2159Bp	4/11/91	**Kinetic Structural Studies of Isocitrate Dehydrogenase Using Laue Crystallography** Barry Stoddard Daniel Koshland Michael Soltis (FRED HUTCHINSON CANCER RCH. CTR.)
2160B	7/12/91	**Multiwavelength X-Ray Analysis of Gene V Protein Crystals Containing Selenomethionine** Thomas C Terwilliger Henry Bellamy R Paul Phizackerley Andrew Wang Hong Zhang (LOS ALAMOS NATIONAL LABORATORY)
2161B	8/29/91	**Structural Studies of the *E. coli* Single Strand Binding Protein** David Ollis John Barton Nicholas Dixon Jennifer Thorn (THE AUSTRALIAN NATIONAL UNIVERSITY)
2162Bp	8/30/91	**Kinetic X-Ray Crystallography of Carbonmonoxy Myoglobin** Joel Berendzen Kelvin Chu Gregory Petsko Dagmar Ringe Ilme Schlichting (LOS ALAMOS NATIONAL LABORATORY)
2163Mp	9/04/91	**The Effect of Dilute Impurities on Bulk Melting** E A Stern Matthew Newville Bruce Ravel (UNIVERSITY OF WASHINGTON)

2165Mp 9/10/91 **Ultra-High Strength-High Temperature Surface Coatings**
John C Bilello
Zofia U Rek
Jun Tao
Mark Vill
Steve Yalisove
Zhen Zeng
(UNIVERSITY OF MICHIGAN)

2166Vp 9/16/91 **Calibration of M.S.S.T.A. Instruments**
Maxwell Allen
Troy W Barbee, Jr.
Craig De Forest
Richard Hoover
Charles Kankelborg
Joakim F Lindblom
Ray O'Neal
Arthur BC Walker
Thomas Willis
(STANFORD UNIVERSITY)

2167B 9/13/91 **Laue Studies of *Rb. sphaeroides* Photosynthetic Reaction Center**
Douglas C Rees
Art Chirino
George Feher
R Paul Phizackerley
Michael Soltis
(CALIFORNIA INSTITUTE OF TECHNOLOGY)

2169Vp 9/16/91 **X-Ray Standing Wave Studies of Adsorption Geometries at Selected Metal III-V Semiconductor Interfaces**
Tom Kendelewicz
Piero Pianetta
William E Spicer
Joe Woicik
(STANFORD UNIVERSITY)

2170Mp 9/16/91 **X-Ray Absorption Spectroscopy of Transformation-Toughene Zirconia Ceramics**
James E Penner-Hahn
I-Wei Chen
Ping Li
(UNIVERSITY OF MICHIGAN)

2171M 9/16/91 **X-Ray Scattering Studies of Epitaxial Calcium Fluoride on Silicon**
C A Lucas
Jeffrey B Kortright
D Loretto
I M Tidswell
Gerard Wong
(LAWRENCE BERKELEY LABORATORY)

2172M 9/18/91 **Interlayer Forces Between Tethered Chains**
Alice P Gast
Mark Fair
(STANFORD UNIVERSITY)

2173M	3/02/92	**High-Pressure Phase Transformation of Mantle Minerals** Murli H Manghnani L C Ming (UNIVERSITY OF HAWAII)
2174B	3/02/92	**Crystallographic Structure Determination of Sulfite Reductase Using Multi-Wavelength Anomalous Diffraction** Brian R Crane Elizabeth D Getzoff Duncan E McRee (THE SCRIPPS RESEARCH INSTITUTE)
2175Mp	3/02/92	**XAFS Investigation of Selected Topics in Coal and Environmental Science** G P Huffman F E Huggins Naresh Shah (UNIVERSITY OF KENTUCKY)
2176Vp	3/03/92	**Growth, Structure and Electronic Properties of Epitaxially Grown Si, Ge and SiGe Structure** Renyu Cao Piero Pianetta (STANFORD SYNCHROTRON RADIATION LABORATORY)
2177M	3/16/92	***In-Situ* X-Ray Absorption Spectroscopy of Transition Metal Macrocycles Adsorbed on High-Area-Carbon** Daniel A Scherson Sunghyun Kim Marnita Sandifer Donald Tryk (CASE WESTERN RESERVE UNIVERSITY)
2178M	3/10/92	**Mechanism of Formation of Synthetic Clay Catalysts by SAXS and ASAXS** P Thiyagarajan K Carrado Keith O Hodgson (ARGONNE NATIONAL LABORATORY)
2179M	3/10/92	**Distribution of Active Sites on Clay Surfaces by SAXS and ASAXS** P Thiyagarajan K Carrado Keith O Hodgson S R Wasserman (ARGONNE NATIONAL LABORATORY)
2180B	3/13/92	**X-Ray Absorption Spectroscopic Studies of Copper-Containing Metalloenzymes** Robert A Scott David M Dooley Shengke Wang (UNIVERSITY OF GEORGIA)

2181Bp 3/13/92 **X-Ray Absorption Spectroscopy Studies of Manganese Redox Enzymes**
James E Penner-Hahn
Martha Ludwig
Rui Mei
Vincent L Pecoraro
Pamela Riggs
Timothy Stemmler
Charles F Yocum
(UNIVERSITY OF MICHIGAN)

2182Mp 3/13/92 ***In Situ* X-Ray Studies of OMVPE Growth**
Paul H Fuoss
Sean Brennan
D W Kisker
R M Lum
Brian Stephenson
(AT&T BELL LABORATORIES)

2184B 3/16/92 **Subunit Assembly and Conformational Changes of Aspartate Transcarbamylase (ATCase)**
Eric R Johnson
Howard Schachman
Hiro Tsuruta
Bingbing Zhou
(UNIVERSITY OF CALIFORNIA at BERKELEY)

2185Mp 3/16/92 **A Multilayer Mirror Monochromator for Dual Energy Digital Subtraction Angiography**
David G Boyers
Adrian Ho
Melvin A Piestrup
Li Qiang
Roman Tatchyn
(ADELPHI TECHNOLOGY)

2186Bp 3/16/92 **XAS Structural Characterization of the Dinuclear Ironcenter in Methane Monooxygenase**
Keith O Hodgson
Jane Dewitt
Britt Hedman
Stephen J Lippard
Amy Rosenzweig
(STANFORD UNIVERSITY)

2187Bp 3/16/92 **Time Resolved Protein Folding Studies Using Laue ("White" Beam) Small Angle X-Ray Scattering**
Sebastian Doniach
Robert Byer
Lingling Chen
David Eliezer
Keith O Hodgson
Hiro Tsuruta
(STANFORD UNIVERSITY)

2188M 3/16/92 **Shallow and Deep Donors in Al_xGa_{1-x} Semiconducting Alloys**
T M Hayes
J Pant

D L Williamson
(RENSSELAER POLYTECHNIC INSTITUTE)

2189Mp 3/16/92 **Speciation of Hazardous Waste by X-Ray Absorption Spectroscopy**
Farrel W Lytle
Mel Lytle
(THE EXAFS COMPANY)

2190Bp 3/25/92 **X-Ray Absorption Spectroscopy of Manganese Involved in Photosynthetic Oxygen Evolution**
Melvin P Klein
Holger Dau
Matthew Latimer
Wenchuan Liang
Theo A Roelofs
Kenneth Sauer
Vittal K Yachandra
J L Zimmermann
(LAWRENCE BERKELEY LABORATORY)

2191Mp 3/30/92 **Proposal to Develop Hard X-Ray Optics and Microimaging Facility**
Richard Bionta
Ken Skulina
(LAWRENCE LIVERMORE NATIONAL LABORATORY)

2192Bp 8/31/92 **XAS Structural Characterisation of a Manganese-Enzyme, Prolidase**
Hans C Freeman
Paul J Ellis
Britt Hedman
Keith O Hodgson
Emma M Proudfoot
(UNIVERSITY OF SYDNEY)

2193M 9/02/92 **XAFS Studies of Perovskite Related Structures at High Pressure**
Robert L Ingalls
Daryl Crozier
B Houser
(UNIVERSITY OF WASHINGTON)

2194Mp 9/03/92 **Determination of the Strain Distribution in Metallic Thin Films and Lines as a Function of Temperature Using GIXS**
John C Bravman
Paul Besser
Sean Brennan
Ram Venkatraman
Rick Vinci
(STANFORD UNIVERSITY)

2195Mp 9/02/92 **Investigation of High Temperature Surfaces by X-ray Spectroscopy**
David L Styris
Richard Gordon
Farrel W Lytle
(PACIFIC NORTHWEST LABORATORIES)

2196V 8/31/92 **Relaxation of High Energy Electronic Excitation in Wide Band Crystals Under VUV and XUV Radiation**
Mickail Terekhin
Andrey Kolmakov
(KURCHATOV INSTITUTE)

2197Mp 8/03/92 **Investigation of Heavily-Doped III-V and II-VI Semiconductors Using Fluorescence EXAFS**
Kin Man Yu
Edith D Bourret
E E Haller
J Jaklevic
Carolyn Rossington
Wladyslaw Walukiewicz
(LAWRENCE BERKELEY LABORATORY)

2198Bp 9/09/92 **Investigation of the Structure of LTA_4**
Robert M Friedman
Leslie Askonas
Farrel W Lytle
(MONSANTO COMPANY)

2199Vp 9/14/92 **High-Photon-Flux Photoemission Studies of Narrow Band Materials**
Jim Allen
R Claessen
Z X Shen
L H Tjeng
(UNIVERSITY OF MICHIGAN)

2200Mp 9/14/92 **Kinetic Studies of OMVPE Growth Using *In Situ* X-ray Scattering**
D W Kisker
Sean Brennan
Paul H Fuoss
R M Lum
Brian Stephenson
(IBM RESEARCH LABORATORY)

2201B 9/15/92 **The Organization of DNA within Mammalian Sperm Cells**
Nicholas Hud
Rod Balhorn
Hirotsugu Tsuruta
(LAWRENCE LIVERMORE NATIONAL LABORATORY)

2202Vp 9/15/92 **Application of Magnetic Circular X-ray Dichroism to Magnetic Multilayers and Imaging of Magnetic Domains**
Joachim Stöhr
B D Hermsmeier
M Samant
(IBM RESEARCH LABORATORY)

2203Mp 9/16/92 **EXAFS Spectroelectrochemistry**
Richard C Elder
William R Heineman
(UNIVERSITY OF CINCINNATI)

2204M 9/16/92 **Characterization of Amorphous to Crystalline Phase Transformation in Silica**
David F Blake
Jack Farmer
Nancy Hinman
(NASA-AMES RESEARCH)

2205Mp 9/17/92 **Uranium Speciation in Soils**
Steve D Conradson
C Chisolm
D W Morris
(LOS ALAMOS NATIONAL LABORATORY)

2206Mp 9/17/95 **Structure-Reactivity-Performance Relationships in Mesoscale Platinum-Based Catalysts**
Steve D Conradson
Patrick G Allen
Shimshon Gottesfeld
Ian D Raistrick
(LOS ALAMOS NATIONAL LABORATORY)

2207Mp 9/17/92 **Local Structure in High Temperature Superconductors**
Steve D Conradson
Jose Mustre De Leon
Ian D Raistrick
(LOS ALAMOS NATIONAL LABORATORY)

2208M 9/18/92 **Measurement of Chemical and Structural Anisotrophy in Amorphous Tb-Fe Thin Films**
Todd Hufnagel
Sean Brennan
Bruce M Clemens
(STANFORD UNIVERSITY)

2209M 9/18/92 **Structural Changes Induced by Magnetic Fields in Magnetostrictive Materials**
Daryl Crozier
Y Bonin
(SIMON FRASER UNIVERSITY)

2210Mp 9/18/92 **Grazing-Incidence XAS Study of Cation Chemisorption at Single-Crystal Oxide Surfaces**
Gordon E Brown
Troy W Barbee, Jr.
John R Bargar
Ping Liu
George A Parks
Per Persson
Ingrid Pickering
Steve Towle
Glenn A Waychunas
(STANFORD UNIVERSITY)

2211Vp 9/25/92 **Electron Spectroscopy of Gases, Solids and Surfaces**
Zahid Hussain
Philip A Heimann
Zheng-Qing Huang
Eric Hudson
Tony Huff
Scot Kellar
Eddie Moler
Barry Petersen
Tobias Reich
David A Shirley
Pradeep Thalappil
Yu Zheng
(LAWRENCE BERKELEY LABORATORY)

ROTATION CAMERA PROPOSALS

2A14B 3/01/91 **Structural Studies of *E. coli* DNA Topoisomerase I**
Alfonso Mondragon
Christopher Lima
Neal Lue
Amit Sharma
(NORTHWESTERN UNIVERSITY)

2A19B 4/22/91 **Summary of Human Recombinant Factor XIII Experiment**

2A39B	1/24/92	**X-ray Data Collection on Crystals of the Hormone Binding Domain of the Thyroid Hormone Receptor Using Low Temperature and Synchrotron Radiation** Mary E McGrath James Apriletti John Baxter Robert J Fletterick Richard Wagner Brian West (UNIVERSITY OF CALIFORNIA at SAN FRANCISCO)
2A40B	1/02/92	**Data Collection of Proteasome Crystals** Bing Jap Wolfgang Baumeister (LAWRENCE BERKELEY LABORATORY)
2A41B	2/11/92	**The Structure of the Heat Shock Transcription Factor (HSF) from *Saccharomyces cerevisiae, Kluyveromyces lactis*** Hillary Nelson Karen Flick Celia Harrison (UNIVERSITY OF CALIFORNIA at BERKELEY)
2A42B	2/27/92	**Crystallographic Analysis of Molybdenum and Tungsten-Containing Proteins** Douglas C Rees Michael Chan Jong-Sun Kim (CALIFORNIA INSTITUTE OF TECHNOLOGY)
2A43B	3/16/92	**High Resolution Refinement of the Structure of HIV-1 Rnase** Howard M Einspahr D Chattopadhyay B C Finzel (THE UPJOHN COMPANY)
2A44B	3/20/92	**Single Crystal Diffraction Data Collection on Channel Forming Natural Insectide Proteins from Bacillus Thuringiensis Kurstaki** Robert M Stroud Doug Freymann V Ramalingam Michael Wiener (UNIVERSITY OF CALIFORNIA at SAN FRANCISCO)
2A45B	5/12/92	**Native Data Collection on the Ferric Binding Protein from *N. gonorrhoeae*** Michele A McTigue (THE SCRIPPS RESEARCH INSTITUTE)
2A46B	9/09/92	**X-ray Diffraction Investigation of Cytochrome Reductase Crystals** Ed Berry Thomas Earnest Li-Shar Huang Bing Jap (UNIVERSITY OF CALIFORNIA at BERKELEY)

2A47B	9/25/92	**Crystallographic Studies of Electron Transfer Proteins** Douglas C Rees Michael Chan Barbara Hsu Leemor Joshua-Tor Tim McPhillips Michael Stowell (CALIFORNIA INSTITUTE OF TECHNOLOGY)
2A48B	9/28/92	**X-ray Diffraction Studies on: (1) Mutants of the ras Oncogene Protein (2) Aspartate Receptor (ligand-binding domain)** Sung-Hou Kim Andrew Bohm H Debondt B Oh Jay Pandit K Phillips X-W Weng J J Yeh (UNIVERSITY OF CALIFORNIA at BERKELEY)
2A49B	10/01/92	**Biotin Repressor - DNA Complex** William R Tulip (UNIVERSITY OF OREGON)
2A50B	10/01/92	**X-ray Crystallographic Studies of Methane Monooxygenase** Stephen J Lippard Christin Frederick Amy Rosenzweig (MASSACHUSETTS INSTITUTE OF TECHNOLOGY)
2A51B	10/07/92	**The Crystal Structure of Colicin Ia: Determination by Cryocrystallography** Michael Wiener Robert M Stroud (UNIVERSITY OF CALIFORNIA at SAN FRANCISCO)
2A52B	10/08/92	**Data Collection for Thymidylate Synthase from *pneumocystis carinii*** Kathy Perry Dan Santi Robert M Stroud (UNIVERSITY OF CALIFORNIA at SAN FRANCISCO)
2A53B	10/14/92	**Structure of Theiler's Virus, Hepatitis A Virus and Influenza Virus neuraminidase** Ming Luo Janakiraman Ken Toth Jun Tsao Clint White Carl Zhang Lan Zhou (UNIVERSITY OF ALABAMA)
2A54B	10/14/92	**Low Resolution Data Collection of Yeast RNA Polymerase II (Pol II)** Peter David Roger Kornberg

(STANFORD UNIVERSITY)

2A55B 10/16/92 **The Denovo Crystal Structure of a Kinase-Enzyme Complex**
Diana B Cherbavaz
Daniel Koshland
David Laporte
Robert M Stroud
(UNIVERSITY OF CALIFORNIA at SAN FRANCISCO)

2A56B 10/16/92 **High Resolution Analysis of Subtilisin Native and Variant Enzymes**
Richard Bott
Shan Wu
(GENENCOR INTERNATIONAL)

2A57B 10/19/92 **Crystallographic Study of HIV-1 Protease in Complex with Non-Peptide Inhibitors**
Earl Rutenber
Charles Craik
George Kenyon
I D Kuntz
(UNIVERSITY OF CALIFORNIA at SAN FRANCISCO)

2A58B 10/20/92 **Multiple Mutants of Thymidylate Synthase**
Robert M Stroud
Dan Santi
(UNIVERSITY OF CALIFORNIA at SAN FRANCISCO)

2A59B 10/20/92 **Heat-Labile Enterotoxin (LT) from *E. coli***
Ethan A Merritt
Wim Hol
Focco van den Akver
(UNIVERSITY OF WASHINGTON)

2A60B 10/26/92 **Data Collection of Mutants from E2pCD of the Pyruvate Dehydrogenase Multienzyme Complex (PDC)**
Jorg Hendle
Arie De Kok
Andrea Mattewi
(UNIVERSITY OF WASHINGTON)

2A61B 11/2/92 **Structural Studies of Receptor Signalling: Crystal Structures of Hormone Receptor Complexes**
Bart De Vos
Charles Eigenbrot
Tony Kossiakoff
Will Somers
(GENENTECH, INC.)

LETTERS OF INTENT

9064B 3/03/92 **Structure of DNA Modified by Cispatin**
Stephen J Lippard
(MASSACHUSETTS INSTITUTE OF TECHNOLOGY)

9065B 3/04/92 **Studies of Gallium Nitrate to Treat Bone Disease**
Lawrence R Bernstein
(MINERAL SEARCH)

9066V	3/05/92	**Circular Magnetic X-Ray Dichroism Experiments** M Samant (IBM RESEARCH LABORATORY)
9067M	3/12/92	**AWAXS of Amorphous Platinum Pyrimidine Derivatives** Ritva Serimaa (STANFORD SYNCHROTRON RADIATION LABORATORY)
9068M	3/13/92	**Study of X-ray Fluorescence Detection Limits of Metallic Contaminants** Michael Madden (INTEL CORPORATION)
9069M	3/13/92	**ASAXS Experiments** Pierre Lecante (CEMES-LOE)
9070M	3/13/92	**ASAXS Experiments II** Pierre Lecante (CEMES-LOE)
9071M	3/13/92	**X-ray Scattering Measurements of Polycrystalline and Single Crystal Magnetic Multilayers** Tom Rabedeau (IBM RESEARCH LABORATORY)
9072M	3/03/92	**Topographic Study of $K(H_{1-x}D_x)_2PO_4$** Jim De Yoreo (LAWRENCE LIVERMORE NATIONAL LABORATORY)
9073B	3/24/92	**Proposal for Mammography Project** John Arthur (STANFORD SYNCHROTRON RADIATION LABORATORY)
9074M	4/01/92	**Total Reflection X-ray Fluorescence** Stephen Laderman (HEWLETT PACKARD)
9075M	4/13/92	**Investigation of the Function of a Catalyst Used to Manufacture Circuit Boards** John Bladon (SHIPLEY COMPANY)
9076M	4/13/92	**Time Resolved Studies of Phase Separation of Di Block Copolymer Mixtures** Thomas P Russell (IBM RESEARCH LABORATORY)
9077B	5/15/92	**Novel Aluminophosphite and Gallophosphite Molecular Sieve Materials** Angus P Wilkinson (UNIVERSITY OF CALIFORNIA at SANTA BARBARA)
9078M	6/06/92	**Chevron Scattering Proposal** Guang Zhang (CHEVRON RESEARCH & TECHNOLOGY COMPANY)

9080M	6/18/92	**Ti Edge Studies** R J Davis (UNIVERSITY OF VIRGINIA)
9081M	6/20/92	**EXAFS Studies** Ingmar Persson (SWEDISH UNIVERSITY OF AGRICULTURAL SCIENCE)
9082M	5/01/92	**LANL Environmental Studies** Steve D Conradson (LOS ALAMOS NATIONAL LABORATORY)
9083M	9/14/92	**SAXS Study of Co Cluster Size in CoCu Granular Alloys** Tom Rabedeau Mike Toney (IBM RESEARCH LABORATORY)
9084B	10/01/92	**MAD Phasing of Crystals of the Heat Shock Transcription Factor** Celia Harrison Hillary Nelson (UNIVERSITY OF CALIFORNIA at BERKELEY)
9085B	10/14/92	**Low Resolution Data Collection of Yeast RNA Polymerase II** Peter David Seth Darst Roger Kornberg (STANFORD UNIVERSITY)
9086M	11/11/92	**EXAFS and Standing Wave Study of Atomic Environment of As in Si** Tom Kendelewicz Gordon E Brown Piero Pianetta William E Spicer (STANFORD UNIVERSITY)
9087V	1/16/92	**Magnetic Dichroic X-Ray Emission Spectroscopy** Anders Nilsson Olle Björneholm Laurent Duda Joseph Nordgren Nial Wassdahl (UPPSALA UNIVERSITET)

RAPID TURN-AROUND EXAFS PROPOSALS

1E07B	11/13/91	**Europium Valence in $EuCo_{2-x}Ni_xP_2$ and $EuNi_{2-x}Cu_xP_2$: an L_{III}-edge X-ray Absorption Spectroscopy (L_{III}-XAS) Study** Robert M Bornick George Kwei Angelica M Stacy (UNIVERSITY OF CALIFORNIA at BERKELEY)
1E08B	11/18/91	**Lanthanum Copper Oxides** Sarah L Stoll George Kwei

Angelica M Stacy
(UNIVERSITY OF CALIFORNIA at BERKELEY)

1E10M	7/24/92	**Determination of the Oxidation States of Uranium and Thorium Compounds** Norm Edelstein (LAWRENCE BERKELEY LABORATORY)
1E11M	9/09/92	**Fluorescence EXAFS Study of Ion Beam Modified III-V and II-VI Compound Semiconductors** Kin Man Yu J Jaklevic Carolyn Rossington Wladyslaw Walukiewicz (LAWRENCE BERKELEY LABORATORY)

PRT PROPOSALS
The spokesperson only is listed on the PRT Proposals

9300	**IBM PRT Time - Beam Line 10-1** Joachim Stöhr
9400	**Center for Materials Research (Stanford University) PRT Time - Beam Line 10-1** Piero Pianetta
9500	**EXXON PRT Time - Beam Line 6** Grayson Via
9600	**Lawrence Berkeley Laboratory PRT Time - Beam Line 6** Philip Ross
9700	**Stanford University PRT Time - Beam Line 5** William E. Spicer
9900	**National Laboratories/University of California PRT Time - Beam Lines 8 & 10** Marvin J. Weber

VIII SSRL EXPERIMENTERS AND PROPOSALS BY INSTITUTION

As of December 31, 1992 there were 432 experimenters from 93 institutions officially listed on active proposals at SSRL. In addition, well over 100 others (graduate students, etc.) participated in work at the laboratory in collaboration with these scientists. The 75 United States institutions listed on active proposals included 35 universities, 26 private institutions and 14 government laboratories.

PRIVATE INSTITUTIONS

Adelphi Technology, AT&T Bell Laboratories, Boeing Company, Chevron Research & Technology Company, Dana Farber Cancer Institute, Deacon Research, E.I. Du Pont de Nemours & Co., Exxon Research & Engineering, Fred Hutchinson Cancer Research Center, Genencor International, Genentech, Inc., Hewlett-Packard, Hirsch Associates, IBM Research Laboratory, Intel Corporation, Mineral Search, Monsanto Company, Raychem Corporation, Surface Interface, Syntex Research, The EXAFS Company, The Upjohn Company, X-Ray Instrumentation Associates, Xerox, Xsirius, Inc., Zymogenetics

GOVERNMENT LABORATORIES

Argonne National Laboratory, Lawrence Berkeley Laboratory, Lawrence Livermore National Laboratory, Los Alamos National Laboratory, NASA- Marshall Space Flight Center, NASA-Ames Research, National Institutes of Health, National Institute of Standards and Technology, Pacific Northwest Laboratories, Sandia National Laboratories, Solar Energy Research Institute, Stanford Synchrotron Radiation Laboratory, US Air Force, US Geological Survey Water Resources Division

UNIVERSITIES

Amherst College, Brandeis University, Brigham Young University, California Institute of Technology, Case Western Reserve University, Colorado School of Mines, Eastern Washington University, Georgia Institute of Technology, Harvard University, Massachusetts Institute of Technology, Northwestern University, Ohio State University, Pennsylvania State University, Rensselaer Polytechnic Institute, Stanford University, The Scripps Research Institute, University of Alabama, University of California, University of Cincinnati, University of Georgia, University of Hawaii, University of Illinois, University of Kentucky, University of Maryland, University of Michigan, University of Minnesota, University of Montana, University of New Hampshire, University of Oregon, University of Texas, University of Virginia, University of Washington, Utah State University, Washington State University, Washington University

FOREIGN INSTITUTIONS

A Ioffe Institute *(Russia)*, The Australian National University *(Australia)*, Chalmers Institute of Technology *(Sweden)*, CISE S.P.A. *(Italy)*, Kurchatov Institute *(Russia)*, Max Planck Institut *(Germany)*, Max-Laboratory *(Sweden)*, National Instititue of Research in Inorganic Materials *(Japan)*, Simon Fraser University *(Canada)*, Swedish University of Agricultural Sciences *(Sweden)*, The University Manchester *(England)*, Universita Di Brescia *(Italy)*, Universitat Bonn *(Germany)*, Universitat des Saarlandes *(Germany)*, University of Groningen *(The Netherlands)*, University of Sydney *(Australia)*, University of Wageungen *(The Netherlands)*, Uppsala Universitet *(Sweden)*

A note about SSRL proposal numbers: The 2000 numbers are peer-reviewed, rated SSRL proposals, the 9000 numbers are letters of intent. The 9300-9900 numbers are PRT proposals. The 8000 numbers are in-house research experiments. The 2A numbers are rotation camera applications and the 1E numbers are rapid turnaround XAS proposals.

AMERICAN CORPORATIONS

ADELPHI TECHNOLOGY

David G Boyers	2185
Adrian Ho	2185
Melvin A Piestrup	2185
Li Qiang	2185

AT&T BELL LABORATORIES

Paul H Fuoss	2182, 2200
R M Lum	2182, 2200

BOEING COMPANY

Robert B Greegor	2136, 2158

CHEVRON RESEARCH & TECHNOLOGY COMPANY

Guang Zhang	9078

DANA FARBER CANCER INSTITUTE

Christin Frederick	2A50

DEACON RESEARCH

Dave Deacon	8115

E.I. DU PONT DE NEMOURS & COMPANY

C A Lundgren	2139

EXXON RESEARCH & ENGINEERING

Daniel A Fischer	8115
Martin L Gorbaty	9503
Keng S Liang	9504
Roger C Prince	9505
Grayson H Via	9500, 9502

FRED HUTCHINSON CANCER RESEARCH CENTER

Barry Stoddard	2159

GENENCOR INTERNATIONAL

Richard Bott	2A56
Shan Wu	2A56

GENENTECH, INC.

Bart de Vos	2A61
Charles Eigenbrot	2A61
Tony Kossiakoff	2A61
Will Somers	2A61

HEWLETT-PACKARD

Stephen S Laderman	9074

HIRSCH ASSOCIATES

Gregory Hirsch	9053

IBM RESEARCH LABORATORY

C R Brundle	2121
George Castro	1021
M de Vries	8119
Curt Erickson	1021
D E Fowler	2121
B D Hermsmeier	2202, 2202
Ting C Huang	1021, 8103
D W Kisker	2182, 2200
A C Luntz	2121
D P Pappas	2121
Tom Rabedeau	9038
Thomas P Russell	9076
M Samant	2202, 2202, 9301
Brian Stephenson	2182, 2200
Joachim Stohr	2111, 2202, 2202, 9300
Mike Toney	9083

INTEL CORPORATION

Jacob Aidelberg	8103
D Brunner	8103
Kim Gupta	8058
Michael Madden	9068

MINERAL SEARCH

Lawrence R Bernstein	9065

MONSANTO COMPANY

Leslie Askonas	2198
Robert M Friedman	2135, 2198
D W Morris	2205

RAYCHEM CORPORATION

K B Schwartz	2155

SURFACE INTERFACE

Chuck Bryson	8115

SYNTEX RESEARCH

John Nestor	8050

THE EXAFS COMPANY

Farrel W Lytle	2135, 2136, 2143, 2158, 2189, 2195, 2198

THE UPJOHN COMPANY

D Chattopadhyay	2A43
Howard M Einspahr	2A43
B C Finzel	2A43

X-RAY INSTRUMENTATION ASSOCIATES

Stephen R Russell	2129
William K Warburton	2129

XEROX

James B Boyce	2138

XSIRIUS, INC.

J S Iwanczyk	2129, 8116

ZYMOGENETICS

Paul Bishop	2A29

AMERICAN LABORATORIES

ARGONNE NATIONAL LABORATORY

E E Alp	8003
K Carrado	2178, 2179
P Thiyagarajan	2178, 2179
S R Wasserman	2179

LAWRENCE BERKELEY LABORATORY

Edith D Bourret	2197
Holger Dau	2190
H Debondt	2A48
Thomas Earnest	2A46
N Edelstein	1E10
Charles S Fadley	9605
Robert Glaeser	9055
E E Haller	2197
Philip A Heimann	2211, 9601
Zheng-Qing Huang	2211
Eric Hudson	2211
Tony Huff	2211
Zahid Hussain	2211, 9609, 9916
J Jaklevic	1E11, 2197
Bing Jap	2A40, 2A46
Scot Kellar	2211
Melvin P Klein	2190
Jeffrey B Kortright	2171
Matthew Latimer	2190
Wenchuan Liang	2190
Z Liliental-Weber	8103
D Loretto	2171
C A Lucas	2171, 9606
Eddie Moler	2211
Barry Petersen	2211
K Phillips	2A48
Tobias Reich	2211
A Robertson	2117
Theo A Roelofs	2190
Philip N Ross	9600, 9603
Carolyn Rossington	1E11, 2197
Kenneth Sauer	2190
David Shuh	9926
David H Templeton	2142
Lieselotte K Templeton	2142
Pradeep Thalappil	2211
I M Tidswell	2171
Wladyslaw Walukiewicz	1E11, 2197, 9607
X-W Weng	2A48
Vittal K Yachandra	2190
Kin Man Yu	1E11, 2197
Yu Zheng	2211
J L Zimmermann	2190

LAWRENCE LIVERMORE NATIONAL LABORATORY

J Akella	2140
A J Arko	8119
Rod Balhorn	2201
Troy W Barbee, Jr.	2166, 2210, 9903
Richard M Bionta	2191
Jim De Yoreo	8103, 9072
Nicholas Hud	2201
Don Kania	2123
John H Kinney	2139
Ken Skulina	2191
G S Smith	2140
Louis J Terminello	9909
James Tobin	9901
Bruce Watkins	9917
Marvin J Weber	9900
S T Weir	2140
Joe Wong	8103, 9902

LOS ALAMOS NATIONAL LABORATORY

Patrick G Allen	2206
Joel Berendzen	2162
C Chisolm	2205
Steve D Conradson	2205, 2206, 2207 9082, 9924
Joyce A Goldstone	2118
Shimshon Gottesfeld	2206
George Kwei	1E07, 1E08, 2118
Jon M Lawrence	2118
Andrew C Lawson	2118
Jose Mustre De Leon	2207
Ian D Raistrick	2206, 2207
Thomas C Terwilliger	2160
Robert B Von Dreele	2118

NASA - MARSHALL SPACE FLIGHT CENTER

Richard Hoover	2166

NASA-AMES RESEARCH

David F Blake	2204
Jack Farmer	2204

AMERICAN UNIVERSITIES

FOREIGN UNIVERSITIES